Atomic Scale Simulations for Waste Form Applications

A dissertation submitted to the University of London
for the degree of Doctor of Philosophy
and the Diploma of Imperial College

by
Antony R. Cleave

Department of Materials
Imperial College of Science, Technology and Medicine 2006

Abstract

A major concern at the current time is the long term storage and the eventual disposal of radioactive waste. The aim of this thesis is, by the use of computer simulation techniques, to examine various topics relating to nuclear waste disposal. These topics include simulation of a possible wasteform material based on the pyrochlore structure, in order to determine: the relative solubilities of uranium and plutonium and also its stability with respect to the related fluorite and δ-phase structures. The results from these are presented in the form of composition maps which facilitates the identification of regions of greatest stability.

Once a waste form has been made, it is important to consider how it becomes damaged associated with to the decay processes of the radioactive species it contains. Molecular Dynamics were used to compare collision cascade events simulating α-recoils for the simple ceramic systems of pure and impure (doped with 0.2% Al) magnesium oxide. Analysis of the resulting cascade simulations showed that the anisotropy associated the direction of the damage profile was totally changed through the addition of impurities.

Acknowledgments

I would like to acknowledge the United States Department of energy for funding my work. On this topic I would also like to mention the hard work of Robin Grimes for selflessly battling the Imperial College bureaucracy, and thus allowing me to receive my bursary. Thanks also go to the Materials Department for providing me with a loan from the hardship fund during the time this war was being waged.

I would like to give special mention to my supervisors, Robin Grimes and Kurt Sickafus, for providing inspiration, assistance and useful discussions throughout this project. Special thanks go to Kurt for inviting me to visit LANL and sweet talking the ladies in the housing office to find me a place to stay (twice).

Thanks go to those in the research group for providing an interesting if variable working environment and special thanks go to Mark Levy for putting up with my continual interruptions via instant message and email throughout the writing of this thesis and for proof reading some of the chapters before passing it onto Robin for a final check. Thanks, yet again, go to Robin for performing the arduous job of proofreading all of my thesis and for giving

me a kick when I needed it!

I would like to acknowledge the work of Anthony Gomez who performed some of the calculations for chapter 4 as part of his final year project. Anthony was of one of the finest project students I have had the pleasure to supervise and I wish him will in whatever he goes on to do.

Thanks go to my family, especially my sister and my father for helping me out with support, money and accommodation when I needed it the most and last, but by no means least. I would like to thank Joy for her continual support and understanding whilst I was writing this thesis. Without her calming influence this would have taken me much longer than it has.

Copyright

Contents

List of Tables

List of Figures

Chapter 1

Introduction

The long term storage and eventual disposal of radioactive waste is a major concern at the current time. In the U.K. solutions to this problem become even more important as, in order to keep our commitment to the Kyoto accord [2] and maintain current energy production, the Government is seriously considering the possibility of building a new generation of nuclear power plants. Uncertainties regarding nuclear waste disposal are likely to be a major hurdle to public acceptance of new nuclear build.

Adding to the radioactive waste stockpile is the highly enriched uranium and plutonium that has been released from the dismantling of nuclear warheads under the strategic arms reduction treaties between the U.S.A. and Russia. This legacy material needs to be stored and disposed of in a form that ensures it cannot be used again in a weapons program.

Current strategy for the disposal of both civilian and military waste involves immobilising in glass, pouring the molten glass into a container and then disposal in a deep geological repository. A future improvement to this would be to immobilise the material in a ceramic and encapsulate this in a steel container before deep disposal. Pyrochlore ceramics have been considered for this application and discussion regarding the use of these and other fluorite related materials as waste forms for radionuclides has been discussed (literature details are given at the beginning of Chapter 5). The particular ability of pyrochlore compounds to accommodate uranium and plutonium has been considered in depth in this thesis.

Before the specifics regarding nuclear waste are discussed it is important to understand the background issues as to what exactly the problem is in the first place and why it is likely to become even more acute in future. This and previous work on wasteform materials for nuclear waste will be discussed in Chapter 2. Chapter 3 describes how the simulation software operates in order to provide an understanding of the limitations and advantages of these techniques. The next chapter (Chapter 4) aims to give greater insight into into three fluorite related phases. In this chapter, the stability of minerals which form in either the pyrochlore structure, the δ-phase or fluorite solid solutions are analysed with respect to composition. All of these materials have been found to be remarkably resistant to amorphisation and as such are interesting candidate phases for a nuclear wasteform. Chapter 5 (incorporating work published in [3]) focuses on the pyrochlore materials previously discussed in Chapter 4. The aim of the work in this chapter is to simulate various solution processes for uranium and plutonium and develop trends in order to predict which pyrochlore composition can accommodate the highest concentration of these dangerous species. Chapter 6 (incorporating work to be published in [4]) moves away from fluorite related materials to a much simpler material, MgO. The aim of this study is, using molecular dynamics, to gain insights into how materials react to decay events. The normal scope of molecular dynamics simulations is extended slightly by incorporating a small concentration of impurity ions into the material in order to more accurately model a real wasteform material and these results are compared to simulations performed in a pure lattice to see if there are any systematic changes. Finally suggestions for further work are given in Chapter 7.

Lesser contributions to collaborative work have also been made and copies of these papers can be found in Appendix C.

1.1 Kröger-Vink Notation

Kröger and Vink proposed a notation to describe point defect chemical reactions [5]. The point defects are assumed to be dilute species, with the solid being the solvent. The nomenclature consists of three parts; the body, the superscript and the subscript. The body represents the defect itself, ie. V for a vacancy or Mg for a magnesium ion. The superscript represents the effective charge of the defect i.e. a magnesium vacancy has an effective charge of $^{2-}$. A positive charge is represented by a dot ($^{\bullet}$) and a negative charge by a prime ($'$) and neutral by ($^{\times}$). The subscript represents the site of the defect or if it is an interstitial, ($_{i}$), ($_{Mg}$) would represent a magnesium lattice site. Several examples in the MgO system follow:

Mg Vacancy

V''_{Mg}

A Mg ion has a charge of $^{2+}$ therefore its absence implies a net charge in the lattice of $^{2-}$.

Mg Interstitial

$\mathrm{Mg}_i^{\bullet\bullet}$

As the previous example except this time there is an extra Mg ion in the lattice so the effective charge is $^{2+}$

Ba^{2+} substitutional on Mg site

$\mathrm{Ba}^{\times}_{Mg}$

Ba^{2+} has the same charge as Mg^{2+} so the lattice remains neutral.

Chapter 2

Literature Review

It is now apparent that global warming is a serious concern for the current century. With the United Nations Framework Convention on Climate Change (UNFCCC) Kyoto protocol [2] calling for a reduction in green house emissions to 92% of 1990 levels for the United Kingdom (U.K.) and 93% of 1990 levels for the United States of America (U.S.A.), other countries have been given similar targets (see reference [2]). The challenge facing the world is to reach or exceed these targets.

In the U.K., the global warming potential from CO_2 emissions in 2002 was greater that the potential for all other greenhouse gases summed together [6] making it the priority concern for any programme to reduce emissions. The report on U.K. emission of air pollutants 1970-2002 [6] also states that the greatest single contribution to CO_2 emissions comes from the public power sector at 29%. This is closely followed by road transport at 22% and these combine to form just over half of the U.K.'s CO_2 output. These two areas obviously have to be the primary targets for any programme to reduce emissions. One of the most promising long term solutions is to switch to alternative, non-polluting, primary energy sources. One way to do this would be to move away from a hydrocarbon based economy to a hydrogen economy to reduce emissions from the transport and industrial sectors.

A large source of radioactive material that has to be dealt with (apart from civilian nuclear power plants which will be discussed later) consists of highly enriched uranium and plutonium resulting from the dismantling of nuclear warheads under the international arms reduction treaties between the U.S.A. and Russia (START I [7], START II [8] and SORT [9]). There are multiple possibilities for this material which include, but are not limited to; processing to form UO_2 pellets for used in conventional nuclear reactors, using the plutonium in fast reactors or mixing it with uranium to form Mixed OXide (MOX) fuel [10]. The seemingly wasteful option is just to dispose of it in a geological repository.

2.1 Alternative Energy Sources

In the U.K. the majority of the electricity has been produced via the burning of fossil fuels which unavoidably releases large quantities of CO_2 into the atmosphere [6, 11–13] (see Table 2.1 for a full breakdown of power generation in the U.K. in 2002). Previous cuts in CO_2 emissions have been made by the closure of old inefficient plants, greater use of nuclear power and more recently, the construction of combined cycle gas turbines (CCGT) [6]. These

Table 2.1: Energy generation in the U.K. in 2002 [12].

Generation Method	Percentage
Gas	38%
Coal	32%
Nuclear	23%
Renewables	3%
Oil and other	4%

cuts are likely to be counteracted soon as many of the current generation of nuclear power plants are approaching the end of their lifespan [12–14] and the drop in nuclear generation is most likely to be filled by new CCGT stations [11], unless new nuclear build is sanctioned by the government. To achieve a substantial drop in greenhouse emissions from power plants, it will be necessary to move away from conventional thermal plants that burn fossil fuels to renewable, nuclear power or other non polluting generation methods will be required [11, 13]. In the following few paragraphs a summary of the advantages and disadvantages of some of the possible generation methods is given.

Table 2.2: Advantages and disadvantages of power generation methods.

Generation Method	Advantages	Disadvantages
Fossil fuels	Small CO_2 reductions available by switching from coal and oil to gas CCTG stations. Cheap to run.	Still Produce large volumes of CO_2. Extracting and sequestering CO_2 is very expensive. Requires imports of gas.
Hydroelectric	No CO_2 emissions. Can vary power output according to demand.	Requires the damming of a suitable river valley.
Solar	Can provide some electricity and most of the hot water for a house during summer No CO_2 emissions.	Minimal benefit during winter months when it is needed most. Current Photovoltaic cells are inefficient.

Continued on next page

Table 2.2 – continued from previous page

	Advantages	Disadvantages
Wind	Once constructed requires little maintainable and produces no CO_2.	Construction produces large quantities of CO_2 via the production of cement. Transient power source dependent on wind speed. Placement issues due to obstructions to low flying aircraft and social issues.
Biomass	Biodiesel can fuel cars and replace oil burners. Biodiesel is carbon neutral.	Biodiesel is more expensive than other sources of oil.
Geothermal	Provides heating and electricity with no CO_2 emissions.	Requires a hydrothermal vent
Tidal	Tidal mills and barrages produce no CO_2	Limited to 4 generating cycles per day with fluctuating output.

Continued on next page

Table 2.2 – continued from previous page

	Advantages	Disadvantages
Wave	The U.K. has a huge coastline for the placement of wave generators	Fluctuating output. Stormy conditions can damage the generators making them expensive to maintain.
Burning waste	Methane can be produced from decomposing organic waste. Decreases the volume of waste going to landfill.	Plants are expensive to build. CO_2 is produced.

2.2 Nuclear Energy

2.2.1 Basic Nuclear Principals

Radioactivity and Nuclear Fission

Many elements exist in nature with a variety of isotopes. Chemically identical, the various isotopes only differ in the number of neutrons in their nuclei. The majority of the isotopes found on earth are stable but several, including uranium 238 (^{238}U), are not and these are termed radioactive elements. These can spontaneously naturally decay to form other elements by three processes; α , β and γ decay. During α-decay a helium nucleus is emitted, with β-decay a high energy electron is formed and γ decay results in the formation of a high energy photon [14, 15]. These will be discussed further in the radiation effects section.

Conversely to the above natural decay processes, a nucleus can be transformed through fission. This usually occurs in highly unstable nuclei, for example if a ^{235}U nucleus absorbs an extra neutron, it undergoes nuclear fission and splits into two or more fragments, which form atoms of other elements along with several other neutrons. The atoms remaining are termed fission products and examples include strontium and xenon. The neutrons produced in the fission process are able to be absorbed by other ^{235}U nuclei and the process can continue in a self sustaining chain reaction if the concentration of ^{235}U in the material is sufficiently high [14, 15].

Radiation Effects

Any material exposed to radioactive or fissile materials will experience some sort of interaction with the radiation. In a nuclear reactor, in addition to the three basic types of radiation, there is also neutron radiation to consider. The different types of radiation interact with materials differently as summarised here:

- Alpha radiation is the least penetrative form of radiation and can be stopped with light shielding such as a sheet of paper. It can, however, have a devastating effect on materials immediately surrounding the decay event such as nuclear fuel or cladding material. The damage is caused by the alpha particle itself and the recoil of the decaying atom. The alpha particle has a significant ionising effect and the recoil atom causes large displacement cascades in the material through both elastic and inelastic collisions with other atoms in the material. Any material designed to store alpha emitters (such as uranium and plutonium) will have to be able to withstand this constant damage. It is relatively straightforward to protect humans from α-particles, although inhalation or ingestion are a particular concern.

- Beta radiation is the result of a neutron decaying into a proton and a high energy electron. This form of radiation is ionising and more penetrative than alpha but less than gamma rays or neutrons.
- Neutron radiation is very penetrating, but less so than gamma [14]. Neutrons can be captured by stable nuclei making them radioactive and thus cause further decay processes. The absorption process itself can also release gamma rays. They can also interact with atoms in solids to produce elastic collisions if their energy is higher than the displacement energy.
- Gamma and X-ray radiation are the most penetrative forms of radiation and are effectively the same since they are both electromagnetic. They require a thick shield of lead or concrete to be stopped. Gamma rays are highly ionising as they can strip electrons off atoms in solids.

2.2.2 Nuclear Reactors

Nuclear plants operate in a very similar manner to conventional coal and oil plants in that fuel is “burnt” to turn water into high pressure steam which then drives a steam turbine to produce electricity. The only difference from the conventional power station is that nuclear fission is the source of heat. This introduces many challenges for which multiple reactor types have been developed. Those currently in use in the U.K. will be described later (Figure 2.1 shows the important parts of a nuclear reactor).

There are two types of fission reactor, which are classified in terms of the speed of the neutrons in the core. Thermal reactors use a moderator to slow the neutrons down close to thermal motion in order to allow ^{235}U atoms to absorb them more easily. Fast reactors dispense with the moderator and utilise the neutrons at the speed they are released. Fast reactors produce more neutrons than are absorbed and these “spare” neutrons can be used to convert a fertile non-fissile fuel such as ^{238}U into plutonium, which is fissile [15]. Such a system can theoretically generate 50 times the energy per kilogramme than a thermal reactor and therefore highly efficient in terms of fuel. Fast reactors are currently at the prototype stage and would be significantly more expensive to construct and thus are uneconomic to build. This is unlikely to change unless the price of uranium climbs [14], and as such all current commercial reactors use thermal neutrons.

There are many designs for nuclear reactors and for brevity, only designs currently operating in the U.K. are considered. For information on other reactor designs see references [14] and [15]. All of the following reactor designs feature a separate coolant and boiler system. This is because the coolant inevitably becomes contaminated with radionuclides and keeping this contained within the reactor core and steam generator limits the amount of contaminated material at the end of plant life. It also means that maintenance can be carried out on the turbines without radiological protection, and that this section does not require shielding. Another common feature with these designs is that the control rods enter from the top of the reactor and are designed to fall into the core in the unlikely event that the control rod drive system fails.

Magnox Reactor

The Magnox design is one of the earliest commercial reactors and is unique to the U.K.. It uses a graphite moderator and CO_2 is blown across the fuel pins to cool them and transfer the heat to the steam generator. The fuel elements are made from natural uranium metal enclosed in Magnox cans. Magnox is a magnesium alloy designed with corrosion resistance in mind and after which the reactor is named. The fuel elements are loaded vertically in a core constructed of graphite blocks and other vertical channels containing withdrawable carbon rods that absorb neutrons and thus are able to control the reaction. Early designs used a steel pressure vessel enclosed in a concrete radiation shield but later designs utilised a combined concrete pressure vessel and shield. Magnox reactors operate at about 400 °C and have a thermal efficiency of 31% [14]. Power stations based on this design had peak electrical outputs between 200 MW and 950 MW [14].

Advanced Gas-Cooled Reactor

Advanced Gas-Cooled Reactors (AGR) are an improvement on the Magnox design. AGRs operate at higher temperatures than Magnox reactors (gas temperatures of up to 650 °C) in order to improve the thermal efficiency and increase the power density. To achieve this, the cooling gas pressure had to be increased, the cladding material was changed to stainless steel and the fuel changed from natural uranium metal to uranium dioxide (UO_2) pellets. This allows higher enrichments to be used and corresponding higher core temperatures. Like the Magnox reactors, AGRs use graphite moderators and a concrete pressure vessel and radiation shield. AGRs have a thermal efficiency of about 42% and current reactors in the U.K. produce between 1110 MW and 1250 MW [14].

Pressurised Water Reactor

About 60% of the world's nuclear reactors are Pressurised Water Reactors (PWR). Like the AGR, they use UO_2 pellets as the fuel. In a PWR, these are contained within a zirconium alloy fuel can to form a fuel rod and these are interspersed with carbon control rods. The reactor is cooled and moderated by high pressure water, to prevent boiling, and is contained in a steel pressure vessel. The high pressure water is pumped through a heat exchanger to boil water at lower pressure and produce steam. The hot water temperature arriving at the heat exchangers is approximately 325 °C [14]. The pressure vessel and steam generation are both enclose in a concrete radiation shield. Sizewell B is the only PWR in the U.K. and it has a thermal efficiency of

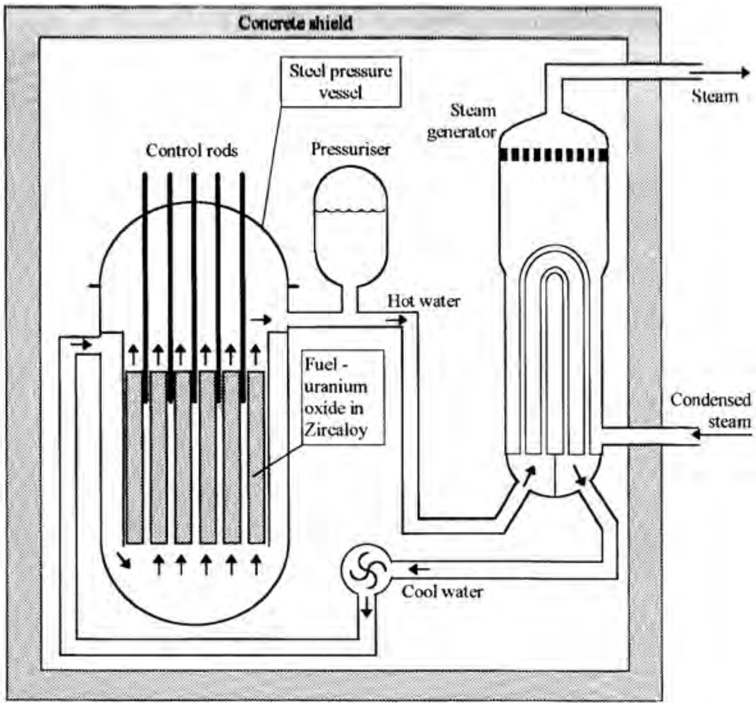

Figure 2.1: Schematic of a PWR reproduced from [15]

32% and provides 1188 MW to the grid [14]. Figure 2.1 shows the design of a PWR.

2.2.3 Fission Products

As mentioned earlier, fission products are the nuclear fragments from the fission of uranium or plutonium atoms in nuclear fuel. Fission products can cause deterioration of fuel properties and gaseous species can be produced that cause high pressure in the fuel pin. Under extreme circumstances a high buildup of these could cause the protective cladding to burst, releasing highly radioactive material into the core, or if the fuel has been removed from the reactor, the environment.

Fission products consist of a wide range of elements between copper and europium [15–17] but most fission products are symmetrically clustered in two broad peaks around elements with mass numbers of 95 and 135. Some of these elements have neutron absorbing properties and the build-up of these elements in the fuel limits the lifespan of the fuel as there are fewer neutrons to cause fission of uranium atoms. This is not the only concern as fission products can have very different chemical and physical properties to that of the fuel matrix [18]. This causes changes in the physical properties of the fuel itself, for example, the thermal conductivity is decreased by the formation of oxides of zirconium, strontium and some of the rare earth elements [16]. This is important as under operating conditions the temperature at the centre of the fuel pin can reach 1500 K and any decrease in the thermal conductivity will cause this to increase further with significant increases able to cause fuel melting. The accumulation of fission products can cause swelling in the fuel which can also increase pressure in the fuel pin and eventually lead to cladding failure [19].

Most primary fission products are unstable due to the difference in proton to neutron ratio between elements with high atomic number and those with small atomic numbers. Uranium has 1.56 times as many neutrons as protons whereas the stable isotopes of fission products, which are much smaller, have neutron to proton ratios much closer to 1. This means that fission products have too many neutrons and they tend to decay quickly by emission of β particles until they are stable. This decay occurs even after the fuel has been removed from the reactor and ^{235}U fission no longer occurs. This means that fuel that has been removed from the reactor needs to be cooled as the process still generates ”quite a lot” of heat [15].

Even though most unstable fission products decay quickly, there are some with half lives from tens to thousands of years, two in particular, iodine-129 and technetium-99, have half lives of 15.7 million years and 212,000 years respectively. Of these two, iodine is more of a concern if it is released into the environment as the human body will tend to concentrate it in the thyroid gland and this will cause tissue damage leading to cancer. For more in-depth discussion of fission products see references [15–21].

2.2.4 The Nuclear Fuel Cycle

The fuel cycle for a nuclear power station is much more complicated than for a traditional fossil fuel power plant. For a coal power station, the fuel is extracted, transported to the plant where it is burnt and any ash is either sold to the construction industry or disposed of. The fuel cycle for a nuclear plant can include all of the steps shown in figure 2.2. When fuel reaches the end of its usable life, it is removed from the reactor and can be reprocessed to reclaim the “unburnt” uranium and plutonium. This process is sometimes called “closing the back end of the fuel cycle” and reduces the amount of fresh uranium that has to be purchased.

Mining

The U.K. has no uranium reserves and most of the supply comes from Australia and Canada. The impurities are removed at the site in order to save

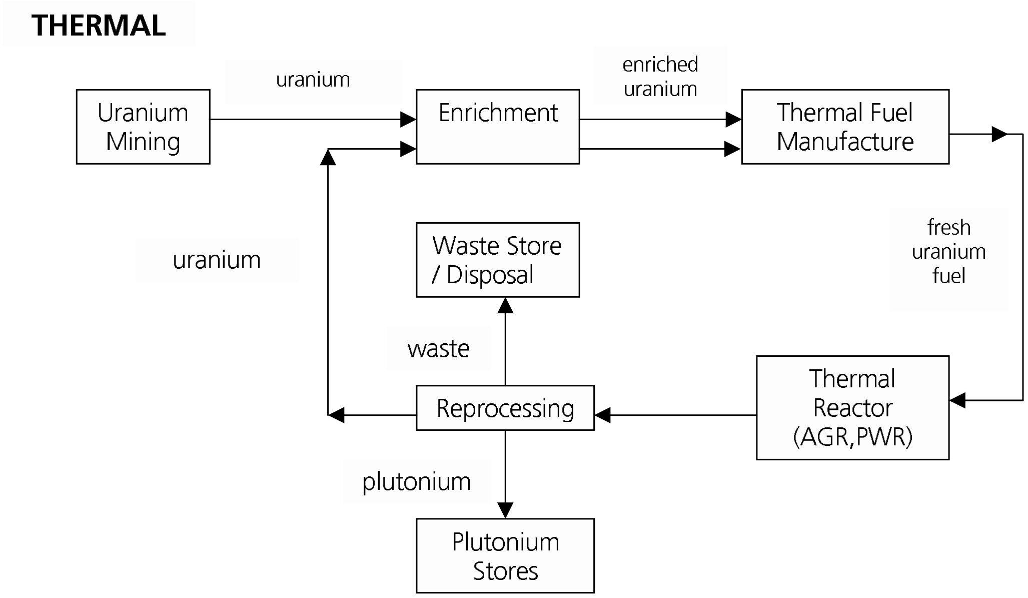

Figure 2.2: The Nuclear Fuel Cycle [14].

on transport costs and the uranium ore concentrate or “yellow cake” is taken to be processed into uranium metal or enriched UO_2 pellets. At this point the levels of radiation are still very low [14].

Processing and Enrichment

If the fuel is to be used in an AGR or PWR reactor, the fuel must be enriched from the natural 0.7% ^{235}U to the operating level for the reactor, normally between 2% and 3.5% ^{235}U. The same effect can also be achieved by mixing with plutonium gained from the reprocessing step, discussed later, to form a mixed oxide fuel.

Once purification is complete, the yellow-cake is converted to uranium hexafluoride (UF_6). This process has several stages and is discussed in depth in reference [15]. Uranium hexafluoride is gaseous, and is spun in a very high speed centrifuge to partially separate the lighter ^{235}U from the heavier ^{238}U. If purification had not been carried out other light gases would exist in the centrifuge and contaminate the enriched product. In France and the U.S.A. a different process is used in which they exploit the different rates at which the two uranium isotopes diffuse through a porous metal membrane [14]. The enrichment process yields large quantities of uranium in which the level of ^{235}U is reduced to about 0.2-0.25%, this is termed depleted uranium. This material is currently stored but it may be used in future fast reactors as a fertile fuel.

Fabrication

The next step in the process is to convert the enriched UF_6 into uranium dioxide for used in AGRs and PWRs. Alternatively, the unenriched uranium ore is converted into uranium metal rods for the use in Magnox reactors see [15] for further details.

The production of oxide fuel from the enriched UF_6 can be performed via two methods, a dry route and a wet route. The dry fabrication process is the most common route so that will be the method explained here, for information of the wet fabrication route see reference [15].

In dry conversion the UF_6 is decomposed by steam to produce UO_2F_2 which is a solid. This is then reduced to UO_2 using either a fluidised bed technology, a two step process using a rotary kiln or a one step process using flame reaction technology [15]. The UO_2 powder produced at the end of this process is then uniaxially pressed into pellets. The shape and size of the pellets differs for different reactors but in the U.K. there are only 2 different designs. Solid pellets are used in most PWRs and annular pellets are used in AGRs. Annular pellets have a cylindrical hole running through the centre of the pellet and thus require a retractable pin in the press. The purpose of this hole is to accommodate distortions in the fuel and fission gasses formed in the reactor. Once the pellets have been pressed, they are sintered at 1750 °C in a reducing atmosphere of hydrogen or a mixture of hydrogen and nitrogen to prevent oxidation and the formation of U_3O_8. This process increases the density of the pellets and gives them the physical properties they require to withstand the high temperature conditions in the reactor.

The pellets are then assembled into fuel pins or elements. These differ wildly amongst the different reactors but a similar process is used for both AGR and PWR fuel elements. In both of these, the fuel pellets are stacked and weighed and then inserted into the cladding. Once this is complete, the cladding is then filled with helium gas and the ends are sealed, welded and tested.

The fuel is then transported and installed into the reactor where it is used until the build-up of neutron absorbing fission products and other detrimental effects, such as fuel swelling, require the fuel to be removed and either disposed of or reprocessed. This completes the front-end of the fuel cycle.

Reprocessing and Recycling or Disposal

After the fuel has been removed from the reactor, it enters the back-end of the fuel cycle. At this point the fuel is highly radioactive due to the presence of fission products. This fuel must be stored and cooled until the level of radioactivity is low enough to allow transport to the reprocessing site or the interim storage facility. The fuel is normally stored in ponds at the reactor site. These ponds are sealed reinforced concrete structures filled with water. This acts as an effective radiation shield and also provides cooling to the fuel which may otherwise heat to the point where the fuel or the cladding becomes damaged enough to release contaminated material into the local environment.

Once the material has cooled sufficiently it is either taken to a storage site or to a reprocessing plant. Reprocessing has several advantages over storage for later disposal and these are listed here:

- Security of Supply: Security of supply is a concern for the U.K. as there are no natural uranium deposits. This means reprocessed uranium is a valuable resource that should not be wasted. Some countries choose to store the spent fuel and leave the reprocessing for later but corrosion of the fuel and cladding materials can be a problem if it is to be stored for long periods.
- Waste Management: The recovery of useful material means that the volume of high level waste that must be disposed of is reduced by a factor of 9 [15]. The radioactive content is also reduced as the alterna-

tive, direct disposal, adds approximately 250kg of plutonium per year to the fuel awaiting burial. Since the medium to long term radioactivity is dominated by plutonium isotopes and daughter products, the radioactivity over 10,000 years can be reduced by over 30%.

- Improved Proliferation Resistance: Proliferation is the unlawful diversion of fissile material. In particular, plutonium is potentially attractive to terrorist organisations. While considerable effort is made to keep this material safe, converting this material into MOX fuel makes it much less attractive as the organisation would not only have to move the bulky material but to chemically separate it before it could be used.

While it is true that reprocessing does substantially reduce the volume of HLW, it does increase the volume of intermediate and low level waste produced [22]. It was estimated by Webster [23] that by 2030 26% of the volume (only 6% by activity) of all radioactive waste in the U.K. will be ILW and a substantial proportion of it will have come from reprocessing. Arm *et al.* [22] propose several concepts to reduce these volumes, one of these is the elimination of one of the solvent extraction cycles during the purification of uranium and plutonium by reducing the flow rate and thereby increasing the extraction efficiency of fission products and minor actinides.

Reprocessing fuel involves separating out the uranium and the plutonium (some of the ^{238}U is transmuted even in thermal reactors) from the rest of the fuel. These 2 elements can consist of 97-99% of the spent fuel with the remaining being high level waste including fission products and some of the minor actinides, including neptunium, americium and californium. While the idea is simple, the mechanics of the process are far from simple and will not be discussed here; for a detailed description of the process see reference [15]. Once reprocessing is complete, the uranium and plutonium are stored waiting to reenter the fuel cycle at the enrichment or fuel fabrication step.

Future Role of Fast Reactors

Reprocessing fuel provides a source of plutonium and while some of this is currently being used in the form of MOX for PWRs and AGRs this material can be used as a fuel for fast reactors. If this is ever started, by using the depleted uranium formed in the enrichment process, this type of reactor can actually produce more new plutonium fuel than it consumes by breeding the ^{238}U to ^{239}Pu. This creates a situation where the cycle is virtually closed.

2.3 Nuclear Waste

2.3.1 Introduction

Any kind of industry develops waste materials along side the desired products and the nuclear industry is no different. The sources of waste in the nuclear industry mainly come from the following operations:

- Reprocessing spent fuel
- Final decommissioning when a plant reaches the end of its lifespan

- Military Waste
- Surplus Materials

Primary wastes from fuel reprocessing include the fission products, minor actinides and the remains of the cladding. Secondary wastes that are formed during reprocessing can include solvents that are no longer recoverable, worn out equipment or clothing and other domestic waste that may have been contaminated with radioactive material. The industry aims to minimise the amount of secondary waste generated and to convert as much of the radioactive material into a form that is both suited to long-term storage and final disposal whilst taking up as small a volume as possible. While doing this the environmental impact should be kept As Low As Reasonably Attainable (ALARA).

Waste Types

In the U.K. solid radioactive waste is normally classified by its radioactive content as high, intermediate, low or very low level wastes (HLW, ILW, LLW, VLLW). These are defined as:

- VLLW: Very Low level wastes can be disposed of with normal household waste. Each cubic metre must contain less than 400 kBq per tonne of beta or gamma activity and less than 40 kBq/t for any single item.

- LLW: Low level waste consist of materials with activities greater than that for VLLW but not more than 4 GBq/t of alpha or 12 Bq/t of beta/gamma activity.

- ILW: Intermediate level waste is classified and anything exceeding the activities for LLW but does not require the heating effect of radioactive decay to be taken into account in the design of storage or disposal facilities.

- HLW: High level waste is classified and any material sufficiently radioactive such that it produces sufficient heat to require special design factors for long term storing and eventual disposal.

HLW mainly consists of fission products after reprocessing. ILW is mainly cladding remnants or plutonium contaminated material that it is not economical to remove (including filters and processing residue). LLW consists of discarded equipment, tools and protective clothing. It also consists of material suspected of being contaminated such as waste paper from offices in controlled areas [15]. These definitions are rather arbitrary in that they only consider current activity without any regard for the half-lives of the material [15].

Liquid wastes are similarly divided into high, medium and low active streams. Current practice for the disposal of both liquid and solid waste in the U.K. will be summarised in the next section.

2.3.2 Current Practice in the U.K.

Liquid Wastes

Over the last 20 years huge improvements have been made to reduce the activity of liquid waste discarded into the sea from the Sellafield reprocessing plant in Cumbria. Figure 2.3 shows the current liquid waste handling process at Sellafield.

In order to reduce the contamination later on in the process, reprocessing is delayed slightly and the fuel is cooled. This allows isotopes with a very short half life, for example ^{131}iodine (8 days) and ^{95}niobium (35 days), to decay to very low levels. Delay periods are also used after reprocessing to reduce the activity of slightly longer lived radionuclides destined for discharge.

The highly active wastes from the first stage of fuel processing contain the majority of the fission products and minor actinides. This waste is concentrated up to 100 times by repeated evaporation. The concentrated residue is stored in cooled double wall stainless steel tanks until it is ready for vitrification, this process will be described in detail in section 2.3.4.

The medium active waste mainly consists of residues from the purification of uranium and plutonium. Some of these can be combined with the highly active stream but those which cannot, for chemical compatibility reasons or simply due to the fact that there is too much, are fed into a separate evaporator and stored.

Before 1980 the medium activity wastes were stored for at least three years

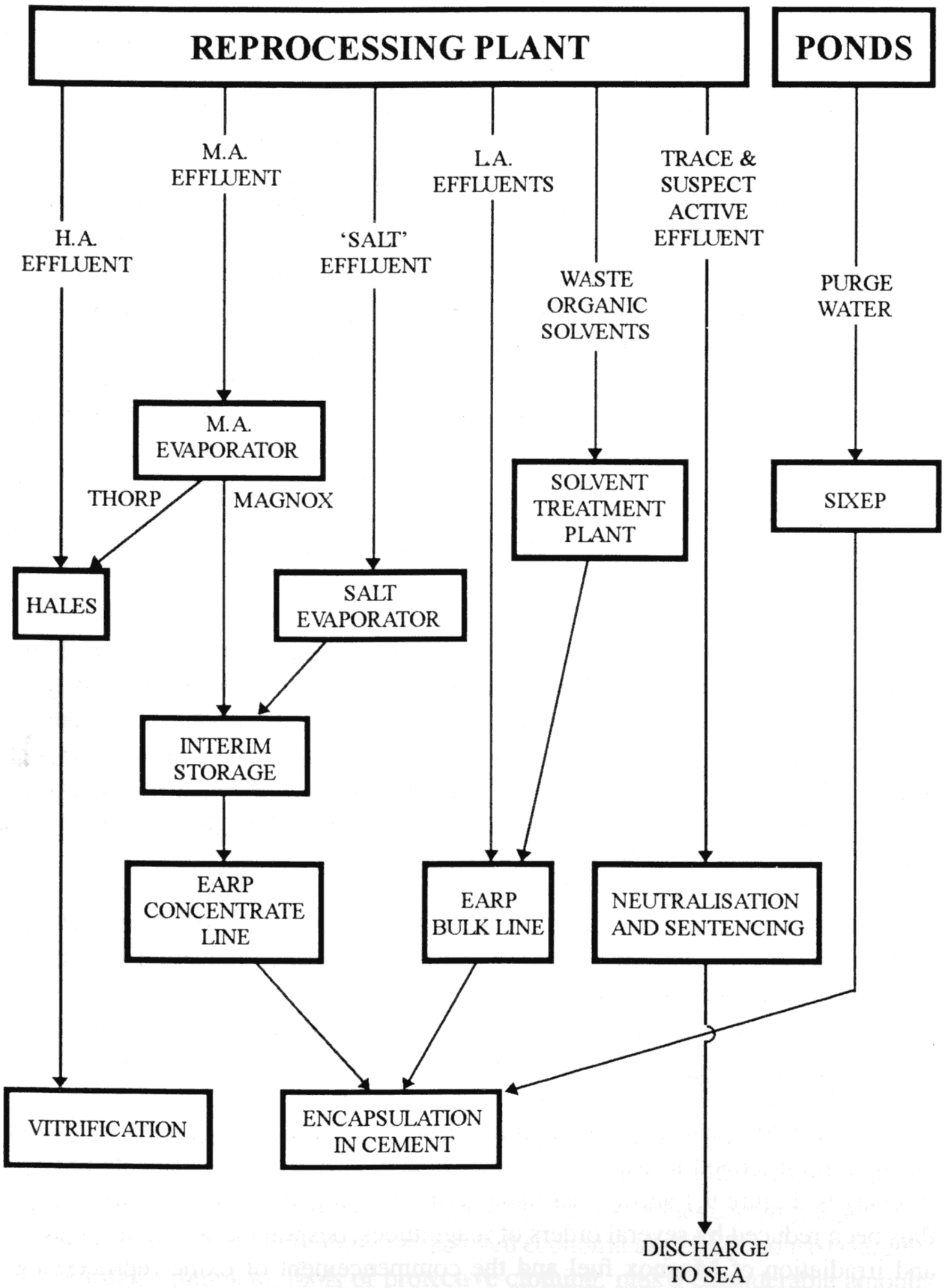

Figure 2.3: Liquid waste treatment at Sellafield [15].

and then discharged to sea. This allowed the almost complete decay of ruthenium, zirconium and niobium which constituted the majority of the activity. After 1980 the process was stopped as it was realised that the activity was now dominated by much the longer lived isotopes of some of the actinides and it was decided to store this material until these could be removed in the enhanced actinide removal plant (EARP).

Salt wastes have a high sodium content and are incompatible with the medium active waste evaporator and thus have their own dedicated device. Like the medium active wastes, these are now processed through EARP.

Strontium and caesium are the main source of contamination from the fuel storage ponds. There are also significant quantities of magnesium hydroxide from corrosion of Magnox fuel cladding. These wastes are too dilute to be processed via an evaporation route and an ion exchange method is used. The details of this process can be found in [15]. This process reduces the levels of strontium and caesium by factors of 500 and 2000 respectively and the remaining liquid waste is discharged into the sea. The solid residues from the ion exchange beds are used to replace fillers, such as sand, in the cement.

EARP takes concentrated residue from the medium active and salt waste evaporators and uses a precipitation and filtration method described in [15] to extract significant quantities of the actinides, cerium, ruthenium and strontium from the liquid before it is tested for activity and either put through the system again or discharged to sea.

2.3.3 Solid Wastes

Solid wastes include fragments of fuel cladding and any radioactive isotopes or toxic materials that have been precipitated or otherwise removed from the liquid waste streams. All types of waste need to be encapsulated for long term storage and other methods for this process will be discussed later in sections 2.3.4 and 2.3.5.

Solid HLW originates from the highly active liquid stream, it is currently solidified by a vitrification process described later in section 2.3.4. Once it has been vitrified and placed inside steel containers, the HLW is stacked up to 10 high in closed tubes in a store cooled by the natural convection of air. At the present time it is planned to store the vitrified waste for 50 years to allow the worst of the radioactivity to decay [14,15]. Currently the U.K. does not have a final strategy for the long term disposal of HLW [24, 25].

ILW has been stored at the Sellafield site in dry or water filled silos according to the content. This requires constant supervision and is not acceptable as a long term solution and so ILW is currently being encapsulated for future long term storage although, like HLW there is no final strategy for the process at the current time [15,24,25] (see section 2.3.8 for information on possible final disposal options.)

In the U.K., cement has been found to be the best encapsulation material for all types of ILW [15]. It has proved superior to other matrices including polymers and polymer modified cements, both during the encapsulation process and after. Ordinary Portland cement (OPC) is unsuitable as an encapsulant as the hydration reaction produces too much heat and leaves too much thermal stress in the material. In order to prevent this, the mixture must be diluted. Many diluting materials have been considered, including sand, pulverised fuel ash, ground blast furnace slag and contaminated clinoptilolite from the ion exchange plant.

The encapsulated waste must remain durable enough for handling for at least 100 years or at least until final disposal. This means the physical and mechanical properties, the chemical and radiation stability, and the leaching behaviour should not change significantly over this period [15].

There are two processes used for the encapsulation of ILW in the U.K., one for solid wastes and the other for slurries. Solid wastes are packed into 500 litre stainless steel drums and the voids are filled with cement. Slurries are mixed with grout forming materials and left to cure in the drums. For both types, the lid is then fitted and the outside is decontaminated with high pressure water jets. The drums are then stored above ground awaiting the construction of a suitable deep geological repository [15, 24, 25].

LLW is placed into drums which are then compacted and loaded into iso freight containers. These are then taken to the U.K. LLW disposal facility at Drigg, near Sellafield, where they are placed in concrete vaults. When these vaults are filled, they will be capped with clay. there is sufficient storage space at the Drigg site to accommodate al the LLW from nuclear power stations and hospitals for many years to come. [15, 24, 25].

2.3.4 Immobilisation in Glasses

Introduction

Immobilisation of highly active waste sludge and plutonium has been or is being achieved via a vitrification process in the U.K, U.S.A., Belgium, India, Japan and Russia [26]. Vitrification involves dissolving (or just encapsulating) the waste into a glassy (vitreous) host material. Once it has been vitrified, the wasteform can then be cast into any suitable structure [27], in the U.K. 400 kg containers are used [15]. It is possible to incorporate up to 25-30 wt % HLW into a glass wasteform [27].

The glass composition is chosen by taking into account factors such as HLW solubility, glass formation temperature and leaching performance under repository conditions. Many compositions have been shown to have the required properties including high thermal and mechanical stabilities. Other advantages that these glass compositions possess include the ability to be formed and processed at relatively low temperatures, they are sufficiently radiation resistant (see section 2.3.6), show high chemically durability, they can accommodate changes in composition due to radioactive decay, furthermore they are tolerant of changes in HLW composition [15, 26, 27]. Many tonnes of vitrified HLW is currently stored in interim storage facilities awaiting construction of geological repositories for permanent disposal [15, 27].

Vitrification Methods

Immobilising nuclear waste in glass was first developed in Canada early in the 1950s using nepheline syenite (a natural silicate mineral) as the host. [27]. The U.K. also started vitrification methods in the 1950s. The initial work considered using natural soils as the base material but these had to be melted at high temperatures (1500 °C) [27] and were later replaced with an alkali-borosilicate glass that melted at lower temperatures (850 °C) [15, 27].

The process involved calcining and then melting HLW and glass frit together in a stainless steel crucible or pot, which also served as the eventual container. Once this process was complete the pot was removed and another put in its place so the process could be repeated [27].

The French approach was similar in many regards but they preferred a continuous melting process over the batch system developed in the U.K. in order to achieve higher throughput. Waste is calcined in a rotary kiln at 850 °C under reduced pressure where it is progressively evaporated to leave as a dry finely divided powder. The calcine is then fused with the base glass in an inductively heated metallic furnace at a wall temperature of about 1100 °C. This furnace is designed to produce at least 25 kg of waste an hour with a waste content of approximately 25% waste loading. When the volume of material in the melter reaches a certain level the product is drained into a stainless steel product container, this generally takes 8 hours [15]. This process is now used in the U.K. at the commercial Sellafield reprocessing plant [15, 27]

Types of Glass Used for HLW Vitrification

Silicate glasses are currently the preferred wasteform for HLW [27]. This is because they readily dissolve a wide range of waste compositions and they are easily modified in well understood ways in order to optimise their properties. They have also been extensively studied as they have been used in the commercial glass industry for decades so they are the best understood glasses [27].

Recently, attention has returned to borosilicate glasses as a wasteform for the surplus uranium and plutonium from civil and military sources and it has been concluded that borosilicate glass is the preferred wasteform for plutonium [27, 28]. This is despite the fact that the solubility of plutonium in these glasses is low (less than 3 wt %) [27].

Phosphate Glasses: Interest in phosphate glasses was high during the early immobilisation studies because of their low glass formation temperatures and high solubilities for metal oxides. Interest soon waned for a number of reasons, including poor chemical durability, low thermal stability and that they are highly corrosive [27]. This highly corrosive nature would severely limit the lifetimes of the melting equipment.

Rare Earth Glasses: There has been limited work on rare earth oxide glasses and only one rare earth borosilicate glass has been commercially considered. This glass has the name “Löflers” glass and was originally developed int the 1930’s as an optical glass [27]. It contains about 55 wt % rare earth oxides and has recently been suggested for the immobilisation of uranium, plutonium and americium as it can accommodate higher concentrations of these elements than a standard borosilicate glass [27].

Durability of Glass Wasteforms

Many factors affect the durability of glass wasteforms, including composition, waste loading, pH, temperature crystallisation effects and effects of radiation damage [27]. Unlike more common glass compositions, which are reasonably resistant to corrosion in acidic solutions, HLW glasses show higher leach rates in acidic solutions which is probably due to the high loading of alkali oxides in the glass [27]. In a closed system these rates decrease with time but if there is transport of these leachates away from the repository, for example if there is flowing water, then these rates remain a constant. The solubility of the leachate can be affected by the pH, especially if it contains Zn, Al, Fe, Ti or Mg [27]. Transport of the leachate away from the glass can be inhibited, and thus the durability is increased, by the formation of solid layers at the surface of the wasteform. It was noted by Chick *et al.* [29] that the durability of the wasteform could be improved by increasing the silica or alumina concentration in a borosilicate glass or by decreasing the amount of alkali oxide.

Solubilities of various elements vary according to their charge state which can change due to reduction or oxidation reactions in the wasteform material. Examples of such materials include the actinides and technetium which show much reduced solubilities in glasses in their 4+ state than in their higher oxidation states. The solubility of iron is also affected by the ratio of Fe^{2+} to Fe^{3+} ions [27]. This means that it is essential to know the elements that are sensitive to this reaction and make sure conditions in the repository are favorable to maintaing the state of maximum solubility.

2.3.5 Ceramic Wasteforms

High level waste and surplus weapons material may also be immobilised in a ceramic wasteform. There are no current commercial operations using this technique although significant interest in the possibility has been shown in the literature [27, 30–60]. Immobilising radioactive elements in a ceramic is based around the idea of emulating naturally occurring minerals that are known to have stably contained radioactive elements for tens to hundreds of millions of years [60]. This can then be used as an argument that man made wasteforms based on these will also remain stable for similar periods of time. Other benefits of ceramic wasteforms include the fact that: they can contain higher loadings of certain waste elements than glasses, they can have higher thermal conductivities (which keeps temperatures at the centre of the wasteform lower and allows for larger containers), they can withstand higher temperatures (occurring due to the internal heating) and as part of a solid solution they can selectively accommodate specific chemical species [60]. The accommodation of HLW in ceramics is fundamentally different from that for glasses as instead of being dispersed randomly throughout the material, the radionuclides are accommodated at specific sites within the lattice forming a dilute solid solution [61]. This means that in order to accommodate the wide range of species that make up HLW, multi-phase systems of complex structures tend to be used [61].

Many different types of ceramic have been considered for the immobilisation of nuclear waste materials including spinel based ceramics, the titanate rich SYNROC family, silicate based ceramics, phosphates, fluorite and related ceramics. These will be discussed here:

SYNROC and Related Ceramics: SYNROC or SYNthetic ROCk is the most widely known ceramic wasteforms and was developed in Australia in the 1970's by Ringwood *et al.* [39,40]. SYNROC is a ceramic wasteform designed to immobilise HLW from reprocessing spent fuel and consists of four titanate phases, "hollandite" $BaAl_2Ti_6O_{16}$, zirconolite $CaZrTi_2O_7$, perovskite $CaTiO_3$ and rutile TiO_2. It also contains small amounts of a dispersed metal alloy [39,40,42] although almost all of the fission products, actinides and processing contaminants are incorporated in the ceramic phases [39, 40, 42]. Various types of SYNROC have been developed for different applications, including SYNROC-C for waste from the reprocessing of spent fuel, SYNROC-D for the disposal of HLW resulting from the U.S.A. defence programme, SYNROC-E is an improvement in SYNROC-C which is encased in rutile to improve its long term performance and SYNROC-F for unprocessed spent fuel [27,42,43].

The hollandite phase has a particularly accommodating structure and possesses a high solubility for ions with a wide range of radii. This is mainly due to the presence of large tunnels along the c-axis [60]. See Figure 2.4 for a representation of this (generated using structural data from [62]). Figure

2.4a shows a view straight down the c-axis and Figure 2.4b is a perspective view showing 2 unit cells along the c-axis. In this structure only half of the Cs-sites are occupied whereas all possible sites are shown here. These tunnels are capable of accommodating ”very large” cations including Ba, Cs, Sr, K and Rb which are fission products of uranium [60]. The smaller octahedral site normally occupied by Ti^{4+} and Al^{3+} can accommodate the medium sized cations including Mo^{4+}, Ru^{4+}, Fe^{3+}, Fe^{2+}, Ni^{2+} and Cr^{3+} [60]. Single phase hollandite ceramics containing Cs and Sr ($CsAl_2Ti_6O_{16}$ and $SrAl_2Ti_6O_{16}$) have been synthesized [60] showing that the hazardous forms of Cs and Sr can also be accommodated successfully. The presence of the large tunnels in the structure may suggest that it is prone to leaching but the large Ba ions present in the tunnels act as plugs to preventing easy transport of HLW ions through the structure.

Zirconolite is the phase responsible for the accommodation of uranium and the tetravalent actinides. It can also accommodate smaller concentrations of trivalent actinides and rare earth elements [42, 60]. It has a monoclinic structure and is related to both the pyrochlore and fluorite structures [60]. Figure 2.5 shows a graphical representation of the structure, generated using structural data from Rossell [63]. Figure 2.5a shows a view of the structure up the c-axis with the a axis going across the page and Figure 2.5b shows a perspective view of the structure. It should be noted that this is an idealised version of the structure since the structural data indicates a degree of cation disorder on all cation sublattices and one of the titanium sites is only half occupied whereas this diagram shows the majority ion on each site and shows all sites as fully occupied. Kesson *et al.* [42] found that U^{4+} is

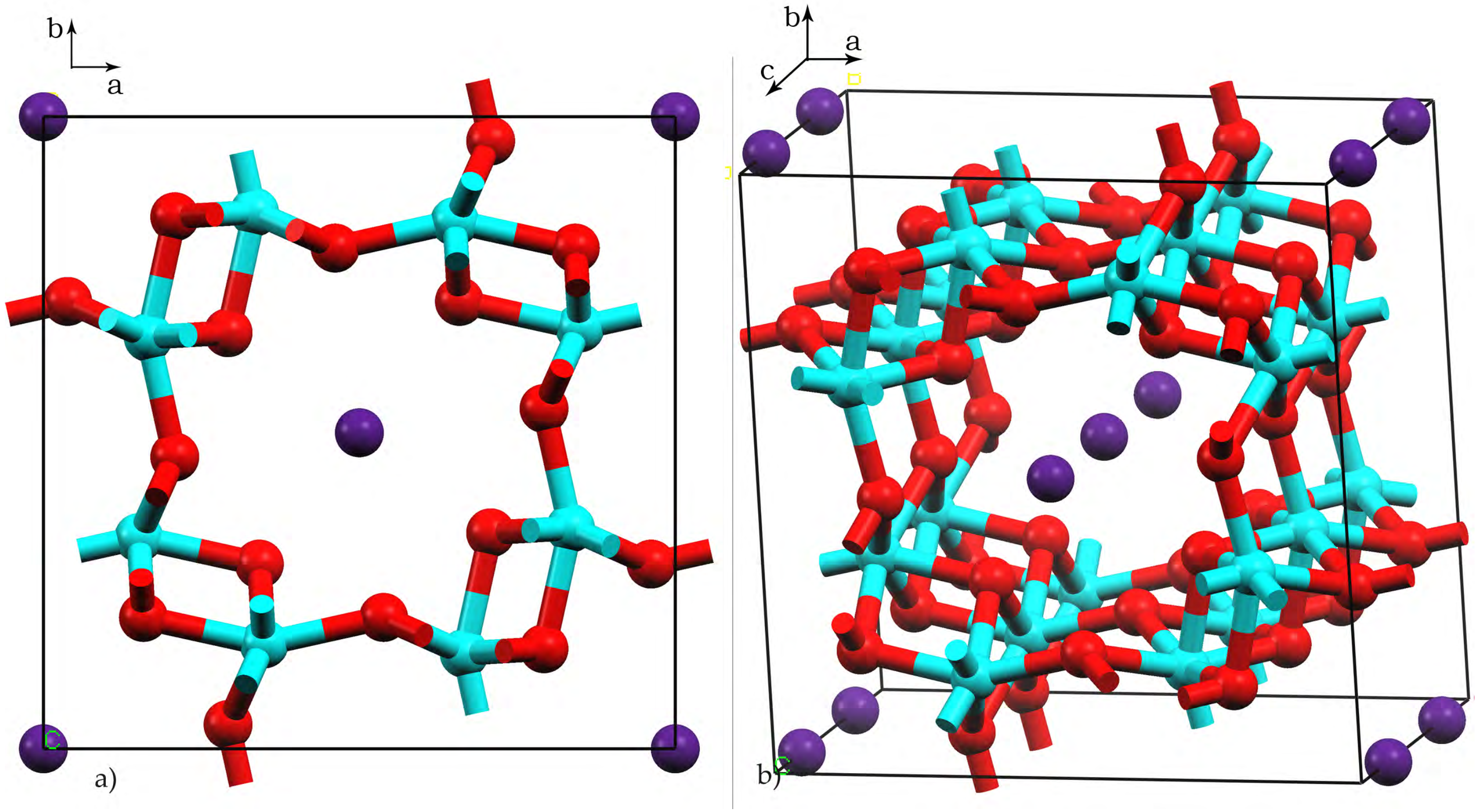

Figure 2.4: The Hollandite Structure. a) View directly down the c-axis b) perspective view. Cs^{4+} ions - Purple, Ti^{4+} Ions - Light Blue, O^{2-} ions - Red.

accommodated at both the Ca and Zr sites when a smaller lower valence cation (for example Mg^{2+}) is allowed to simultaneously be accommodated at the Zr site. This allows the loading of UO_2 to be increased from the 13 wt % that is apparent at just the Zr site to 26 wt % with coupled substitution onto both sites [42]. Thorium, like uranium seems to substitute onto both Ca and Zr sites but it substitutes preferentially onto the Ca site with charge compensation by small 2+ cations on the Zr site. This way 20 wt % ThO_2 has been accommodated into the zirconolite phase [42]. The high loadings of actinides (compared with borosilicate glasses) that are possible in zirconolites has meant that significant work has been undertaken by research groups throughout the world with the aim of using these phases for the immobilisation of actinides and weapons grade material with and without using the other SYNROC phases [41–53, 56].

The final major phase in the SYNROC system is perovskite $CaTiO_3$ (see figure 2.6 generated using structural data from Chakhmouradian *et al.* [64]). Figure 2.6a shows a view from the front of the structure with the a-axis across the page and c axis vertical, Figure 2.6b shows a top down view of the structure with tha a-axis across the page and b-axis vertical and 2.6c shows a perspective view. This phase is also known to accommodate many elements in solid solution. The primary reason for its inclusion into SYNROC is for the accommodation of Sr^{2+} onto the Ca site and U^{4+} onto the Zr site. Substitution of Mo^{4+}, Zr^{4+}, Nb^{5+}, Pu^{4+}, Ru^{4+}, Fe^{3+}, Cr^{3+} and Al^{3+} onto the titanium site and Ba^{2+}, Na^{+}, Cd^{3+}, Cm^{3+}, Am^{3+}, Pu^{3+} and rare earth $(RE)^{3+}$ onto the Ca site have been reported [60].

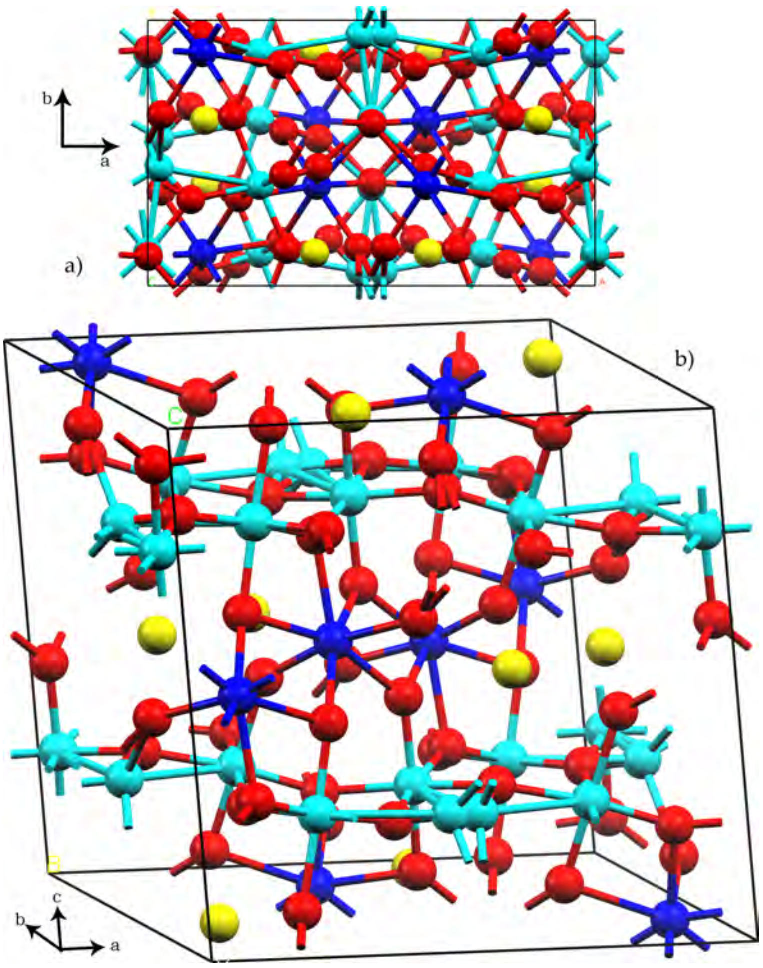

Figure 2.5: The Zirconolite Structure. a) view along c-axis, b) perspective view. Ca^{2+} ions - Yellow, Ti^{4+} ions - light blue, Zr^{4+} ions - dark blue, O^{2-} ions - red

The rutile phase (TiO_2) is normally a relatively minor constituent but in SYNROC-E it is the dominant phase as all the other phases are encapsulated inside it [42]. It is used as an extra barrier to impede the flow of contaminated material into the environment. In other SYNROC variants rutile is formed when processing and tailoring additions are not adequately controlled [60].

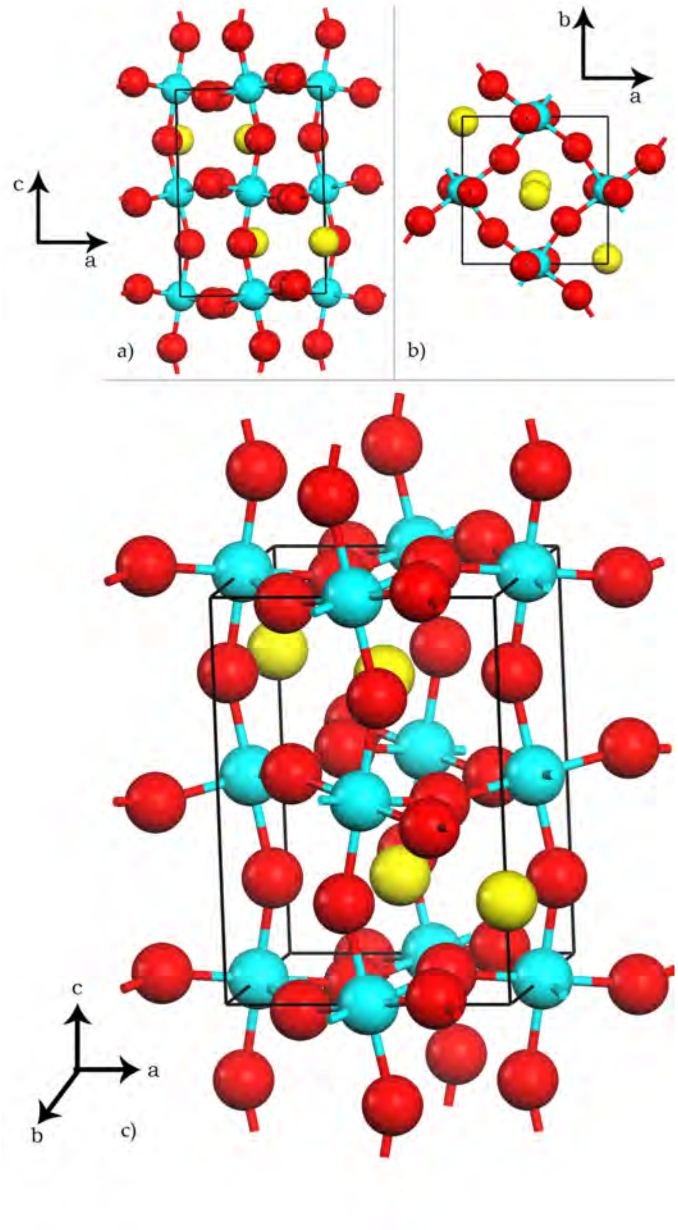

Figure 2.6: The Orthorhombic Perovskite Structure ($CaTiO_3$). a) View from front with the c-axis up the page; b) view from top, a-axis across the page; c) perspective view. Ca^{2+} ions - yellow, Ti^{4+} ions - light blue, O^{2-} ions - red.

Smith *et al.* performed a study on the durability of SYNROC containing 10% simulated waste [43]. They placed a sample in doubly deionised water held it at 150 °C for up to 532 days. After this time period they performed scanning electron microscopy on the sample and the leachate was analysed for its composition. They concluded that SYNROC is highly durable even under these conditions and that most of the material leached from the material originates in the minor phases which make up less than 5% of the material. Analysis of the leachate showed that leach rates of Al, Ba, Ca, Ce Cs,Mo, Nd and Sr range from 0.017% to 0.093% after 337 days. The analysis of the relative corrosion resistance of the major phases showed zirconolite to be the most resistant since it showed no alteration even after 532 days. The hollandite phase was the next most stable, showing only small crystals of anatase forming on the surface and lastly, the perovskite phase was least corrosion resistant major phase and showed corrosion to a depth of $< 0.2\ \mu$ m (less than half the grain size) after 532 days [43].

The study described above does not consider the effects of radiation damage on the ceramic. Furthermore, due to the types of material immobilised in the different components, different types of damage will be incurred. The hollandite will be subjected to α-particle and β/γ irradiation whereas the perovskite and the zirconolite phases will be subject to α-decay processes and α recoil events as well [61]. It has been assumed that β/γ irradiation has virtually no lasting effect on any of these species [61] and work has been carried out using various techniques to simulate α-particle and α-recoil events in these phases (including computer simulations described in chapter 6). This will be discussed in greater detail in section 2.3.6 but, in summary, the zirconolite [65–67] and perovskite [61] phases undergo α-decay induced amorphisation with a volume change between 6 and 8% and the hollandite changes structure with an associated volume change of up to 2.5% [61]. Volume changes are detrimental to ceramic wasteforms as these materials are brittle and can cause the material to fracture and become more prone to leaching.

Phosphate Ceramics: There are some naturally occurring phosphate minerals based on monazite that are known to contain actinide elements. Lanthanide phosphate materials based on this have been prepared by various techniques on a laboratory scale and a wide range of HLW materials can be incorporated into these materials. Leach resistance and radiation tolerance of wasteforms based on this system are reported to be good [27].

Samples of monazite in nature have been found with significant concentrations of actinides. Samples from Italy have been found to contain about 15 wt % UO_2 and 11 wt % ThO_2 and this suggests that these materials could be good candidate hosts for the more massive actinides, like plutonium, not normally found in the environment. The long term stability of these compounds is good as samples of monazite found in Brazil have been dated at over 2 billion years old [27]. They also posses a negative temperature coefficient of solubility meaning that as the material cools more HLW can be dissolved into it. This is a useful property to have as the wasteform will be subject to the internal heating effect of radioactive decay to start with and this will slowly decrease with time and for conventional ceramics this means a decrease in solubility with temperature which could lead to leaching problems thousands of years in the future.

Lanthanide phosphates exist in a several different structures including tetragonal, hexagonal and monoclinic and have high transition temperatures [27]. This is good as it means as the wasteform cools with time it is unlikely to go through structural changes. Unfortunately, they also possess high melting points, in excess of 2150 °C. This makes them expensive to produce and special processing techniques have been developed to reduce the formation temperature. Wet chemistry techniques have been used to form highly reactive precursor powders and these can then be hot pressed or sintered at 1300 °C to achieve theoretical densities of up to 97% [27] with up to 50% of HLW simulant loading.

Silicate Based Ceramics: The first demonstration that ceramics could be used to immobilised nuclear waste were the “supercalcine” ceramics developed at Pennsylvania State University by McCarthy *et al.* [60]. Their approach was to add Si , Al, Ca and Sr oxides to the waste before it was calcined so that each radionuclide is immobilised in one or more phase of the resulting ceramic. These ceramics were complicated polyphase materials, containing up to 9 separate phases [60]. The key phases in the material are pollucite ($CsAlSi_2O_6$), scheelite ($CaMoO_4$), fluorite ($[U,Zr,Ce]O_2$), apatite ($Ca_5(PO_4)_3OH$) and monazite.

There has been some more recent work on apatite minerals for the immobilisation of radionuclides to identify diffusion rates of immobilised species [55, 68, 69]. Meis *et al.* [55] state that the fluorapatite phase should be a good material for the immobilisation of plutonium whereas Martin *et al.* [68] find that there is preferential diffusion of rare earth elements to surfaces in hydroxyapatite and suggests that these materials are more suitable as backfilling materials (see section 2.3.8 for an explanation of backfilling).

Another silicate ceramic that has been receiving attention is zircon [69–76]. Zircon ($ZrSiO_4$) is a stable mineral that contains radioactive U and Th in nature [71]. Natural zircons have been found with uranium and thorium concentrations of up to 10 wt % can be very durable [71]. It has been studied extensively as it is used for the dating of minerals by analysing the U:Pb ratio [27,71]. Furthermore Pu can completely substitute for Zr to form $PuSiO_4$ which makes it a very good prospective material for the long term disposal of weapons plutonium [27, 71]. In dissolution tests, even once it has undergone α-induced amorphisation, the dissolution rate of zircon is 2 orders of magnitude slower than that of borosilicate glass [71]. One drawback is the very large volume change on amorphisation of 18 - 20% [71, 73]. It is suggested that annealing of the damage by self heating (in a wasteform doped with 10 wt % ^{239}Pu) can maintain the crystallinity if the temperature remains above 225 °C [71]. Several processing operations have been developed at the laboratory scale for the production of zircon and Pu containing zircon and these include a sol gel route and hot pressing [27].

Fluorite Related Ceramics Other ceramics are being considered for use as materials for the immobilisation of HLW and these are generally variants of the fluorite structure (including pyrochlore). These will be discussed in depth later on in chapter 5.

2.3.6 Radiation Effects In Wasteform Materials

Introduction

The dominant source of radiation in an immobilised HLW form will vary with time but consists mainly of α-decay of actinide elements (mostly U, Np, Pu Am and Cm on commercial wastes) and β-decay of fission products (including ^{137}Cs and ^{90}Sr) [77]. Minor contributions are made by spontaneous fission of the actinides and although α-neutron reactions are yet another source of fission fragments and neutrons, compared with α and β-decay events, these are rare.

During the first 500 years, the accumulated damage is mostly due to the β-decay of the shorter-lived fission products (28.1 years for ^{90}Sr and 30.2 years ^{137}Cs). After about 1000 years the damage processes become dominated by α-decay (the half life of ^{239}Pu is 2.411×10^4 years) [77].

Decay events can cause damage in one of three ways:

1. Elastic collisions between the particle (the β-particle/α-particle/α-recoil nucleus) and the atoms in the host matrix. This can cause atomic displacements creating isolated Frenkel defect pairs (a vacancy and interstitial of the same species) or intense collision cascades.

2. Ionization effects associated with the α-particles, β particles and γ rays.

3. The transmutation of radioactive nuclei into different elements.

Out of these three effects, it is displacement processes that cause most damage as these cause rearrangements of the crystal structure and impact the physical and chemical processes of the material the most [77]. A very comprehensive study of α–decay damage in actinide bearing minerals was performed by Lumpkin [78]. Each α-decay event results in an average of 1500 ion displacements while a β-decay even only causes around 0.15 [77]. One of the differences between glass wasteforms and oxide ceramic based wasteforms is that oxide ceramic wasteforms seem to suffer little from ionisation events [77] whereas complex borosilicate glasses have been show to decompose by a ionisation driven process that produces baubles containing molecular oxygen [79].

The cumulative radiation dose that a wasteform will receive can be very high. Table 2.3 shows the anticipated cumulative doses for α and β radiations for waste glasses produced at the Savannah River Plant in South Carolina [80]. This shows that a glass wasteform containing 25% HLW (Defense Waste) will experience in excess of 0.0025 displacements per atom (dpa) or about 7×10^{10} rads in just 1000 years [77]. Cumulative doses for wasteforms containing commercial waste are several orders of magnitude higher than this due to the high concentration of fission products. After about 10,000 years, a SYNROC wasteform containing a 20 % loading of commercial waste will have absorbed a dose corresponding to 4×10^{18} α-decay events per gram or 0.32 dpa. A wasteform containing zircon will become metamict (or amorphous) at doses as low as 0.3dpa [77].

Table 2.3: Cumulative decay events and dose for a nuclear waste glass [80]

Time (years)	α-Decays per gram	β-Decays per gram	α-Dose (rad)	β-Dose (rad)
1	2×10^{14}	5×10^{16}	2×10^{7}	6×10^{8}
10	2×10^{15}	5×10^{17}	2×10^{8}	6×10^{9}
100	2×10^{16}	2×10^{18}	2×10^{9}	3×10^{10}
1,000	1×10^{17}	5×10^{18}	9×10^{9}	6×10^{10}
10,000	3×10^{17}	5×10^{18}	3×10^{10}	8×10^{10}
100,000	5×10^{17}	5×10^{18}	4×10^{10}	1×10^{11}
1,000,000	1×10^{18}	5×10^{18}	8×10^{10}	1×10^{11}

Radiation Damage Processes

When any solid is irradiated three basic responses are possible. It can be subject to heating, experience localised displacement of ions or become globally disordered. This section covers how the different kind of radiation affect the nuclear waste and how different kinds of wasteform perform.

Heating: When any kind of radiation is absorbed by a solid the temperature of the solid will increase. The size of this increase depends of several factors: The rate at which the energy is absorbed, the physical properties of the material (e.g. the specific heat or the thermal conductivity)and the rate that the material can conduct the heat away to the surroundings. With commercial HLW loadings significant heating is possible and when placed in repository conditions could reach temperatures at high at 600 °C [77]. Even after 100 years temperatures are likely to remain as high as 300 °C and this can have significant effects on the radiation response of the material. Figure

2.7 shows 2 plutonium hemispheres from the core of a nuclear weapon that have been placed on top of each other. The heating effect causing it to glow red-orange is entirely down to radiation self heating.

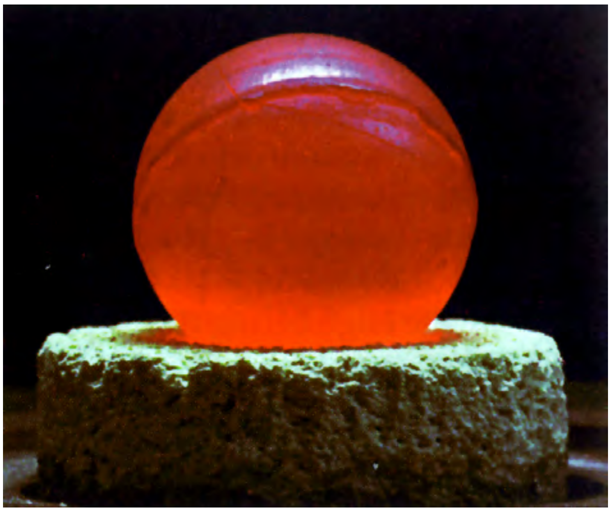

Figure 2.7: Radiation induced self heating 2 joined hemispheres of plutonium for use in a nuclear weapon [81].

Irradiation by α-particles and α-recoils: This is the most important form of radiation damage as it has the largest effect on the structure of the material. Typical energies of an α-particle are in the range of 4.5-5.5 MeV and the recoil atom has an energy in the range of 10-100 keV. Even though the α particle carries 98% of the energy of the decay event it has been calculated that this only accounts for accounts for a small fraction of the displacement energy imparted to the ions in the solid (between 6 and 11%) [77]. The reason for this counter-intuitive effect is due to the two primary ways in which moving particles can deposit their energy. These are: displacive (elastic collisions) or ionisation (inelastic) processes. Which of these that dominates depends on the relative velocity of the moving particle and that of the electrons orbiting the target ion. If the velocity of the particles is higher than the speed of the electrons then the dominating process will be electronic excitation but if it is moving slower, the probability of electronic excitation is small and most of the kinetic energy will be transferred to the nucleus. A rough rule for determining the dominating process is given by Ewing [77]: inelastic processes are important if the energy, expressed in keV, is greater then its atomic mass. Thus an α-particle with a mass 4 and energy 5,000 keV is predominantly slowed due to electronic excitation and an alpha recoil ion with mass 234 and an energy of 100 keV is stopped mainly via ballistic collisions. This means that an α-particle has lost most of its kinetic energy through electronic stopping before it can displace an ion in the solid. Therefore very few atoms are displaced by an α-particle and and furthermore this particle can travel a considerable distance of between 10 and 20 μm before it is stopped.

Irradiation by α-particles (and other light, high energy species) tends to result in the scattering of small numbers of ions along the entire path. This results in small clusters of Frenkel defects forming a damage track. This makes recombination of these defects relatively easy as they are surrounded by a large region of undamaged material [77].

In ceramic wasteforms (and most other solids) the only structural consequence of the electronic excitation is heating but in those affected by radiolysis (notably some borosilicate glasses), bond breaking and atomic displacements can occur. This effect allows crystalline silica (SiO_2) to undergo amorphisation by electrons which have an energy less than the displacement energy of the ions [82]. A similar effect has been observed in borosilicate waste glasses which can decompose by absorbing this ionizing energy and produce bubbles of molecular oxygen [79].

The heavier but lower energy α-recoil particle accounts for about 89% of the displacement energy in SYNROC [77] and unlike the α-particle these travel only very small distances, on the order of tens of nanometres (a factor of 1000 less than the range of the α-particle). This results in a large number of displaced ions in a small volume of the solid which can cause localised disordering. This is harder to anneal out than the small number of displaced atoms scattered widely as much of the surrounding order has been removed from the structure.

When an α-particle stops it becomes a helium atom and if the temperature of the wasteform is high enough to allow these to move through the material, they can collect and form helium bubbles in the material. The presence of these bubbles can have significant effects on the mechanical properties of the material, especially if they are located at grain boundaries [77].

Irradiation by β-particles: As mentioned earlier, in nuclear wasteforms β-particles are high-energy electrons formed mainly by the decay of fission products. Because of their very low mass β-particles tend to only create single displacement evens resulting in a Frenkel pair while the rest of their energy is dissipated via electronic excitation [77]. This means that β-particles have a very small damaging effect on most ceramic wasteforms but they could have a large effect on materials which are significantly affected by radiolysis.

β-decay is the principal cause of heating during the first 500 years and plays an important role in the recovery processes that occur in the wasteform.

Irradiation by γ-rays: Irradiation by γ-rays can only directly induce atomic displacements in materials susceptible to radiolysis. They can produce energetic electrons via interactions with solids but as mentioned in the discussion of β-particles, these are very inefficient in producing displacement events and combined with the low rate of production of these electrons, γ-rays are not a significant source of radiation induced structural changes in wasteform materials.

2.3.7 Other Options

It is impossible to eliminate all radioactive waste but there are technologies being proposed that, if implemented, could significantly reduce the quantity of waste ending up in geological repositories. Part of this has already been discussed in the reprocessing section (2.2.4) where recycling of uranium and plutonium (from both civil and defence sources) was discussed. While this redirects the majority of the volume of material from spent fuel away from encapsulation and burial, it still leaves the minor actinides and fission products to be stored. As shown in Figure 2.8 the radiotoxicity of the fission and activation products falls off to virtually zero after about 500 years whereas the radiotoxicity of the actinides and daughter products remains on the order of the original ore even after 1,000,000 years. If the actinides could be removed from the wasteform than the complexity of the disposal process would be significantly reduced. There is only one way that this process can be accelerated and this is by transmutation of these elements in pressurised water reactors, fast breeder reactors and possibly accelerator driven systems [83–87].

2.3.8 Final Disposal

Introduction

No matter how hard we try to reduce the volume of nuclear waste that has to be disposed of, either by reprocessing fuel or by the proposed transmutation of radioactive elements mentioned in section 2.3.7, there will always be some waste remaining that requires disposal. There are two seemingly incompatible approaches to the final disposal of nuclear waste. One is to concentrate and contain and the other involves dilution and dispersal. Both of these options are being used in the U.K. at the Sellafield reprocessing facility. The low level liquid wastes (after as much radioactive material is removed as possible) is pumped out to sea where it is diluted and eventually dispersed by the tides and ocean currents whereas the HLW is concentrated and then encapsulated into a glass wasteform awaiting later disposal.

Geological Repositories

It is almost certain now that the final resting place for high and intermediate level nuclear wastes will be in deep geological repositories [14, 15, 25, 77, 88–94]. The idea behind a repository is to store all the material in one place in such a way that the material does not re-enter the biosphere until the radioactivity has reduced to a level close to the natural background. Current policy for the Yucca Mountain repository in Nevada, U.S.A. is that it is necessary to demonstrate that no material will escape from the site for 10,000 years [93]. This may seem to be a long time but the radiotoxicity of the actinides in the wasteform remain higher than that for the natural uranium ore from which it was extracted for approximately 1,000,000 years see figure 2.8. The functions of a repository, according to the International Atomic Energy Agency (IAEA), change with time and are discussed in detail in the 2003 technical report [94] and summarised here:

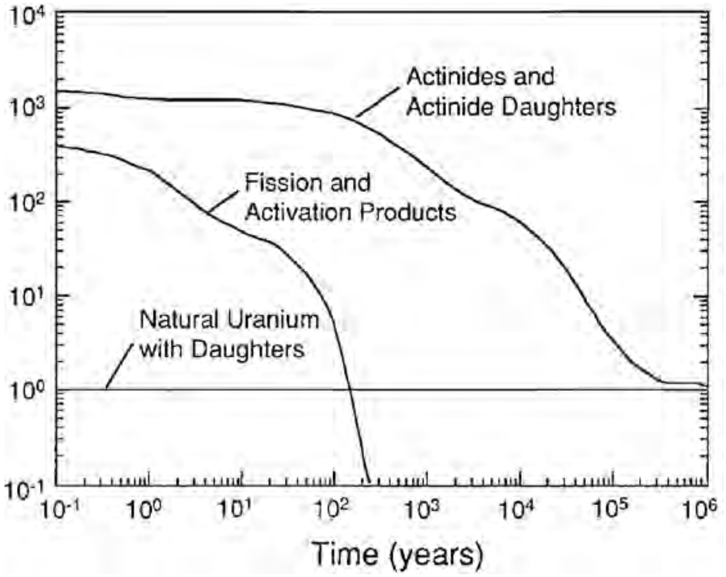

Figure 2.8: Relative radiotoxicity on inhalation of spent nuclear fuel with a burnup of 38 megawatt days/kg U. The radiotoxicity values are relative to the radiotoxicity (horizontal line) of the quantity of uranium ore that was originally mined to produce the fuel (eight tons of natural uranium yields one ton of enriched uranium, 3.5% ^{235}U) [95]

For the first few hundred years of its life, the repository should isolate the material from the fluctuation conditions on the surface and protect the biosphere from any contaminations i.e. while the radioactivity is at its peak. This should also be done in such a way as to isolate it from human activities so that it will be difficult and unlikely that it is disturbed either deliberately or accidentally. After the level of radioactivity has substantially decayed (after a few thousand years) the focus of the repository starts to shift from the complete containment philosophy to the acceptance that leaching of waste outside of the repository barriers is no longer serious. Processes should be in place that delay this point for as long as technically possible and keep this rate as low as possible. One way of ensuring this is the multi-barrier approach which will be discussed next. The final stage of the repository is to enable dispersion of the long lived radionuclides through the rocks that make up the repository. This can take many forms but one idea is for the dispersed material to encounter large bodies of water such that on return to the biosphere in tens or hundreds of thousands of years the concentrations are sufficiently dilute as to pose no threat.

In order to contain the waste for such long periods of time and eventually limit the rate of escape, repositories are designed around a multi-barrier approach similar to a set of Russian dolls [94, 96]. This idea is based on the fact that it cannot be guaranteed that any single barrier is capable of stopping the waste from escaping for a long time. The first barrier consists of the wasteform itself which is designed to be as durable as possible. This is then placed and welded inside a metal canister (e.g. stainless steel or copper [15, 94]). This container is then surrounded in a metallic overpack. Overpack and canisters are designed to protect the wasteform from corrosion more than act as a barrier against the release of the radioactive material.

They can be made from either corrosion resistant materials or a corrodible metal. If corrodible metals are used they should be of sufficient thickness to last until the short lived fission products have decayed. Once corrosion is complete the expected corrosion products (iron oxyhydroxides) can help further trap any radionuclides that have leached from the waste [94]. Corrosion resistant overpack materials (such as copper or titanium) have the potential to keep the wasteform isolated from water for much longer periods (100,000 years), maybe to the point where most mobile radionuclides have decayed to activities similar to natural uranium ore [94].

Once the waste packages have been loaded into the repository, backfill materials are packed around them. These vary depending on position in the repository and can include compacted bentonite clays to be packed around the HLW packages, crushed rock from the excavation process and concrete for use in regions for ILW [94]. The purpose of the bentonite clay around the HLW is threefold: The first is to limit the flow of water to and from the waste packages, bentonite clay has very low hydraulic conductivity. The second is, through its plastic nature, to isolate the package from damage due to small rock shifts caused by the heating effect of the waste or from minor earth tremors [94]. The final reason is that the clay has a sorption capacity that slows the migration of radionuclides. The crushed rock filling the rest of the repository (once sealed) is there to reduce the flow of water through the tunnels and provide structural support. In areas around the compacted bentonite, a mixture of bentonite powder and rock should be used as the clay expands upon contact with water and the backfill material must be dense enough to stop this material escaping.

The repository itself should be located in a geologically stable region. In this case stable means that there is a low probability of the site being damaged by earthquakes, volcanic activity, meteorite impact and flooding. Ideally due to the time periods involved it should also be in a region unlikely to be affected by the glaciation that may occur in another ice age. The repository should be made of impermeable rock so that, in the unlikely event of the container leaking, no waste will escape the region into the biosphere. This is also important as the atmospheric conditions in the repository should be kept constant as a change from reducing conditions to oxidising conditions, or vice versa, would change the behaviour of many of the material currently being researched [97]. Table 2.4 Shows the locations of major geological radioactive waste disposal research projects worldwide.

Table 2.4: Locations of major geological radioactive waste disposal research and operational projects [98]

Country	Location	Facility	Lithography	Age	Depth(m)
Belgium	Mol	URL	Clay	Paleocene	220
Canada	Lac du Bonnet	URL	Granite	Archean	420
Germany	Asse	URL	Salt	Permian	925
Germany	Gorleben	RCF	Salt	Permian	840-1200
Germany	Konrad	RCF	Sedimentary	Jurassic	1000
Germany	Morsleben (ERAM)	RCF	Salt	Permian	500
Japan	Tont	URL	Granite Margin	Cretaceous	150
Siberia	Tomsk	Aquifer	Sandstone	Cretaceous	300-400
Sweden	Stripa	URL	Granite Basement	Proterzoic	-
Sweden	Aspo	URL	Crystalline Basement	Proterzoic	450
Switzerland	Grimsel	URL	Granodiorite	Miocene	450
Switzerland	Mont Terri	URL	Clay	Jurassic	-
USA	Carlsbad (WIPP)	Repository	Salt	Permian	655
USA	Yucca Mountain	RCF	Tuff	Miocene	300

URL: Underground Research Laboratory

RCF: Rock Characterisation Facility

Chapter 3

Methodology

3.1 Introduction

All simulations carried out in this work are based on the classical Born model of ionic solids [99] in which the lattice is constructed from a periodic array of charged spherical ions. The interaction between ions is partitioned into two components. The first is a long range electrostatic interaction (Φ_{LR}) and the second is a short range interaction (Φ_{SR}) that acts mainly as a repulsive force that prevents two oppositely charged ions from colliding to form a singularity but it may also contain an attractive component. These combine as per Equation 3.1 to contribute to the total energy (Φ). Figure 3.1 shows a graphical representation of the short range, long range and total interaction energy between a pair of ions oppositely charged ions.

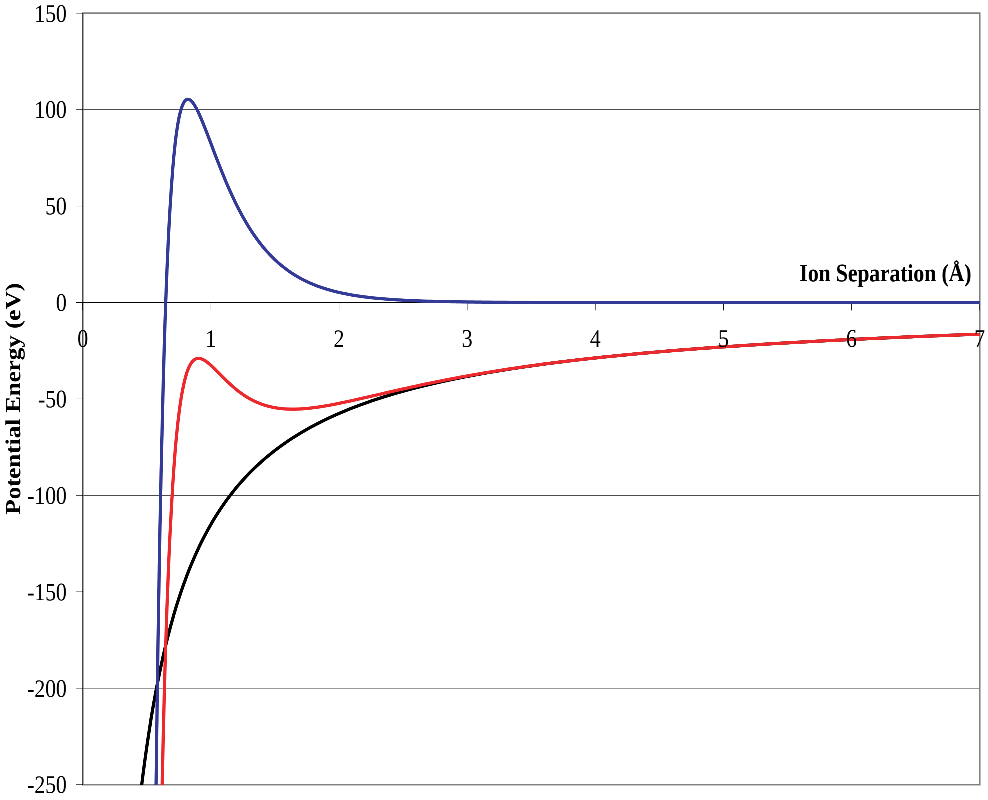

Figure 3.1: Graph of the interaction energy between two oppositely charged ions showing the contribution from the short range interaction (Blue), the long range Coulombic interaction (Black) and the total interaction (Red).

$$\Phi = \Phi_{SR} + \Phi_{LR} \tag{3.1}$$

The general interaction between all the ions in a solid containing many ions can be very complicated but it can be written simply as a series of summations involving increasing numbers of ions as per equation 3.2 i.e. two-body, three-body and n-body terms.

$$\Phi = \Phi_0 + \sum_{ij} \Phi_{ij} + \sum_{ijk} \Phi_{ijk} + \sum_{ijkl} \Phi_{ijkl} + \dots \tag{3.2}$$

where ij represents interactions between pairs of ions, ijk triplets, and higher order terms. Φ_0 is a function of the local environment and defines the zero energy. It is generally ignored as differences in energy are usually the important factor.

In an ionic solid (including all of the compositions studied) the interaction between ion pairs dominate and all the other terms can be omitted. This is known as the pair-wise approximation and is used throughout this work.

3.2 Atomic interactions Using Pair Potentials

The Long Range Interaction

By simplifying all the interactions to include only the pairwise, the long range interaction can be defined relatively simply. As mentioned earlier, it is essentially the electrostatic interaction between the ion pair and as such can either be attractive, in the case of oppositely charged ions, or repulsive if they are of like charge. Equation 3.3 shows the long range interaction energy(Φ_{LR}) of two ions (ion i and ion j) with charges q_i and q_j at a separation of r_{ij} (ε_0 is the permittivity of free space).

$$\Phi_{LR}(r_{ij}) = \frac{q_i q_j}{4\pi\varepsilon_0 r_{ij}} \tag{3.3}$$

While the definition of the long range interaction is simple, calculating it explicitly would be computationally expensive due to the slow rate at which contributions to the interaction energy fall off with distance $\left(i.e. \frac{1}{r_{ij}}\right)$. This means that for each ion, a huge number of interactions must be considered in order to compute this interaction with any accuracy. Fortunately, Ewald [100] developed an approximate method of calculating this summation which involves splitting the calculation into a short range real space component and a long range reciprocal space component [101]. The mathematics behind this are quite in depth and beyond the scope of this thesis. The result is that this allows the interaction to be calculated much more rapidly. This method is implemented in both molecular statics codes used during the course of this work (CASCADE [102] and GULP [103]). A simplified explanation of this method is given in Appendix B of "Introduction to Solid State Physics" by Charles Kittel [101].

3.2.1 The Short Range Interaction

Whereas the idea behind the long range interaction is very simple to understand, the origins of the short range interaction are more complicated. It is important to understand where this term originates from and how it is described as it is this contribution to the interaction that has the greatest effect on the accuracy of the simulations run in this study.

The short range interaction can be either completely repulsive or have a combination of repulsive and attractive components dependent on the ions that are interacting. The repulsive interaction originates from the overlap of the electron clouds of both atoms at very small ionic separations. This is partly due to the Pauli exclusion principal [104], with the rest of the contribution due to nuclear-nuclear interactions. The generalised version of the Pauli exclusion principal states that no two fermions can share the same quantum state. When the electron clouds overlap the Pauli exclusion principal forces the ground state charge distribution of the electrons to have a higher energy. This increase in energy is manifested as a repulsive force that increases in strength as the ions are moved closer together.

At slightly larger separations, an overall small attractive force can exist which is generally known as the van der Waals - London interaction. This attraction is due to the spontaneous formation of instantaneous dipoles on each of the interacting ions. London was able to determine a general expression for this interaction by describing dipole formation as a correlated motion of the electrons in both atoms [105–107]. London found that for the case of pair of identical ions i and j, this force varies as a function of r_{ij}^{-6} where r_{ij} is the separation of the ions. Clearly this force will be stronger between polarisable ions.

The short range interaction is clearly complex and consequently it is possible to approximate it using a number of functional forms. The potentials used in this study and some of the other possible approximations will now be discussed.

Potential Forms

The earliest attempt to couple a short range repulsive potential with the Long range Coulomb interaction was attempted by Born and Landé [108] and the short range component was described by the following equation.

$$\Phi_{ij} = \frac{b}{r_{ij}^n} \tag{3.4}$$

where b and n are variables chosen to reproduce the equilibrium interionic separation; early work took n = 9. This model was later expanded when quantum mechanical calculations proved that, while it was a useful approximation, it was not correct for all materials. With this in mind, Born and Mayer [109] developed a short range potential of the form:

$$\Phi_{ij} = Ae^{-\frac{r_{ij}}{\rho}} \tag{3.5}$$

where A and ρ are variable parameters. So far, none of the potentials have considered the van der Waals interaction. The Lennard-Jones potential [110] combines the repulsive form from Equation 3.4 with an attractive van der Waals potential using the r_{ij}^{-6} dependence determined by London. The strength of this effect can be adjusted by varying the parameter C.

$$\Phi_{ij} = \frac{b}{r_{ij}^n} - \frac{C}{r_{ij}^6} \tag{3.6}$$

In modern calculations n is normally 12. This potential is often used to model non-bonded interactions such as those in liquids and gasses. If the

$\left(\frac{b}{r_{ij}^{n}}\right)$ term from the Lennard-Jones potential is removed and replaced with the more flexible two parameter exponential version from the Born-Mayer potential (Equation 3.5) then the result is the Buckingham potential [111].

$$\Phi_{ij} = Ae^{-\frac{r_{ij}}{\rho}} - \frac{C}{r_{ij}^{6}} \tag{3.7}$$

where, as before, A, ρ and C are parameters which are varied in order to reproduce experimental data. This is the potential form employed for many of the interatomic potentials used in this study although, due to the obvious case when C=0, some of the potentials used are of the Born-Mayer type. It should be noted that the short range interaction shown in figure 3.1 used the Buckingham potential model. Tables listing the Buckingham potential parameters used in this study are given in the respective chapters to avoid the confusion of which potentials are used in which circumstance.

Due to the short range nature of these potentials, a cut-off value beyond which they are no longer evaluated is used. The purpose of this is to reduce computation times since beyond a few lattice spacings, the contribution to the interaction is negligible (see figure 3.1). The value of this cut-off is normally determined by running a series of identical calculations with increasing values of the short range cut-off and plotting this against lattice energy. When this value reaches a plateau, further increases to the short range cut-off do not contribute to the energy and thus the cut-off value is chosen.

3.2.2 Derivation of Short Range Potentials

The potentials in chapter 4 were modified from Minervini *et al.* [112] in order to more accurately reproduce the lattice parameters of the pyrochlore and the δ-phase (see chapter 4). This was performed by a purely empirical approach.

Empirical potential fitting is an iterative process whereby the potential parameters are varied in order to minimise the discrepancies between the simulation result and experimental data. In this study, only the parameters for chapter 4 were newly derived, and each potential was fitted to its basic oxide and any pyrochlore or δ-phase compound for which experimental data was available. In this system efforts were made to make sure that the sum of the deviations from the experimental lattice parameter was less than 1%.

3.3 Ionic Polarisability

The response of an ion's electric charge density to an electric field is simulated via the shell model of Dick and Overhauser [113] (note: only for those systems where it is required and feasible to implement i.e. not for molecular dynamics). The shell model is an addition to the Born model of the lattice that provides a method for predicting the effects of ionic polarisation. The addition of shells to ions in the lattice increases the computational time and memory requirements for the simulation as it adds many-body terms to the calculation. This means that it is not reasonable (and nor is it required) to add shells to all species. In order to decide whether or not an ion requires

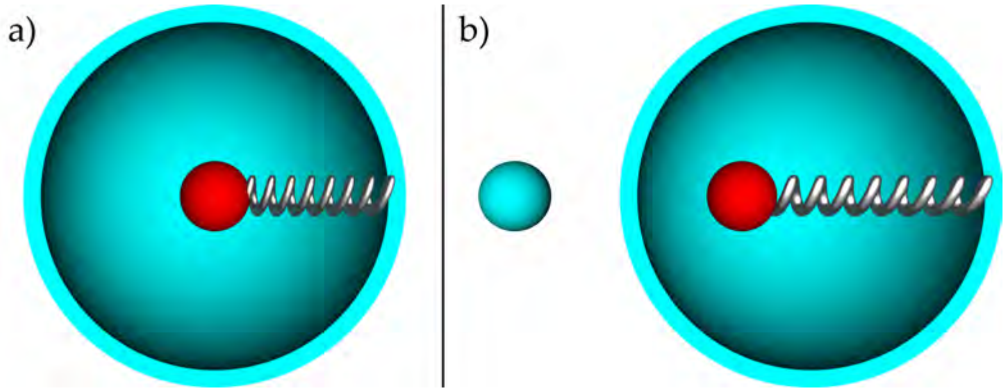

Figure 3.2: Graphical representation of the shell model showing a) no displacement, unpolarised b) displacement of the core from the centre, polarisation. In both figures, the red sphere represents a core with charge $+Xe$, the surrounding hemisphere represents the massless shell with charge $-Ye$ and the spring is representative of the isotropic force constant k. In b) the light blue sphere represents a negatively charged ion.

a shell, the electronic polarisability on the ion must be taken into account. Generally it is found that shells are required for anions, $O^{2=}$ for example, but not necessarily for cations, e.g. Mo^{4+}.

The Dick and Overhauser shell model for ionic polarisability [113] is used throughout. This model describes an ion as having a central core with charge Xe, representing the nucleus, and a shell of charge Ye, representing the electrons. These two charges are balanced so that the sum of $(X + Y)\,e$ is the same as the valence state of the ion. Generally the core is given a slightly positive charge and the shell is negative to balance this. These are coupled together via a harmonic force constant k (see figure 3.2). This allows the shell to move with respect to the core, thus simulating a dielectric polarisation. Using this description, the polarisability of an isolated ion, α, is given by equation 3.8:

$$\alpha = \frac{1}{4\pi\varepsilon_0}\left(\frac{Y^2}{k}\right) \tag{3.8}$$

Where Y is the charge on the shell, α is the polarisability (Å^3), k is the harmonic force constant (eVÅ^{-2})

Although no new shell model parameters were defined during the course of this study, it is still important to understand how such parameters were developed. Shell parameters are added to reproduce polarisability and therefore are fitted against the dielectric and elastic properties of a crystal. Since the polarisability has a particularly strong influence on the high frequency dielectric constant, it is generally the main observable parameter used to fit X, Y and k.

This model allows the coupling of the short range interaction to the polarisability and in this work it is assumed that (where present) short range interactions only interact between shells. This increases the complexity of the model as the position of the cores is now affected by a many-body interaction based on the electrostatic interactions with the shells and cores within the system, the two-body interactions of the shells and the force constant k. This added complexity allows the simulation of systems with greater accuracy than via a rigid-ion model.

This implementation of the shell model is limited as it cannot reproduce materials that violate the Cauchy relationship [114]. This relationship indicates that (for cubic crystals) the elastic constants c_{12} and c_{44} are equal. Unfortunately real materials can violate this and these two values can be quite different. This can be fixed to allow for Cauchy violations where $c_{12} < c_{44}$ by assigning a real radius to the shell and allowing it to change depending on the conditions, this model is termed the breathing shell [115]. Further modifications are also possible, for example, the elliptical breathing shell model [116] in which the shell can distort elliptically as well as change radius. This allows deviations of the form $c_{12} > c_{44}$. Unfortunately, these breathing shell parameters are notoriously difficult to parameterise and it has not been possible to implement here.

3.4 Static Calculations

3.4.1 Energy Minimisation

As the potential model used in the simulations is an approximation to reality, the force field predicted by the model does not exactly reproduce that determined by experiment. This means that even though the ions are placed in the ideal configuration as dictated by experiment, they may not be in the lowest energy state with respect to the approximated interionic potentials. Before a defect calculation is run or even the lattice energy is determined, it is important to allow the ions to relax to their lowest energy configuration with respect to the potentials used (otherwise any subsequent changes to ion positions may include a term associated with the movement of ions to their equilibrium positions). Obviously great care is taken to ensure that discrepancies with experimental data are kept to a minimum during the fitting process. This is done to ensure the greatest possible agreement between the simulated lattice and reality.

The simulation codes used minimise the lattice iteratively. During this process, the forces on each ion are calculated and then the ion is shifted slightly in proportion to the force acting on it. This continues until the forces acting on all the ions are zero.

It is possible to minimise the lattice at a constant volume or a constant pressure. Under constant volume conditions, the edges of the cell are held fixed and the ions can only move by varying their locations within the cell relative to the strains experience by each ion in the cell. Under constant pressure minimisation, the unit cell dimensions are also allowed to change such that the strains on the cell are minimised as well as those for the ions within it (clearly, in general this affords a more realistic simulation). As there are fewer degrees of freedom available for constant volume calculations, they take less time and as such many of the early energy minimisation calculations used this method. Due to advances in computer technology over the years, this optimisation is no longer required and all of the energy minimisation calculations in this thesis were performed under constant pressure conditions (interestingly many quantum mechanical simulations still use the constant volume approximation).

As mentioned earlier, the aim of the minimisation process is:

$$F = \frac{\partial U_L}{\partial r} = 0 \tag{3.9}$$

where F is the force on the system, U_L is the lattice energy and r is the coordinate system.

If the lattice energy of a system of N ions with coordinates, r, is $U_L(r)$ then the lattice energy at a new set of coordinates r' is:

$$U_L(r') = U_L(r) + \vec{g^T} \cdot \vec{\delta} + \frac{1}{2}\vec{\delta^T} \cdot \mathbf{W} \cdot \vec{\delta} \tag{3.10}$$

where $\vec{\delta}$ is a generalised strain vector with $3N$ displacement components, $\vec{\delta r}$, and 6 bulk strain components, $\vec{\delta\varepsilon}$;

$$\vec{\delta} = \left(\vec{\delta r}, \vec{\delta\varepsilon}\right) \tag{3.11}$$

$\vec{g}$ corresponds to the first derivatives of the lattice energy with respect to displacement and strain;

$$\vec{g} = \left(\frac{\partial U_L}{\partial r}, \frac{\partial U_L}{\partial \varepsilon}\right) \tag{3.12}$$

and $\mathbf{W}$ is a matrix that contains the corresponding second derivatives;

$$\mathbf{W} = \begin{pmatrix} \frac{\partial^2 U_L}{\partial r \partial r} & \frac{\partial^2 U_L}{\partial r \partial \varepsilon} \\ \frac{\partial^2 U_L}{\partial \varepsilon \partial r} & \frac{\partial^2 U_L}{\partial \varepsilon \partial \varepsilon} \end{pmatrix} \tag{3.13}$$

the new coordinates are related to the old coordinates by

$$r' = \Delta\varepsilon \cdot (r + \delta r) \tag{3.14}$$

where $\Delta\varepsilon$ is the Voight matrix representation of $\vec{\partial\varepsilon}$

$$\Delta\varepsilon = \vec{\partial\varepsilon} = \begin{pmatrix} \delta\varepsilon_1 & \frac{1}{2}\delta\varepsilon_6 & \frac{1}{2}\delta\varepsilon_5 \\ \frac{1}{2}\delta\varepsilon_6 & \delta\varepsilon_2 & \frac{1}{2}\delta\varepsilon_4 \\ \frac{1}{2}\delta\varepsilon_5 & \frac{1}{2}\delta\varepsilon_4 & \delta\varepsilon_3 \end{pmatrix} \tag{3.15}$$

In the simulation codes used, the simulation iterates closer and closer to the goal of zero force on the ions until the energy change is less than a predetermined value.

3.4.2 Defect Calculations

Once the lattice energy has been minimised with respect to ion positions, defects can be introduced, for example an ion can be removed to create a vacancy. The lattice will respond to the presence of this defect by further relaxation around this defect and it is assumed that the majority of this relaxation occurs close to the defect and that the extent of relaxation decreases with distance. This makes it reasonable to split the lattice up into a series of different concentric spherical regions in which progressively more approximate methods are used to calculate the lattice response to the defect with increasing distance (figure 3.3 shows this).

The region containing and immediately surrounding the defect is called Region I, this extends from the centre of the defect site to a predetermined radius. In this region, the interactions are calculated explicitly with the ions being allowed to relax to zero strain. Beyond this boundary, the lattice relax-

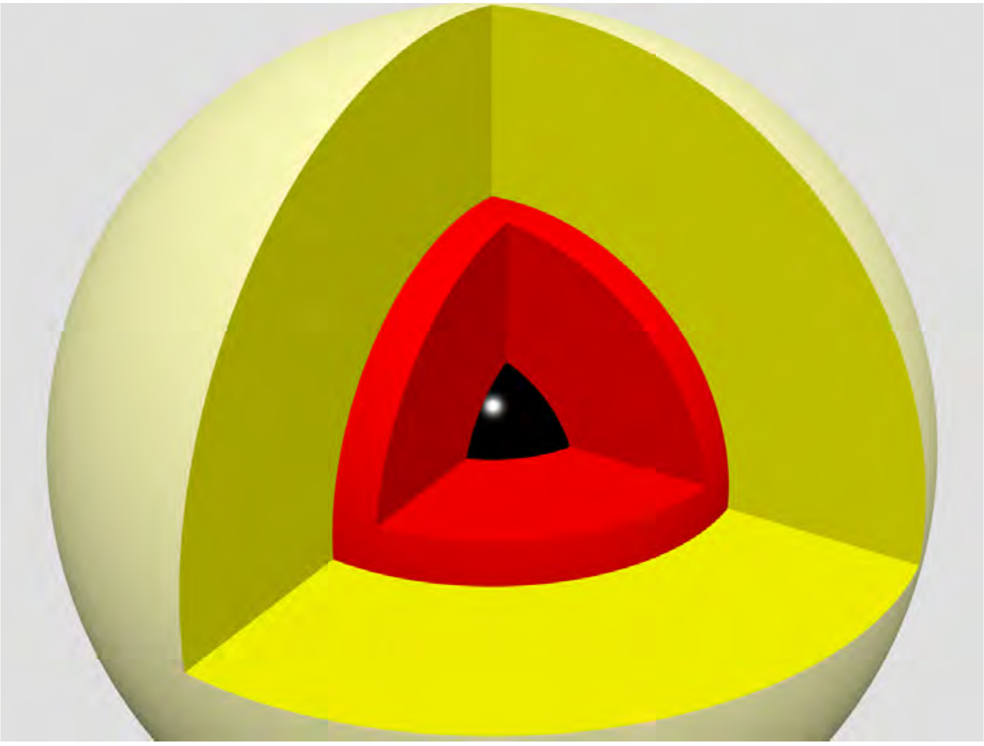

Figure 3.3: Graphical representation of the multi region approach for defect energy calculations. The defect(s) are coloured black, region I is red and region IIa is yellow. Region IIb is represented by the grey background and extends to infinity from the outside surface of region IIa (pale yellow).

ation of the defect is much smaller and as such, a more approximate method can be used. This outer region, termed region II, extends from the edge of this region to infinity.

Region II is further subdivided into two regions, IIa and IIb, where region IIa acts as a buffer layer between region I and region IIb. In region IIa, ion displacements are inferred from the Mott-Littleton approximation [117] but interactions with region I are calculated by explicit summation. This means that region IIa must always be at least the size of region I plus the short range cut-off, such that the ions at the edge of region I can interact with the ions in region IIa. The response of the ions in region IIa, due to a defect at a distance, r, is due to the polarisation, P, calculated using the Mott-Littleton approximation [117]. For large distances

$$P = \frac{q\vec{r}}{4\pi r^3}\left(1 - \frac{1}{\varepsilon}\right) \tag{3.16}$$

where q is the charge of the defect and ε is the static dielectric constant of the crystal.

The total energy introduced to the lattice via the incorporation of a defect, E_d, is the sum of the energies in each region

$$E_d = E_I(\vec{r}) + E_{I-II}(\vec{r},\vec{\zeta}) + E_{II}(\vec{\zeta}) \tag{3.17}$$

where E_I is the energy due to the interactions of the ions in region I with their displacements given by the displacement vector $\vec{r}$; E_{II} is the energy of region II with an ion displacement vector $\vec{\zeta}$; and E_{I-II} is the energy due to the interaction between region I and II ions. It is not possible to calculate this explicitly since region II extends to infinity and thus would require the sum of an infinite number of displacements. However, since the displacements in region II are very small a quasi harmonic approximations is valid such that:

$$E_{II} = \frac{1}{2}\vec{\zeta} \cdot \mathbf{A} \cdot \vec{\zeta} \tag{3.18}$$

where $\mathbf{A}$ is the force constant matrix. Substituting equation 3.18 into 3.17 and differentiating with respect to $\vec{\zeta}$, the equilibrium displacements in region

II are given by:

$$\frac{\delta E}{\delta \zeta} = \left.\frac{\delta E_{I-II}(\vec{r}, \vec{\zeta})}{\delta \vec{\zeta}}\right|_{\vec{\zeta}=\vec{\zeta_e}} + \mathbf{A}\vec{\zeta_e} \tag{3.19}$$

where $\vec{\zeta_e}$ is the equilibrium value of $\vec{\zeta}$ corresponding to $\vec{r}$. When this is substituted into equation 3.18 and then back into equation 3.17, the defect energy dependence of the energy of region II is removed as shown in Equation 3.20

$$E_d = E_I(\vec{r}) + E_{I-II}(\vec{r}, \vec{\zeta}) - \frac{1}{2}\left.\frac{\delta E_{I-II}(\vec{r}, \vec{\zeta})}{\delta \vec{\zeta}}\right|_{\vec{\zeta}=\vec{\zeta_e}} \cdot \vec{\zeta_e}\vec{\zeta_e} \tag{3.20}$$

3.5 Molecular Dynamics Calculations

3.5.1 Background

Molecular dynamics simulations are fundamentally different from the energy minimisation process discussed previously. Energy minimisation processes relax the system to a local energy minimum with respect to the interatomic potentials used. While valuable, it cannot give any information about how such a system can vary as a function of time. This is where molecular dynamics (MD) becomes useful.

MD is a computer simulation technique where a set of interacting ions is allowed to evolve in time by integrating the laws of motion. In a MD simulation containing N ions, each ion, i, is assumed to obey Newton's laws of motion and, most importantly, Newton's first law such that:

$$F_i = m_i\mathbf{a}_i \tag{3.21}$$

where F_i is the force act on each individual ion due to interactions with all the other ions, m_i is the mass of that ion and $\mathbf{a}_i$ is equal to $\frac{d^2\mathbf{r}_i}{dt^2}$ (the acceleration of that ion).

There are many similarities between MD and the static calculations described previously in that the forces between the ions are based on a pair potential approximation where the interaction energy, Φ, for any two ions, i and j, with positions, $\mathbf{r}_i$ and $\mathbf{r}_j$, can be expressed in the form:

$$\Phi(\mathbf{r}) = \sum_j \sum_{j>i} \phi(|\mathbf{r}_i - \mathbf{r}_j|) \tag{3.22}$$

where ϕ is a combination of long range and short range interactions as per Φ in Equation 3.1 and the $j > i$ term in the second summation means each interaction is only considered once.

3.5.2 Time and System Size Limits

The size of the simulation is limited by the amount of memory available to the computer and while technically there is no limit to the amount of time that can be simulated, a practical limit is imposed by the short time-steps required for an accurate simulation (on the order of 10^{-15} s). Simulations of metal systems (where only 1 or 2 types of atom exist and only very short range forces need to be considered) have been made in which of millions of atoms have been simulated for nanoseconds. Simulations of ceramic systems where the short range interaction acts over 5-10 Å and the even longer range Coulombic interaction needs to be considered, make it necessary to limit the system sizes in order to simulate any meaningful period of time. The simulations run during the course of this work consist of individual runs containing about 98000 ions that were simulated for 6 ps.

3.5.3 Potentials Models for Molecular Dynamics Simulations

Short Range Interactions

While the Buckingham potential form works well for simulations reasonably near equilibrium conditions, it encounters problems with simulations where ions are likely to reach very small separations, such as simulations of collision cascade events. This is due to the fact that at very small separations, the Buckingham potential (with a non zero C-term) tends towards $-\infty$ (see figure 3.4). Even for Born-Mayer type potentials, the short range interaction is overly attractive at short range and therefore at very small separations a screened Coulomb potential (in this case the Ziegler-Biersack-Littmark or ZBL potential) was used [118]. In order for there to be a smooth transition between the short range potential and the ZBL potential, a spline was used to connect these such that the first and second derivatives of both potentials

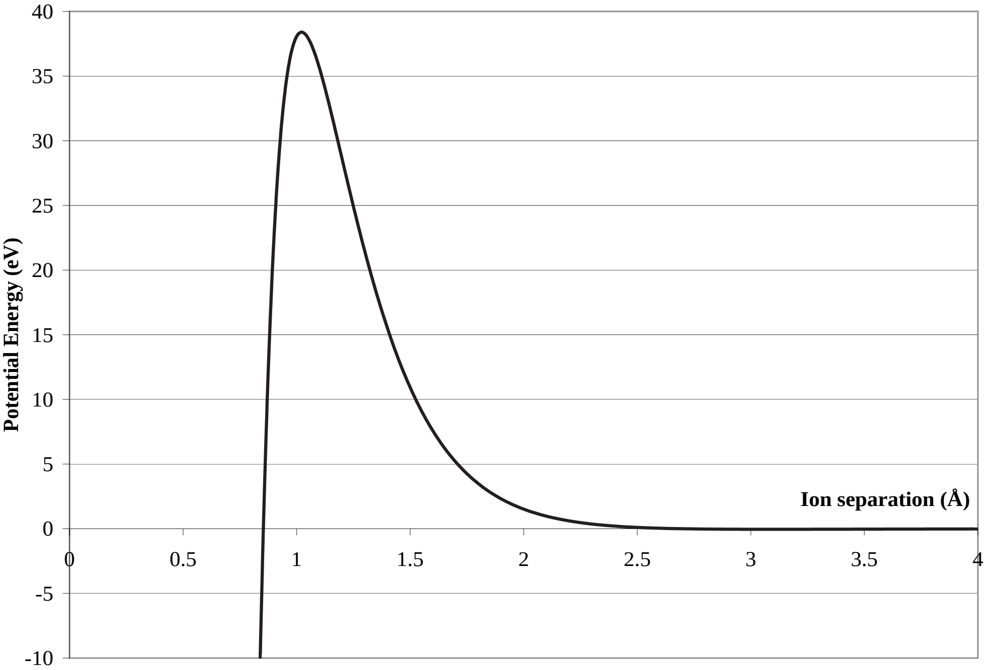

Figure 3.4: Graph showing the tendency for the Buckingham potential to tend to $-\infty$ at small ion separations when using a non-zero C-term.

were preserved. The general breakdown of the interactions is:

$$\Phi(r) = \begin{cases} \text{ZBL} & r < r_0; \\ g(r) & r_0 \leqslant r < r_1; \\ Ae^{-\frac{r}{\rho}} - \frac{C}{r^6} + V(r) & r_1 \leqslant r < r_2; \\ V(r) & r \geqslant r_2. \end{cases} \tag{3.23}$$

where V(r) is the Coulombic interaction and $g(r)$ is the splining function which is given by

$$g(r) = e^{\left(f_1 + f_2 r + f_3 r^2 + f_4^3 r + f_5 r^4\right)} \tag{3.24}$$

It should be noted that for cation-cation interactions no short range Buckingham potential is used, therefore the short range term in equation 3.23 reduces to just the repulsive Coulomb interaction between r_1 and r_2 and this is then splined to the ZBL potential.

Table 3.1 shows the parameters used to spline the short range interaction to the ZBL potential, table 3.2 gives the radial cut-offs for all the species in the system. The Buckingham potential parameters used in the MD simulations will be reorted in chapter 6. These parameters were previously used to study collision cascades in spinel [119].

Table 3.1: The parameters for the spline to the ZBL interaction.

	f_1	f_2	f_3	f_4	f_5	f_6
Mg-Mg	14.4507	-47.7977	122.4210	-175.9999	125.1304	-34.1480
Mg-Al	10.6531	-17.0984	27.9501	-36.8467	28.3526	-8.5504
Mg-O	11.0765	-31.3878	118.9207	-302.6137	367.5647	-167.4741
Al-Al	10.3578	-112.8183	9.4511	-1.2318	-1.0544	0.1604
Al-O	11.0284	-28.5714	95.3424	-217.4885	242.7988	-107.0122
O-O	9.9306	-17.4669	25.3341	-19.0023	6.6210	-0.8289

Table 3.2: Cut-off parameters used in MD simulations of pure and Al doped MgO (r_2 was 7.2Å for all interactions).

	r_0 (Å)	r_1 (Å)
Mg-Mg	0.5	1.05
Mg-Al	0.5	1.05
Mg-O	0.15	0.80
Al-Al	0.3	1.05
Al-O	0.15	0.8
O-O	0.2	1.05

Long Range Interactions

While many MD simulation packages use the Ewald sum (like the energy minimisation packages mentioned earlier) to calculate the long range Coulombic interactions, the MD code used in this thesis employs the Distributed Parallel version of the fast Multipole Tree Algorithm (DPMTA) library by Rankin [120]. This method uses multipole expansions to reduce the scaling from a system containing N particles from N^2 to $N \log N$, or for special situations, N [120]. A mathematical breakdown of how this method works will not be given here as it is beyond the scope of this thesis and detailed information can be found in [120] and [121]. A simple but brief introduction into the workings of the fast multipole algorithm is also given in [122].

Multipole expansions take advantage of the fact that at sufficiently great distances a group of charged particles can be represented as a single multipole expansion. As shown in figure 3.5, the many individual interactions between a single distant particle with all the particles in a group may be represented by a single interaction of the distant particle with the multipole expansion for the entire group.

Even though this method is only exact in a system containing an infinite number of particles, it is known to converge quite rapidly [120]. This allows these expansions to be truncated at a relatively small size whilst still maintaining a small error. Interactions between ions with small separations are calculated directly and it is for large separations that multipole expansions replace the direct calculation.

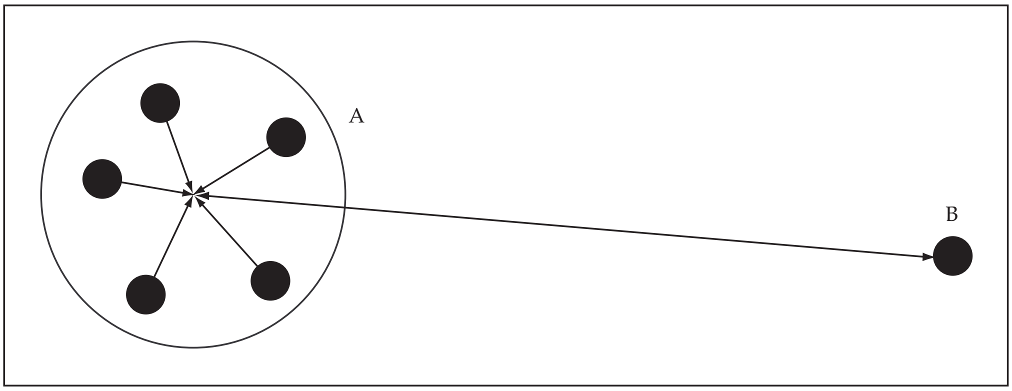

Figure 3.5: A multipole representation of a group of particles (A) interacting with a distant particle (B). Reproduced from [120].

3.5.4 Time Integration Algorithm

The core of any MD code is the time integration algorithm. This is required to integrate the equations of motion for the interacting ions and follow their paths. The solutions to this algorithm are calculated using finite difference methods in which time exists in discrete increments. By knowing the positions and some of the derivatives (see equations 3.25 and 3.26) at time, t, it is possible to integrate these to calculate the values at a time $t + \Delta t$. By making Δt small enough, the error is reduced, but never completely removed (the Verlet algorithm, for example, has an error associated with the timestep proportional to Δt^4). Another source of error is due to the rounding error associated with the finite accuracy of the processor. In this work, 64 bit representations of the properties are used in order to minimise these errors. In the current implementation of the simulation code, the timestep is a variable and scales with respect to the fastest moving ion in the system. This allows a much smaller timestep (sometimes as low as 0.08 fs) to be used at the start of the simulation so that accuracy is maintained when a few ions have very high kinetic energies (peaking at 1 or 2 keV), whilst allowing the timestep to grow (to a maximum of 1.05 fs) once the ions in the system slow down. Consequently the simulation completes faster and time is not wasted calculating more timesteps than necessary.

Verlet Algorithm

The Verlet algorithm [123] is one of the most common integration algorithms used for MD simulations. The basic concept is to construct two, third order Taylor series expansions for the positions, $\mathbf{r}(t)$, one forward and one backwards in time. Calling the velocity $\mathbf{v}$, the acceleration $\mathbf{a}$, and the third derivatives of $\mathbf{r}$ with respect to t, $\mathbf{b}$ gives:

$$\mathbf{r}(t+\Delta t) = \mathbf{r}(t) + \mathbf{v}(t)\Delta t + \frac{1}{2}\mathbf{a}(t)\Delta t^2 + \frac{1}{6}\mathbf{b}(t)\Delta t^3 + O(\Delta t^4) \tag{3.25}$$

$$\mathbf{r}(t-\Delta t) = \mathbf{r}(t) - \mathbf{v}(t)\Delta t + \frac{1}{2}\mathbf{a}(t)\Delta t^2 - \frac{1}{6}\mathbf{b}(t)\Delta t^3 + O(\Delta t^4) \tag{3.26}$$

These equations are then added together and rearranged to yield:

$$\mathbf{r}(t+\Delta t) = 2\mathbf{r}(t) - \mathbf{r}(t-\Delta t) + \mathbf{a}(t)\Delta t^2 + O(\Delta t^4) \tag{3.27}$$

which is the basic form of the Verlet equation. Since Newtonian mechanics are assumed, $\mathbf{a}(t)$ is just the force divided by the mass and the force is a function of the ion positions $\mathbf{r}(t)$:

$$\mathbf{a}(t) = -\left(\frac{\nabla\Psi(\mathbf{r}(t))}{m}\right) \tag{3.28}$$

The popularity of this algorithm is due to the simplicity of implementation, its accuracy and stability. One of the problems is that it is often necessary to generate ion velocities, this information is often subsequently inferred in order to calculate the kinetic energy of the ions. In fact, this is commonly used to test that conservation of energy is being maintained as this is a good indication that the step size is small enough.

While it is possible to calculate the velocities using

$$\mathbf{v}(t) = \frac{\mathbf{r}(t+\Delta t) - \mathbf{r}(t-\Delta t)}{2\Delta t} \tag{3.29}$$

the errors as a function of step size are significantly larger than those for positions (proportional to Δt^2 rather than Δt^4). In order to deal with this, a better implementation of this algorithm has been developed which is used in this work and is termed the velocity-Verlet algorithm. In this method, the positions, accelerations and velocities are calculated at time $t + \Delta t$ using the following equations:

$$\mathbf{r}(t+\Delta t) = \mathbf{r}(t) + \mathbf{v}(t)\Delta t + \frac{1}{2}\mathbf{a}(t)\Delta t^2 \tag{3.30}$$

$$\mathbf{v}\left(t + \frac{\Delta t}{2}\right) = \mathbf{v}(t) + \frac{1}{2}\mathbf{a}(t)\Delta t \tag{3.31}$$

$$\mathbf{a}(t) = -\left(\frac{\nabla\Psi(\mathbf{r}(t+\Delta t))}{m}\right) \tag{3.32}$$

$$\mathbf{v}\left(t+\Delta t\right) = \mathbf{v}\left(t + \frac{\Delta t}{2}\right) + \frac{1}{2}\mathbf{a}(t+\Delta t)\Delta t \tag{3.33}$$

3.6 Simulation Codes Used

Three simulation codes were used in total, two static energy minimisation codes and one molecular dynamics code. The energy minimisation codes were; CASCADE (Cray Automated System for the CAlculation of Defect Energies) [102] and GULP (General Utility Lattice Program) [103]. CASCADE was developed at the Daresbury Laboratory for the CRAY computer and was based on HADES (Harwell Automatic Defect Examination System) code [124]. The molecular Dynamics code is called LBOMD [125] and was developed at Loughborough University.

Chapter 4

Relative Stabilities of Pyrochlore ($A_2B_2O_7$), Disordered Fluorite ($[AB]_2O_7$) and the δ-Phase ($A_4B_3O_{12}$)

4.1 Introduction

Materials with the fluorite BO_2 and disordered fluorite structure $(AB)_2O_{8-x}$ have been found to be remarkably resistant to radiation induced amorphisation [126–129]. Using this nomenclature A represents a trivalent cation and B represents a tetravalent cation. Examples of these include UO_2 [126], monoclinic zirconia [127], cubic stabilized zirconia [127–129], $Y_2Ce_2O_7$ and

$La_2Ce_2O_7$ [130], and $Er_2Zr_2O_7$ [131,132]. Although at first glance these last three material my appear to be pyrochlore (discussed next), they actually form in the disordered fluorite structure [130]. Due to this high radiation tolerance, they have been considered for combined inert matrix fuel forms and wasteforms for the “burning” and final disposal of Pu and the minor actinides [133,134].

Pyrochlore ($A_2B_2O_7$) compounds are related to the fluorite structure and the nature of this relationship will be considered in the crystallography section (section 4.2.1). They form over a huge compositional range due to the flexibility of the structure and this was explored in depth in the review by Subramanian [135]. As stated earlier, the pyrochlores considered in this study are formed by combining a trivalent “A” cation and a tetravalent “B” cation although pyrochlores can also form in the ${A^{2+}}_2{B^{5+}}_2O_7$ stoichiometry [135]. Due to this wide compositional range, pyrochlore compounds have many different properties and they have been used, or are being put forward as materials for use in diverse applications including solid electrolytes [136–140], anodes [140–144] and cathodes [140,145–147] for fuel cells and sensors, catalysts [148–150], dielectrics [151–155] and materials for the encapsulation of actinides and other nuclear wastes (see chapter 5).

Another fluorite related phase which also forms in the A_2O_3-BO_2 system is the δ-phase. Unlike the pyrochlore system which has been studied extensively, much less is known about these compounds. There have only been a few studies into this system, mainly as passing interest in technologically important systems like indium-doped tin oxide (ITO) [156] and cubic stabilised zirconia [157–159]. There have been a few studies specifically aimed at compounds in this system including the study by Lopato *et al.* [160] in which the synthesis and thermal expansion properties of these phases were determined and a study by Thornber *et al.* [161] in which the crystal structures of $Sc_2Zr_5O_{13}$ and $Sc_4Zr_3O_{12}$ were determined.

In order to understand these related materials better, it is important to know what phases will be formed when a mixture of simple oxides are combined (synthesis). For example, when Yb_2O_3 and ZrO_2 are combined, will a δ-phase or a pyrochlore or a fluorite structure result? In this chapter, an extensive range of compositions will be investigated using atomistic simulation in order to provide greater insights into this complicated question. The results will be plotted in the form of a phase map in which A cations, ordered by ionic radius are shown, increasing along the y-axis, B cations, also ordered by ionic radius, increase along the x-axis and the points on the map indicate compounds simulated. The colour of the point will indicated which phase is most stable. This information can then be used to guide experimental studies into the relative radiation durabilities of the corresponding materials which can then be use to gauge potential performance+ as a wasteform material

4.2 Literature Review

4.2.1 Crystallography

The fluorite, pyrochlore and δ phases are all related. As the stoichiometry changes from BO_2 to $A_2B_2O_7$ to $A_4B_3O_{12}$ the anion to cation ratio decreases and is shown in table 4.1. It is easy to see how this has been achieved going from the fluorite to the pyrochlore phases as they are conceptually similar but the δ-phase is more difficult to visualise. Figure 4.1 shows a full unit cell of the fluorite structure and figure 4.2 shows an idealised 1/8 unit cell of pyrochlore with all the oxygen ions at the positions they would occupy if it had adopted the fluorite structure. From these it is clear that one of the oxygen ion positions that was occupied in the fluorite structure is now absent and the cation sublattice now exhibits an alternating ABAB pattern. This results in a doubling of the cubic unit lattice parameter from approximately 5 to 10Å.

Table 4.1: Anion to cation ratios from fluorite to δ-phases. M represents any metal, or the number of cations.

Compound	Stoichiometry	Anion - Cation Ratio
Fluorite	MO_2	2.000
Pyrochlore	M_4O_7	1.750
δ-phase	M_7O_{12}	1.714

The structure in figure 4.2 is an idealised version to aid comparison and does not show the way way in which the anions restructure around the 8a site or how the structure orders. This is shown in figure 4.3. The figure was generated used the structural data for $Gd_2Sn_2O_7$ from Kennedy *et al.* [162].

Part a) of this figure shows that the 48f oxygen ions relax away from their ideal fluorite position, moving towards the unoccupied site (the 8a site in fluorite). The degree of relaxation is termed the x parameter as it refers to the condition of the 48f site coordinates (x, $\frac{1}{8}$, $\frac{1}{8}$) [163]. The ideal fluorite positions occur with an x parameter of 0.375 and this idealised structure is shown in Figure 4.3b) which also makes the cation ordering of the system clear. For $Gd_2Sn_2O_7$ the value of x is 0.3348 [162].

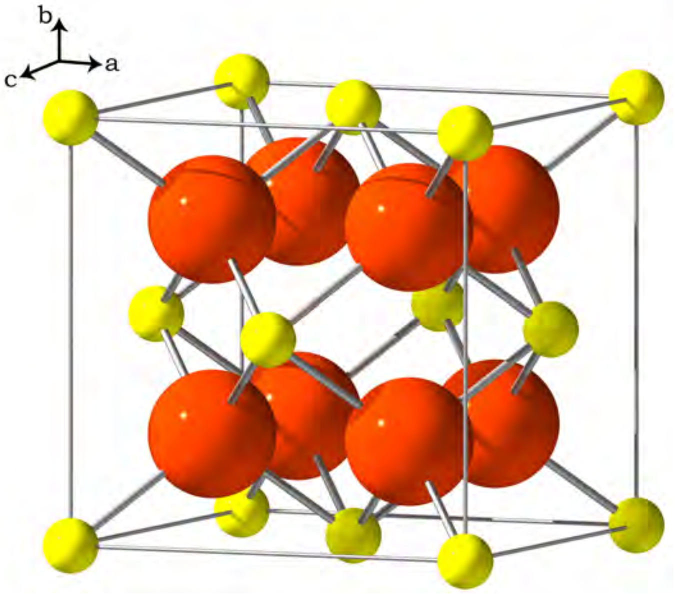

Figure 4.1: The Fluorite Structure. Small yellow spheres are B^{4+} ions, large red spheres are O^{2-} ions.

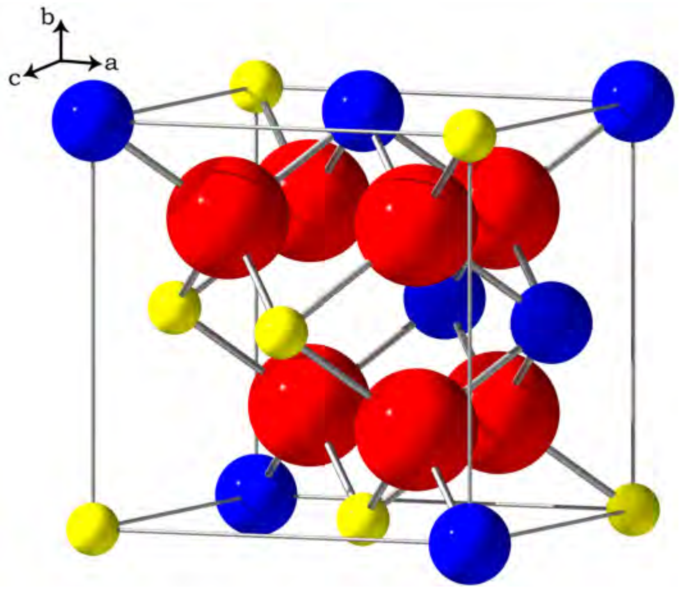

Figure 4.2: The Pyrochlore Structure (1/8 unit cell). Larger blue spheres are A^{3+} ions, small yellow spheres are B^{4+} ions, large red spheres are O^{2-} ions.

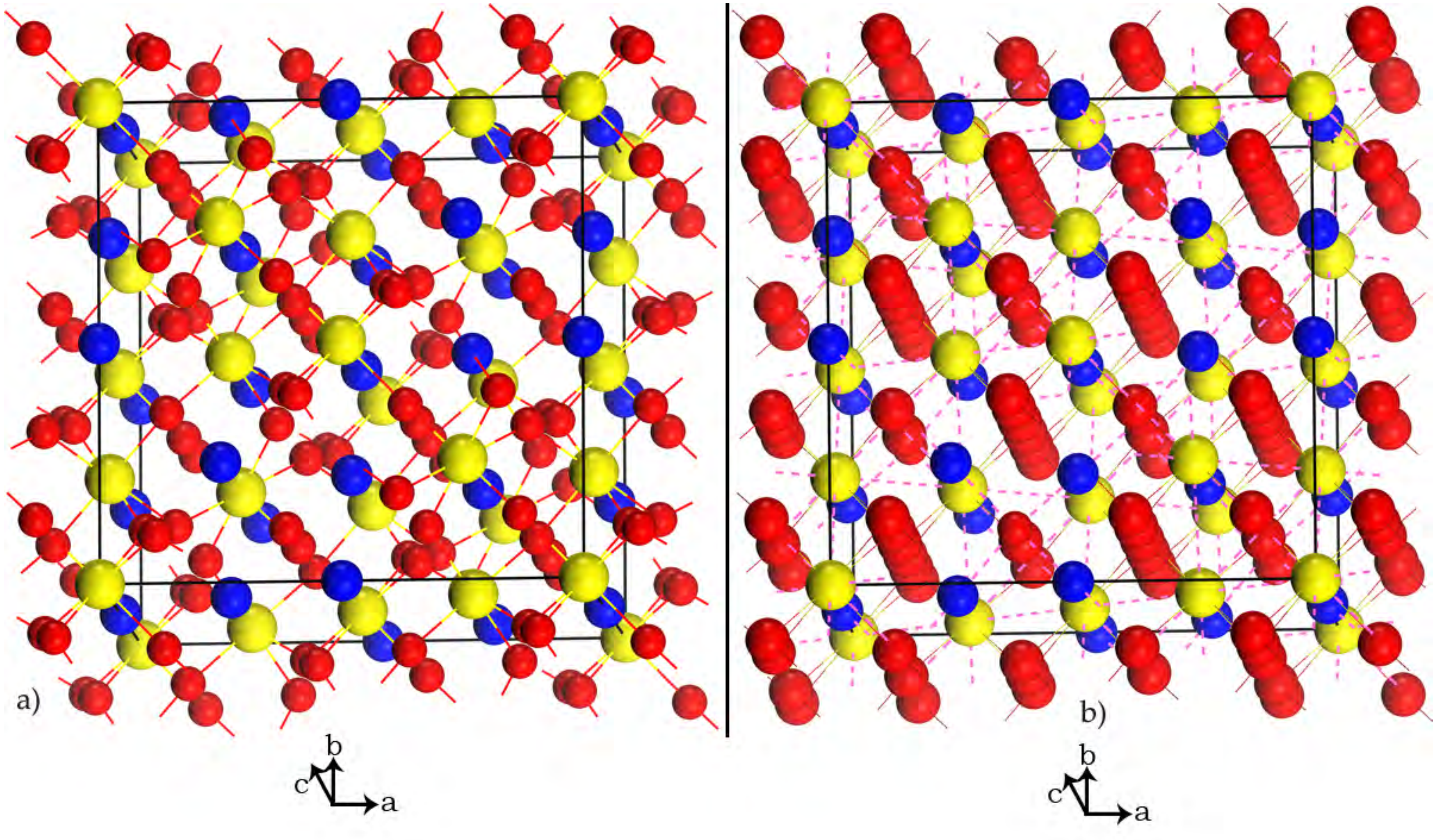

Figure 4.3: The Pyrochlore Structure (Full unit cell). a) Showing relaxed $Gd_2Sn_2O_7$ positions ($x = 0.3348$). b) Showing idealised fluorite positions ($x = 0.375$).

As mentioned earlier there are compounds that form with the pyrochlore stoichiometry ($A_2B_2O_7$) but do not actually form in the cubic pyrochlore structure. There are at least 2 variants, one is the disordered fluorite ($[AB]_2O_7$) which tends to form in the large B cation, small A cation region and the other forms a monoclinic structure which tends to form in the large A cation, small B cation region of the compositional space.

The disordered fluorite structure exhibits the $Fm\bar{3}m$ space group and has 50% A and B cation occupancy on the cation sublattice and a $\frac{7}{8}$ occupancy on the 8c oxygen sublattice [164, 165]. Figure 4.4 shows a schematic of the disordered fluorite structure generated using structural data from [164].

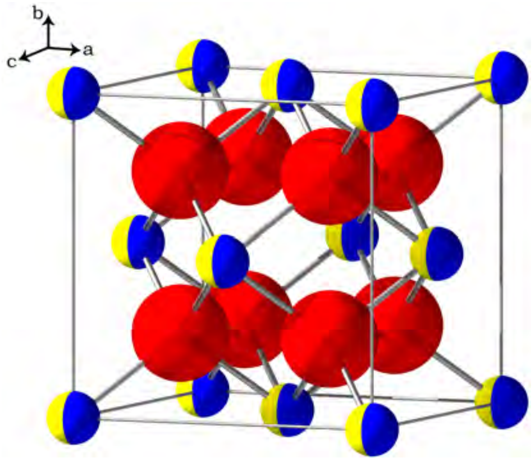

Figure 4.4: The Disordered Fluorite Structure. Mixed A and B cations randomly distributed over the cation sublattice are determined by yellow/blue hemispheres and the $\frac{7}{8}$ occupied O sublattice is represented by red spheres.

The monoclinic structure forms in the $P2_1$ space group and structural data has been derived by Schmalle *et al.* [166] for the $La_2Ti_2O_7$ compound. The structure is shown in figure 4.5.

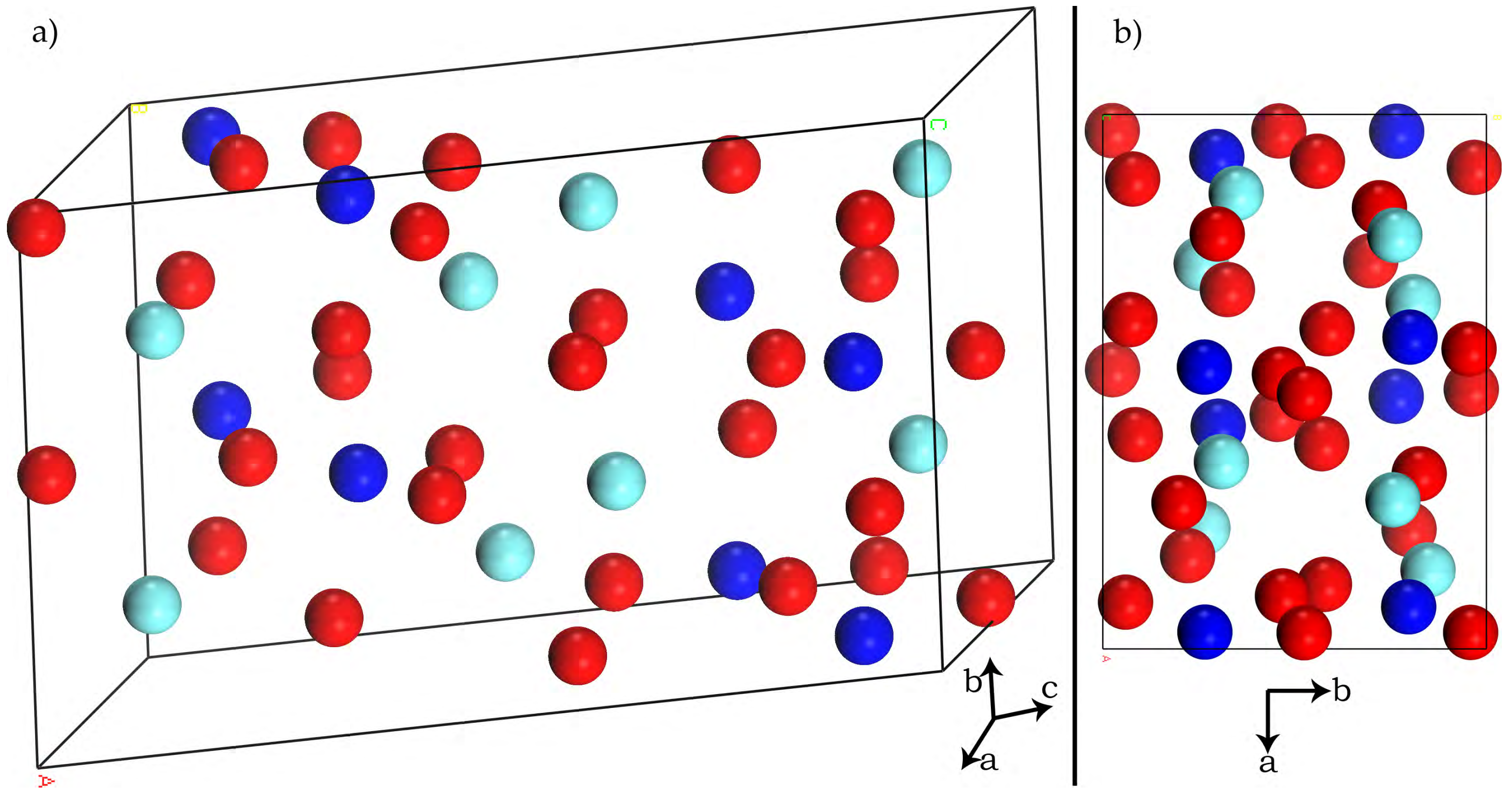

Figure 4.5: The Monoclinic Pyrochlore Structure. Light blue spheres are A^{3+} ions, dark blue spheres are B^{4+} ions, red spheres are O^{2-} ions. a) Perspective view, b) view down the c-axis. Created using structural data from Schmalle *et al.* [166].

The δ-phase ($A_4B_3O_{12}$) forms in a rhombohedral structure (in the R$\bar{3}$ space group) although it is more commonly represented in a hexagonal form [1, 156–161, 167]. Until recently the structure was usually defined as per Red'ko and Lopato [1] (data for $Sc_4Zr_3O_{12}$ reproduced in table 4.2). These authors define the cation sublattices a disordered mixture of Sc and Zr. Two theoretical studies by Bogicevic *et al.* [158] and Bogicevic and Wolverton [157] have refined this further for $Y_4Zr_3O_{12}$ and $Sc_4Zr_3O_{12}$ respectively to produce coordinates which can be represented in the R3 space group without disordered cations. This makes it possible to run computer simulations that can easily be compared with systems that are not disordered. The data for $Sc_4Zr_3O_{12}$ is shown in table 4.3 and a graphical representation is shown in Figure 4.6.

Table 4.2: Crystal Structure of $Sc_4Zr_3O_{12}$. Space Group R$\bar{3}$, a = b = 9.396Å, c = 8.706Å $\alpha = \beta = 90°$, $\gamma = 120°$. Reproduced from Red'ko and Lopato [1].

Ion	Site	x	y	z	Occupancy
$Zr^{4+}(1)$	3a	0.0000	0.0000	0.0000	0.429
$Sc^{3+}(1)$	3a	0.0000	0.0000	0.0000	0.571
$Zr^{4+}(2)$	18f	0.2903	0.4096	0.0161	0.428
$Sc^{3+}(2)$	18f	0.2903	0.4096	0.0161	0.572
$O^{2-}(1)$	18f	0.2990	0.4530	-0.2300	1.000
$O^{2-}(2)$	18f	0.3010	0.4540	0.2780	1.000

Table 4.3: Crystal Structure of $Sc_4Zr_3O_{12}$. Space Group R3, a = b = 9.532Å, c = 8.823Å $\alpha = \beta = 90°$, $\gamma = 120°$. adapted from Bogicevic and Wolverton [157].

Ion	Site	x	y	z	Occupancy
$Zr^{4+}(1)$	3b	0.6159	0.5445	0.6840	1.0
$Sc^{3+}(1)$	3b	0.8817	0.5877	0.9832	1.0
$Sc^{3+}(2)$	1a	0.6667	0.3333	0.3247	1.0
$O^{2-}(1)$	3b	0.0376	0.8204	0.8886	1.0
$O^{2-}(2)$	3b	0.3086	0.8440	0.7823	1.0
$O^{2-}(3)$	3b	0.6375	0.5208	0.9397	1.0
$O^{2-}(4)$	3b	0.8424	0.5436	0.7252	1.0

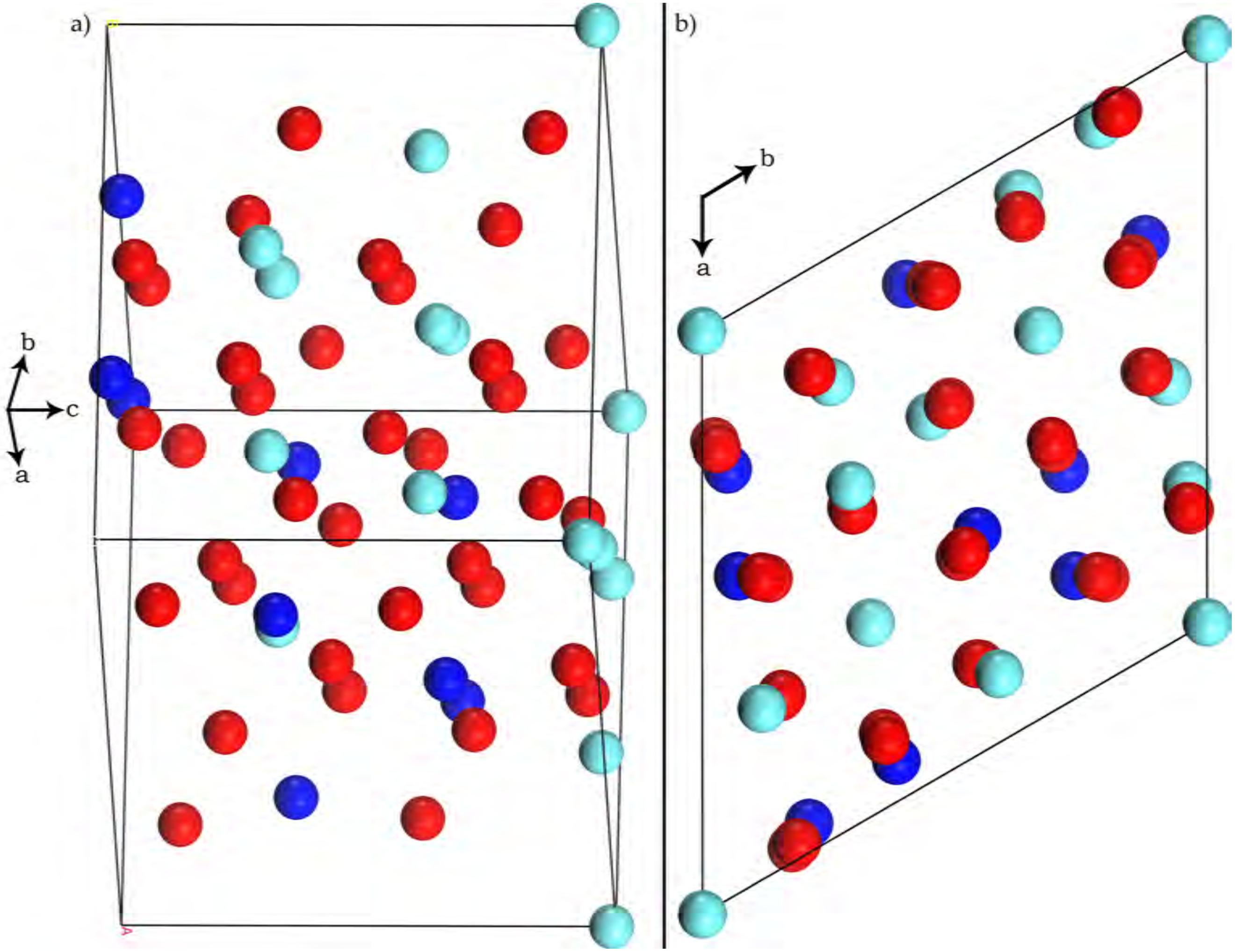

Figure 4.6: The Ordered δ-phase Structure. Light blue spheres are A^{3+} ions, dark blue spheres are B^{4+} ions, red spheres are O^{2-} ions. a) perspective view, b) view down c-axis.

4.2.2 Experimental Work

There has been a great deal of experimental work focusing on pyrochlores and fluorites, ranging from full scale phase diagram construction to structural studies using X-ray and neutron diffraction. Comparatively, less work has been performed on the δ-phase and the boundaries between the pyrochlore phase and δ-phases are uncertain. Some of the structural studies and phase diagrams will now be summarised and discrepancies highlighted.

Phase diagrams

There have been quite comprehensive studies on the titanate, hafnate and zirconate systems and some examples of these are show in figures 4.7 to 4.18. These figures will now be examined in order of B cation radius as they will appear in the results.

The titanate systems show a compound with pyrochlore stoichiometry ranging all the way from A cations Nd to Lu, even though, according to Subramanian [135], $Nd_2Ti_2O_7$ does not form in the cubic system. By examining figures 4.7, 4.8 and 4.9 it is possible to see both common features and differences which will now be discussed. They all predict formation temperatures for the pyrochlore compounds to be about 1800 °C and the existence of the A_2TiO_5 compound.

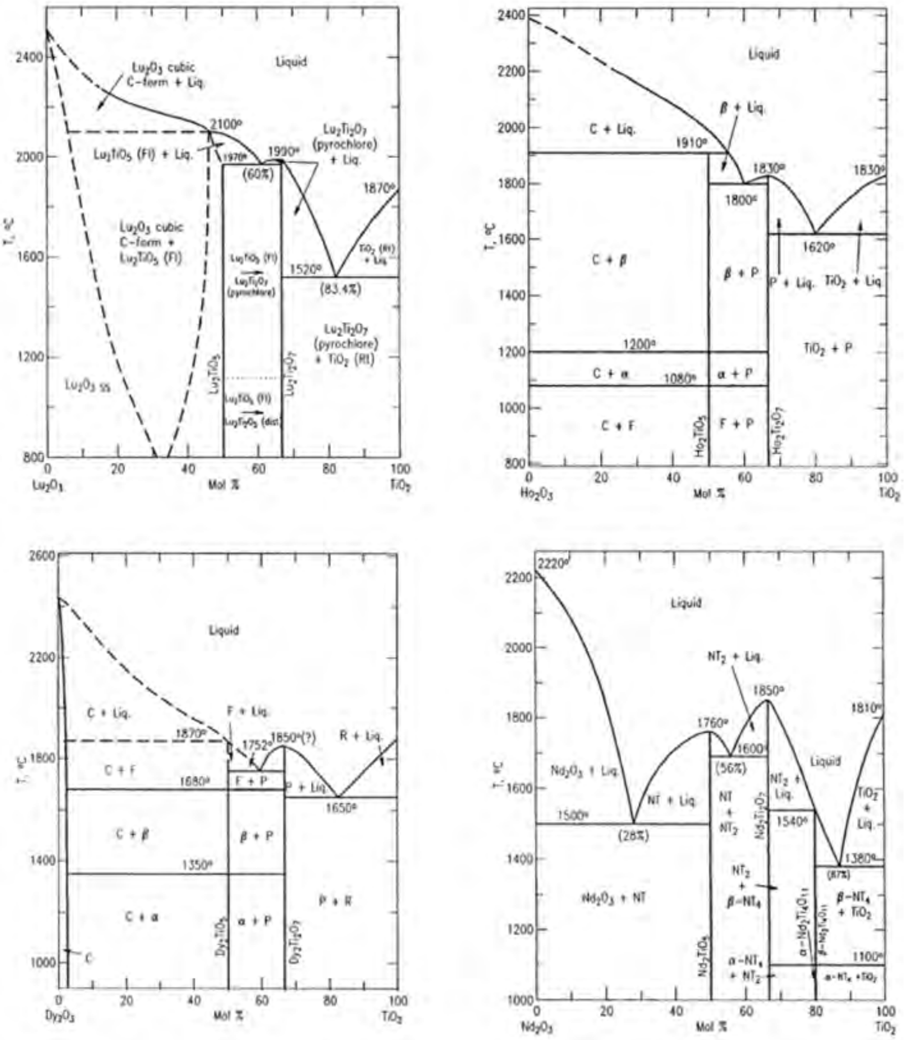

Figure 4.7: Phase Diagrams of A_2O_3 - TiO_2 systems, A = Lu, Ho, Dy and Nd. All showing a $A_2Ti_2O_7$ pyrochlore phase. Reproduced from [168–170]. C = cubic bixbyite, P = pyrochlore, R = rutile, F = fluorite, NT = Nd_2TiO_5.

All the systems in figure 4.7 show the pyrochlore as a line compound indicating no solid solution with either A_2O_3 or TiO_2 at any temperature, however, the Y_2O_3 - TiO_2 system shown in figure 4.8 shows a limited solid solubility.

It is tempting although incorrect to draw conclusions about differences between related but chemically different systems. Figure 4.9 shows 2 phase di-

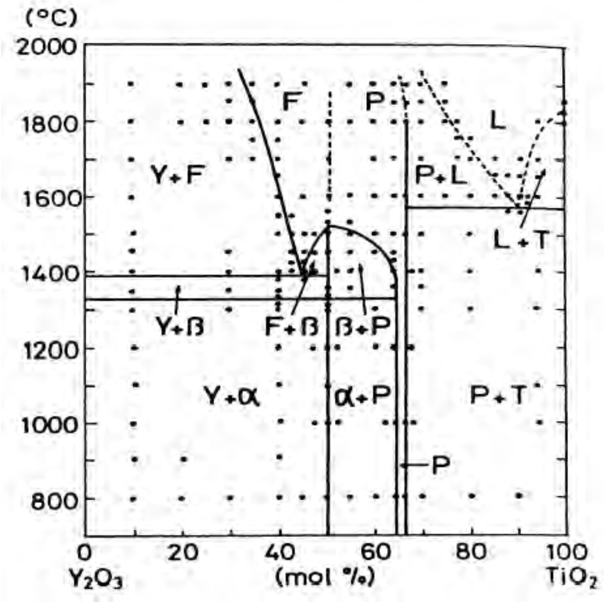

Figure 4.8: Phase Diagram of Y_2O_3 - TiO_2 system, reproduced from [171]. Y = Y_2O_3, P = pyrochlore, T = TiO_2 (rutile).

agrams for the Sm_2O_3 - TiO_2 system generated by different research groups and gives a good opportunity for comparison. There are quite obvious differences between the work by the different groups, one indicating the pyrochlore as a line compound, similar to the systems described in Figure 4.7, and the other showing a region of solid solution.

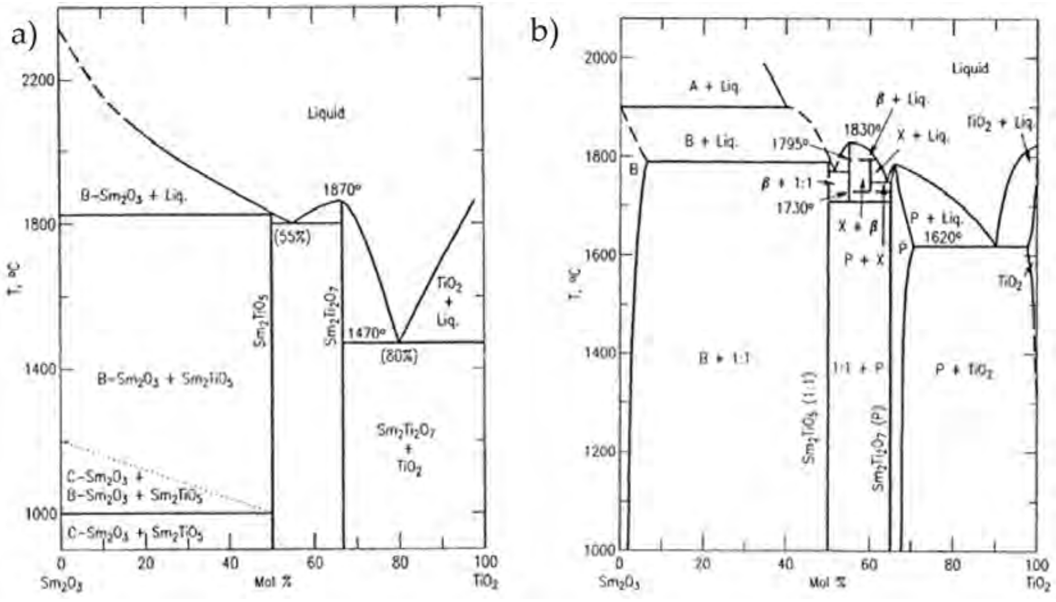

Figure 4.9: A comparison of 2 Sm_2O_3 - TiO_2 phase diagrams from different research groups. a) reproduced from [172]. b) reproduced from [173].

A very comprehensive set of phase diagrams is found by moving up in B cation radius to examine the A_2O_3 - HfO_2 systems. While Hf compounds were not specifically modelled in this study, the ionic radius of Hf^{4+} is 0.71 Å which places it in between Sn^{4+} (0.69 Å) and Zr^{4+} (0.72 Å), (ionic radii from Shannon [174]). This means that it is possible to interpolate between the two to generate results for Hf. By looking at the phase diagrams in figures 4.10 to 4.13 it is clear that the region of pyrochlore stability has significantly changed with respect to the titanate systems in that the pyrochlore phase is only stable for smaller A cations ranging from La to Tb.

Figure 4.10 shows phase diagrams in the system A_2O_3 - HfO_2 where the A cation is small. It can be noted here that all of these systems show an extensive fluorite solid solution field and no pyrochlore phase. These phase

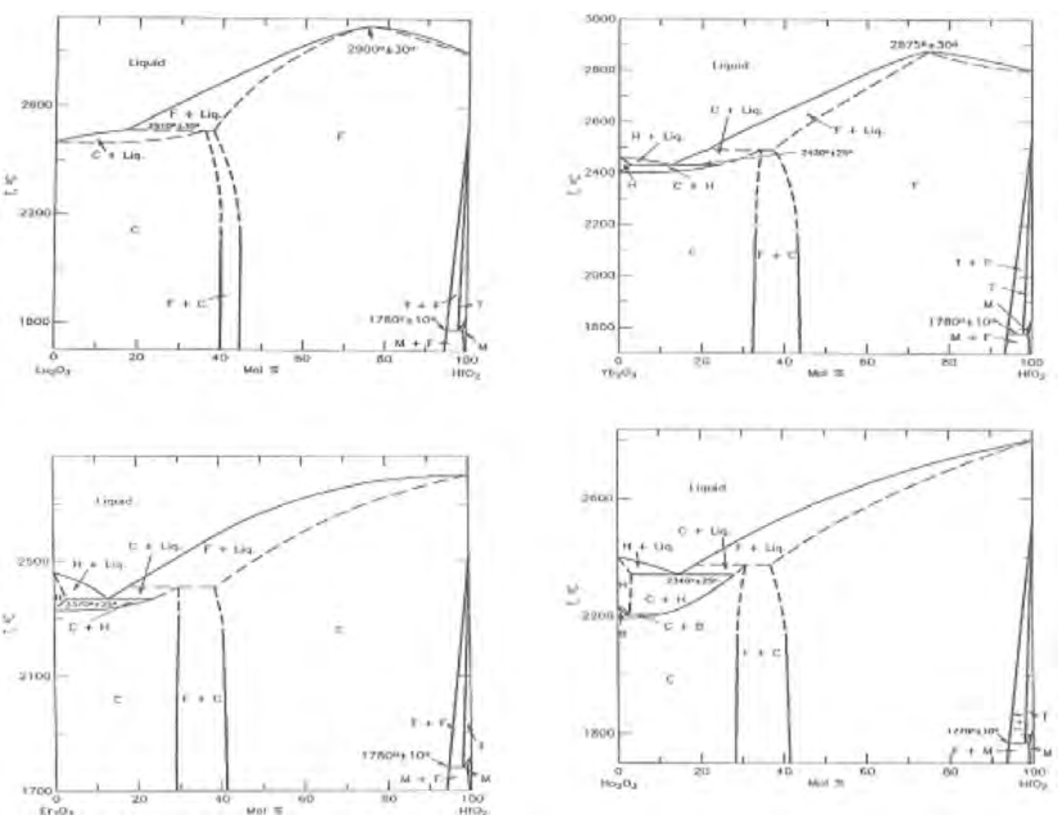

Figure 4.10: Phase diagrams of A_2O_3 - HfO_2 systems with small A^{3+} cations, A = Lu, Yb, Er and Ho. Reproduced from [175]. C = cubic bixbyite, F = fluorite, H = hexagonal, M = monoclinic, T = Tetragonal.

diagrams are all in the very high temperature region and none show any temperatures below 1700 °C. Whilst this should be low enough to show the formation of a pyrochlore phase (should one exist for these compositions), it is not enough to allow the formation of the δ-phase which tends to form between 1100 and 1600 °C [160, 167].

More recently Duran and Pascual [167] have revisited the Yb_2O_3 - HfO_2 system, taking measurements at significantly lower temperatures. By doing this they managed to identify both the δ-phase $Yb_4Hf_3O_{12}$ and another compound with hexagonal symmetry, Yb_6HfO_{11}. Duran and Pascual [167] also progressively heated the δ-phase to 1600 ± 25 °C whereupon it underwent an order-disorder transformation to the disordered fluorite structure.

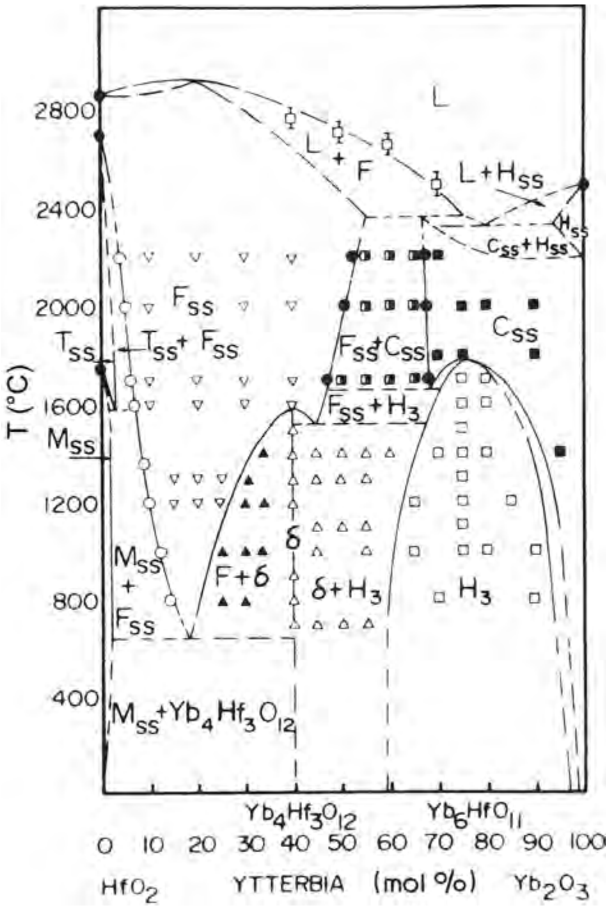

Figure 4.11: Phase diagram of the Yb_2O_3 - HfO_2 system. Reproduced from [167].

Lopato *et al.* [160] have performed a more detailed study considering just the δ-phase compounds and they found that, in the hafnate system, the δ-phase forms for A cations ranging from Sc to Er but specifically not for Ho and Dy. It would therefore be prudent to expect that, if low temperature phase diagrams were plotted for the other systems in figure 4.10, except perhaps the Ho_2O_3 - HfO_2 system, that they would contain features similar to figure 4.11.

Figure 4.12 shows the hafnate systems for A cations with intermediate radii; Dy, Tb, Gd and Eu. In this figure the transition between pyrochlore-forming and non-pyrochlore forming compositions can be seen. All of these phase diagrams predict an order-disorder transition between the fluorite phase and the pyrochlore phase (where it exists) and that as the A cation become larger, the transition temperature moves higher.

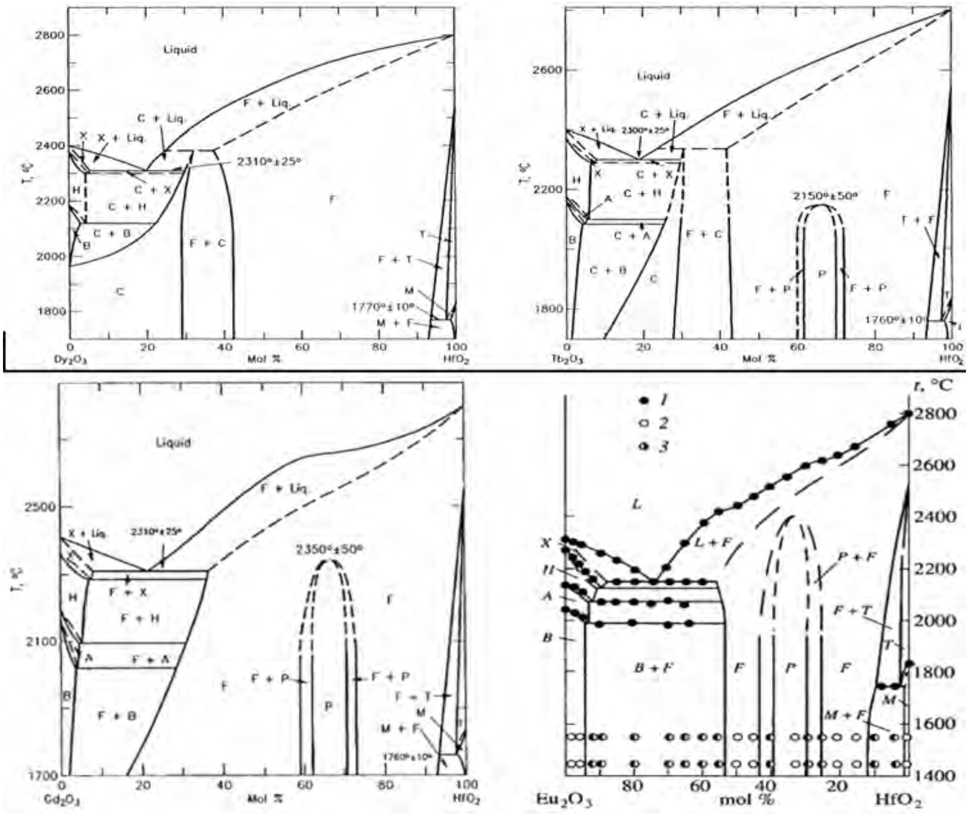

Figure 4.12: Phase diagrams of A_2O_3 - HfO_2 systems with intermediate A^{3+} cations, A = Dy, Tb, Gd and Eu. Reproduced from [176, 177]. C = cubic bixbyite, B = B-rare earth, H = hexagonal, F = fluorite, M = monoclinic, T = tetragonal, P = pyrochlore.

Figure 4.13 is the final figure based on the hafnate system and looks at the larger A cations including, Sm, Nd Pr and La. In this series, the pyrochlore phase becomes stable all the way up to the liquidus temperature and thus no longer exhibits a solid state order-disorder transition. The extent of solid solutions is also quite pronounced unlike in the titanate phases.

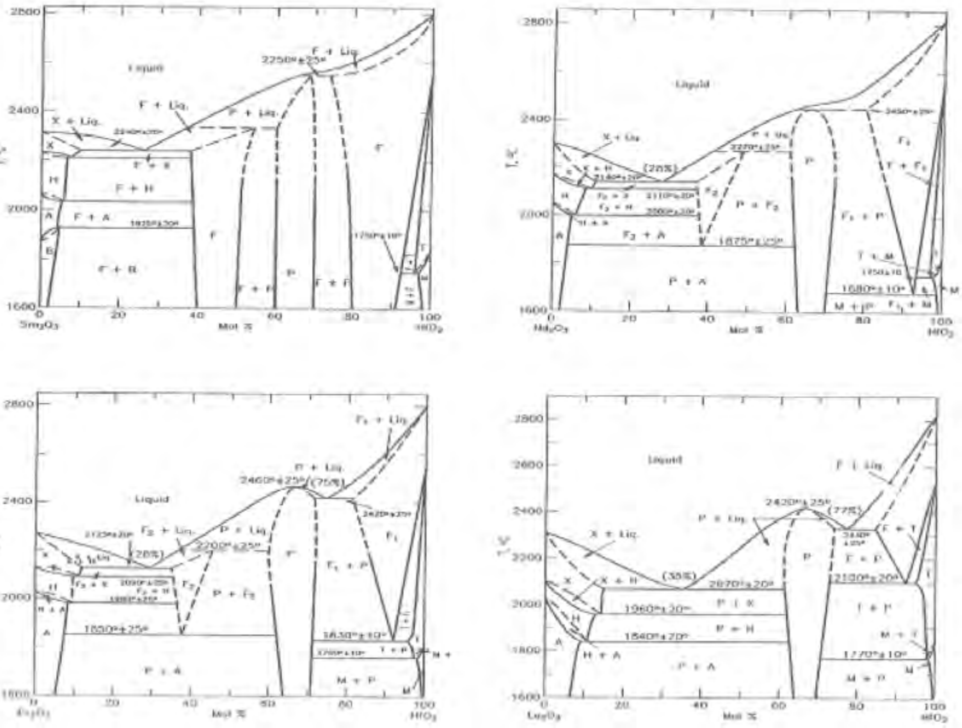

Figure 4.13: Phase diagrams of A_2O_3 - HfO_2 systems with large A^{3+} cations, A = Sm, Nd, Pr and La. Reproduced from [178]. A = A-rare earth, B = B-rare earth, P = pyrochlore, H = hexagonal, F_1 and F_2 = fluorite, M = monoclinic, T = tetragonal.

All of the phase diagrams in the A_2O_3 - HfO_2 system except for the second Yb_2O_3 - HfO_2 were generated by the same research group. This has the advantage that it is likely that the same methods and equipment was used for all the studies, making them self consistent and less prone to the inconsistencies shown in the titanate system.

Finally the zirconate system will be considered. In many of these phase diagrams the pyrochlore phase regions are extrapolated but for the purposes of this study which is focused on predicting the phase boundaries this is not an issue. Figure 4.14 shows three different systems in all of which the pyrochlore phase is stable. There are 2 versions of the Sm_2O_3 - ZrO_2, both of which imply the pyrochlore forms by an order- disorder transformation but they disagree as to the temperature at which the transformation occurs.

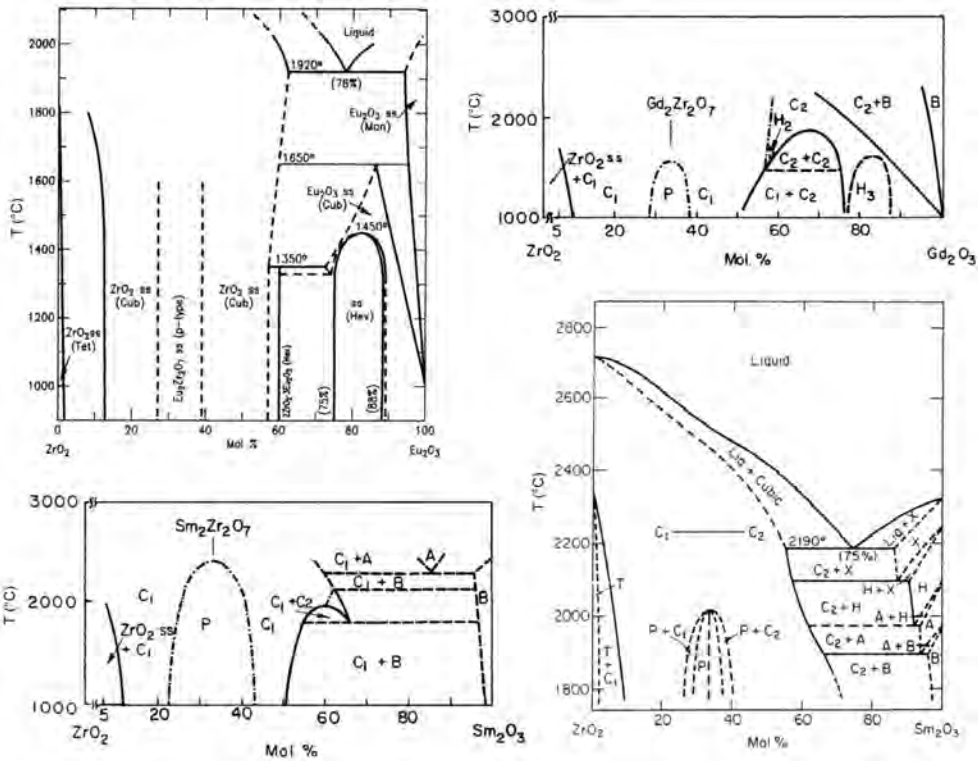

Figure 4.14: Phase diagrams of A_2O_3 - ZrO_2 systems with large A^{3+} cations, A = Eu, Gd, and Sm. Reproduced from [179–181]. T = tetragonal, C_1 = cubic ZrO_2, P = Pyrochlore, C_2 = cubic Sm_2O_3, A = A-rare earth, B = B-rare earth, H = hexagonal.

One of the more studied zirconate systems is that for the La_2O_3 - ZrO_2 system and several examples are shown in figure 4.15. In contrast to the zirconate pyrochlores with small A cations (and similarly the hafnate pyrochlores) the pyrochlore phase forms directly from the liquid although the various authors disagree at what temperature this occurs.

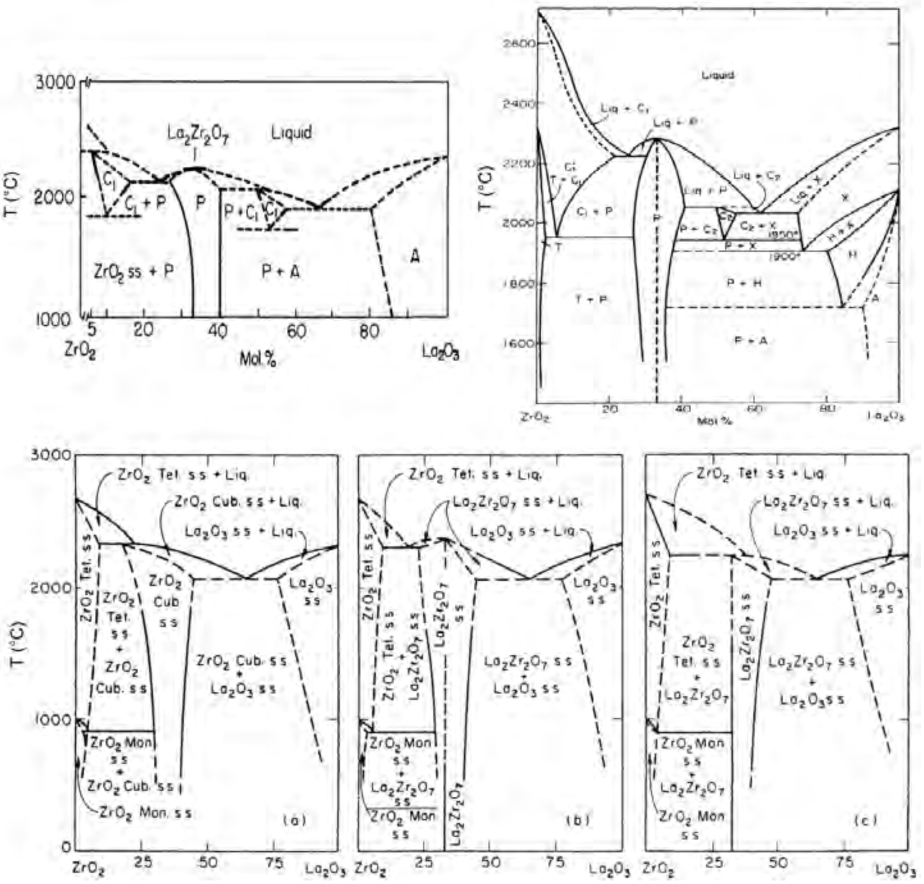

Figure 4.15: Several versions of the La_2O_3 - ZrO_2 phase diagram. Reproduced from [180–183].

Figure 4.16 shows 2 strikingly different phase diagrams for the Nd_2O_3 - ZrO_2 system. One of these predicts the pyrochlore as a line compound forming from the melt and the other predicts from an order-disorder transformation.

However, they both agree that the pyrochlore phase should exist for this combination of elements.

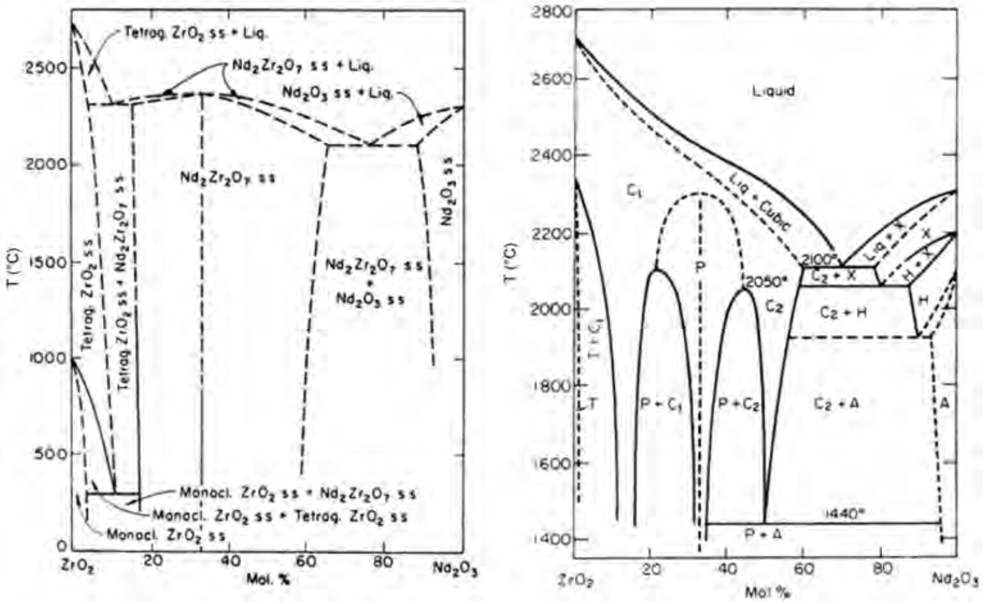

Figure 4.16: Two versions of the Nd_2O_3 - ZrO_2 phase diagram. Reproduced from [180, 182, 183]. T = tetragonal, C_1 = cubic ZrO_2, c_2 = cubic Nd_2O_3, P = pyrochlore, A = A-rare earth, H = hexagonal.

More recently there has been work to calculate phase diagrams using thermodynamic modelling. Results from 2 groups are shown in figure 4.17. Yokokawa *et al.* produced phase diagrams for both the La_2O_3 - ZrO_2 and Y_2O_3 - ZrO_2 systems whereas Chen *et al.* (lower figure) concentrated on just the Y_2O_3 - ZrO_2 system. Comparing the 2 theoretical phase diagrams for the yttria system in this figure, a high degree of similarity is apparent. Both predict that no pyrochlore phase forms but that a $Y_4Zr_3O_{12}$ δ-phase forms at about 1600 K. This is in agreement with the work of Lopato *et al.* [160] who produced δ-phase zirconates for A cations ranging from Sc to Y but not including Dy. Both phase diagrams concur that this is a solid state order-disorder transformation from the fluorite phase.

Comparing the theoretical La_2O_3 - ZrO_2 results with the experimental diagram shown earlier in figure 4.15, it can be seen that the pyrochlore phase exists and that it forms directly from the melt in both cases but some of the details differ. The theoretical study predicts a line compound and the experimental study shows quite extensive solid solution.

The Y_2O_3 - ZrO_2 system has received enormous attention due to the use of Yttria-Stabilised-Zirconia (YSZ) as an oxygen ion conducting electrolyte for solid oxide fuel cells and oxygen sensors [159]. Figure 4.18 shows several experimental phase diagrams of this system which can also be compared with the theoretical systems in figure 4.17. By comparing all of these phase diagrams it is most probable that the phase diagrams produced by Stubican *et al.* [185,185] are the most reliable as the others miss formation concerning the δ-phase compound $Y_4Zr_3O_{12}$ which has been shown to form by several independent groups [158–160]. It is as important to note that while the other phase diagrams do not predict a δ-phase compound, they also do not predict a pyrochlore and instead just have a region of disordered fluorite solid solution. It is likely, therefore, that this is the first stable δ-phase in the series.

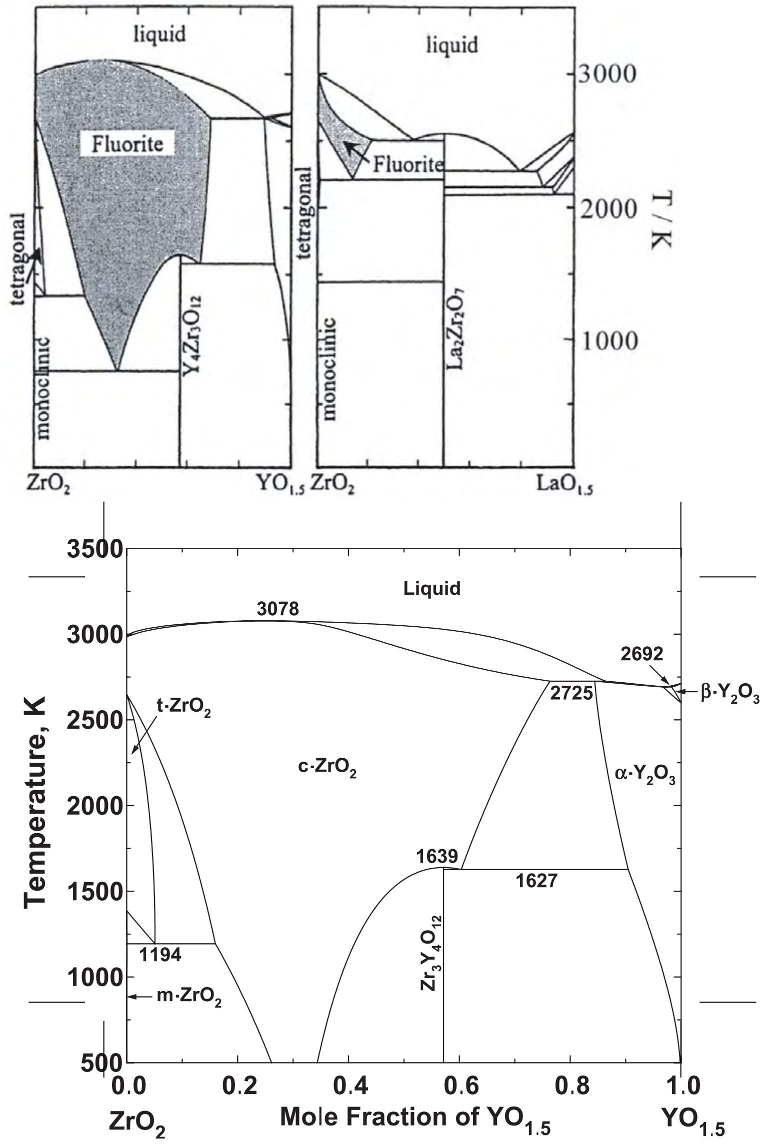

Figure 4.17: Calculated ZrO_2 - A_2O_3 phase diagrams. Reproduced from [159, 184].

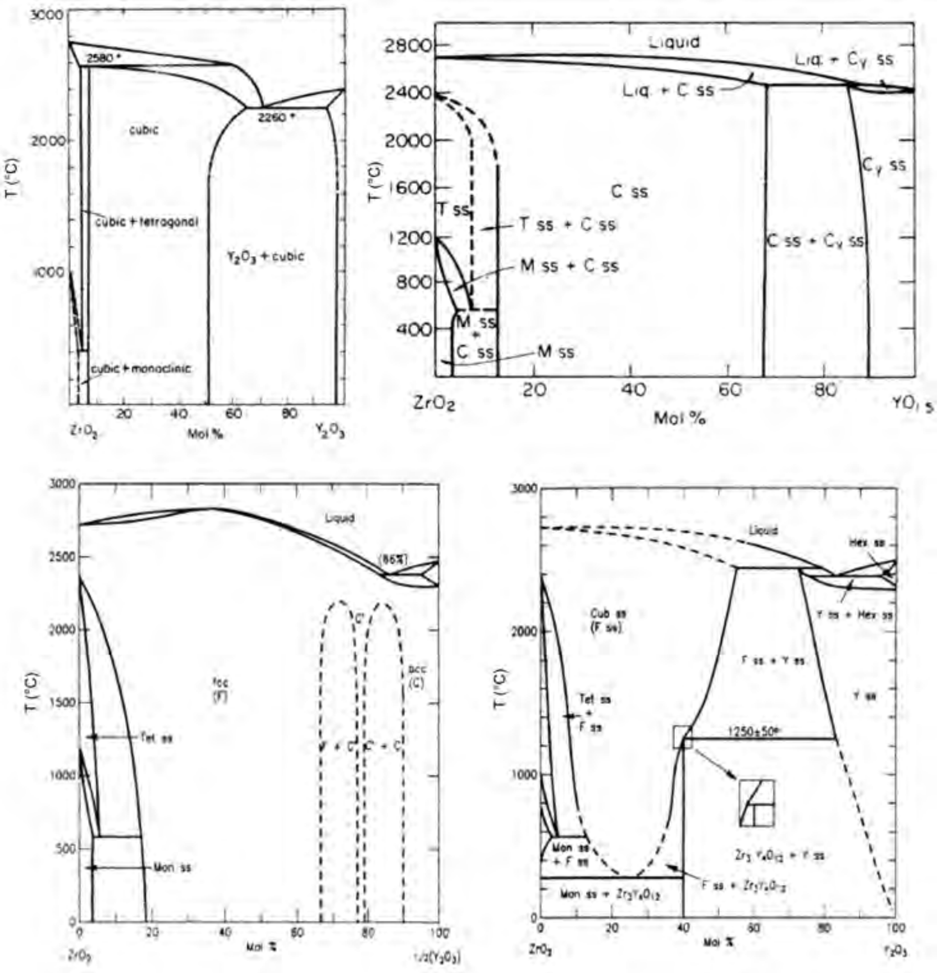

Figure 4.18: Four versions of the ZrO_2 - Y_2O_3 phase diagram. Top two reproduced from [186] and [187] respectively and [188, 189] and [185, 190] for the bottom two.

Structural Studies

While only a limited range of phase diagrams in the A_2O_3 - BO_2 system have been generated, there is a much wider range of structural data based on X-ray and neutron diffraction studies. A summary of compounds that form in each system will be given here along with the references where that data can be found. This will be presented in the form of a composition map. A point indicates that a material has been synthesized with that composition and the colour will show which phase(s) have been observed and the source of the information. Much of the non pyrochlore data was located using the online Inorganic Crystal Structures Database (ICSD) [191].

The structural data extends the information on pyrochlore stability, providing information mainly on the titanate, ruthenate and stannate systems (see figure 4.19, red points). By including data from Subramanian (yellow points in figure 4.19) [135] it is nearly possible to completely define the pyrochlore stability field although gaps and uncertainties still exist. It should be noted that of the plumbate pyrochlores, only $La_2Pb_2O_7$ has been found to form at atmospheric pressure while the others were formed by Sleight [192] at a pressure of 3 kbar at 700 °C. It should also be noted that some of the zirconate pyrochlore and δ-phases have also been formed in a disordered fluorite system. It is the aim of this work to resolve these uncertainties.

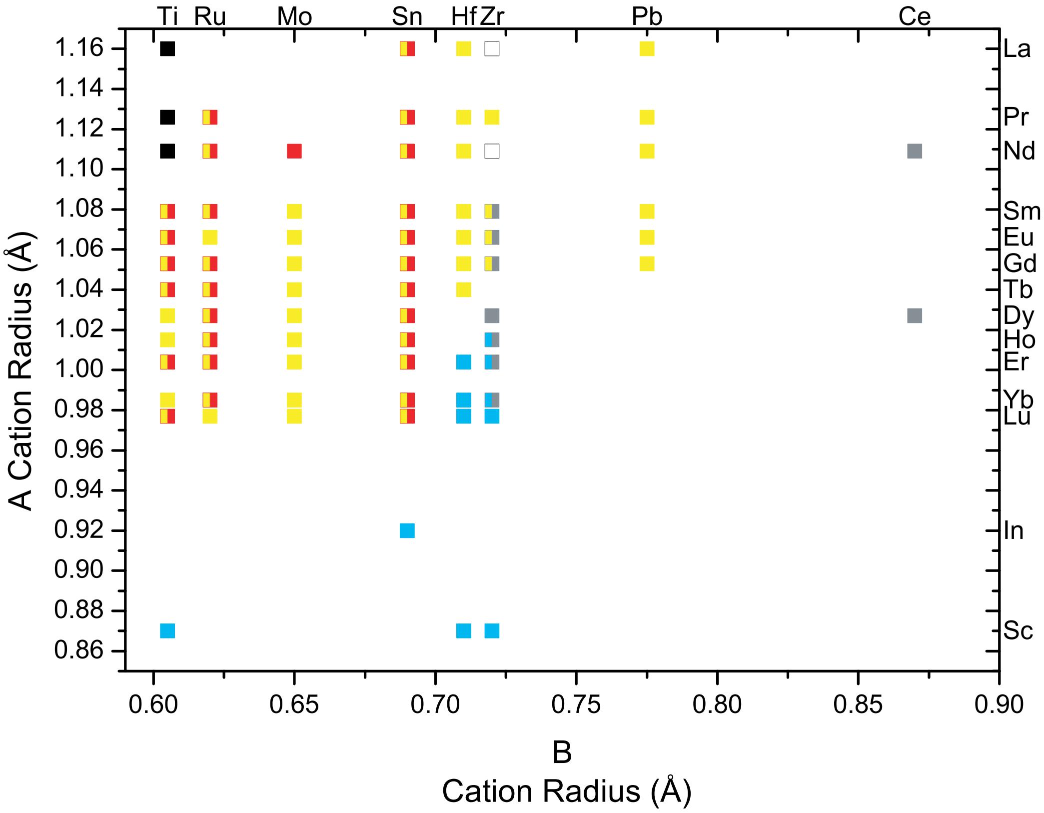

Figure 4.19: A phase map constructed from literature studies. Key: Black: Monoclinic $P2_1$ structure, Red: Cubic $Fd\bar{3}m$ pyrochlore structure from structural studies [193–211], Yellow: Cubic $Fd\bar{3}m$ pyrochlore structure from Subramanian [135] Cyan: Rhombohedral $R\bar{3}$ δ-phase from structural data [1, 156, 160, 212–214], Grey: Disordered fluorite $Fm\bar{3}m$ from structural data [215–218], combinations indicate it has been found in more than one phase or location and an empty box indicates that it has been found as pyrochlore in structural work and the Subramanian review [135] and as a disordered fluorite phase.

4.2.3 Theoretical Studies

There have been several attempts to model pyrochlore compounds on a scale similar to this work. These include work by Minervini *et al.* [112] who examined the relationship between the oxygen positional parameter and disorder. In this work Minervini *et al.* set out to develop a set of interatomic potentials based on a partial charge model to successfully reproduce the experimentally measured x parameter for a wide range of pyrochlore compounds. They were able to reproduce these values with a high degree of success but in order to reproduce experimental values for the x parameter a varying degree of disorder was required. Without this disorder, the x parameters predicted in this study were systematically low and previous work by Wuensch *et al.* [219] had found that while the lattice parameters (to which the potentials in this study were fitted) were not significantly increased by small amounts of disorder, the x parameter was influenced in a much more significant way. A defect cluster containing a cation antisite and an oxygen Frenkel pair was used to simulate disorder and the defect energy of this was used to predict the amount of disorder for each composition. The greatest amount of disorder was found in the pyrochlores with small A cations and large B cations. These potentials were used as a starting point for this study.

Stanek *et al.* [220] attempted to model the extent of non-stoichiometry in the pyrochlore systems and how it varies over the wide compositional range. They achieved this by modelling different solution mechanisms that simulated the various ways that the structure can accept excess A_2O_3 or BO_2 and calculating the solution energies of the process. The mechanisms for BO_2 excess considered B cation substitution on to the A cation lattice with charge compensation via A cation vacancies, B cation vacancies and compensation via oxygen interstitials. The mechanisms for A_2O_3 excess considered A cation substitution onto B sites with charge compensation via oxygen vacancies, A interstitials and B interstitials. They found that the most favourable mechanisms for BO_2 excess (for regions where the pyrochlore is stable) involved compensation via A cation vacancies and that for excess A_2O_3 involved compensation via oxygen vacancies. The Kroger-Vink notation [5] for these two mechanisms is given in equations 4.1 and 4.2.

$$7BO_2 + 4A_A^{\times} \rightarrow 3B_A^{\bullet} + V_A^{'''} + 2A_2B_2O_7 \tag{4.1}$$

$$2A_2O_3 + 2B_B^{\times} + O_O^{\times} \rightarrow 2A_B^{'} + V_O^{\bullet\bullet} + A_2B_2O_7 \tag{4.2}$$

This was an unexpected result as it was generally assumed that pyrochlore would behave like a fluorite (in which BO_2 excess is compensated for by oxygen interstitials) as it had been considered to be simply an oxygen deficient ordered fluorite. In the region very close to the pyrochlore to fluorite transition, Stanek *et al.* [220] found that the preference indeed changes to oxygen interstitial compensation. They went on to postulate that there should be some non-stoichiometry in the titanate system although it may take some time for equilibrium to be reached as cation migration is required for this to occur (cation migration is much slower than anion migration in fluorite related systems).

The variation in activation energies for oxygen migration in the pyrochlore system was modelled by Pirzada *et al.* [221]. In this work they found that the lowest energy migration path for oxygen ions was via an oxygen vacancy (48f) mechanism. In the pyrochlore system this vacancy can "split" [222] for certain compositions. This involves another 48f oxygen adjacent to the vacancy relaxing towards the 8a site forming a cluster of two oxygen vacancies with an oxygen interstitial in between them. This is oriented along a <110> direction (the oxygen interstitial does not occupy the 8a site) and tends to occur for a small number of stable pyrochlores near the pyrochlore - fluorite transition. Migration calculations were performed for both these situations (split vacancies and normal vacancies). For the majority of pyrochlores where the oxygen vacancy it not split, the migration path is a simple <100> type hopping process. For the compositions where the oxygen vacancy does split, the situation is more complicated and details can be found in [221]. The energies were found to agree with the limited experimental data available and the trends show that, in general, the activation energy for oxygen migration decreases rapidly with increasing B cation radius showing little A site dependence until the zirconate pyrochlores are reached. At this point, decreasing A cation radius has a significant reducing effect on the activation energy, although, this may have something to do with the changeover from a symmetrical to a split vacancy starting with $Pr_2Zr_2O_7$.

Minervini *et al.* looked in detail at the disorder processes that occur in pyrochlores [223]. They found that by plotting the formation energy of a clustered cation antisite pair and an oxygen Frenkel pair (a 48f oxygen vacancy and an oxygen interstitial on the 8a site) as a contour map that the 2.8eV contour accurately reproduced the boundary of the pyrochlore phase stability region (see figure 4.20). The authors stated that while this value may seem to be large at first, they used a full ionic model which tends to overestimate

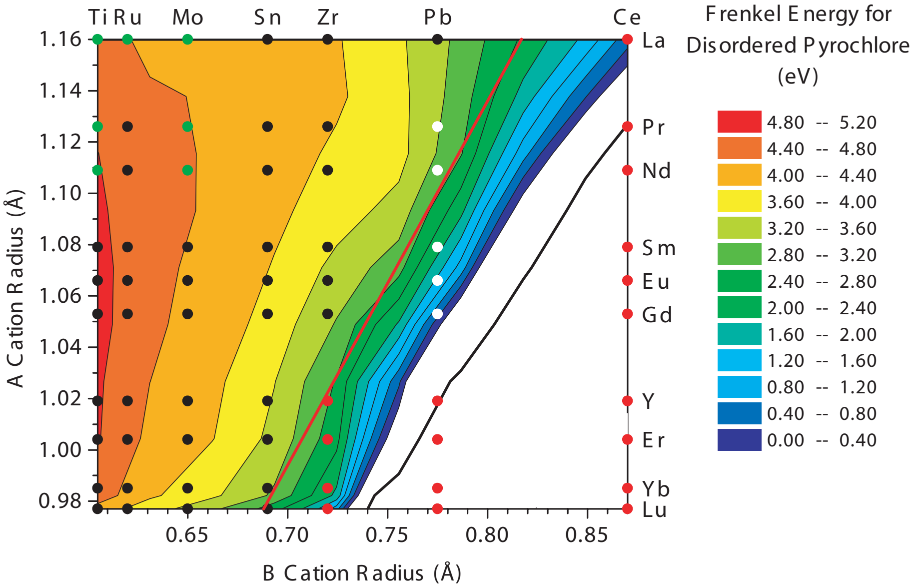

Figure 4.20: Contour Map of the defect formation energy for an anion Frenkel adjacent to a cation antisite pair. Reproduced from Minervini *et al.* [223].

the disorder enthalpy. It should be noted that the δ-phase was not considered in this study. Panero *et al.* [224] have also looked at intrinsic defects in pyrochlores from a first principals approach. They showed that cation antisite defects reduce the energy for the formation of an oxygen Frenkel pair and went on to suggest that the disordering process was driven by the presence of cation disorder since the formation of an oxygen Frenkel pair in a fully ordered system has a much greater energy. They also found that the zirconate pyrochlores show a much greater degree of disorder but they predict that defect formation in the stannate pyrochlores is more like the titanates than other theoretical studies have predicted. They explain this by pointing out that Sn - O bonding is more covalent than that for Ti or Zr and that bonding type as well as ionic radii is also a factor.

Stanek and Grimes [225] used the cation antisite and oxygen Frenkel pair cluster used by Minervini [223] to simulate the disordering process in pyrochlore and hence calculate the order - disorder temperatures for the Hafnate pyrochlores. This was achieved by plotting the logarithm of the defect energy against 1/T where T is the transition temperature for experimentally determined compounds. A linear fit was calculated and then predicted temperatures were obtained. Rushton *et al.* [226] recently extended this work to include the zirconate pyrochlores and a graph from this work, showing the transition temperatures for the hafnates and the zirconates is reproduced in figure 4.21.

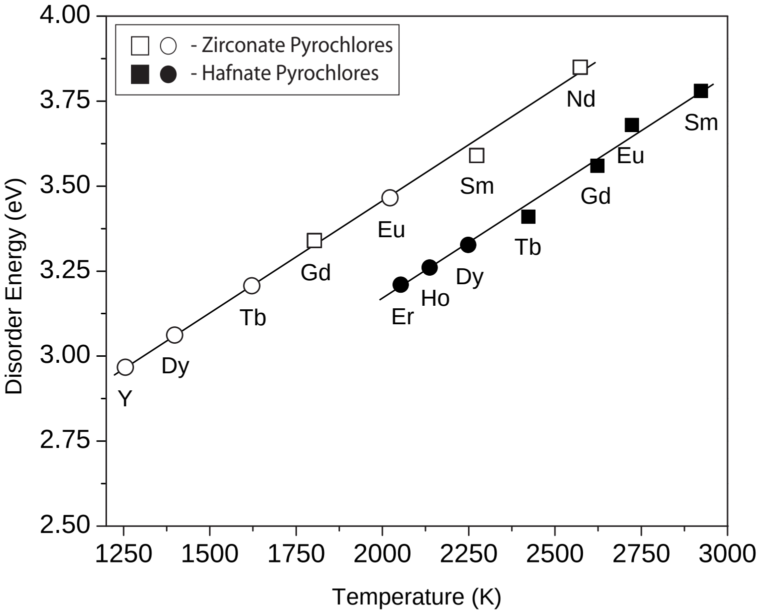

Figure 4.21: Pyrochlore to defect fluorite transition temperatures for zirconate and hafnate pyrochlores squares indicate experimental disorder temperatures and circles indicate predicted values. Reproduced from [226].

There have been several other studies to examine specific pyrochlore compositions rather then predicting trends across the entire range. Wilde and Catlow [227] looked at diffusion and defects in $A_2B_2O_7$ with A and B consisting of Gd, Y and Zr, Ti respectively. Their results indicate that diffusion is effected by hopping between 48f sites and that these compounds exhibit high solubility for divalent cations such as Ca and Sr. The same authors also performed a molecular dynamics study on $Gd_2Zr_2O_7$ to look into the oxygen ion mobility [228]. They found that once again disorder is very important in this system, in the perfectly ordered system there was very little migration but by introducing some disorder to the system oxygen could be induced to diffuse through the system.

As mentioned earlier there have been very few theoretical studies on the δ-phase. Of note, however, is the work by Bogicevic *et al.* [157, 158] on the ordering of the ions in this structure. These authors considered yttria [158] and scandia [157] stabilised zirconia. They identified 104 possible configurations for ordering 7 cations in an fcc cell (as per the fluorite structure). Only two of these were determined to have rhombohedral cell vectors. For these two systems the oxygen ions were then added as they would be in the fluorite system and all the symmetrically distinct ways of removing two oxygen ions were considered in order to yield the $Y_4Zr_3O_{12}$ stoichiometry. This yielded 45 possible systems which were then subject to energy minimisation to find the lowest energy configuration. This study was based on the first principals using the VASP code. VASP (Vienna Ab-initio Simulation Package) is a package for performing ab-initio quantum-mechanical molecular dynamics (MD) using pseudopotentials and a plane wave basis set [229].

4.3 Methodology

In order to determine the phase composition regions and their limits it was decided to use the data from Minervini *et al.* [223] to model the pyrochlore to disordered fluorite transition. This was chose because, as mentioned in section 4.2.3, this agreed with the available experimental data. This leaves 2 transitions to consider, as show in mechanisms 4.3 and 4.4. In these mechanisms the compound (e.g. $A_2B_2O_7$) represents the lattice energy of the indicated system. If the reaction energy is negative it means that the transition is energetically favourable. Clearly this is a very simple approach which assumes that the internal energy change (given by the energy minimisation approach) is completely dominant over, for example, vibrational energy terms. Although it is desirable to employ a free energy minimisation approach, a code capable of performing this type of calculation was not obtainable at the time (see further work section for more discussion and later in this chapter). Also, the aim here is to provide an approximate map or guide to the overall phase composition relationships which rely on trends rather than absolute energy values.

$$\mathrm{A_2B_2O_7} \rightarrow \mathrm{A_4B_3O_{12}} + \mathrm{BO_2} \tag{4.3}$$

$$\mathrm{A_2B_2O_7(cubic)} \rightarrow \mathrm{A_2B_2O_7(monoclinic)} \tag{4.4}$$

Partial charge potentials were derived as described in chapter 3, using the potentials from Minervini *et al.* [112] as a starting point. These original potentials were adapted in order to reproduce as closely as possible the exper-

Table 4.4: Percentage volume changes with respect to experimental data using the short range interatomic potentials from table 4.5. Volume changes in black were fitted to the pyrochlore structure, those in red were fitted to the delta phase and blue indicates monoclinic. Those which are blank indicate either a disordered fluorite forms experimentally for that composition or there was no experimental data to fit to. Averages do not include monoclinic data.

	Ti	Ru	Mo	Sn	Hf	Zr	Pb	Average
La	4.99			0.20	-0.87	-0.49	-0.35	-0.22
Pr	4.78			0.31	-1.77	-0.60	-0.20	-0.52
Nd	4.31	-0.46		0.15	-0.51	-0.67	-0.44	-0.46
Sm	0.21	-0.40	-0.40	0.55	-0.25	0.35	0.13	0.03
Eu	0.65	-0.31	0.03	0.60	0.18	1.15	0.26	0.37
Gd	0.47	-0.01	0.56	0.78	0.35	1.12	0.50	0.54
Tb	0.25	-0.39	0.66	0.60	0.40			0.28
Dy	0.25	-0.33	0.89	0.53	0.47			0.34
Y	0.42	-0.20	0.94	0.60	0.40	-0.83		0.22
Ho	0.31	-0.45	0.81	0.56	0.71	-0.54		0.23
Er	0.04	-0.10	1.16	0.60	-0.70	-0.13		0.15
Yb	0.56	-0.29	1.35	0.69	-0.83	-0.45		0.17
Lu	0.41	-0.62	1.38	0.68	-0.60	-0.42		0.14
In				-0.32				-0.32
Sc	0.53					0.35		0.44
Average	0.32	-0.24	0.30	0.47	-0.23	-0.10	-0.02	

imental unit cell volume of: the pyrochlore compounds, the δ-phase and the simple A_2O_3 and BO_2 oxides (see table 4.4 for the actual volume changes). A shell model was employed for the oxygen ions. Cation shells particularly for zirconium ions had been used in previous studies but caused problems (core-shell separation) in conjunction with small A cation zirconate pyrochlores (that needed to be calculated in order to ascertain the stability of the δ-phase in this region). Removing them seemed to have very little impact on either the lattice energy or the unit cell volume.

Once the potentials had been derived the perfect lattice calculations were run

Table 4.5: Short range potential parameters used for this study. Harmonic oxygen core-shell parameter $k = 32.0$.

Species	A (eV)	ρ (eV)	C (eV Å^6)
$O^{1.7-} \leftrightarrow O^{1.7-}$	4870.00	0.2670	77.00
$La^{2.55+} \leftrightarrow O^{1.7-}$	2306.26	0.3263	23.25
$Pr^{2.55+} \leftrightarrow O^{1.7-}$	2236.02	0.3225	23.94
$Nd^{2.55+} \leftrightarrow O^{1.7-}$	2205.88	0.3206	22.59
$Sm^{2.55+} \leftrightarrow O^{1.7-}$	2179.20	0.3181	21.49
$Eu^{2.55+} \leftrightarrow O^{1.7-}$	2172.45	0.3168	20.59
$Gd^{2.55+} \leftrightarrow O^{1.7-}$	2165.40	0.3158	19.90
$Tb^{2.55+} \leftrightarrow O^{1.7-}$	2137.47	0.3138	19.25
$Dy^{2.55+} \leftrightarrow O^{1.7-}$	2130.65	0.3121	18.68
$Y^{2.55+} \leftrightarrow O^{1.7-}$	2107.60	0.3109	17.51
$Ho^{2.55+} \leftrightarrow O^{1.7-}$	2113.67	0.3110	18.16
$Er^{2.55+} \leftrightarrow O^{1.7-}$	2103.60	0.3097	17.55
$Yb^{2.55+} \leftrightarrow O^{1.7-}$	2075.26	0.3076	16.57
$Lu^{2.55+} \leftrightarrow O^{1.7-}$	2069.99	0.3067	16.87
$In^{2.55+} \leftrightarrow O^{1.7-}$	2001.65	0.3016	11.85
$Sc^{2.55+} \leftrightarrow O^{1.7-}$	1944.21	0.2960	11.85
$Ti^{3.4+} \leftrightarrow O^{1.7-}$	1865.80	0.2946	0.00
$Ru^{3.4+} \leftrightarrow O^{1.7-}$	1883.39	0.2954	0.00
$Mo^{3.4+} \leftrightarrow O^{1.7-}$	1901.50	0.3011	0.00
$Sn^{3.4+} \leftrightarrow O^{1.7-}$	1945.41	0.3099	13.66
$Zr^{3.4+} \leftrightarrow O^{1.7-}$	1953.80	0.3111	5.10
$Pb^{3.4+} \leftrightarrow O^{1.7-}$	2005.10	0.3203	19.50
$Ce^{3.4+} \leftrightarrow O^{1.7-}$	2058.36	0.3292	22.50

using the CASCADE code [102] as described in chapter 3. The potentials used are presented in table 4.5.

4.4 Results and Discussion

In order to model the hypothetical cubic pyrochlore and δ-phases in the transition regions, the lattice parameters for known systems were extrapolated with respect to A and B cation radii. The systems were then simulated and the resulting lattice energies combined, as per mechanisms 4.3 and 4.4, to calculate the most stable phase.

The initial results were disappointing as it was found that none of the monoclinic phases were stable with respect to the cubic pyrochlore system and only a few of the experimentally confirmed δ-phase compounds were found to be stable (Yb-Sc zirconates and $In_4Sn_3O_{12}$ but not $Sc_4Ti_3O_{12}$).

Considering the cubic pyrochlore to monoclinic transition first, it was found that the reaction energies were 0.81 and 1.29 eV per formula unit in favour of the cubic phase for $La_2Ti_2O_7$ and $Nd_2Ti_2O_7$ respectively (but these are small with respect to the total lattice energies of -270.47 and -273.03 eV). However it should be noted that the hypothetical cubic phases had final cell volumes (after relaxation) much closer to the predicted ones than the monoclinic phases. The hypothetical cubic phases show volume discrepancies of +0.12% and +0.8% (for $Nd_2Ti_2O_7$ and $La_2Ti_2O_7$ respectively) whereas the volume discrepancies after relaxation for the monoclinic phases were +4.31% and +4.99% (for $Nd_2Ti_2O_7$ and $La_2Ti_2O_7$). This suggests that these potentials, while sufficient to model a cubic system lack terms that would aid in representing a monoclinic system. It is, nevertheless, impressive that the monoclinic phases are reproduced so well (see table 4.4) and suggests only modest improvements will be necessary (see further work for more information).

This seemingly excessive preference for cubic systems may be partly due to the use of centro-symmetric potentials as these almost certainly favour a cubic symmetry over the monoclinic system. A way of getting around this problem would be to use an elliptical breathing shell model [116] for the oxygen and re-derive a potential based on that to fit both the monoclinic phase and the cubic phase equally well, without compromising the δ-phase system too much. Unfortunately neither of the two codes available at the time (CASCADE [102] and GULP [103]) implemented an elliptical breathing shell model so this was unable to be tested and this should be investigated in further work when codes implementing this feature are available.

In order to address the problem regarding the delta phase transition point (initially the calculations only predicted that the Yb-Sc zirconates and $In_4Sn_3O_{12}$ were stable with respect to the pyrochlore structure) it was necessary to reconsider whether the ordered δ-phase structure is what is actually forming in reality. In all experimental systems this system is reported to be completely disordered on the cation sublattice as opposed to what is being simulated here. Modelling the disordered system would require large supercells and a Monte-Carlo type approach. This would have been much more computationally challenging. As a compromise, an approximate configurational entropy contribution (see appendix A for details) to the lattice energy was computed for the cation disorder at order-disorder transition temperature given by Duran and Pascual [167] (i.e. 1600 °C). By including this it was possible to predict much more closely the cubic pyrochlore to δ-phase transition point for the zirconates. Nevertheless, it was found that $Y_4Zr_3O_{12}$ and $Ho_4Zr_3O_{12}$ were still slightly more stable as pyrochlores but that this preference was less than 0.09 eV so these have been included in figure 4.22 as points that have been confirmed as delta phase compounds. The final phase map is shown in figure 4.22.

The potential model does not yet reproduce the monoclinic phases sufficiently accurately according the criteria used to derive the potentials (deviations in the unit cell volume of $> 1.5\%$ were deemed unrepresentative of the real material). Even if they were included, the results predict a result known to be untrue. Due to this, the experimentally determined points have been used to define the phase stability of the diagram. Without further work it is difficult to say for certain what happens in this region and therefore it is suggested that all of the the compounds inside the line in the upper left form non-cubic materials with the $A_2B_2O_7$ stoichiometry. These materials may be monoclinic as per the titanate compounds or something else.

On the other side of the map the boundary between the disordered fluorite and the pyrochlore phase was not explicitly calculated in this study but as mentioned earlier the 2.8 eV contour, taken from Minerlvini *et al.* [223] (see figure 4.20) was used. This predicts that two of the rare earth plumbates previously only observed at high pressure by Sleight [192] may be stable under normal conditions and as such these have been included on the pyrochlore side of the line.

Considering next the δ-phase region, this study predicts 5 new compounds with this structure: $Sc_4Ru_3O_{12}$, $Sc_4Mo_3O_{12}$, $Sc_4Sn_3O_{12}$, $Lu_4Sn_3O_{12}$, $Yb_4Sn_3O_{12}$. It also predicts the stability of 3 previously unknown pyrochlore compositions ($In_2Ti_2O_7$, $In_2Ru_2O_7$ and $In_2Mo_2O_7$). Due to the inability to probe the δ-phase fluorite transition it is assumed that while the δ-phase is stable with

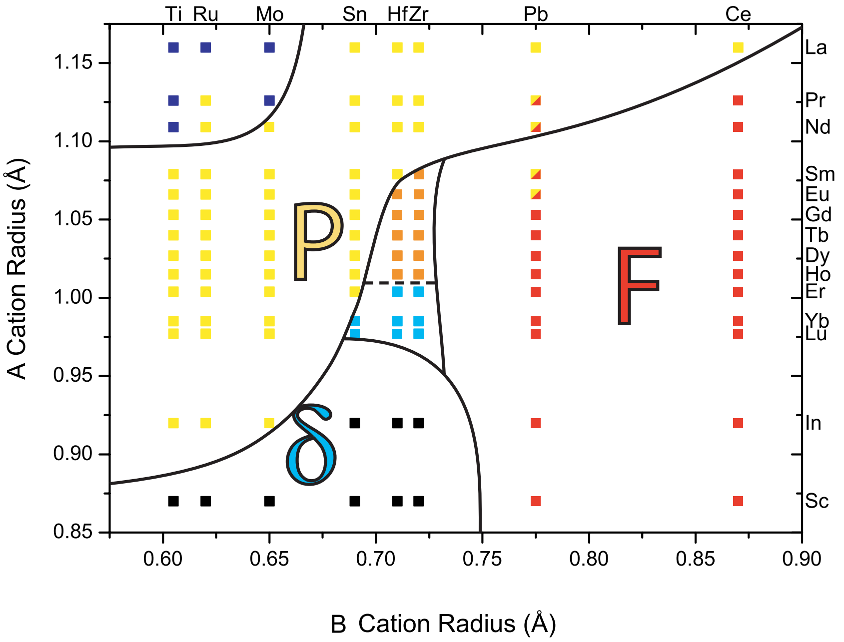

Figure 4.22: Phase map showing the stability of cubic $A_2B_2O_7$, non cubic $A_2B_2O_7$, disordered fluorite and $A_4B_3O_{12}$ phases at low temperatures. Key: Blue = Non cubic (possibly monoclinic pyrochlore), Yellow = Cubic Pyrochlore forming from the melt, Orange cubic pyrochlore formed by order-disorder transformation, Black = δ-phase postulated to form from the melt, Light Blue = δ-phase formed by and order-disorder transformation, Red = disordered fluorite, Yellow/Red cubic pyrochlores formed by Sleight under high pressure [192].

respect to the pyrochlore phase for some of the plumbates, since none have been formed experimentally it is prudent to assume that these phases remain as fluorite. Further work is clearly necessary to bring greater understanding and certainty to this region of the phase map.

The central region of figure 4.22 is the most complex area and technically interesting region. In this region the pyrochlore and δ-phases have been given 2 colours depending on how they are predicted to form. Pyrochlores in orange were previously identified by Stanek *et al.* [230] and Rushton *et al.* [226] to undergo a solid state pyrochlore to fluorite order-disorder transformation and in agreement with the phase diagrams the temperature at which this occurs increases with A cation radius. By carefully examining the phase diagrams dealing with the larger A cation hafnate pyrochlores it was decided to draw the line for this upper boundary between $Eu_2Hf_2O_7$ and $Sm_2Hf_2O_7$. This was then extended to ensure the pyrochlore phase region included the two plumbate pyrochlores and this extension also included $La_2Ce_2O_7$. In their phase diagram of the Yb_2O_3 - HfO_2 system, Duran and Pascual [167] show $Yb_4Hf_3O_{12}$ forms via an ordering process from the fluorite phase, analogous to that observed with the pyrochlores. It is therefore suggested that like the pyrochlore system, this transition temperature will rise the further away from the pyrochlore to δ-phase boundary (i.e. decreasing A cation radius) until the phase is stable up to the melting point. A tentatively boundary has been marked for this transition but there is no way of determining this from the results presented here.

Many of the materials that have been found to show high resistance to radiation damage tend to appear in the centre of this diagram, close to the pyrochlore to fluorite or pyrochlore to δ-phase boundary. All of the systems in this region demonstrate a large degree of intrinsic disorder and as such the disordering processes caused by atomic displacements have little overall effect. The material examined by Sickafus *et al.* [131, 132] ($Er_2Zr_2O_7$) is actually on the border of all three phases and this suggests that the δ-phase compound with the same cations (if processing conditions allow it to form from the fluorite) may also be worth studying as would other materials in this region such as $Er_4Hf_3O_{12}$ and $Lu_4Zr_3O_{12}$. Compositions in this region are also the ones that exhibit the greatest degree of non-stoichiometry.

Figure 4.23 shows the expected stability for these compounds at high temperatures (e.g. 2000 K). At such temperatures the pyrochlore and δ-phases that undergo an order-disorder transition have become fluorite. This is also the expected phase after extensive radiation damage as preliminary work on $Yb_4Zr_3O_{12}$ by Sickafus and Valdez [231] has shown. In this most recent work, Sickafus and Valdez carried out "ion beam" irradiation studies and found that under "high doses", this material is transformed back to the fluorite phase.

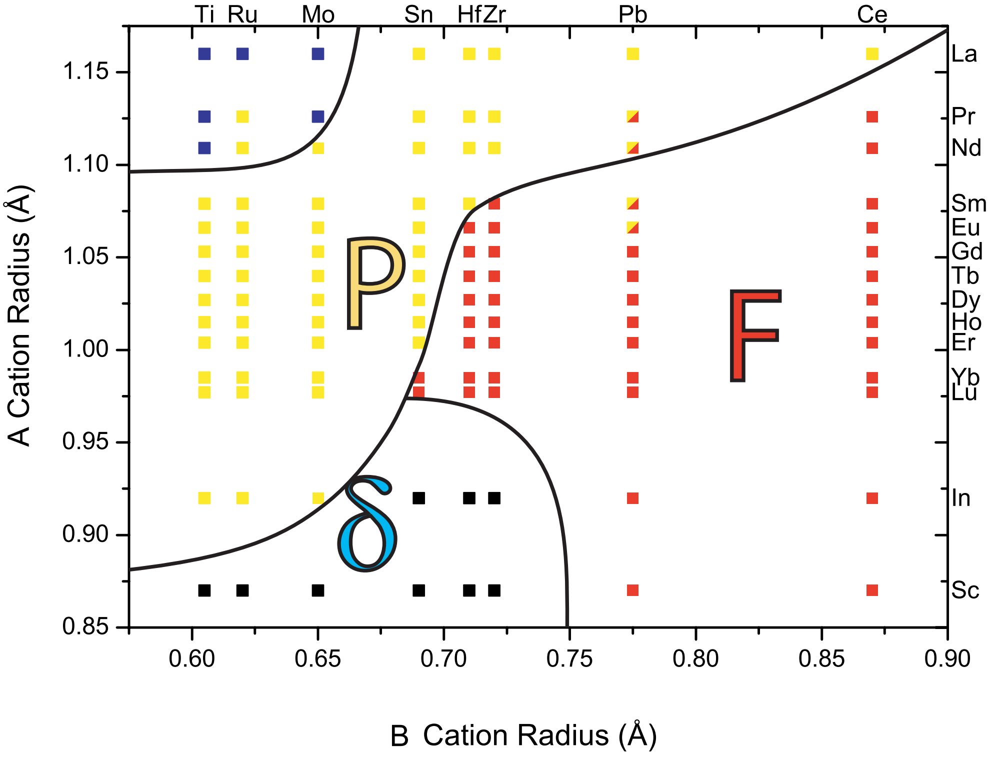

Figure 4.23: Phase map showing the stability of cubic $A_2B_2O_7$, non cubic $A_2B_2O_7$, disordered fluorite and $A_4B_3O_{12}$ phases at high temperatures. Key: Blue = Non cubic (possibly monoclinic pyrochlore), Yellow = Cubic Pyrochlore, Black = δ-phase, Red = disordered fluorite, Yellow/Red cubic pyrochlores formed by Sleight at 300 Kbar [192].

4.5 Conclusions

Phase maps have been produced to provide a general understanding of the relative stability of the pyrochlore, δ-phase and disordered fluorite systems as a function of composition using a combination of atomistic simulation and experimental data. A set of potentials has been derived that almost perfectly reproduce both the cubic pyrochlore to δ-phase transition and the structures of both compounds. Further work needs to be performed to develop a potential set to model correctly the cubic pyrochlore to monoclinic transition.

Further work, including both simulation and experimental work needs to be done with the plumbates and the cerates to identify which phases form with these combinations of cations as the projected fluorite field here is essentially an assumption based on limited experimental data.

Chapter 5

Actinide Accommodation in Pyrochlores

Some of this work has previously been published in Philosophical Magazine [3]

5.1 Introduction

As mentioned in the general literature review (section 2.3.5), there has been significant interest in the use of ceramics for the immobilisation of nuclear waste and actinides in particular. Of these it was also mentioned in chapter 4 that fluorite related materials including fluorite solid solutions $Er_2Zr_2O_7$ (i.e. Er_2O_3 - ZrO_2) and $Er_2Ce_2O_7$ [132, 232] have been shown to have remarkable resistance to amorphisation under "heavy ion" irradiation. Similar results were found for the pyrochlore $Gd_2Zr_2O_7$ [35]. On the other hand, Lian *et al.* showed that $La_2Zr_2O_7$ pyrochlore "will undergo" amorphisation [233], however it is still a radiation tolerant material when compared with most ceramics.

If these oxide materials are to be used as host phases for actinides it is important to understand how the $A_2B_2O_7$ compounds might incorporate large actinide ions in their structure. It would also be interesting to know how this varies as a function of composition. Thus, using atomic scale computer simulation, the solution energies of uranium and plutonium in both trivalent and tetravalent states have been predicted within pyrochlore oxides. Results will be reported in the form of contour maps that present solution energy as a function of composition (contour maps will be explained in section 5.3).

5.2 Literature Review

5.2.1 Background and History

Pyrochlore materials and other fluorite related ceramics have generated significant interest for the purpose of immobilising actinides and other nuclear wastes [30–37, 61, 77, 232–247]. The crystallography and phase stability of pyrochlore compounds were discussed in chapter 4 and it was also mentioned that there is a huge range of possible pyrochlore compositions. Chakoumakos [248] reports that there have been at least 440 synthetic compounds with the pyrochlore structure alone and pyrochlore minerals have been found in rock formations in locations around the world [31]. Naturally-occurring pyrochlores have been found containing both uranium and thorium [31,78,249] and Lumpkin [78] reports that natural pyrochlores have been found containing up to 30 wt% UO_2 and 9 wt% ThO_2. It is therefore unsurprising that pyrochlore and related structures have been present in the earliest nuclear waste forms [31].

During the 1980's, much of the research into the SYNROC wasteform was performed [78] and this research gained more importance in the 1990's when options to immobilise the plutonium from dismantled nuclear weapons were required [31]. With the immobilisation of weapons Pu in mind, the U.S.A. settled on a collection of titanate phases very similar to the original SYNROC composition mainly due to its proven chemical durability [31]. As mentioned in section 2.3.5 the SYNROC phase designed to accommodate most of the actinides (and Pu in particular) was zirconolite ($CaZrTi_2O_7$). In their study into Np and Pu doping of zirconolite, Begg *et al.* [45] found when the zirconolite phase is doped with approximately 20 mole% PuO_2 a mixture of $Ca_{0.95}Pu_{0.23}Zr_{0.87}Ti_{1.93}O_7$ zirconolite and $Ca_{0.95}Pu_{0.90}Zr_{0.28}Ti_{1.84}O_7$ pyrochlore was formed. It is clear that this pyrochlore can accept much higher loadings of Pu than the zirconolite (this case shows nearly a four fold increase). A similar result was found in earlier work when a number of studies where performed doping zirconolite with ^{238}Pu (half life 87.7 years) in order to assess it's stability under α-decay (see references 42-46 in [31]). The samples doped with 4 mole% $^{238}PuO_2$ stayed monoclinic but samples doped with more than 8 mole% $^{238}PuO_2$ were reported to form a "cubic zirconolite" phase. This was subsequently shown to be a defective pyrochlore structure (reference 47 in [31]).

5.2.2 Previous Work on the Solubility of Actinides in Pyrochlore

5.2.3 Solution Studies

The issue of actinide accommodation has already been tested experimentally in lanthanum zirconate by [240, 242] through the preparation of compositions $[La_{1-x}Pu_x]_2\,Zr_2O_{7+y}$ compositions with x ranging from 0 ($La_2Zr_2O_7$) to 1 ($Pu_2Zr_2O_7$). Kulkarni *et al.* [242] produced samples with intermediate values of x at 0.25 and 0.5. This was achieved by mixing oxide powders and graphite (to reduce the Pu^{4+} to Pu^{3+}) and heating to 1400 °C in a helium atmosphere. They found that all of the compounds formed cubic pyrochlore with the lattice parameter decreasing linearly with increasing Pu content. This shows complete solid solubility of Pu in $La_2Zr_2O_7$ [242]. These authors also described $Pu_2Zr_2O_7$ [242] but this will be discussed in the next section.

Yamazaki *et al.* [240] examined the same system in greater depth. They sampled x from 0 to 0.3 in steps of 0.05 and 0.3 to 1.0 in steps of 0.1 making it possible to be more certain as to the extent of solubility. They too opted for the powder processing route but heated the mixtures in 3 different atmospheres, a vacuum, an 8% hydrogen-helium atmosphere and air, all at 1500 °C. The samples formed in the hydrogen-helium atmosphere were further treated at 1700 °C for 5 hours in order to reduce the plutonium valence.

Looking at the air sintered samples first, Yamazaki *et al.* [240] found that the lattice parameter only increases linearly with increasing Pu content until x=0.1. Beyond this point further increasing the Pu content has no effect on the lattice parameter so they determine the solubility limit for air sintered samples to be 10 mole %. From this and the fact that Ce (a close chemical analogue for Pu) is tetravalent when heated in air this low value was used by the authors to justify that the majority of the Pu in the material was tetravalent. They also found that an air heated solution consisting of 80 mole % Pu formed a single fluorite phase and the 100% Pu sample showed a mixture of a fluorite phase and tetragonal zirconia. The vacuum heated samples showed a solution limit at about 35 mole % and further increases in Pu content resulted in the formation of a two phase fluorite - pyrochlore region. This indicates that under vacuum conditions, a significant amount of the Pu^{4+} was reduced to Pu^{3+} but the relative amounts could not be confirmed by the authors. The region from 80 mole to 100 mole % showed only a single fluorite phase. The samples heated under the most reducing conditions agree with the results from Kulkarni *et al.* [242] in that under these conditions, the lattice parameter continues to decrease with increasing Pu content throughout the entire range showing a single pyrochlore type phase throughout. They found that samples between 50 and 80 mole % Pu showed a mixture of pyrochlore and a cubic type phase but they surmised that as both end members were pyrochlore the phases in between were likely to be pyrochlore-like phases, however, the characteristic diffraction peaks were weak so this could not be confirmed [240].

Since both studies established that plutonium could exhibit either trivalent or tetravalent charge states depending on the preparation temperature and pO_2, the solution of both Pu^{3+} and Pu^{4+} will be modelled here. Uranium is considered in both trivalent and tetravalent states as, although U_2O_3 has not been formed experimentally, UO_2 shows considerable hypo-stoichiometry (i.e. UO_{2-x}) and the formation of the sub-stoichiometric oxide could be indicative of the formation of U^{3+}. Details on the derivation of the U^{3+} potential will be discussed in section 5.3.

$[Ln\text{-}Pu]_2Ti_2O_7$ compositions have been fabricated by Shoup *et al.* [36] where Ln = Gd, Er and Lu. Considered as solid solutions of $Pu_2Ti_2O_7$ in $LnTi_2O_7$ the solution limit was considerable in each case with the value for the Lu variant largest at 33 mol% and the value for Gd smallest at 16 mol%.

Previous solution energy simulations have been carried out by Weber *et al.* [234] by substituting Pu^{3+} and Pu^{4+} in the pyrochlore and fluorite forms of $Gd_2Zr_2O_7$. It was found that Pu^{3+} substituted most readily for Gd^{3+} in both structures (-1.00eV/Pu and -1.55eV/Pu respectively). The Pu^{4+} ion was found to be most stable at the Zr^{4+} sites in pyrochlore and fluorite with energies of -0.26eV and -0.45eV.

The accommodation of Pu^{4+} in pyrochlores has also been considered experimentally via a co-doping approach [37]. In this case, the plutonium ions are assumed to occupy A sites with compensation by Ca^{2+} also on A sites. The rationale for this mechanism is provided by the existence of the mineral zirconolite (discussed previously) [41, 78] and the mineral betafite which has the formula $CaUTi_2O_7$ [38]. Natural zirconolites are known to accommodate uranium ions (see section 2.3.5). However, the zirconolite structure is distinguished from pyrochlore by the formation of complex ordered layers which also results in the possibility of polymorphs [41]. Also, recently [30] evidence has been published which suggests that while plutonium resides on the A sites as Pu^{3+}, uranium occupies the B site as a U^{5+} ion. This last case was not considered in this study due to time constraints.

Extreme Doping Studies (Formation of $Ac_2B_2O_7$)

While pyrochlores have been shown to accommodate large quantities of PuO_2 or Pu_2O_3, several groups have managed to form pyrochlores with the formula $Ac_2B_2O_7$ where Ac is either Pu, Cf or Am and B is either Ti or Zr [36, 240, 242, 250]. Both Kulkarni *et al.* [242] and Yamazaki *et al.* [240] managed to form $Pu_2Zr_2O_7$. Shoup *et al.* managed to form a monoclinic $Pu_2Ti_2O_7$ which may or may not be isostructural with the monoclinic $La_2Ti_2O_7$ synthesised by Schmalle *et al.* [166] and very recently Sykora *et al.* [250] synthesised both $Am_2Zr_2O_7$ and $Cf_2Zr_2O_7$ for a self irradiation study that will be discussed in more depth later. In their study, Kulkarni *et al.* [242] found that $Pu_2Zr_2O_7$ oxidised easily in air at temperatures below 600 °C to reform in the disordered fluorite structure ($[Pu_{0.5}Zr_{0.5}]O_2$). Repository conditions are likely to be strongly reducing (except for the Yucca Mountain repository in Nevada which will be oxidising [251]). so this transition is unlikely given proper handling of the material but even if it does occur, the volume change caused by this change is very small. The measured a lattice parameter for the pyrochlore as 10.592 Å and the fluorite structure was 5.273 Å [242]; allowing for the fact that both structures are cubic and that the lattice parameter for pyrochlore is twice the size of the fluorite this corresponds to a volume reduction of 1.3% associated with this transformation. These studies demonstrate an ability for materials with the pyrochlore structure to accommodate high concentrations of actinides.

5.2.4 Irradiation Effects in Pyrochlores

General radiation effects and radiation induced damage in wasteforms were discussed in section 2.3.6. The methods used to study the effects of α-decay in wasteform materials using experimental techniques include doping with short lived actinides such as ^{238}Pu or ^{244}Cm (half-lives 87.7 and 18.1 years respectively), ion-beam irradiation (implantation) studies and studying natural analogues. Computer simulation techniques generally examine the behaviour of a single decay event using molecular dynamics models. A review of irradiation studies on pyrochlore systems including both experimental and theoretical methods will now be presented.

Doping with Short Lived Actinides

By doping with short lived actinide species, it is possible to accelerate the dose rates by several orders of magnitude over that which a real wasteform will experience [31] and it allows simulation of damage to the bulk of the material rather than just the a few tens of microns away from the surface [252] as with ion-beam studies. By accelerating the dose rate in this manner it is possible to simulate the cumulative dose that a wasteform would experience over hundreds or thousands of years in time periods short enough for experimental observations to be carried out. This type of study is the most realistic way of simulating radiation damage in prospective wasteforms but only a few places in the world are capable of performing such studies due to the equipment required to handle such materials.

Strachan *et al.* started a series of experiments in 1999 in which they doped a series of titanate ceramics with ^{238}Pu and ^{239}Pu [253] and stored them at a range of temperatures from ambient to 250 °C until the ^{238}Pu sample became fully amorphous or the damage reached saturation point [252–254]. The ceramics tested are the three phases that comprise the U.S.A.'s wasteform for weapons plutonium not suitable for conversion to MOX fuel: a $CaUTi_2O_7$ pyrochlore, a $CaZrTi_2O_7$ zirconolite and a UTi_2O_6 brannerite compound. The samples were synthesised with a Pu content roughly equal to 10 wt%, with the exception of the brannerite phase which did not form and was not considered further.

Once synthesized, all samples were analysed using X-Ray Diffraction (XRD) patterns, density measurements and photographs for later comparison and an initial 3 day leach test was carried out [253]. Results from this test for the ^{238}Pu doped samples showed relatively high but comparable leach rates for both the pyrochlore and the zirconolite. The authors point out that these samples were newly formed at this point and this may cause strange results due to unreacted materials and grain boundary phases [253]. In the most recent paper from the same group [252], they attribute this initial high rate to radiolysis effects on the leachant that caused enhanced dissolution.

This work was continued in 2001 by Strachan *et al.* [254]. At this point, due to differences in composition, the pyrochlore phase had received a dose of about 3×10^{18} α-decays per gram and the zirconolite had received 2×10^{18} α-decays per gram. For these two compounds, the authors report that the pyrochlore should be almost completely amorphous and the zirconolite should be 80% amorphous [254]. While not strictly comparable as these materials are being examined for the immobilisation of actinides, it was mentioned in table 2.3 that a nuclear waste glass would experience 1×10^{18} α-decays per gram after 1,000,000 years. It was found, as expected, that all samples containing ^{238}Pu show some volume change, the density reduction is reported for the pyrochlore to be 8% and the zirconolite showed a more considerable density reduction of 15% even though it has received a lower dose [254]. These values are for the room temperature specimens.

XRD patterns of the room temperature samples showed that after one year in a titanate ceramic doped with ^{238}Pu the pyrochlore phase had become amorphous. The zirconolite constituent seemed to be more resilient but it had experienced a lower dose [254]. As will be mentioned later, it has been noted that there is considerable variation in the amorphisation resistance in the pyrochlore system and the titanate system is more susceptible then the zirconate system so a different composition may not have amorphised. However, for this system, after this time, the authors report the only crystalline phases present in the pyrochlore material were from a TiO_2 rutile, HfO_2 solid solution. They attribute this to the low solubility of PuO_2 in rutile so that the number of ^{234}U recoil atoms that reach these phases is lower than for the sample as a whole.

In the same report, the authors give the results for a 350-day dissolutions study on the ^{239}Pu-doped samples and 3-day dissolution studies on the ^{238}Pu-doped samples (longer was not possible due to radiolysis of the water). Details of the leaching study can be found in [254]. In summary, comparing the rates for the ^{239}Pu sample with the ^{238}Pu-doped sample shows that the radiation damaged sample showed a leach rate about 1000 times faster for the release of Pu and 700 times for the U [254]. While these seem alarmingly large changes, the leach rates are still on the order of milligrams per square metre per day.

In the concluding paper published recently by the same group [252] where they repeated some of their earlier work, they found that there is virtually no difference (within experimental uncertainties) between the samples doped with ^{238}Pu and ^{239}Pu and concluded that even though the samples become amorphous, there is no change in the dissolution rate caused by radiation damage. They calculated the final dose that the ^{238}Pu doped ceramic has received to be 7.5×10^{18} α-decays per gram and that for a material doped with 10 wt% ^{239}Pu this would correspond to a period of 970 years in the repository. After this period, they predict a volume increase of about 7% due to amorphisation but no cracking or degradation of the samples was observed. They go on to state that either the pyrochlore or the zirconolite would be good candidates for the immobilisation of Pu.

Another actinide doping study was mentioned earlier in the section regarding the formation of the americium and californium zirconate pyrochlores by Sykora *et al.* [250]. They formed “very small” samples by mixing stoichiometric quantities of zirconyl nitrate with either $CfCl_3$ or AmO_2. The samples were dried and calcined at temperatures of up to 1500 °C. The authors found that the californium pyrochlore formed without any problems in air but the americium required a 4% hydrogen in argon atmosphere to prevent it oxidising to Am^{4+} [250]. Sykora *et al.* [250] performed XRD on the samples after 1 month and then after 2 years of self irradiation. After a month, both materials were still crystalline. The californium isotope (^{249}Cf) used in this study had a shorter half life (351 years) than the americium isotope (mass number or half-life not given) and the authors report the final analysis of the americium pyrochlore as work in progress [250]. Both of the samples were shown to exhibit slight swelling of the lattice parameter during the early part of the study which the authors surmised was due to either the accumulation of point defects from α-decay, the inclusion of helium in the matrix or a combination of both. The californium compound lost the characteristic pyrochlore diffraction lines after 6 months of self irradiation (a corresponding dose of 1.17×10^{24} α-decay per gram [250]). While the material no longer exists in the pyrochlore structure, Sykora *et al.* [250] report that the diffraction pattern was indicative of a solid solution of mixed dioxides or an oxygen deficient fluorite structure but not amorphous like the titanate systems discussed earlier. The pyrochlore structure can be regained by reheating [250]. They found similar results for the americium pyrochlore and the ability to resist amorphisation at such high doses whilst incorporating such large proportions of actinide species shows that the resistance to amorphisation from α-decay is a hugely variable parameter in the pyrochlore compositional field.

Ion Beam Irradiation Studies

By using an accelerated beam of heavy ions, it is possible to simulate similar damage levels to what would correspond to several thousand years of α-decay in a real wasteform in a few days [31]. Ion beam irradiation facilities are far more widespread than laboratory facilities equipped to handle highly radioactive species such as ^{238}Pu [252–254]. The problems with ion beam irradiation studies is that they can only damage a small region close to the surface (a few tens of microns) and they only produce damage that is similar to alpha decay, although, in their review, Ewing *et al.* [31] report that results are consistent with highly damaged ^{244}Cm doped samples. Ewing *et al.* go on to say that ion-beam irradiation studies can provide a reasonable representation of the worst case effects of radiation damage on chemical durability over the intervals of interest for actinide containing wasteforms [31].

There have been numerous ion-beam irradiation studies on pyrochlores and the related disordered fluorite structure [233, 235, 246, 247, 255–263]. The disordered fluorite structure is relevant here due to the fact that many pyrochlores undergo a disordering transformation under irradiation to fluorite [247].

Examining the latter stages of radiation damage first, Sickafus *et al.* [132,232] demonstrated that fluorite solid solutions (i.e. $Er_2Zr_2O_7$ and $Er_2Ce_2O_7$), showed remarkable resistance to amorphisation under heavy ion irradiation. In their study, Sickafus *et al.* [132] bombarded both the $Er_2Ti_2O_7$ pyrochlore and the $Er_2Zr_2O_7$ disordered fluorite with 350-keV Xe^{++} ions at the temperature of 120 K in order to inhibit recovery processes. While the titanate system became amorphous at a fluence of 1 × 10^{15} Xe ions per cm^2, the disordered fluorite system remained crystalline until the experiment was ended at a fluence of 1 × 10^{16} Xe ions per cm^2.

In the pyrochlore system, ion-beam radiation studies have tended to concentrate on the titanates, which tend to readily undergo amorphisation at relatively low doses. The zirconate systems require significantly higher doses to become amorphous or undergo a disordering transformation to form a defective fluorite structure which may or may not become amorphous. Some of the ion-beam irradiation studies will now be reviewed in greater depth.

Wang and coworkers [263] compared the resistance of a $Gd_2Ti_2O_7$ pyrochlore and a $CaZrTi_2O_7$ zirconolite by bombarding them whilst simultaneously monitoring the system using Transmission Electron Microscopy (TEM). They bombarded the materials with 3 types of ion beam over a wide range of temperatures between room temperature and 1000 °C. The three types of ion beam were 1.5 MeV Xe^+, 1 MeV Kr^+ and 0.6 MeV Ar^+ [263] and the dose rate was 8.5 × 10^{11} ions per cm^2 per second. The authors found that the $Gd_2Ti_2O_7$ pyrochlore gradually disordered into the disordered fluorite structure and partially amorphised until the transformation was complete when the entire system became amorphous. At room temperature, this occurred at a fluence of 7.57 × 10^{14} ions per cm^2. Wang *et al.* concluded that the gradual and concurrent amorphisation and fluorite transformation originated from different regions of the cascades caused by the bombardment. The central core of the cascade where damage is greatest becomes amorphous, whilst the outer regions are merely disordered forming a fluorite structure [263]. The zirconolite that was also studied became amorphous at a slightly lower dose of 6×10^{14} ions per cm^2 but it showed a more complicated structural transition. Wang *et al.* [263] found that after a fluence of about 2×10^{14} ions per cm^2 a partially cation disordered pyrochlore had formed. This disappears at twice the fluence and only a disordered fluorite structure is left. This then slowly amorphises until it becomes fully amorphous at 6×10^{14} ions per cm^2 [263].

Begg *et al.* [260] also considered the ion irradiation of titanate pyrochlores but they also looked into the effect that amorphisation has on the dissolution rates. This group also use *in-situ* TEM to monitor the amorphisation process and they used 0.6 MeV Bi^+ ions as the bombarding species. The pyrochlores studied included the Gd, Y, Sm and Lu titanates. The effect of temperature on the was also considered in the range 20 to 1000 K so that temperature variation of the critical irradiation dose could be determined (as in the previous study by Wang *et al.* [263]). They found that there is no significant effect on the critical dose by varying the A cation with all the titanate pyrochlores tested having a critical temperature somewhere close to 975 °C [260]. They also found that all of these titanate pyrochlores undergo room temperature amorphisation at a low dose (about 0.18 dpa in this case). Like the previous study [263] they found that the pyrochlore showed a combined amorphisation and transformation to fluorite until amorphisation was complete.

Moving on to the leach results from the same study; samples 10mm × 10mm × 1mm were prepared and polished to a 0.5μm finish. These were then irradiated on both large faces to a fluence of 5 ions per nm^2 (using 2 MeV Au^{++} ions). This produced an amorphous layer about 380 nm thick on each sample [260]. After 15 days at a temperature of 90 °C and at pH 2 the dissolution rates for Gd and Ti ions from the $Gd_2Ti_2O_7$ sample were 15 times higher than for the undamaged sample. After 21 days, the dissolution rates dropped slightly to a factor of 10 higher for Gd and 2 for Ti ions. The much slower rate for Ti dissolution was found to be due to the formation of anatase (TiO_2) on the surfaces of the damaged specimens. They noted that this order of magnitude change in dissolution rate upon amorphisation is consistent with previous work on ^{244}Cm doped $Gd_2Ti_2O_7$ [260]. The $Y_2Ti_2O_7$ sample showed similar results for the Ti dissolution rate but no change in the Y dissolution rate although the rate of dissolution of Y from the crystalline sample was reported as equivalent to the amorphous dissolution rate of Gd. The $Lu_2Ti_2O_7$ sample showed enhanced dissolution rates of a factor of 5 after 9 days and at the end of the study this had reduced to a factor of 3. The Ti leach rates from the same sample initially peaked at 20 times higher than the crystalline sample and ended up 9 times greater [260]. In general, leach rates increase substantially upon amorphisation and thus compositions that do not amorphise are preferable.

Moving from titanate pyrochlores to the zirconates, Lian *et al.* studied the ion-irradiation effects on $A_2Zr_2O_7$ pyrochlores where A is La, Nd, Sm or Gd using by 1.5 MeV Xe^+ ions and performing *in-situ* TEM observations [233, 257]. They also performed a 200 keV Ti ion implantation on bulk $Gd_2Zr_2O_7$ to a very high dose of 1×10^{17} ions per cm^2 and studied the evolution of the microstructure using cross sectional TEM. Lian *et al.* found that all of the zirconate pyrochlores underwent a disordering transformation to the disordered fluorite structure as in the titanate system. Of all the samples tested only $La_2Zr_2O_7$ showed similar behaviour to the titanates. All the others slowly disordered forming a disordered fluorite structure. Even though $La_2Zr_2O_7$ became amorphous, it was significantly more resistant than the titanates studied by Begg *et al.* [260], only amorphising at room temperature at a dose of 5.5 dpa (compared with 0.18 dpa). All the other zirconates remained crystalline defect fluorites even with irradiation temperatures as low as 25 K even after doses of 7 dpa. The ion implanted bulk sample of remained $Gd_2Zr_2O_7$ crystalline fluorite and the calculated dose in the surface region was about 100 dpa [233]. In this study they compare $Gd_2Zr_2O_7$ with the results from Sickafus *et al.* [127] where they discuss the amorphisation resistance of radiation induced cubic zirconia (pure monoclinic zirconia that has become cubic upon ion irradiation) which has been shown to resist amorphisation to 680 dpa.

Molecular Dynamics Studies

Molecular dynamics (MD) simulations are able to simulate a single cascade, something that is usually very difficult to observe. Conventional MD calculations, however, are very limited in terms of the timescale of the simulations with current computing resources generally proceeding up to some tens of picoseconds.

There have been two MD simulations studied recently that have attempted to model both the effect of displacement cascades caused by α-recoil atoms

[264,265] and one that considered the global amorphisation of $La_2Zr_2O_7$ [266]. Purton and Allan [264] ran five calculations with PKA (primary Knock-on Atom) energy less than 10 keV and 2 calculations between 10 and 20 keV in both $Gd_2Ti_2O_7$ and $Gd_2Zr_2O_7$. They found that the number of defects was significantly greater in the titanate case and that there was a significant difference in the configuration of the final defects. They stated that the $Gd_2Zr_2O_7$ cascade had an elongated or cylindrical shape and had a very ordered structure and that many of the oxygen ions become associated with the 8a lattice position in the pyrochlore space group and thus became more fluorite like [264] in agreement with experimental studies. Contrasting with this, the $Gd_2Ti_2O_7$ pyrochlore was reported to have a more ellipsoidal structure and have an amorphous core with no obvious ordering. Purton and Allan attributed this difference to the ability of $Gd_2Zr_2O_7$ to accommodate disorder and show increased ionic conductivity over $Gd_2Ti_2O_7$.

Chartier *et al.* have performed an in depth MD study of the $La_2Zr_2O_7$ system [265] in which they analysed many properties in order to ensure their potentials would reproduce the system as well as possible. Before considering recoil events, they calculated the average and the minimum displacement energies for all the species (averages calculated over 14 different directions) Oxygen has the lowest average displacement energy of 38 eV, next comes La with 153 eV followed by 188 eV for the Zr. They define the displacement energy to be the minimum kinetic energy transferred from the PKA to an atom along a given crystallographic direction yielding a Frenkel pair [265].

The recoil event simulations of Chartier *et al.* were set up in a simulation cell containing about 152000 atoms (consisting to an 8 × 8 × 8 supercell). One of the Zr^{4+} atoms at approximately $(\frac{1}{4}, \frac{1}{4}, \frac{1}{4})$ in the supercell was replaced with a U^{4+} which was then equilibrated to 350 K under constant pressure conditions. The cascade simulations were then run using periodic boundary conditions under constant volume conditions with a PKA energy of 6 keV in the [111], [322], [211] and [221] directions. They found that the peak number of displacements occurs at about 30fs into the cascade where 807 oxygen ions, 171 lanthanum ions and 91 zirconium ions have been displaced. A rapid recovery stage was then observed until about 900fs at which they observed about 40% of the displaced ions had returned to their previous or to equivalent lattice sites. This was then followed by a much slower process where roughly 10% of the remaining oxygen interstitial ions migrated back to lattice sites [265]. The authors note that they saw oxygen ions at the 8a site returning to the 48f site up to 4ps into the cascade although no more occupancies were noted until the end of the cascade after 7.5ps. They report that all directions produced similar effects but that the [111] and [322] directions produced 20% more defects. They attribute this to the fact that the first atom hit by the PKA is different for the two classes of direction yielding different sub-cascades [265]. They also note that no cation interstitial ions remain at the end of the cascade, only antisite defects. They go on to conclude that during isolated cascade events $La_2Zr_2O_7$ retains its crystallinity with over 90% of the initially displaced atoms returning to equivalent sites after 1ps and that the average number of residual interstitial ions produced by a 6 keV U PKA is about 70.

Chartier *et al.* also attempted to used molecular dynamics techniques to simulate disorder induced amorphisation in $La_2Zr_2O_7$ [266]. In order to achieve this they first tested their system to see if they could produce a disordered fluorite system. This required a cell containing 704 atoms initially in a pyrochlore structure in which half the cations were randomly swapped into antisite configurations and then the system was allowed to relax using MD for 18 ps. No deliberate oxygen disorder was introduced [266]. During this period, the oxygen ions spontaneously moved and generated a disordered fluorite system.

In order to explore the transition of the pyrochlore to the disordered fluorite, Chartier *et al.* used 140 different configurations of the cell just described containing different numbers of cation antisite defects ranging from 0 to 100%. They noted that disorder on the anion sublattice follows the cation sublattice on almost a 1:1 ratio and therefore conclude that disorder on the cation sublattice directly drives the anion disordering process [266]. In order to simulate the pyrochlore to fluorite transformation under more realistic radiation damage processes, Chartier *et al.* introduced different random concentrations (up to 16%) of Frenkel pairs in the lattice, and this was carried out in a ratio of 2:1 La to Zr Frenkel pairs in order to reproduce the numbers seen in previous MD simulations [265]. They estimate that complete transformation to the fluorite system will occur at a concentration of 20%. To go on to model the amorphisation process, Chartier *et al.* introduced small numbers of Frenkel pairs into the disordered fluorite cell under constant pressure and constant volume simulations. Under the constant volume regime, they found that no matter how many Frenkel pairs were introduced, no amorphisation occurred but under constant pressure conditions, an introduction of 10% Frenkel pairs (equal numbers of cations) results in an amorphous transition [266]. This difference between the constant volume and constant pressure regimes seems logical as experimentally, there is an associated volume change upon amorphisation for the pyrochlores [254]. Chartier *et al.* [266] went on to conclude that $La_2Zr_2O_7$ transforms to a fluorite structure when the Frenkel pair to cation ratio reaches 0.2 and that subsequent irradiation introduces more Frenkel pairs that are sufficient to drive the amorphisation process. They also state that the necessity to reach this critical concentration of Frenekl pair defects is the reason that $La_2Zr_2O_7$ is so difficult to amorphise at room temperature as, at this temperature, the cations have sufficient mobility to move back from the interstitial sites to equivalent lattice sites [266].

5.3 Methodology

5.3.1 Interatomic Potentials

The full charge interatomic potentials from Minervini *et al.* [223] and Stanek *et al.* [230] were used to model the pyrochlore compounds and the U^{4+} potential from Busker *et al.* [267] was used to simulate UO_2. Potential parameters for U^{3+}, Pu^{3+} and Pu^{4+} were derived for this study. Since no structural data for compounds containing U^{3+} ions could be found, rendering the multi fitting procedure described in chapter 3 impossible, this potential was derived differently using a method similar to that used by Butler *et al.* [268]. In this procedure, the interatomic interactions were plotted for the Pu^{3+} and the

Pu^{4+} and the difference between the two was calculated. The U^{4+} potential was plotted and then the difference between the Pu^{3+} and the Pu^{4+} was subtracted. A line of best fit taking the mathematical form of the Buckingham potential was fit to this new curve (see equation 3.7) and the A, ρ and C parameters thereby identified. All potentials used are shown in Table 5.1. The shell model was used for the oxygen, zirconium and lead ions and these parameters are reported in table 5.2

Special attention has been paid to the derivation of a new Pu^{3+}-O^{2-} short-range potential. The parameters were selected to best fit the lattice parameters of Pu_2O_3, $CrPuO_3$ and $AlPuO_3$ while exactly reproducing the lattice parameter of stoichiometric $Pu_2Zr_2O_7$ reported in reference [240] (i.e. 10.70Å). In previous computational work [234] potentials were fitted to a lattice parameter corresponding to a hyper-stoichiometric $Pu_2Zr_2O_7$ material i.e. containing Pu^{4+} [240, 242].

The energy minimisation atomic scale simulation approach described (see chapter 3) has been used successfully to predict various properties of $A_2B_2O_7$ pyrochlores, including oxygen migration [221], intrinsic disorder process energies [223] and nonstoichiometry formation via solution of excess BO_2 or A_2O_3 [220]. One approximation that should be mentioned is that all pyrochlores are treated as cubic. While this is the case for the majority of pyrochlore compositions, there are a few titanates with large lanthanide cations and $Pu_2Ti_2O_7$ which exhibit a monoclinic distortion [135, 223] (see also chapter 4).

Table 5.1: Full charge short range potential parameters used to describe interactions between all the ions in this study.

Species	A (eV)	ρ (eV)	C (eV Å^6)
$O^{2-} \leftrightarrow O^{2-}$	9547.960	0.21920	32.00
$La^{3+} \leftrightarrow O^{2-}$	2088.890	0.34600	23.25
$Pr^{3+} \leftrightarrow O^{2-}$	2055.350	0.34380	23.95
$Nd^{3+} \leftrightarrow O^{2-}$	1995.200	0.34300	22.59
$Sm^{3+} \leftrightarrow O^{2-}$	1944.440	0.34140	21.49
$Eu^{3+} \leftrightarrow O^{2-}$	1925.710	0.34030	20.59
$Gd^{3+} \leftrightarrow O^{2-}$	1885.750	0.33990	20.34
$Dy^{3+} \leftrightarrow O2-$	1807.840	0.33930	18.77
$Er^{3+} \leftrightarrow O^{2-}$	1739.910	0.33890	17.55
$Yb^{3+} \leftrightarrow O^{2-}$	1649.800	0.33860	16.57
$Lu^{3+} \leftrightarrow O^{2-}$	1618.800	0.33849	19.27
$U^{3+} \leftrightarrow O^{2-}$	1165.65	0.376582	0.00
$Pu^{3+} \leftrightarrow O^{2-}$	1150.745	0.37430	12.10
$Ti^{4+} \leftrightarrow O^{2-}$	2131.040	0.30380	0.00
$Ru^{4+} \leftrightarrow O^{2-}$	1215.780	0.34410	0.00
$Mo^{4+} \leftrightarrow O^{2-}$	1223.970	0.34700	0.00
$Sn^{4+} \leftrightarrow O^{2-}$	1414.320	0.34790	13.66
$Zr^{4+} \leftrightarrow O^{2-}$	1502.110	0.34770	5.10
$Pb^{4+} \leftrightarrow O^{2-}$	1640.340	0.35070	19.50
$U^{4+} \leftrightarrow O^{2-}$	1761.775	0.356421	0.00
$Pu^{4+} \leftrightarrow O^{2-}$	1762.840	0.35420	11.48

Table 5.2: Shell parameters used to describe interactions between all the ions with shells in this study.

Species	Charge	k
O^{2-}	-2.04	32.0
Zr^{4+}	-0.05	189.7
Pb^{4+}	-0.05	205.0

5.3.2 Contour Maps

All results are presented in the form of host lattice composition contour maps (see figures 5.1 to 5.12). These show the results as a two dimensional surface where the x-axis represents increasing B cation radius and the y-axis represents increasing A cation radius. Isolines link compositions of equal energy and the shade of the areas bounded by these lines indicates an energy interval as shown in the separate scale. On the energy surface, actual calculations (i.e. experimentally observed pyrochlore forming compositions, see figure 4.19 in chapter 4) are marked by points whose shape represents the solution mechanism from which the energy for that composition is taken.

5.4 Results and Discussion

5.4.1 Solution Mechanisms

As in previous work by Weber *et al.* [234] solution is considered with respect to the binary oxides MeO_2 and Me_2O_3 where Me is either U or Pu (although experimental data for U_2O_3 could not be located, here it is assumed to form isostructurally with Pu_2O_3). Since these simple oxides have a different stoichiometry to a host pyrochlore it will be necessary to form charge compensating defects. Solution process energies are then composed of a number of individual defect energies. Possible solution processes are described by equations 5.1 to 5.14 using Kröger-Vink notation [5]. Solution processes which involve cation interstitial ions will not be reported as it was found that the corresponding solution energies are highly unfavourable, similar results were reported by Williford and Weber [234].

Equations 5.1 through 5.3 describe the solution of Me_2O_3 into $A_2B_2O_7$ pyrochlore with compensation by oxygen vacancies $\left(V_O^{\bullet\bullet}\right)$. These mechanisms maintain the pyrochlore A:B ratio but not the pyrochlore oxygen stoichiometry. Equation 5.1 assumes the actinide exclusively occupies the A sites in the pyrochlore. Equation 5.2 assumes equal A and B site occupation of the actinide ions and equation 5.3 assumes only B site occupation (note that equation 5.2 is related to equations 5.1 and 5.3 through antisite disorder). Equation 5.4 assumes that the actinide ion exclusively occupies the A site but allows the formation of excess A_2O_3 (i.e. we introduce Me_2O_3 into the lattice and remove A_2O_3) and consequently the A:B ratio is no longer maintained but the oxygen stoichiometry is unaltered (this is the same as equation 1 in [234]). Equation 5.5 assumes that the actinide ion occupies the B site, but results in the formation of excess BO_2. Consequently neither the A:B ratio nor the oxygen stoichiometry are maintained (this is the same as equation 2 in [234]).

$$2\mathrm{Me}_2\mathrm{O}_3 + 4A_A^{\times} + 2B_B^{\times} + \mathrm{O}_O^{\times} \longrightarrow 4\mathrm{Me}_A^{\times} + 2A_B^{\prime} + V_O^{\bullet\bullet} + A_2B_2\mathrm{O}_7 \qquad (5.1)$$

$$2\mathrm{Me}_2\mathrm{O}_3 + 2A_A^{\times} + 2B_B^{\times} + \mathrm{O}_O^{\times} \longrightarrow 2\mathrm{Me}_A^{\times} + 2\mathrm{Me}_B^{\prime} + V_O^{\bullet\bullet} + A_2B_2\mathrm{O}_7 \tag{5.2}$$

$$2\mathrm{Me}_2\mathrm{O}_3 + 2A_A^{\times} + 4B_B^{\times} + \mathrm{O}_O^{\times} \longrightarrow 2B_A^{\bullet} + 4\mathrm{Me}_B^{\prime} + V_O^{\bullet\bullet} + A_2B_2\mathrm{O}_7 \tag{5.3}$$

$$\mathrm{Me}_2\mathrm{O}_3 + 2A_A^{\times} \longrightarrow 2\mathrm{Me}_A^{\times} + A_2\mathrm{O}_3 \tag{5.4}$$

$$\mathrm{Me}_2\mathrm{O}_3 + 2B_B^{\times} + \mathrm{O}_O^{\times} \longrightarrow 2\mathrm{Me}_B^{\prime} + V_O^{\bullet\bullet} + 2B\mathrm{O}_2 \tag{5.5}$$

Equations 5.6 through 5.8 describe the solution of PuO_2 and UO_2 (i.e. MeO_2) with compensation via oxygen interstitial ions (i.e. $\mathrm{O}_i^{\prime\prime}$ where in all cases the interstitial site is the unoccupied 8a lattice position of the Fd$\bar{3}$m space group). Equation 5.6 assumes the actinide exclusively occupies the A sites in the pyrochlore. Equation 5.7 assumes equal A and B site occupation of the actinide ions and equation 5.8 assumes B site occupation. Equation 5.9 assumes that the actinide ion exclusively occupies the A site but allows the formation of excess $\mathrm{A}_2\mathrm{O}_3$ (equation 4 in [234]) and Equation 5.10 assumes that the actinide ion occupies the B site, allowing the formation of excess BO_2 (this is equation 3 in [234]).

$$4\mathrm{MeO}_2 + 4A_A^{\times} + 2B_B^{\times} \longrightarrow 4\mathrm{Me}_A^{\bullet} + 2A_B^{\prime} + \mathrm{O}_i^{\prime\prime} + A_2B_2\mathrm{O}_7 \tag{5.6}$$

$$4\mathrm{MeO}_2 + 2A_A^{\times} + 2B_B^{\times} \longrightarrow 2\mathrm{Me}_A^{\bullet} + 2\mathrm{Me}_B^{\times} + \mathrm{O}_i^{\prime\prime} + A_2B_2\mathrm{O}_7 \tag{5.7}$$

$$4\mathrm{MeO}_2 + 2A_A^{\times} + 4B_B^{\times} \longrightarrow 2B_A^{\bullet} + 4\mathrm{Me}_B^{\times} + \mathrm{O}_i^{\prime\prime} + A_2B_2\mathrm{O}_7 \tag{5.8}$$

$$2\mathrm{MeO}_2 + 2A_A^{\times} \longrightarrow 2\mathrm{Me}_A^{\bullet} + \mathrm{O}_i^{\prime\prime} + A_2\mathrm{O}_3 \tag{5.9}$$

$$\mathrm{MeO}_2 + B_B^{\times} \longrightarrow \mathrm{Me}_B^{\times} + B\mathrm{O}_2 \tag{5.10}$$

Equations 5.11 through 5.14 describe the solution of $\mathrm{MeO_2}$ via the formation of charge compensating A cation vacancies $\left(V_A^{'''}\right)$. Equations 5.11 through 5.13 are equivalent to 5.6 through 5.8. As such these mechanisms maintain the A:B ratio of the pyrochlore. Equation 5.14 is equivalent to equation 5.9 (this is equation 5 in [234]).

$$7\mathrm{MeO_2} + 8A_A^{\times} + 4B_B^{\times} \longrightarrow 7\mathrm{Me}_A^{\bullet} + V_A^{'''} + 4A_B^{'} + 2A_2B_2\mathrm{O}_7 \tag{5.11}$$

$$7\mathrm{MeO_2} + 4A_A^{\times} + 4B_B^{\times} \longrightarrow 3\mathrm{Me}_A^{\bullet} + 4\mathrm{Me}_B^{\times} + V_A^{'''} + 2A_2B_2\mathrm{O}_7 \tag{5.12}$$

$$7\mathrm{MeO_2} + 4A_A^{\times} + 7B_B^{\times} \longrightarrow 7\mathrm{Me}_B^{\times} + 3B_A^{\bullet} + V_A^{'''} + 2A_2B_2\mathrm{O}_7 \tag{5.13}$$

$$3\mathrm{MeO_2} + 4A_A^{\times} \longrightarrow 3\mathrm{Me}_A^{\bullet} + V_A^{'''} + 2A_2\mathrm{O}_3 \tag{5.14}$$

Next solution mechanisms that involve co-doping were considered (such mechanisms were not considered in [234]). Equation 5.15 describes solution of trivalent $\mathrm{Pu^{3+}}$ or $\mathrm{U^{3+}}$ accompanied by additional $\mathrm{B^{4+}}$ ions. Equation 5.16 assumes tetravalent $\mathrm{PuO_2}$ or $\mathrm{UO_2}$ and additional $\mathrm{A^{3+}}$ ions.

$$\mathrm{Me_2O_3} + 2B\mathrm{O}_2 + 2A_A^{\times} + 2B_B^{\times} \longrightarrow 2\mathrm{Me}_A^{\times} + 2B_B^{\times} + A_2B_2\mathrm{O}_7 \tag{5.15}$$

$$2\mathrm{MeO_2} + A_2\mathrm{O}_3 + 2A_A^{\times} + 2B_B^{\times} \longrightarrow 2A_A^{\times} + 2\mathrm{Me}_B^{\times} + A_2B_2\mathrm{O}_7 \tag{5.16}$$

$$2\mathrm{Pu}_A^{\times} + A_2B_2\mathrm{O}_7 \longrightarrow 2A_A^{\times} + \mathrm{Pu}_2B_2\mathrm{O}_7 \tag{5.17}$$

$$\mathrm{CaBO_3} + \mathrm{MeO_2} + BO_2 + 2A_A^{\times} \longrightarrow \mathrm{Ca}_A^{'} + \mathrm{Me}_A^{\bullet} + A_2B_2O_7 \tag{5.18}$$

Equation 5.15 results in a solid solution of $\mathrm{Me_2B_2O_7}$ and $\mathrm{A_2B_2O_7}$. The stability of this solid solution is investigated through equation 5.17 which allows the solid solution to decompose into the two component pyrochlores. This is equivalent to the process investigated by Shoup *et al.* (1996) for Pu.

Equation 5.16 results in a composition that can be considered a solid solution between $A_2Me_2O_7$ and $A_2B_2O_7$, except that no $A_2Me_2O_7$ pyrochlores have been observed. However, on the basis of these atomistic simulations it is found that $La_2Pu_2O_7$ and $Pr_2Pu_2O_7$ are stable with respect to PuO_2 and A_2O_3 and that $La_2U_2O_7$ is stable with respect to La_2O_3 and UO_2. Of course, Pu^{4+} is only stable at higher oxygen pressures, in which case it is possible that Pr (but not La) will also attain a tetravalent charge state, resulting in a fluorite solid solution. The predicted lattice parameter of stoichiometric $La_2Pu_2O_7$ is 11.14 Å, that of $Pr_2Pu_2O_7$ is 11.05 Å and $La_2U_2O_7$ is 11.23 Å. Predicted lattice parameters and formation energies of other actinide containing pyrochlores are mentioned later in section 5.4.2.

The final solution mechanism, equation 5.18, also concerns the co-solution of tetravalent uranium or plutonium onto trivalent A pyrochlore sites. This solution is charge compensated by Ca^{2+}, also on A sites. The mechanism is the dilute limit equivalent of the pyrochlore formation mechanism investigated by Huifang *et al.* [37]. The calcium is assumed to be provided in the form of a perovskite; $CaBO_3$ (see equation 5.18).

The sum of the individual defect energies and formation energies from equations 5.1 through 5.16 cannot be directly compared until they have been normalised. This process and its rationale is described in reference [5] and an example is given in appendix B. The normalisation factors for equations

5.1 through 5.16 are simply equal to the number of defect species on the right hand side of the equation. For example, with mechanism 5.1 the factor is 7 and for mechanism 5.2 it is 5. Only normalised energies will be presented in the subsequent sections.

5.4.2 Formation of Actinide Pyrochlores

Finally reactions that describe the formation of Pu^{3+} and U^{3+} actinide pyrochlores are also considered (equations 5.19 and 5.20).

$$\mathrm{Me_2O_3} + 2\mathrm{BO_2} \longrightarrow \mathrm{Me_2B_2}O_7 \tag{5.19}$$

$$\mathrm{A_2O_3} + 2\mathrm{MeO_2} \longrightarrow \mathrm{A_2Me_2}O_7 \tag{5.20}$$

The predicted lattice parameters and formation energies are given in table 5.3 which shows that all $U_2B_2O_7$ and $Pu_2B_2O_7$ pyrochlores are stable with respect to the basic oxides. The lattice parameters for the three $A_2Me_2O_7$ pyrochlores mentioned in the solution mechanisms section are also given. While the hypothetical $U_2B_2O_7$ pyrochlores are not predicted to be as stable as their Pu counterparts they are all predicted to form from mixtures of U_2O_3 and BO_2. They are considered hypothetical, however, as U_2O_3 has not been found to form experimentally and therefore $U_2B_2O_7$ will not be stable with respect to oxidation to a $U_2B_2O_8$ or $(U,B)O_2$ fluorite solid solution. Similarly as found by Kulkarni *et al.* [242] it is likely that the Pu^{3+} containing materials will easily oxidise to form fluorite solid solutions rather than pyrochlores.

Table 5.3: Predicted formation energy and lattice parameter for simulated actinide pyrochlores.

Compound	Lattice Parameter (Å)	Formation Energy (eV)
$U_2Ti_2O_7$	10.305	-1.10
$U_2Ru_2O_7$	10.413	-1.60
$U_2Mo_2O_7$	10.482	-1.68
$U_2Sn_2O_7$	10.639	-1.61
$U_2Zr_2O_7$	10.777	-1.49
$U_2Pb_2O_7$	10.914	-1.06
$La_2U_2O_7$	11.233	-0.76
$Pr_2U_2O_7$	N/A	0.34
$Pu_2Ti_2O_7$	10.228	-2.23
$Pu_2Ru_2O_7$	10.332	-2.61
$Pu_2Mo_2O_7$	10.402	-2.62
$Pu_2Sn_2O_7$	10.560	-2.40
$Pu_2Zr_2O_7$	10.700	-2.16
$Pu_2Pb_2O_7$	10.837	-1.62
$La_2Pu_2O_7$	11.139	-1.19
$Pr_2Pu_2O_7$	11.048	-0.14
$Nd_2Pu_2O_7$	N/A	0.12
$Sm_2Pu_2O_7$	N/A	0.47

5.4.3 Solution Results

Symbols used on Contour Maps

On the following contour maps:

- Diamond shaped points represent mechanism 5.4.
- Square shaped points represent mechanism 5.6.
- Circular shaped points represent mechanism 5.7.
- Triangle shaped points represent mechanism 5.10.
- Star shaped points are used for co-solution or co-doping mechanisms where only one reaction was considered per plot including mechanisms 5.15, 5.16 and 5.18. The mechanism will be specified in the figure caption.
- Pentagon shaped points represent mechanism 5.17.

5.4.4 Solution of Pu_2O_3 and U_2O_3 into Pyrochlores

Initially the approach of Williford and Weber [234] was followed and the solution of the binary oxide Pu_2O_3 via a number of mechanisms (equations 5.1-5.5) was compared. However, given the observations in $Gd_2Zr_2O_7$ by the previous authors [234] interstitial compensation mechanisms were not taken into account but a greatly extended set of oxygen vacancy compensation mechanisms was considered. This selection of solution mechanisms is further justified by the work on A_2O_3 excess non-stoichiometry [220] which showed that interstitial mechanisms were considerably less favourable compared to oxygen vacancy compensation over the whole compositional range.

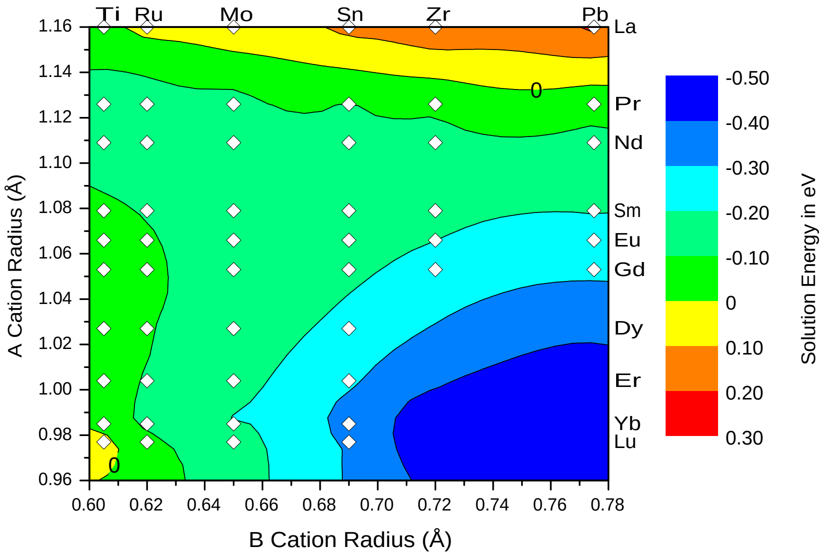

Figure 5.1: Solution of Pu_2O_3 (eV) into pyrochlores. All actual compositions are indicated by points on the map. Diamond shaped points indicate mechanism 5.4.

Results for the solution of Pu_2O_3 are presented in figure 5.1. For each composition the energy selected for the map corresponds to the lowest energy solution mechanism (this will also be the case in subsequent maps). Since at each composition the shape of the point is a white diamond, this indicates that the lowest energy mechanism was independent of composition and corresponds to equation 5.4. Thus, not only is the same lowest solution mechanism in $Gd_2Zr_2O_7$ as Williford and Weber [234] reported but this observation holds true for all the pyrochlores. Consequently, the solution of Pu_2O_3 always results in Pu^{3+} ions exclusively occupying the A sites.

As with the previous work [234], a negative solution energy for Pu_2O_3 in $Gd_2Zr_2O_7$ is also found and this value is -0.23eV. As compositions approach those pyrochlores with either: (1) larger A cations; or (2) small lattice parameters (this includes many of the titanates); solution energies approach zero and become positive. Such compositions may therefore be less useful for fabricating materials under reducing conditions.

This observed lowest energy solution mechanism is a consequence of the Pu^{3+} ion substituting for an isovalent A site ion with a radius of 1.00Å which places it toward the low end of A cation radii for pyrochlores. Thus there is never much lattice relaxation associated with this substitutional defect and consequently the energy for this process is lower than the energies for equations the process in 5.2, 5.3 and 5.5 which have Pu^{3+} ions substituting onto the smaller B^{4+} sites. Equation 5.4 is more favourable than equation 5.1 because the energy to form A_2O_3 is lower than that for the formation of an A cation anti-site defect and $A_2B_2O_7$. Nevertheless equation 5.1 is the next most favourable but it is always more than 0.58eV less favourable than equation 5.4.

Results for the solution of U_2O_3 into pyrochlores are now presented in figure 5.2. At first glance is appears very similar to that for the solution of Pu_2O_3 as the contour shapes are similar and again solution across the entire range is dominated by isovalent substitution of U^{3+} onto the A site (as in equation 5.4). It should be noted that while most solution energies for Pu^{3+} were negative, those for U^{3+} are mostly positive with the solution energies on average 0.3 eV higher than for the equivalent Pu^{3+} solution. This means that only $Yb_2Sn_2O_7$ and $Lu_2Sn_2O_7$ show negative solution energies although $Gd_2Zr_2O_7$ is very close to zero at 0.017 eV.

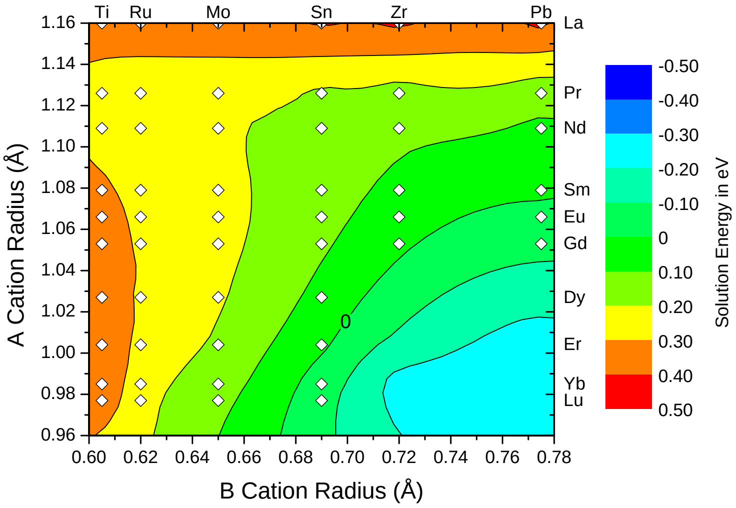

Figure 5.2: Solution of U_2O_3 (eV) into pyrochlores. All actual compositions are indicated by points on the map. Diamond shaped points indicate mechanism 5.4.

Alternative co-solution mechanisms for Pu_2O_3 with BO_2 (i.e. equation 5.15) are now examined and the results are shown in Figure 5.3. This mechanism represents a possible fabrication process. It is immediately apparent that co-solution energies are significantly more negative than for simple Pu_2O_3 solution and also shows a stronger compositional variation (i.e. more contours). However, although the resulting compositions $A_{2-x}Pu_xB_2O_7$ may be stable with respect to the simple starting oxides, the equation hides the possibility that decomposition to a mixture of $A_2B_2O_7$ and $Pu_2B_2O_7$ may occur. This is investigated in Figure 5.4 where negative energies imply that decomposition is just favourable for pyrochlores with A cation radii smaller than Nd. However, the predicted internal energies for such a de-mixing are very small, never larger than 0.13eV per $Pu_2B_2O_7$. Certainly the configurational entropy of mixing of two pyrochlores (a term not included in these calculations) would ensure that the solid solutions remain mixed; furthermore cation migration activation energies are known to be high in pyrochlores [269]. Consequently, under reducing conditions where Pu^{3+} remains stable with respect to Pu^{4+}, significant solid solubility of $Pu_2B_2O_7$ in $A_2B_2O_7$ is expected (unless there is an excess of A_2O_3 in which case the results presented in Figure 5.1 have significance). This is supported by the experimental data of Shoup *et al.* [36] in that they observed extensive solid solubility of $Pu_2Ti_2O_7$ in $Ln_2Ti_2O_7$. However, contrary to the present predictions which would suggest increasing solubility with increasing A host cation radius (as the host cation approaches the Pu^{3+} radius), Shoup *et al.* [36] observed a decreasing solubility with increasing A cation radius.

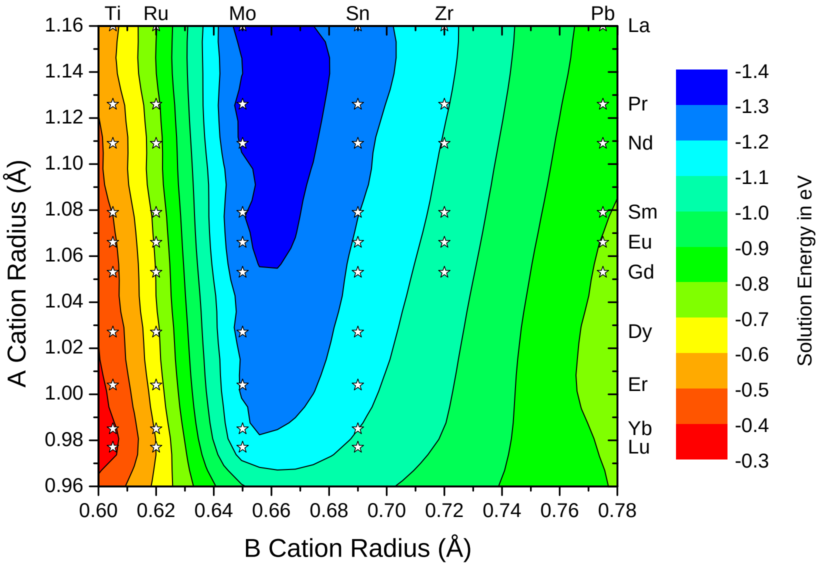

Figure 5.3: Energies of Pu_2O_3 and BO_2 co-solution in pyrochlores via mechanism 5.15.

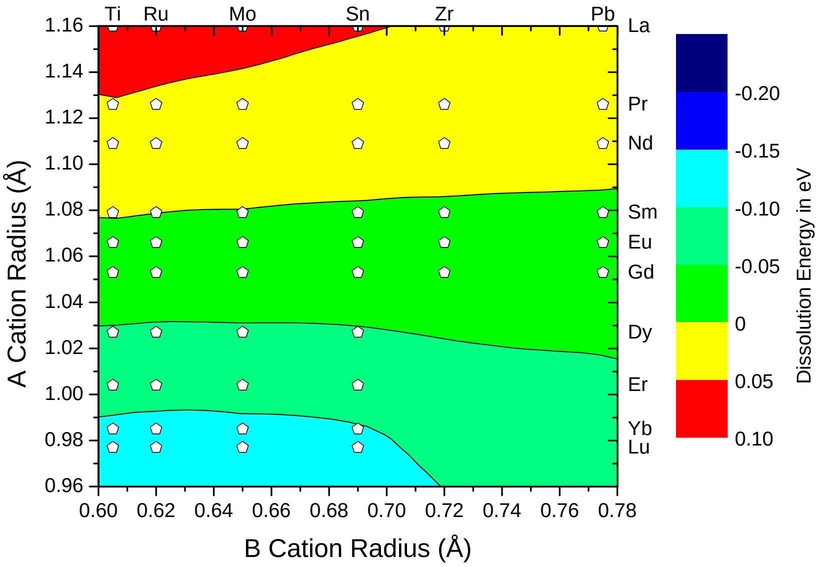

Figure 5.4: Energy to dissociate $A_{2-x}Pu_xB_2O_7$ into $A_2B_2O_7$ and $Pu_2B_2O_7$ via mechanism 5.17.

The results for the equivalent U^{3+} co-solution are presented in figure 5.5. As can be seen by comparing this with figure 5.3, there are both similarities and differences. The same trends are noted in that all the values are negative indicative that this process is favourable for all pyrochlore compositions unlike the simple solution method described by equation 5.4 and shown in figure 5.2. Another similar trend is that the solution energies are at a minimum for the molybdate pyrochlores but the depth of this minimum is no where near as great, being about 0.5 eV higher that for the Pu doped material. As with Pu^{3+} solution, decomposition to form a mixture of $A_2B_2O_7$ and $U_2B_2O_7$ was considered. It is found that this process is more favourable than for Pu^{3+}, this is most likely due to the slightly larger cation radius of U^{3+} (1.025 Å [174]), placing it in the mid range of stable pyrochlore forming compounds. The decomposition energy for this process reaches a maximum of about 0.2 eV which may be significant enough to allow this to proceed if conditions ever become reducing enough to form U^{3+}.

As an alternative to co-solution, the possibility that defect clusters might form as a result of solution via equations 5.1, 5.2 and 5.3, through the association of oppositely charged defects [223,267] was also considered. Although the clusters were stable with respect to the isolated defects, this did not cause any solution mechanisms to be as stable as either equation 5.4 or 5.15 (in which defects are charge neutral and thus have negligible binding energies).

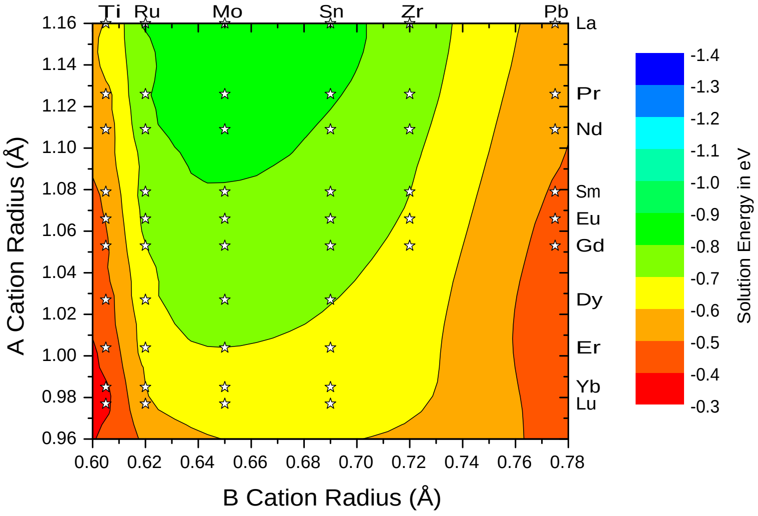

Figure 5.5: Energies of U_2O_3 and BO_2 co-solution in pyrochlores via mechanism 5.15

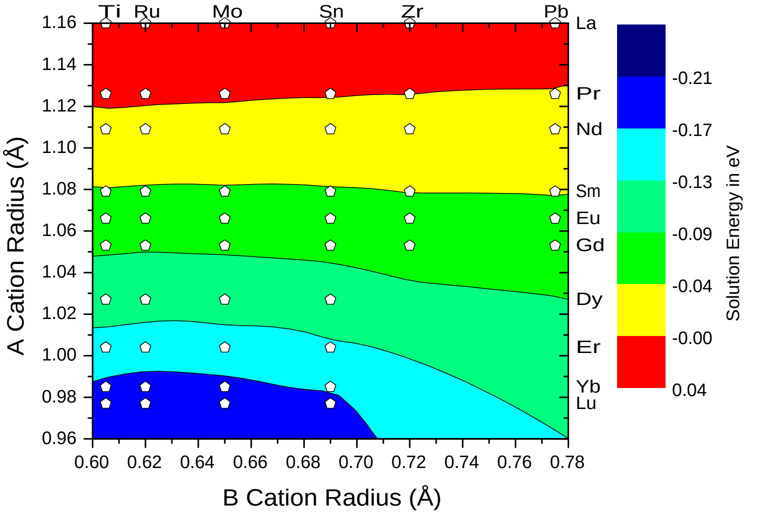

Figure 5.6: Energy to dissociate $A_{2-x}U_xB_2O_7$ into $A_2B_2O_7$ and $U_2B_2O_7$ via mechanism 5.17

5.4.5 Solution of PuO_2 and UO_2

Results for Pu^{4+} solution from PuO_2 are presented in figure 5.7. By examining the $Gd_2Zr_2O_7$ composition first, it can be seen that the figure shows a white circle and thus equation 5.7 is the lowest energy solution mechanism at this composition and Pu^{4+} will occupy both A and B cation sites. This is different to the prediction of Williford and Weber [234] who favoured equation 5.10 in which Pu^{4+} occupies only B cation sites. However, these authors did not consider equation 5.7 although the difference between equations 5.7 and 5.10 at this composition is only 0.17 eV. If the calculations for equations 5.7 and 5.10 are repeated using the potentials of Williford and Weber [234], it is found that the difference between the equations is reduced to only 0.05eV, but equation 5.7 remains energetically more favourable. In all cases energies are positive indicating a significant limit to the solubility of PuO_2 in $Gd_2Zr_2O_7$ this type of process.

Now the solution of PuO_2 is considered over the broad range of pyrochlore compositions. For the most stable pyrochlore forming materials (i.e. away from the large B cation, small A cation region, see [223]) figure 5.7 shows that equation 5.10 does now become more favourable than equation 5.7. Finally for stannates with small A cations equation 5.6 is preferred so that Pu^{4+} substitutes exclusively on the A cation site. However, the difference between equations 5.6 and 5.7 is never greater than 0.06 eV.

Despite the availability of different solution mechanisms, solution energies remain positive. As such, the solution of PuO_2 is clearly less favourable compared to the solution of Pu_2O_3.

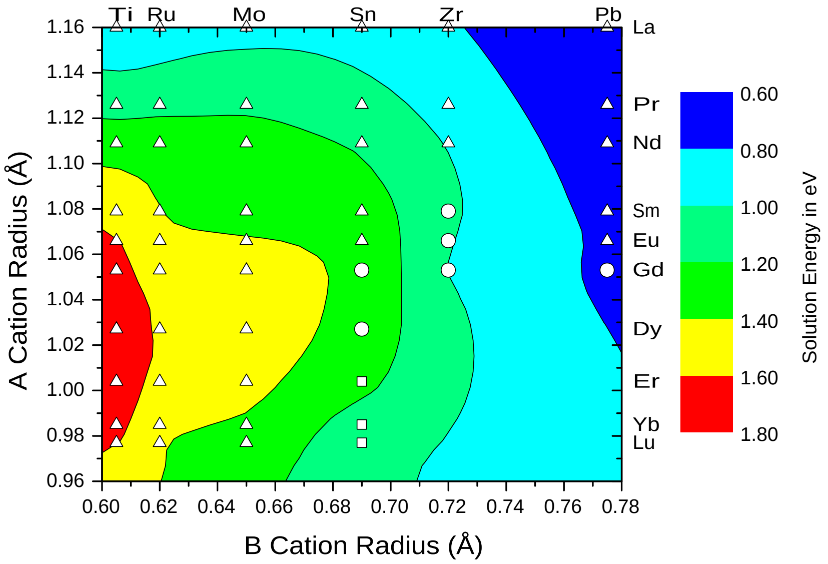

Figure 5.7: Energies of solution of PuO_2 into pyrochlores. The triangle shaped points show where mechanism 5.10 is most favourable, white circles correspond to mechanism 5.7 and white squares to mechanism 5.6.

Differences in preferred solution mechanism have been noted previously between the more stable pyrochlore forming compositions and compositions approaching the pyrochlore to fluorite boundary [220]. With this in mind, the reason why $Gd_2Zr_2O_7$ pyrochlore (which is close to fluorite forming compositions) shows a preference for equation 5.7 is that it incorporates oxygen interstitial ions, O_i''. These charge compensating defects occupy the 8a Wyckoff site which is occupied in fluorite but not in pyrochlore. Away from the pyrochlore fluorite boundary greater distortions of the lattice around the 8a site make it less favourable to accommodate an oxygen interstitial ion.

Figure 5.8 shows the calculated energies for the solution of UO_2. These values are very similar to those for Pu^{4+}, however, there are marked differences in preferred solution mechanisms. In particular, there is a broad compositional region between equations 5.6 or 5.7 and 5.10 where the preferred mechanism is equation 5.11. In this case the charge compensating defect is an A cation vacancy. This type of mechanism was previously identified as important in the study of BO_2 excess nonstoichiometry in pyrochlores [220]; consequently it is not surprising to find it is important here. If the energies for equations 5.11 and 5.10 are compared in this compositional region, the difference is always less than 0.30 eV. Furthermore, the differences between equations 5.11 and 5.7 are always less than 0.15 eV (for the same compositional region). What therefore emerges is the possibility of a complex equilibrium between equations 5.6, 5.7, 5.10 and 5.11 with only a small difference between the three energies of solution at a given position within this extended compositional range. Nevertheless, there are differences in the overall solution energy for UO_2 between compositions and it is expected that this reflects a real variation in the extent of UO_2 solution (throughout differences rather than absolute values are emphasised).

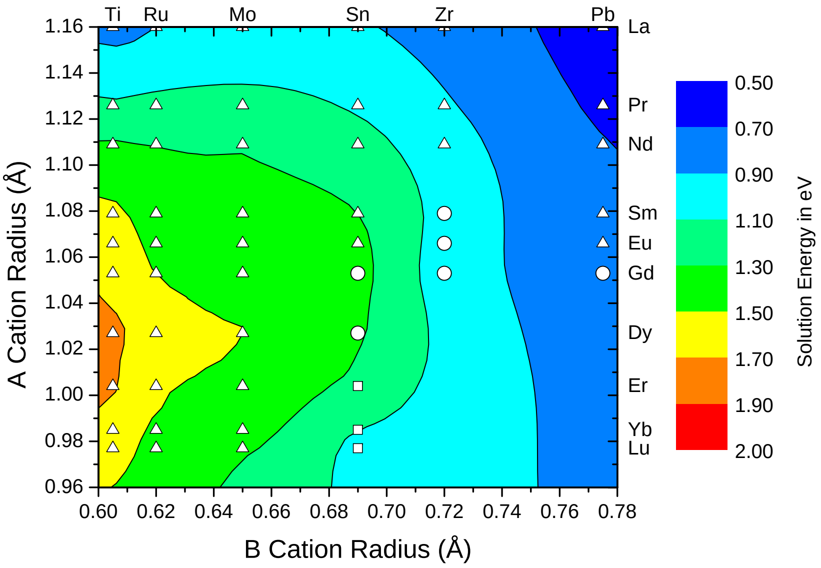

Figure 5.8: Solution energies for UO_2 into pyrochlores. The triangle shaped points show where mechanism 5.10 is the most favoured, white circles to mechanism 5.7 and white squares to mechanism 5.6.

Finally, the co-solution of PuO_2 and A_2O_3 is considered as a mechanism for overcoming the positive solution energies for Pu^{4+} described in figure 5.7. This results in a material with a composition $A_2\left(B_{1-x}Pu_x\right)O_7$. If the PuO_2 and Gd_2O_3 co-solution is considered first, the result which is presented in figure 5.9, shows that co-solution only lowers the solution energy from 0.98 eV (via equation 5.7) to 0.46 eV (equation 5.16). Nevertheless, clearly solution is still not favourable. However, if the broader compositional range is considered, solution is predicted to be favourable for materials with large A cations, independently of the B cation radius. This is a considerable improvement over solution of PuO_2 alone but only in this upper half of the compositional range (compare to figure 5.7). By comparing figures 5.7 and 5.9 it is also clear that the compositional variation in co-solution energies is

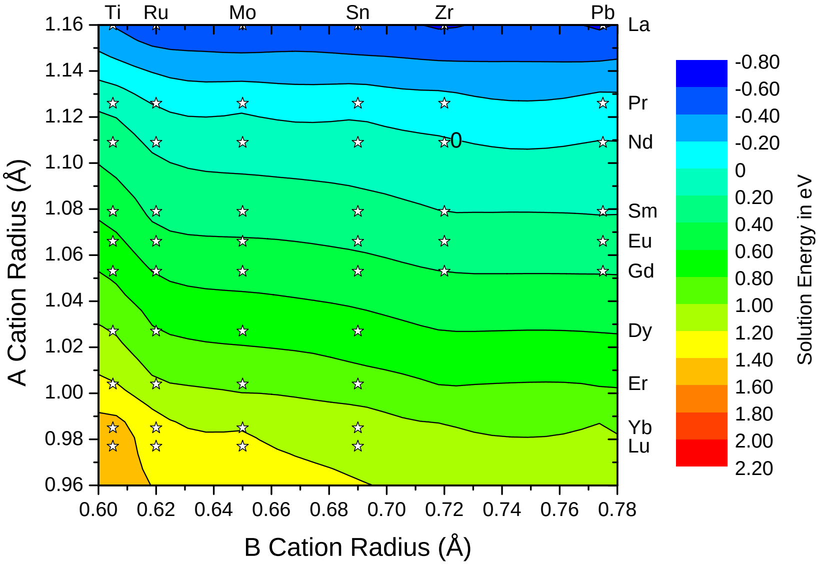

Figure 5.9: Co-solution energies for PuO_2 and A_2O_3 into pyrochlores via mechanism 5.16.

greater than for the simple solution mechanisms.

Results for co-solution of UO_2 show essentially the same trends in solution energies as a function of A and B host cation size (see figure 5.10). However, as with simple solution mechanisms, UO_2 co-solution is consistently less favourable than PuO_2 co-solution (by between 0.2-0.4 eV)

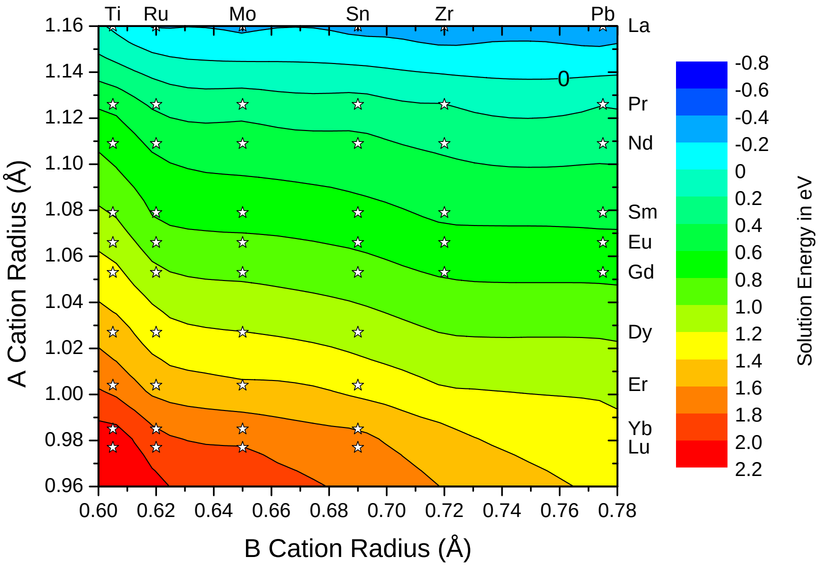

Figure 5.10: co-solution energies for UO_2 and A_2O_3 in pyrochlores via mechanism 5.16.

5.4.6 Solution of PuO_2/UO_2 with compensation via Ca^{2+}

The results of the Ca^{2+} mediated co-solution mechanism (equation 5.18) are presented for Pu^{4+} in figure 5.11. The essential feature of this figure is the generally small compositional variation in solution energy, especially with respect to A cation radius. This is surprising since both Ca^{2+} and Pu^{4+} substitute onto the A site, however, their A site energy variation when combined with the compositional variation in $A_2B_2O_7$ lattice energy, effectively cancel to yield little A site dependence. The small positive solution energies also indicate that the plutonium solution limit may be low and an associated zirconolite or betafite like phase may form. Ideally a phase equilibria investigation is now required to further the study of actinide accommodation.

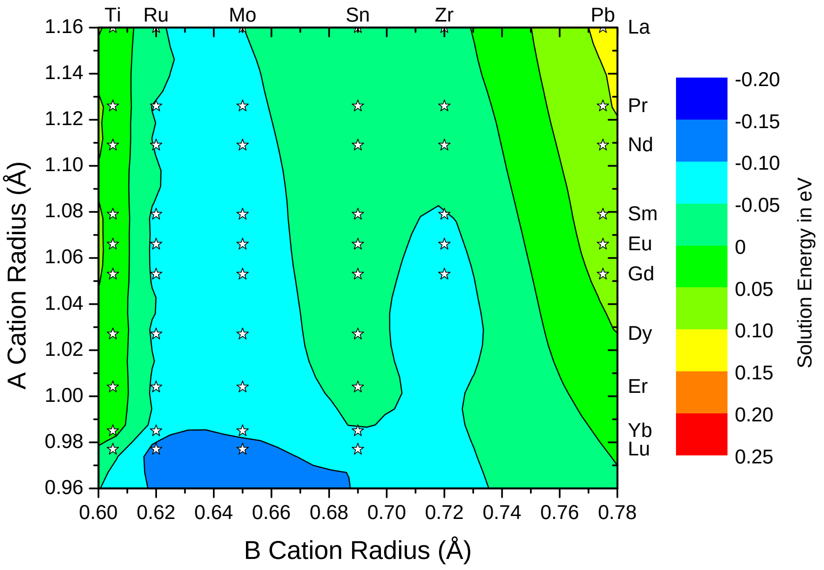

Figure 5.11: co-solution energies for PuO_2 and $CaBO_3$ into pyrochlores via mechanism 5.18.

If figures 5.11 and 5.9 are compared (noting the scale differences), it is at once apparent that equation 5.18 provides a much lower solution energy for compositions with smaller A cations (below Nd) but not for larger A cations (above Nd). Equivalent results are seen for U^{4+} by comparing figures 5.10 and 5.12. Indeed solutions of Pu^{4+} and U^{4+} via equation 5.18 have generally similar energies. An exception to this is in the titanate pyrochlores (comparing figures 5.11 and 5.12) where it seems U^{4+} solution is rather less favourable than Pu^{4+}. This may have a bearing on the observations of [30] who observed Pu^{4+} in calcium titanate pyrochlores and U^{5+} rather than U^{4+}.

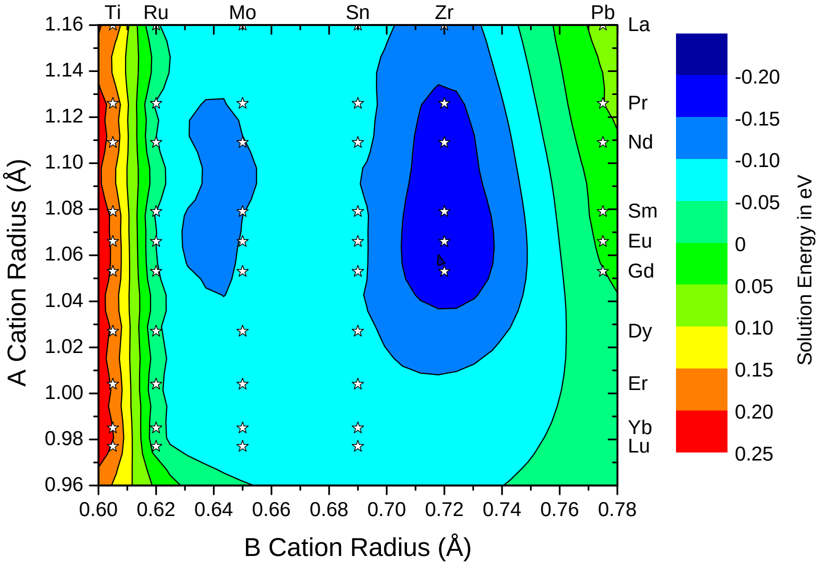

Figure 5.12: Co-solution energies of UO_2 and $CaBO_3$ into pyrochlores via mechanism 5.18.

5.5 Summary

The aim of this study is to provide predictions for how solution mechanisms and energies of trivalent Pu^{3+} and U^{3+} and tetravalent Pu^{4+} and U^{4+} might vary as a function of composition in pyrochlore oxides. Solution of simple sesquioxides and dioxides has been considered and extended to consider co-solution mechanisms, although all types are likely to be of interest given the complexity of processes that occur during fabrication of nuclear materials and in their subsequent aging. Waste form solution chemistry is indeed rich and varied. Consequently, it is not intended to imply that even a majority of the possible processes that might occur in these systems have been investigated. However, it is hoped that the results might provide a direction or framework on which further studies can be based. For example, since computational resources continue to grow apace, it will become typical to extract free energies of solution from such atomistically based complex reactions [270]. Furthermore it will be possible to routinely calculate these energies using quantum mechanical techniques. For more simple systems and single compositions this is already the case [224]. In the meantime discussions can be based on relative energies calculated more approximately, as here.

In the results section variations across compositions were discussed in detail. For example, the simulations are consistent with the solution of Pu^{3+} from Pu_2O_3 proceeding via a single mechanism independent of composition (see figure 5.1) while the solution mechanism for Pu^{4+} varies greatly as a function of composition (see figure 5.7). A comparison between ions can also be made so that the relative solution of plutonium charge states can be considered, as can Pu^{4+} versus U^{4+}. From analysis of the latter pair, we find that, for a given host lattice, UO_2 is somewhat less soluble than PuO_2 (compare figures 5.7 and 5.8 for simple solution, figures 5.9 and 5.10 for co-solution); this comes about because the ionic radius of U^{4+} is slightly larger than the radius of Pu^{4+} [174]. The result is useful since it gives some credence to the idea that data involving U^{4+} may provide a useful upper bound for the behaviour of Pu^{4+} (although the redox behaviour of U^{4+} is rather different to Pu^{4+}). Similarly by comparing figures 5.1 and 5.7 it can be seen that the solution energy for Pu^{3+} is always less than Pu^{4+}. This implies that it is possible to accommodate more Pu^{3+} ions than Pu^{4+} into the same amount of host matrix. If Pu^{3+} is incorporated and the conditions in the repository change so that these ions are oxidised into their 4+ state then this would cause problems as the matrix will become supersaturated with Pu^{4+} and segregation would begin to occur. The most likely destination for the excess Pu^{4+} ions would be the grain boundaries and surfaces of the material, which would increase the rate of leaching of plutonium from the material. Finally, it was shown that these simulations are consistent with co-solution providing energetically favourable solution mechanisms (although more work is required with respect to the Ca^{2+} mediated reaction to include the more complex zirconolite phases and calculations of U^{5+} explicitly).

Chapter 6

The Effect of Aluminium Impurities on Collision Cascades in MgO

Much of this work has previously been published in Nuclear Instruments and Methods in Physics Research Section B: Beam Interactions with Materials and Atoms [4]

6.1 Introduction

Whilst recent molecular dynamics studies on metals have examined the interaction of cascade events in alloys (i.e. disordered combinations of metals) and near defects like grain boundaries [271–273], no previous work on ceramic systems has taken account of deviations from perfect systems free from any kind of defect (examples of work on pure systems include [264,265,274–276]). The idea that a conventional ceramic such as MgO is free from defects is, of course, a fallacy. The influence of even a small concentration of impurities on the evolution of a damage cascade has, however, never been considered. This is, perhaps, understandable since a realistic level of impurity is tenths of a percent. In this study, 0.2% of the Mg^{2+} cations will be replaced with Al^{3+} ions (i.e. substitutionally). This will cause a charge imbalance which needs to be compensated. Previous work has shown that by far the lowest energy charge compensation mechanism is facilitated by Mg^{2+} vacancies [277]. Thus 0.1% of the original Mg^{2+} ions are removed to leave vacant lattice sites. Overall this is equivalent to doping MgO with Al_2O_3 as in equation 6.1.

$$\mathrm{Al_2O_3} + 3\mathrm{Mg}_{Mg}^{\times} + 3\mathrm{O}_{O}^{\times} \rightarrow 2\mathrm{Al}_{Mg}^{\bullet} + \mathrm{V}_{Mg}^{\prime\prime} + 3\mathrm{MgO} \qquad (6.1)$$

Although 0.2% Al^{3+} ions and 0.1% cation vacancies is a small concentration of defects, there are strong Coulomb interactions between the species. Consequently neutral defect clusters will form of the type $\left\{Al_{Mg}^{\bullet} : V_{Mg}^{\prime\prime} : Al_{Mg}^{\bullet}\right\}^{\times}$. The structure of such defect clusters has been investigated previously and shown to be linear such that the three defects are aligned along <100> [277]. The change in lattice parameter with defect concentration predicted from such a defect cluster model has been shown to afford good agreement with experimental observations. Thus, the simulation cell will consist of an otherwise perfect MgO lattice with these defect clusters randomly distributed in order to reach this concentration of impurities. An example of the cell used is given later on in the methodology section (Section 6.3).

The aim of this study is to analyse the effect of impurities in ceramics on cascade events specifically for the ceramic MgO. This was chosen for the same reason as in the electron irradiation study by Kinoshita *et al.* [278], that is it is a simple model material that can give insights into general effects without the complexities that other multicomponent cation solids might present.

Here, PKAs of 1 keV and 2 keV will be modelled using atomic scale molecular dynamics simulation (MD). A set of twenty distinct directions have been selected and both Mg^{2+} and O^{2-} PKAs will be modelled in each case. The crucial difference between this study and previous research is that here both atomically pure and aluminium doped systems are considered. Thus a total of 40 simulations are carried out within a pure MgO lattice and a further 40 simulations for a doped MgO lattice (for the same set of directions, which start from different points within the simulation cell).

6.2 Literature Review

6.2.1 Background

Kinchin and Pease (K-P) first reported a model to describe the accumulation of radiation induced damage exactly fifty years ago [279]. Since this time a number of approximations and limitations of the model have been discussed and improvements suggested (see for example [280–284]). Nevertheless, K-P (albeit modified) is still widely used as a basis for the discussion of results generated experimentally and via computer modelling. Indeed K-P was recently used to discuss atomic scale computer simulation results of cascade damage in MgO [285]. Fifty years ago computer simulation did not even exist!

The K-P model provides an estimation of the number of atoms permanently displaced from their lattice sites (N_d) per primary knock-on atom (PKA) by means of the relations shown in Table 6.1, where E is the energy of the PKA and E_d is the threshold energy.

N_d	Energy (E) of PKA
0	$0 < E < E_d$
1	$E_d < E < 2E_d$
$\frac{E}{2E_d}$	$2E_d < E < E_1$
$\frac{E_1}{2E_d}$	$E_1 < E < ?$

Table 6.1: The Kinchin - Pease (K-P) model criteria [279–282]

Inherent in the model is the assumption that recoil atoms lose energy in excess of E_1 only through electron excitation. Below E_1 the recoil atoms lose energy only through hard-core elastic scattering. Furthermore, if an atom receives energy greater than E_d, it is permanently displaced and if an atom receives energy less than E_d, it will return to its lattice site. This applies to any atom in the lattice being displaced as a consequence of a PKA incident from any direction. Consequently since K-P does not account for recombination, it predicts a maximum number of displaced atoms which will become important when it comes to the analysis of the results.

Amongst the most prominent deficiencies of this most simple interpretation of K-P is therefore the lack of crystal species differentiation. In a ceramic material such as MgO, there are two differently charged species of usually quite different sizes. It seems unlikely that they will exhibit the same displacement energies (and, in fact, in MgO they do not [285]). This could be corrected simply by having two values of E_d, one for the cation and one for the anion [284]. However, this does not correct for the crystallographic anisotropy associated with the PKA incident direction. Numerous modelling studies have shown that, for a range of materials, E_d (or N_d) can vary considerably with incident direction (see for example [119, 285–287]). A single value of E_d within K-P therefore represents some sort of average over both species and crystallographic direction. All of these studies were performed on atomistically pure systems and it seems likely that a random distribution of aliovalent defects would tend to disrupt this and make the system behave more isotropically.

6.2.2 MgO

MgO is an engineering ceramic with a huge range of uses from buffer layers to produce highly textured superconducting films exploiting the lattice parameter [288] to electrical insulation in heating elements which require moderate thermal conductivities and a high electrical resistivity [289]. Due to this huge range of uses it is one of the most well understood materials and this, combined with the fact that it has also been successfully modelled using pair potentials [277, 286, 290–293] makes it logical for this simple material to be used in this first study of the effect impurities have on collision cascades.

Crystallography

MgO is one of the most simple oxides and forms in the rock-salt crystal structure with a lattice parameter of 4.214 Å [294]. It consists of close packed oxygen ions with all of the octahedral interstitial positions occupied by magnesium ions. This is show in figure 6.1.

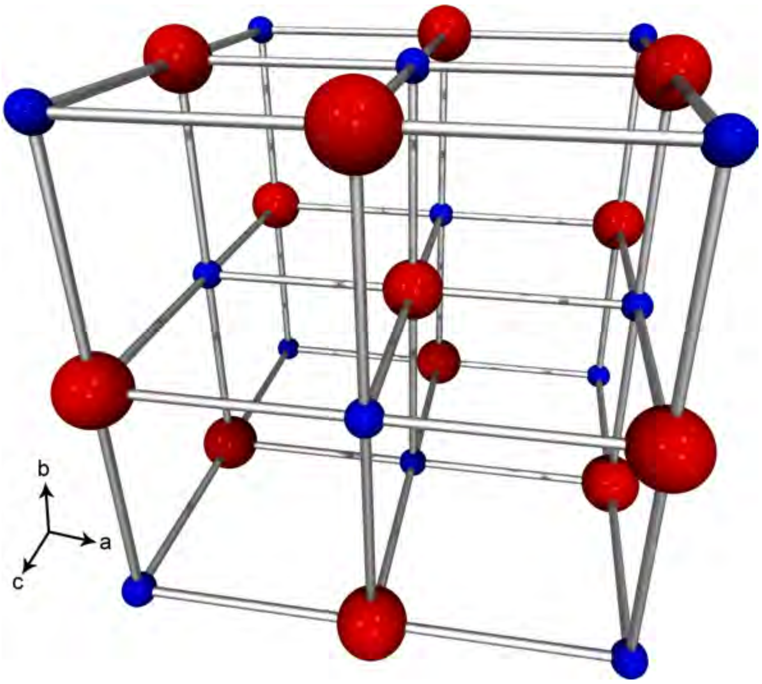

Figure 6.1: A full unit cell of MgO (generated using structural data from [294]). Smaller blue spheres are Mg^{2+} ions and larger red spheres represent O^{2-} ions.

6.2.3 Previous Studies in MgO

Kinoshita *et al.* [278] examined the kinetics of point defects formed by the electron irradiation of MgO in the mid 1980s. They irradiated single crystals of MgO from different sources with 1 MeV electrons at a range of temperatures between 25 °C and 1000 °C [278]. They found that at low temperatures of about 330 °C, interstitial dislocation loops tend to nucleate but that as the irradiation temperature is increased, the density of these loops tends to decrease and they take on an obvious loop shape see figures 6.2 and 6.3 (these are figures 2 and 4 from Kinoshita *et al.* [278]) which show the low and high temperature irradiations respectively. By considering the kinetics of the system [278] (which is beyond the scope of this study) they concluded that interstitial loops nucleate from one or two pairs of Mg and O interstitials below 600 °C and that growth of these loops occurs above 600 °C.

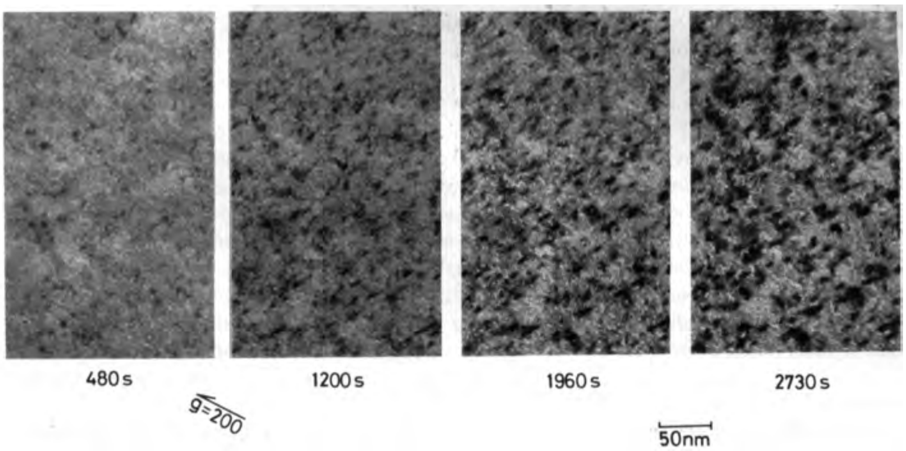

Figure 6.2: Formation and growth of interstitial dislocation loops in MgO irradiated aproximately along <001> at 600 K with a 1 MeV electron flux of 2 × 10^{23} e/m^2 (reproduced from [278]).

Alves *et al.* recently carried out some work into the recovery from radiation damage in MgO for both pure samples and samples doped with 400 ppm Li doped MgO [295]. In this work, they irradiated single crystals of pure and Li doped MgO with 175 keV Li$^+$ ions to a dose of 1 × 10^{17} ions/cm^2 and analysed the damage and recovery at various temperatures using Rutherford Backscattering/Channelling Spectroscopy(RBS) and optical absorption spec-

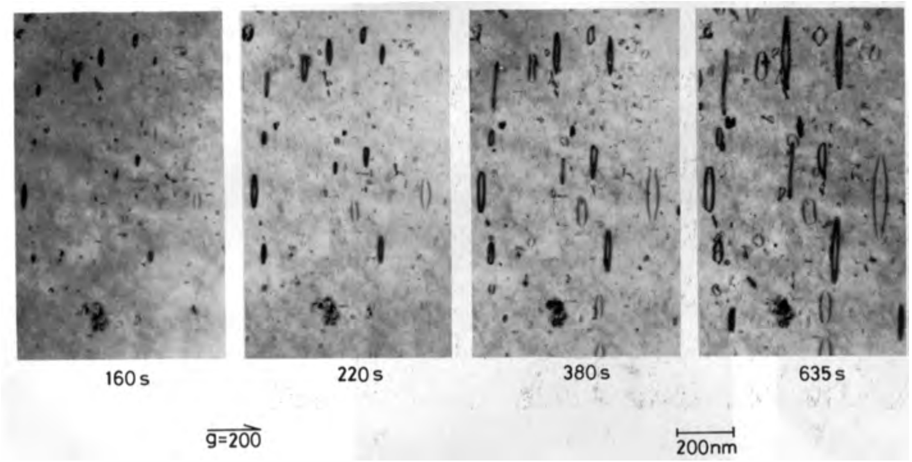

Figure 6.3: Formation and growth of interstitial dislocation loops in MgO irradiated aproximately along <001> at 1085 K with a 1 MeV electron flux of 4×10^{23} e/m^2. The loops are perfect dislocation loops with $\frac{1}{2}$<101> Burgers vectors lying on (101) planes elongated along <010> directions (reproduced from [278]).

troscopy. They found that for both pure and doped samples, implantation of Li^+ ions causes significant damage as shown by the enhanced dechannelling in the RBS measurements [295]. Alves *et al.* found that for the Li doped sample, after annealing at 1250 K the damage responsible for the dechannelling had virtually completely disappeared. The pure case was more complicated due to polishing damage on the surface causing dechannelling to a depth of 200nm [295]. They noted implantation damage below this depth due to the implantation of Li. Upon annealing at temperatures of 1025K they found the dechannelling yield in the deeper region fell off from an initial 70% to 48% [295]. They do not report a similar state for the doped sample or a result for annealing at 1250 K for the pure sample, making comparison difficult. They do, however, report an intermediate annealing temperature of 875 K for the pure sample where the normalised dechannelling yield is 56%. This may be indicative that doping with Li increases the ability for the material to recover from radiation damage.

Considering next the optical absorption results. Before implantation, the Li doped sample showed a strong absorption band at 1.8 eV which Alves *et al.* associated with the $[\mathrm{Li}]^0$ centres. After implantation this was joined by another strong absorption peak at 5.0 eV which they associated with F^+ centres (an electron trapped at an anion vacancy) [295]. Upon annealing the damage causing the 5.0 eV peak was eliminated and this also causes the intensity of the 1.8 eV band ($[\mathrm{Li}]^0$ to decrease [295]. Alves *et al.* [295] found that recovery of defects in the damaged pure sample starts at about 500 K and recovery was complete at 1250 K.

Gonzáles *et al.* [296] also looked at Li doped MgO but they examined its properties under neutron irradiation at energies greater than 100 KeV. Again single crystals of MgO were used and pure and doped samples were irradiated. Two dopants were considered. The first set, as in the previous study, was doped with 400 ppm Li ions and the other set was doped with an undocumented concentration of hydrogen [296]. All three groups were irradiated at temperatures of 325 ± 20 K. Analysis of the damage was performed using optical absorption spectroscopy. Gonzáles *et al.* found (as Alves *et al.* confirm [295]) that irradiation of MgO produces F^+ centres in the MgO causing a large absorption band at 5.0 eV. In [296] they show a log-log plot of neutron dose against the absorption coefficient of the 5 eV band (and link this directly to the concentration of F^+ centres) and they find that below 1×10^{18} neutrons per cm^2 (above which all samples are virtually identical) the pure case shows the highest concentration, followed by the hydrogen doped case and finally the least damaged sample is the Li doped MgO [296]. They compare this result with previous work by Sibley and Chen [297] which appears to show conflicting results. Sibley and Chen [297] noted that a sample containing 50 ppm Fe ions showed the opposite effect, i.e. it damaged faster than the pure case and they attributed this to the trapping of displaced interstitials by impurities thus preventing them from recombining with vacancies [297].

By doping with hydrogen Gonzáles *et al.* created a very cloudy crystal containing high concentrations of cavities about 0.6 μm in size containing hydrogen gas [296]. They found that after irradiation to 1×10^{17} neutrons/cm^2 the size of the 5.0 eV peak associated with anion vacancies and F^+ centres is obviously smaller corresponding to a 35% lower vacancy concentration [296]. They attribute this decrease in anion vacancy concentration to the migration of these vacancies to the hydrogen filled cavities, an effect proposed by originally Henderson *et al.* [298]. After the same neutron dose, the Li doped sample showed an even lower anion vacancy concentration than the hydrogen doped sample with 70% fewer than the pure case although as mentioned earlier, this suppression of vacancy formation disappears at higher doses of 1×10^{18} n/cm^2. Gonzáles *et al.* propose that the reason for the reduced vacancy concentration is partly due to the presence of hydrogen filled microcavities that have been previously observed in Li doped MgO [296] although they state that this can only account for a small amount of the total. They go on to state that the main reason for the apparent loss of oxygen vacancies is due to the capture of hydride ions, thus causing them to be camouflaged as $[H^-]^+$ centres (an oxygen vacancy occupied by a proton).

The conflicting results obviously require further work to clarify exactly what occurs.

These studies on nominally pure and intentionally doped samples show that even in a very simple ceramic system very complex damage and recovery processes occur. The use of atomistic simulation can help in the understanding of such complicated systems by eliminating some of the unknowns. While it is not possible (or at least very difficult) to examine a single cascade in a real material, it is possible to carry out many simulations and construct an average cascade. Efforts should be made to examine carefully the behaviour of defects indicated in the experimental work. Unfortunately it is very difficult to model F^+ centres with MD simulations as these are electronic defects. As such a full electronic structure model may be required to simulate them correctly. Others, such as the hydrogen ion trapped on an anion vacancy are much easier to simulate and if MD simulations are performed it should be simple to test whether this defect forms. Other simulations could be performed to measure activation energies for the diffusion of anion vacancies to surfaces although, this seems somewhat unlikely as it has been shown that interstitial migration barriers are much lower than those for vacancies in MgO [299].

6.3 Methodology

The potentials that describe the interactions between ions were derived previously to model cascades in $MgAl_2O_4$ spinel [119]. They assume full ionic charges on all ions with the Coulomb interactions calculated using the fast multipole method implemented by Rankin [120]. Additional pairwise additive short-range interactions of the Buckingham form also operate between ions [119] and these parameters are listed in table 6.2. A smooth cutoff is applied to these terms at distances greater than 7.4 Å for anion - anion interactions and 5.0 Å for cation - anion interactions. At the very short interionic distances experienced by particles in the initial phase of the cascade, the potential was replaced by a screened Coulomb interaction [300]. This was smoothly splined to the outer potential by ensuring that the first and second derivatives were continuous.

Table 6.2: Full charge short range potential parameters used to describe interactions between all the ions in this study. Reproduced from [4].

Species	A (eV)	ρ (eV)	C (eV Å^6)
$O^{2-}\leftrightarrow O^{2-}$	9547.960	0.21916	32.00
$Mg^{2+}\leftrightarrow O^{2-}$	1279.69	0.29969	0.00
$Al^{3+}\leftrightarrow O^{2-}$	1374.79	0.30130	0.00

The molecular dynamics simulations were carried out in charge neutral simulation cells that contained either 48669 Mg^{2+} cations, and 48669 O^{2-} anions in the pure lattice cases or 48522 Mg^{2+}, 98 Al^{3+} cations and 48669 O^{2-} anions for the doped lattice simulations. The velocity Verlet algorithm was used to evolve the system as implemented in the code LBOMD [125] and described in chapter 3. The cell was simulated using non-periodic boundary conditions with the outer 2 layers of atoms fixed. An image showing the distribution of the defects in the cell is shown in figure 6.4.

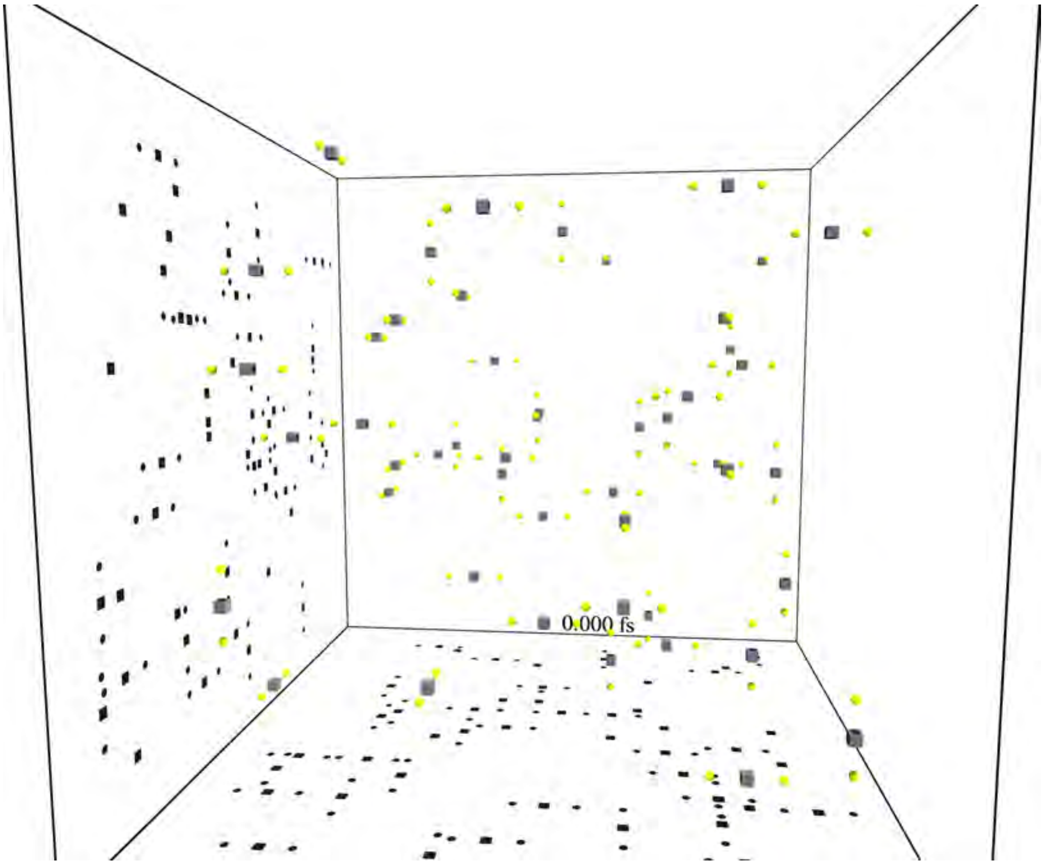

Figure 6.4: Starting configuration for all cascades doped with 0.2% Al. Grey cubes represent V''_{Mg} and yellow spheres represent $Mg^{\bullet}_{Al}$. Shadows are projected onto both the left and bottom faces in order to aid three dimensional visualisation.

6.4 Results and Discussion

Before the results of the radiation damage cascade simulations are discussed the simulated properties of MgO will be compared with experimental (e) and *ab inito* simulation values (s). These results are shown in table 6.3. As can be seen the potentials reproduce the structure very well with the lattice parameter within 0.36% of experimental values.

Table 6.3: Comparison of the predicted lattice parameter with experimental and *ab initio* simulation data

Source	Lattice Parameter (Å)	% Difference
Predicted	4.199	N\A
Tsirel'son *et al.* [294] (e)	4.214	0.36
McCarthy and Harrison [301] (s)	4.195	-0.10
Taylor [302] (e)	4.211	0.29
Hirata *et al.* [303] (e)	4.203	0.10

6.4.1 Variation with Direction and Doping

In order to quantify the effect that a displacement cascade has on the lattice it is necessary to select a number of criteria by which the damage process can be assessed. This can include, for example, properties such as the peak number of Frenkel pairs (P_F) and the time at which this occurred (P_t). These are measures of the damage progression and occur towards the end of the ballistic stage of the cascade (≈0.1 ps). Other properties include the total number (N_d) and types of residual defects left once the thermal-spike has dissipated (≈6 ps). At this point the ions in the damaged region are close to being in thermal equilibrium with the remainder of the lattice. There can, however, be considerable energy retained by those residual defects. Related to this is the final number of atoms (N_T) displaced from their original lattice sites (even if they return to equivalent lattice sites) since it provides an alternative measure of how much the lattice has been disrupted and is the equivalent of N_d in K-P. Finally, the maximum distance between residual defects is reported. This is a particularly simple way to estimate the effective size of the cascade (more sophisticated measures based on volume are under development).

Results for these six criteria are presented in Table 6.4a and 6.4b for 1 keV PKA cascades and in Table 6.5a and 6.5b for 2 keV PKA cascades. For each table the first set of columns report results for the undoped (pure) lattice, the middle set of columns are for the alumina doped lattice and the third set show differences between doped and pure results. Beneath each column is the property value average over all directions. Under the average is the standard deviation (SD) in the property value.

The first point to recognise is that the property values for the undoped cases show considerable variation with PKA incident direction, in agreement with previous observations [119, 285–287]. Nevertheless, all the average property values are large compared to their SDs. In general terms, for the alumina doped lattice simulations, the situation is very similar: considerable variation in property values between directions is observed. Furthermore, the average values generated in the doped lattice are not so different to those for the undoped lattice (within a SD). However, for a specific direction, and for a specific PKA type and energy, the results for the undoped and doped lattice simulations are often considerably different (simply follow across rows in Tables 6.4 and 6.5). This is made clear by the variation of values in the third set of difference columns. The average differences for a given property are also calculated. These average difference values are always smaller than the corresponding standard deviations and in some cases dramatically so. Conversely and crucially the average difference values are small compared to the absolute property values.

The dopant level investigated here, 0.2% Mg^{2+} replaced by Al^{3+}, is clearly a)

	Pure									Doped									Difference								
Direction	Peak No Frenkel Pairs (P_F)	Peak Time (fs) (P_T)	Displaced Atoms (N_T)	Total Defects (N_d)	Total Mg_i	Total O_i	Total V_{Mg}	Total V_O	Max dist between defects (Å)	Peak No Frenkel Pairs (P_F)	Peak Time (P_T) (fs)	Displaced Atoms (N_T)	Total Defects (N_D)	Total Mg_i	Total O_i	Total V_{Mg}	Total V_O	Max dist between defects (Å)	Peak No Frenkel Pairs (P_F)	Peak Time (fs) (P_T)	Displaced Atoms (N_T)	Total Defects (N_d)	Total Mg_i	Total O_i	Total V_{Mg}	Total V_O	Max dist between defects (Å)
021	87	86.7	23	8	2	2	2	2	36.4	124	97.2	23	10	3	2	3	2	13.6	37	10.6	0	2	1	0	1	0	-22.7
100	73	88.1	17	6	2	1	2	1	18.0	114	96.8	22	10	2	2	4	2	21.5	41	8.7	5	4	0	1	2	1	3.5
10 31	72	128.6	22	8	3	1	3	1	33.4	99	109.7	26	8	2	2	2	2	25.9	27	-18.9	4	0	-1	1	-1	1	-7.5
10 52	71	94.7	10	6	2	1	2	1	33.4	86	101.2	33	12	2	4	2	4	53.9	15	6.4	23	6	0	3	0	3	20.5
110	77	85.4	19	6	2	1	2	1	29.4	98	99.2	22	6	2	1	3	1	26.6	21	13.8	3	0	0	0	1	0	-2.8
111	102	97.0	22	6	1	2	1	2	29.2	83	90.1	19	8	3	1	3	1	23.1	-19	-7.0	-3	2	2	-1	2	-1	-6.1
123	84	98.9	13	6	2	1	2	1	27.8	113	89.1	22	2	1	0	1	0	20.6	29	-9.8	9	-4	-1	-1	-1	-1	-7.2
134	101	88.3	24	10	3	2	3	2	22.4	80	93.0	30	9	1	3	2	3	32.8	-21	4.7	6	-1	-2	1	-1	1	10.4
221	101	103.1	23	8	3	1	3	1	32.7	79	91.0	15	4	0	1	2	1	25.6	-22	-12.1	-8	-4	-3	0	-1	0	-7.2
257	85	95.7	24	2	1	0	1	0	26.0	89	99.8	29	4	0	1	2	1	17.8	4	4.2	5	2	-1	1	1	1	-8.2
432	96	108.7	14	2	1	0	1	0	35.8	94	97.7	19	8	2	2	2	2	27.5	-2	-11.1	5	6	1	2	1	2	-8.2
522	81	95.4	18	8	3	1	3	1	26.7	124	84.1	22	7	2	1	3	1	23.4	43	-11.3	4	-1	-1	0	0	0	-3.3
537	86	96.6	15	8	3	1	3	1	33.5	73	104.6	13	2	1	0	1	0	40.6	-13	8.0	-2	-6	-2	-1	-2	-1	7.1
20 74	91	103.6	20	6	2	1	2	1	34.4	100	90.4	21	5	1	1	3	1	16.5	9	-13.2	1	-1	-1	0	1	0	-17.8
441	58	105.2	17	10	4	1	4	1	34.5	105	113.0	10	4	2	0	2	0	28.8	47	7.8	-7	-6	-2	-1	-2	-1	-5.7
443	99	91.1	16	6	1	2	1	2	32.7	127	114.2	21	5	1	1	2	1	16.9	28	23.1	5	-1	0	-1	1	-1	-15.9
510	82	88.2	17	6	2	1	2	1	31.8	81	84.7	25	6	1	2	2	2	25.7	-1	-3.5	8	0	-1	1	0	1	-6.1
511	73	99.7	18	4	1	1	1	1	32.8	110	100.9	17	4	1	1	2	1	29.0	37	1.2	-1	0	0	0	1	0	-3.8
533	96	93.4	25	6	2	1	2	1	21.5	103	102.9	27	9	1	3	2	3	21.4	7	9.4	2	3	-1	2	0	2	-0.1
860	122	98.2	27	8	2	2	2	2	23.2	110	91.4	15	7	2	1	2	1	24.6	-12	-6.9	-12	-1	0	-1	0	-1	1.4
Average	86.85	97.33	19.20	6.50	2.10	1.15	2.10	1.15	29.79	99.60	97.55	21.55	6.50	1.50	1.45	2.25	1.45	25.80	12.75	0.21	2.35	0.00	-0.60	0.30	0.15	0.30	-3.99
SD	14.60	9.81	4.48	2.14	0.85	0.59	0.85	0.59	5.26	16.31	8.58	5.84	2.76	0.83	1.05	0.72	1.05	8.99	22.94	11.10	7.31	3.39	1.19	1.17	1.18	1.17	9.72

b)

	Pure									Doped									Difference								
Direction	Peak No Frenkel Pairs (P_F)	Peak Time (fs) (P_T)	Displaced Atoms (N_T)	Total Defects (N_d)	Total Mg_i	Total O_i	Total V_{Mg}	Total V_O	Max dist between defects (Å)	Peak No Frenkel Pairs (P_F)	Peak Time (fs) (P_T)	Displaced Atoms (N_T)	Total Defects (N_d)	Total Mg_i	Total O_i	Total V_{Mg}	Total V_O	Max dist between defects (Å)	Peak No Frenkel Pairs (P_F)	Peak Time (fs) (P_T)	Displaced Atoms (N_T)	Total Defects (N_d)	Total Mgi	Total Oi	Total VMg	Total VO	Max dist between defects (Å)
021	93	91.9	16	6	0	3	0	3	23.0	92	92.9	15	2	0	1	0	1	21.7	-1	1.0	-1	-4	0	-2	0	-2	-1.3
100	70	83.8	9	6	2	1	2	1	23.6	77	88.7	12	4	0	1	2	1	22.2	7	4.9	3	-2	-2	0	0	0	-1.3
10 31	79	91.4	22	8	2	2	2	2	40.5	75	91.3	10	4	0	2	0	2	33.2	-4	-0.2	-12	-4	-2	0	-2	0	-7.3
10 52	88	86.1	17	4	1	1	1	1	33.6	95	90.1	23	2	0	1	1	1	18.2	7	4.0	6	-2	-1	0	0	0	-15.3
110	82	90.7	18	8	2	2	2	2	27.5	132	105.9	38	7	1	2	2	2	34.0	50	15.2	20	-1	-1	0	0	0	6.5
111	78	93.7	10	4	2	0	2	0	24.1	111	94.1	24	6	2	1	2	1	14.1	33	0.3	14	2	0	1	0	1	-10.0
123	88	80.5	24	4	1	1	1	1	21.0	83	78.6	18	8	2	2	2	2	22.4	-5	-2.0	-6	4	1	1	1	1	1.4
134	46	90.1	6	2	0	1	0	1	37.8	80	95.4	21	10	3	2	3	2	31.7	34	5.2	15	8	3	1	3	1	-6.2
221	93	86.5	17	8	3	1	3	1	23.9	83	90.5	21	5	0	2	1	2	32.2	-10	4.0	4	-3	-3	1	-2	1	8.3
257	84	98.7	13	6	2	1	2	1	23.0	117	88.5	23	7	1	2	2	2	20.4	33	-10.2	10	1	-1	1	0	1	-2.5
432	58	86.4	10	6	2	1	2	1	35.8	110	100.4	28	5	0	2	1	2	13.4	52	14.0	18	-1	-2	1	-1	1	-22.3
522	100	75.5	39	10	3	2	3	2	25.8	103	91.8	28	5	1	1	2	1	20.9	3	16.3	-11	-5	-2	-1	-1	-1	-5.0
537	84	84.2	15	4	1	1	1	1	31.8	75	96.5	18	4	1	1	1	1	27.0	-9	12.3	3	0	0	0	0	0	-4.8
20 74	89	95.6	18	6	2	1	2	1	33.9	71	85.2	11	2	0	1	0	1	30.8	-18	-10.4	-7	-4	-2	0	-2	0	-3.1
441	94	92.4	25	4	1	1	1	1	18.9	75	78.7	18	6	0	2	2	2	28.5	-19	-13.7	-7	2	-1	1	1	1	9.6
443	77	102.5	16	4	0	2	0	2	27.0	139	104.6	29	8	2	2	2	2	20.0	62	2.0	13	4	2	0	2	0	-7.0
510	84	91.7	30	14	5	2	5	2	26.3	107	94.1	31	11	0	5	1	5	24.7	23	2.5	1	-3	-5	3	-4	3	-1.6
511	107	84.0	24	6	2	1	2	1	27.7	104	85.1	24	4	0	1	2	1	27.4	-3	1.1	0	-2	-2	0	0	0	-0.2
533	104	90.1	10	4	0	2	0	2	26.4	83	93.5	22	6	0	2	2	2	28.9	-21	3.4	12	2	0	0	2	0	2.6
860	96	83.5	7	4	1	1	1	1	34.4	69	91.2	27	7	1	2	2	2	27.3	-27	7.7	20	3	0	1	1	1	-7.1
Average	84.70	88.97	17.30	5.90	1.60	1.35	1.60	1.35	28.28	94.05	91.84	22.05	5.65	0.70	1.75	1.50	1.75	24.95	9.35	2.87	4.75	-0.42	-0.95	0.37	-0.16	0.37	-3.33
SD	14.63	6.33	8.25	2.71	1.23	0.67	1.23	0.67	5.98	20.50	7.05	7.10	2.48	0.92	0.91	0.83	0.91	6.10	26.51	8.10	10.20	3.42	1.81	1.01	1.64	1.01	7.55

Table 6.4: Properties of 1 keV Cascades for a) Mg^{2+} and b) O^{2-} primary knock-ons.

a)

	Pure									Doped									Difference								
Direction	Peak No Frenkel Pairs (P_F)	Peak Time (fs) (P_T)	Displaced Atoms (N_T)	Total Defects (N_d)	Total Mg_i	Total O_i	Total V_{Mg}	Total V_O	Max dist between defects (Å)	Peak No Frenkel Pairs (P_F)	Peak Time (P_T) (fs)	Displaced Atoms (N_T)	Total Defects (N_D)	Total Mg_i	Total O_i	Total V_{Mg}	Total V_O	Max dist between defects (Å)	Peak No Frenkel Pairs (P_F)	Peak Time (fs) (P_T)	Displaced Atoms (N_T)	Total Defects (N_d)	Total Mg_i	Total O_i	Total V_{Mg}	Total V_O	Max dist between defects (Å)
021	175	109.6	46	12	3	3	3	3	50.5	179	90.5	42	12	3	3	3	3	46.5	4	-19.2	-4	0	0	0	0	0	-4.1
100	160	102.1	38	12	3	3	3	3	43.6	176	95.2	41	10	2	2	4	2	46.9	16	-6.9	3	-2	-1	-1	1	-1	3.3
10 31	158	100.5	38	14	5	2	5	2	47.3	118	102.3	67	13	3	3	4	3	62.1	-40	1.9	29	-1	-2	1	-1	1	14.8
10 52	188	103.7	49	12	3	3	3	3	35.2	161	92.0	39	11	1	3	4	3	39.6	-27	-11.7	-10	-1	-2	0	1	0	4.4
110	206	111.0	49	6	2	1	2	1	24.5	163	87.2	56	18	3	5	5	5	37.7	-43	-23.8	7	12	1	4	3	4	13.2
111	184	122.1	44	14	4	3	4	3	57.5	248	107.7	60	12	3	2	5	2	26.9	64	-14.4	16	-2	-1	-1	1	-1	-30.6
123	173	96.8	32	12	3	3	3	3	39.0	184	92.3	41	11	2	2	5	2	35.6	11	-4.6	9	-1	-1	-1	2	-1	-3.5
134	151	102.0	34	8	4	0	4	0	45.8	317	143.3	84	13	2	4	3	4	27.5	166	41.3	50	5	-2	4	-1	4	-18.3
221	144	103.1	25	10	3	2	3	2	43.6	149	114.7	62	8	2	2	2	2	58.4	5	11.6	37	-2	-1	0	-1	0	14.7
257	156	83.5	39	8	3	1	3	1	42.1	196	108.9	45	5	1	1	2	1	44.9	40	25.4	6	-3	-2	0	-1	0	2.7
432	155	116.4	54	16	4	4	4	4	59.7	166	120.1	47	11	3	2	4	2	57.8	11	3.7	-7	-5	-1	-2	0	-2	-1.9
522	158	87.8	32	8	3	1	3	1	38.2	202	114.2	38	7	1	1	4	1	39.6	44	26.5	6	-1	-2	0	1	0	1.4
537	143	99.2	39	12	4	2	4	2	41.3	197	101.3	45	12	3	2	5	2	43.7	54	2.0	6	0	-1	0	1	0	2.4
20 74	91	103.6	20	6	2	1	2	1	34.4	100	90.4	21	6	1	1	3	1	25.9	9	-13.2	1	0	-1	0	1	0	-8.5
441	58	105.2	17	10	4	1	4	1	34.5	149	113.7	42	8	2	1	4	1	62.6	91	8.5	25	-2	-2	0	0	0	28.1
443	99	91.1	16	6	1	2	1	2	32.7	127	114.2	21	5	1	1	2	1	16.9	28	23.1	5	-1	0	-1	1	-1	-15.9
510	82	88.2	17	6	2	1	2	1	31.8	81	85.5	25	7	1	2	2	2	25.7	-1	-2.6	8	1	-1	1	0	1	-6.1
511	73	99.7	18	4	1	1	1	1	32.8	110	100.9	17	5	1	1	2	1	29.0	37	1.2	-1	1	0	0	1	0	-3.8
533	96	93.4	25	6	2	1	2	1	21.5	103	102.9	27	9	1	3	2	3	21.4	7	9.4	2	3	-1	2	0	2	-0.1
860	122	98.2	26	10	3	2	3	2	23.3	110	91.4	15	8	2	2	2	2	24.7	-12	-6.9	-11	-2	-1	0	-1	0	1.4
Average	138.60	100.86	32.90	9.60	2.95	1.85	2.95	1.85	38.97	161.80	103.43	41.75	9.55	1.90	2.15	3.35	2.15	38.67	23.20	2.57	8.85	-0.05	-1.05	0.30	0.40	0.30	-0.30
SD	41.97	9.53	12.01	3.35	1.05	1.04	1.05	1.04	10.33	55.81	14.11	17.96	3.36	0.85	1.09	1.18	1.09	14.02	47.44	16.77	15.65	3.55	0.83	1.53	1.10	1.53	12.82

b)

	Pure									Doped									Difference								
Direction	Peak No Frenkel Pairs (P_F)	Peak Time (fs) (P_T)	Displaced Atoms (N_T)	Total Defects (N_d)	Total Mg_i	Total O_i	Total V_{Mg}	Total V_O	Max dist between defects (Å)	Peak No Frenkel Pairs (P_F)	Peak Time (fs) (P_T)	Displaced Atoms (N_T)	Total Defects (N_d)	Total Mg_i	Total O_i	Total V_{Mg}	Total V_O	Max dist between defects (Å)	Peak No Frenkel Pairs (P_F)	Peak Time (fs) (P_T)	Displaced Atoms (N_T)	Total Defects (N_d)	Total Mgi	Total Oi	Total VMg	Total VO	Max dist between defects (Å)
021	200	105.3	40	10	3	2	3	2	33.0	175	101.2	33	9	1	2	4	2	46.8	-25	-4.2	-7	-1	-2	0	1	0	13.8
100	181	97.4	30	8	2	2	2	2	36.9	170	89.6	44	15	3	3	6	3	37.7	-11	-7.8	14	7	1	1	4	1	0.8
10 31	159	116.7	49	12	3	3	3	3	39.7	122	97.2	33	15	3	3	6	3	65.0	-37	-19.5	-16	3	0	0	3	0	25.3
10 52	170	92.5	42	10	3	2	3	2	49.0	157	98.7	33	9	1	2	4	2	56.5	-13	6.2	-9	-1	-2	0	1	0	7.5
110	182	97.3	47	10	4	1	4	1	40.7	139	112.4	26	12	4	1	6	1	60.2	-43	15.1	-21	2	0	0	2	0	19.6
111	169	85.1	46	8	2	2	2	2	53.2	139	115.6	37	7	0	2	3	2	50.1	-30	30.5	-9	-1	-2	0	1	0	-3.2
123	188	97.7	46	12	2	4	2	4	37.0	187	117.3	48	10	2	3	2	3	48.1	-1	19.5	2	-2	0	-1	0	-1	11.1
134	167	91.2	27	6	1	2	1	2	35.3	125	102.3	21	8	3	1	3	1	57.2	-42	11.1	-6	2	2	-1	2	-1	21.9
221	224	105.4	35	8	1	3	1	3	53.0	168	115.5	51	13	2	3	5	3	63.7	-56	10.1	16	5	1	0	4	0	10.6
257	135	95.7	35	10	2	3	2	3	58.6	156	102.4	38	11	3	1	6	1	60.0	21	6.6	3	1	1	-2	4	-2	1.4
432	143	105.5	22	8	2	2	2	2	60.3	167	103.3	71	19	4	5	5	5	46.6	24	-2.2	49	11	2	3	3	3	-13.7
522	127	107.6	25	8	2	2	2	2	60.3	172	94.0	45	13	1	4	4	4	57.2	45	-13.6	20	5	-1	2	2	2	-3.1
537	126	110.2	29	6	1	2	1	2	56.2	155	100.0	42	13	3	3	4	3	53.2	29	-10.2	13	7	2	1	3	1	-3.0
20 74	89	95.6	18	6	1	2	1	2	33.9	71	85.2	11	2	0	1	0	1	30.8	-18	-10.4	-7	-4	-1	-1	-1	-1	-3.1
441	94	92.4	25	4	1	1	1	1	18.9	75	78.7	18	6	0	2	2	2	28.5	-19	-13.7	-7	2	-1	1	1	1	9.6
443	77	102.5	18	6	1	2	1	2	28.0	139	104.6	29	7	1	2	2	2	20.0	62	2.0	11	1	0	0	1	0	-8.0
510	84	91.7	30	14	5	2	5	2	26.3	107	94.1	30	11	0	5	1	5	24.7	23	2.5	0	-3	-5	3	-4	3	-1.6
511	107	84.0	24	6	2	1	2	1	27.7	211	110.8	33	4	0	2	0	2	37.2	104	26.7	9	-2	-2	1	-2	1	9.5
533	104	90.1	10	4	0	2	0	2	26.4	160	104.4	39	11	3	2	4	2	48.6	56	14.3	29	7	3	0	4	0	22.2
860	96	83.5	7	4	1	1	1	1	34.4	140	107.8	15	9	1	3	2	3	53.6	44	24.4	8	5	0	2	1	2	19.2
Average	141.10	97.38	30.25	8.00	1.95	2.05	1.95	2.05	40.44	146.75	101.75	34.85	10.20	1.75	2.50	3.45	2.50	47.28	5.65	4.37	4.60	2.05	-0.21	0.37	1.53	0.37	6.85
SD	43.38	9.07	12.21	2.83	1.19	0.76	1.19	0.76	12.83	34.64	10.20	13.76	4.01	1.41	1.19	1.93	1.19	13.28	42.38	14.58	16.48	4.06	1.93	1.30	2.17	1.30	11.22

Table 6.5: Properties of 2 keV Cascades for a) Mg^{2+} and b) O^{2-} primary knock-ons.

small. It is therefore not surprising that the average difference values are small compared to average property values. In other words, the overall effect on the lattice is not very great. However, this hides the significant effect that dopants have on properties predicted for a specific cascade generated by a PKA in a specific direction. In specific cases, the influence can be enormous, (though not always so). This is because, at this level of dopant (randomly distributed through the lattice), some cascades encounter more defects than others. Unfortunately, it has only been been possible to carry out one cascade simulation per direction for each PKA and energy combination. Presumably with higher PKA energies (and thus larger cascades), the number of defects encountered by cascades originating from different PKA directions is more similar.

What the study has shown is that the effect on N_d (and perhaps E_d) due to PKA orientation, predicted from perfect lattice simulations, is not a true reflection of reality. It is suggested here that the orientation anisotropy of N_d (and E_d) for a real material (i.e. one that incorporates a population of defects) should be rather less than for a hypothetical perfect lattice. This is because the change in property values due to having dopants in the lattice is small and while the individual differences can be large, they are not systematic. As such it should be expected that a different random distribution of defects should have a different effect on individual cascades. Exactly what the real orientation dependence for the present doped MgO lattice might be is yet to be derived since it requires sufficient results for each PKA to average over calculations repeated with different random dopant distributions.

Above, a rather general effect has been discussed, which conceivably might be caused by any suitable type of (scattering) defect population. A specific effect due to the charge compensating magnesium vacancies (V_{Mg}'') is now considered. To this end, it is necessary to compare the average values for N_d between a pure and doped lattice for a specific PKA species and energy. The values are fairly similar. However, the contributions to the average N_d values due to magnesium interstitial ions (Mg_i) are systematically smaller in the doped lattice than in the corresponding pure material. This is because ions generated during the cascade are being annihilated by pre-existing lattice V_{Mg}'' defects (and thus do not count as defects). Examples are shown in figure 6.5. Consequently, the number of $Mg_i^{\bullet\bullet}$ ions is less than V_{Mg}'' in the doped lattice (but these populations are, of course, equal in the pure material). (In an equilibrium situation this would be interpreted as a manifestation of the cation Frenkel equilibrium. Perhaps the initial stages of such a process are being seen here). Interestingly this reduction in $Mg_i^{\bullet\bullet}$ defects is being balanced by an increase in both O_i'' and $V_O^{\bullet\bullet}$ defects (this is how N_d remains constant).

There are a number of other systematic changes that deserve comment. For all four combinations of PKA and energy, it is predicted that, in the doped lattice, there is a greater peak number of Frenkel pairs (P_F) and longer peak time (P_t). This subsequently translates into a greater number of displaced atoms (N_T). Conversely the nominal "size" of the cluster (maximum distance between defects) does not increase systematically. Caution should be taken when drawing conclusions from these data, however, since as previously mentioned, variations between specific directions are much greater than the

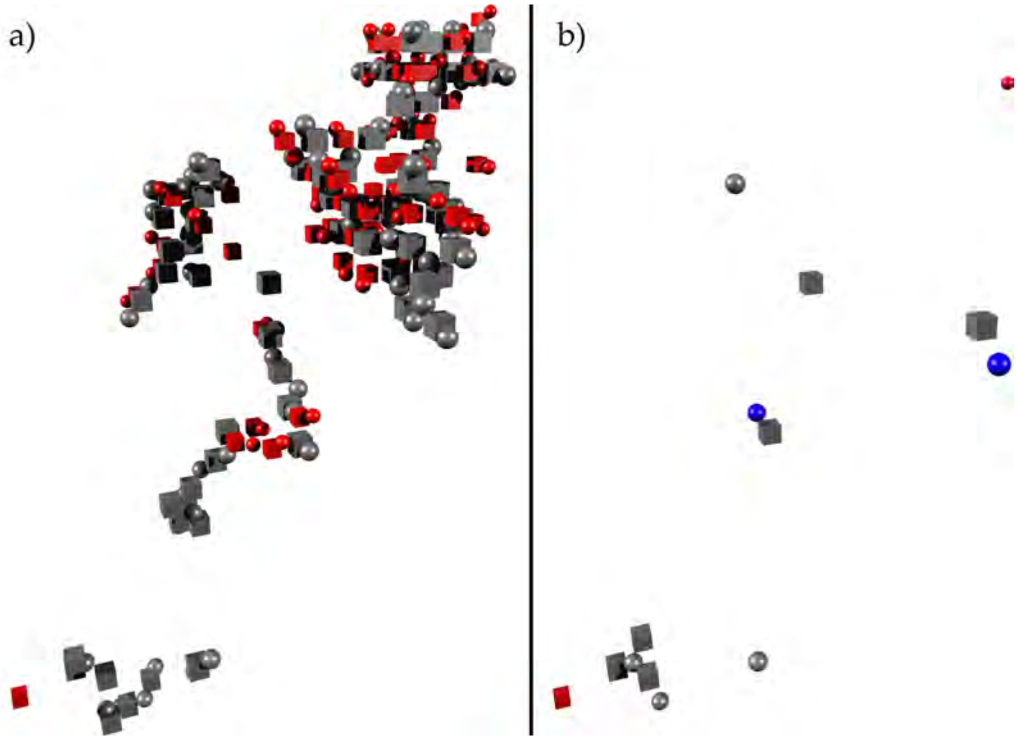

Figure 6.5: Damage induced by a 2 keV O^{2-} PKA in an alumina doped MgO lattice at a) peak damage (0.85 ps) and b) once the thermal-spike has dissipated (6 ps). Red indicates oxygen defects, grey magnesium defects; spheres are interstitial ions, cubes are vacancies. The blue spheres are magnesium ions that now occupy previously vacancy cation sites. Al impurities are not show in this figure.

change in average values. Nevertheless, that data would be commensurate with the view that, overall, the effect of the dopants is to slightly increase the disruption to the lattice but that does not translate to an increase in number of residual defects, N_d, once the thermal-spike has dissipated.

6.4.2 Examination of Some of the final Defect Clusters

Before some of the more common defect clusters are described, the nomenclature will be explained. In the following pages, intrinsic defects refer to those intrinsic to the MgO system and include $\mathrm{Mg}_i^{\bullet\bullet}$, O_i'', V_{Mg}'' and $\mathrm{V}_O^{\bullet\bullet}$; extrinsic damage is classified as those defects due to impurities, in this case $\mathrm{Mg}_{Al}^{\bullet}$ and the charge compensating V_{Mg}'' defects above the intrinsic concentrations; and finally the radiation damage which can include defects of all kinds. This means that it is possible for defects caused by the radiation damage to anneal out the pre-existing damage due to the impurities.

In the doped case, many of the defects generated in the cascades at the 1 and 2 keV PKA energies studied, consist of isolated defects and small clusters of two or sometimes three interstitials. There is a strong tendency in the doped case for a magnesium interstitial ion produced from the cascade to migrate onto one of the extrinsic vacancies. An example of this is shown in figure 6.6a which shows an example from a 2 keV <110> Mg^{2+} PKA cascade. Figure 6.6b shows another common defect found in a different region of the same cascade. While this again shows the ability of the extrinsic vacancy to attract magnesium interstitials, it also shows the propensity of the $\mathrm{Al}_{Mg}^{\bullet}$ substitutional defects to attract and trap oxygen interstitials. This configuration also forms when a magnesium-oxygen interstitial dimer migrates close to the $2\mathrm{Al}_{Mg}^{\bullet}$:$\mathrm{V}_{Mg}''$ system. It is also possible for an oxygen ion to be trapped by the $\mathrm{Al}_{Mg}^{\bullet}$ defect without the Mg ion residing on the extrinsic vacancy as shown in figure 6.7.

Occasionally trimer interstitial groupings are formed (as observed in previous

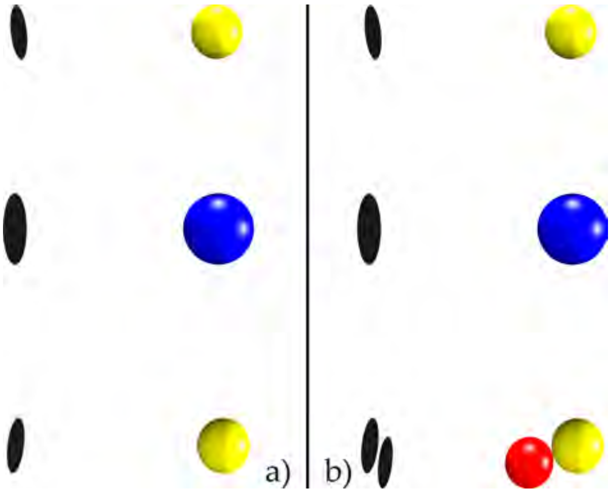

Figure 6.6: Simple defects found in 2% Al doped MgO. a) Radiation damage induced Mg interstitial captured by an extrinsic vacancy b) Same as a) but with a trapped O interstitial. Yellow sphere = $Al^{\bullet}_{Mg}$, blue sphere = $Mg^{\times}_{Mg}$, red sphere = O''_i.

Figure 6.7: O''_i trapped by $Mg^{\bullet}_{Al}$. Yellow = $Mg^{\bullet}_{Al}$. grey = V''_{Mg}. red = O''_i.

work [299]) in linear <100> combinations. Figure 6.8 shows an example $O''_i Mg^{\bullet\bullet}_i O''_i$ trimer that was formed as a consequence of the <134> 2 keV Mg^{2+} PKA simulation. These have been found to form in both pure and doped systems but are so infrequent that it is not possible to say if doping has any affect on the frequency of their occurrence. They seem to be less stable than the Mg-O interstitial dimer defect clusters in that (in this case) the oxygen defects tend to hop around the central Mg defect. On one occasion a defect of this type was seen to recombine with nearby vacancies by migrating

Figure 6.8: $\mathrm{O}_i''\mathrm{Mg}_i^{\bullet\bullet}\mathrm{O}_i''$ trimer. Grey sphere = $\mathrm{Mg}_i^{\bullet\bullet}$, red sphere = O_i''.

one hop along a <111> direction and then dissociating into a dimer and an oxygen interstitial.

Another relatively common defect is shown in figure 6.9. This is classified as a split di-vacancy and tends to form whenever there are 2 vacancies in a <111> configuration. If this occurs, the ion that forms the final corner of the three lattice sites migrates to the central interstitial site. Figure 6.9 shows the Mg version of this defect with an extrinsic V_{Mg}'' as one of the vacancies in the cluster. This has been shown to be more common than the O variant in the doped case due to the extrinsic Mg vacancies. In the pure case there seems to be no preference.

Due to the fact that vacancies are significantly less mobile than interstitials, it is far more common to see larger clusters of vacancies than interstitials as once a vacancy cluster forms, it is much less likely to move. It is also possible for uncommon configurations to remain to the end of the simulation. Figure 6.10 provides examples of two different configurations of vacancy trimers, a) shows a $\mathrm{V}_{Mg}''\mathrm{V}_O^{\bullet\bullet}\mathrm{V}_{Mg}''$ right angle configuration from the 2 keV <573> O^{2-} PKA in doped MgO and b) shows a linear $\mathrm{V}_O^{\bullet\bullet}\mathrm{V}_{Mg}''\mathrm{V}_O^{\bullet\bullet}$ cluster from the 2 keV

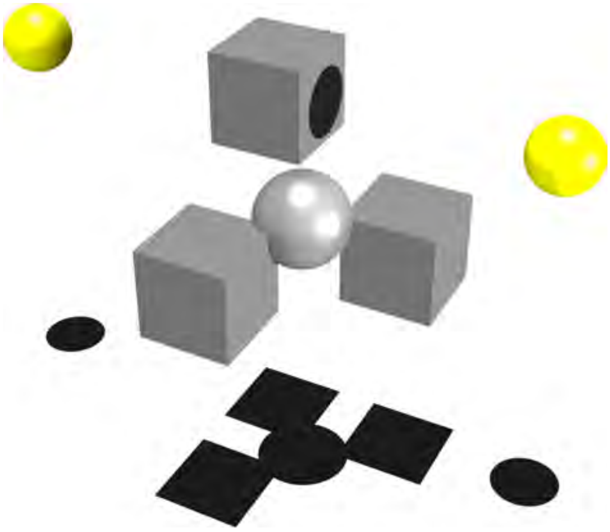

Figure 6.9: Split di-vacancy utilising an extrinsic V''_{Mg}. Grey cube = V''_{Mg} grey sphere = $Mg_i^{\bullet\bullet}$, yellow sphere = $Mg_{Al}^{\bullet}$.

<510>O^{2-} PKA in pure MgO.

This concludes the summary of defect clusters that were seen more than once. In isolated cascades there were highly complex defect configurations involving larger numbers of interstitials and vacancies but these were observed only once and are therefore not representative of the cascades as a whole. It is likely that the most important set of defects considered here were those pertaining to the capture of magnesium interstitial ions and the trapping of oxygen interstitials at the aluminium impurities as this is likely to have significant impact on recovery processes.

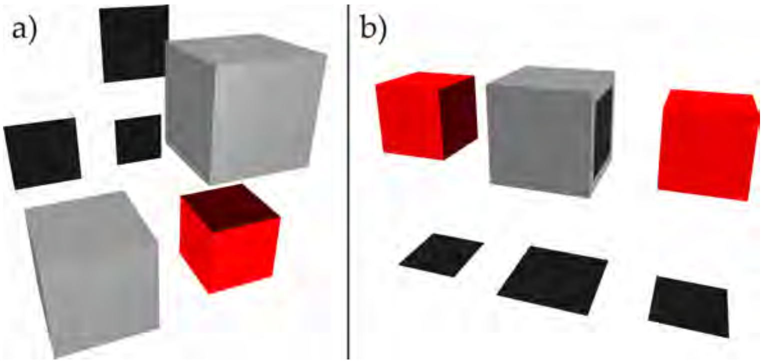

Figure 6.10: Vacancy trimer configurations. Grey cube = V''_{Mg}. Red cube = $V^{\bullet\bullet}_{O}$.

6.5 Conclusions

In their seminal paper Kinchin and Pease reported a model through which it is possible to estimate the maximum number of atoms permanently displaced from their lattice sites per PKA. Amongst the approximations in their model they neglected the anisotropy of E_d associated with the PKA incident direction and hence also the anisotropy in N_d. A number of computer simulation studies have focused on this issue, all of which assumed initially perfect lattice structures. It has been shown that the assumption of a perfect lattice is dubious because the variation in the predicted properties of a cascade, depends upon the local distribution of defects as much as it does on the PKA direction. Consequently, It is suggested that the anisotropy assumed from perfect lattice simulations is flawed and that any anisotropy should be much reduced as a result of the presence of lattice defects. Fifty years on it seems that at least one of the assumptions made by Kinchin and Pease may have been closer to the truth than has more recently been suggested.

Aside from the anisotropy issue it is difficult to quantify any substantial and systematic effect that the defects have on the evolution of the cascades due to insufficient results. It is possible, however, to postulate that recovery processes predicted by examining pure lattices are likely to be significantly modified. This can be justified by the analysis of the final defect population, mainly the trapping of oxygen interstitials adjacent to the Al substitutional defects and the similar effect the extrinsic vacancies have on the magnesium interstitials. It appears that such binding effects are significant although further work will be required to analyse this properly; see chapter 7 for more information.

Chapter 7

Further Work

7.1 Fluorite Related Phases

7.1.1 Pyrochlore

The primary aim of any further work in relation to this topic will be to develop a potential model, most probably using elliptical breathing shells, in order to accurately model the monoclinic to cubic pyrochlore transition. It may be advisable to attempt a more rigorous modelling approach using quantum mechanical techniques similar to those of Bogicevic *et al.* [158] to gain information with which to fit the breathing shell parameters since no elastic constant data for the monoclinic phase is available in the literature. Once this model has been developed, it can then be used to extend this work to the large A small B cation region of compositional space where the current model fails.

7.1.2 Disorder Processes Resulting in Fluorite

Calculations should also be performed to probe the pyrochlore and δ-phase to disordered fluorite compositional boundary. Following on from the work of Chartier *et al.* [266] who used molecular dynamics to simulate a disordered fluorite system, it may be possible to use this technique to gain further insight into these materials. It may also be possible to use MD to examine disordered versions of the δ-phase in order to directly calculate this instead of relying on the configurational entropy term as at present. Failing this a Monte-Carlo method could be used on a large supercell of the δ-phase to model the disorder process at this composition.

7.1.3 Amorphisation of the δ-phase

Since the δ-phase has been shown to have a very high resistance to amorphisation [231], simulations should be carried out to increase our understanding of this system. This should start with a calculations to determine the intrinsic defects as this will allow a preliminary ordering of the amorphisation resistance. It should also be possible to use molecular dynamics to study the effect of α-recoil collision cascades in order to understand why this system is resistant to amorphisation. It will facilitate comparison with the pyrochlore and fluorite and allow the related structures to be ranked by their amorphisation resistance. These simulations would confirm whether the δ-phase does amorphise or if it transforms to fluorite and identify defect clusters that may form during this process. The transformation process may be difficult to simulate with MD as it involves a rhombohedral to cubic conversion and undoubtedly a volume change and up to this point all simulations have been carried out under constant volume conditions. The reverse of this process could be simulated by quenching from a melt, or Monte-Carlo techniques could be used to disorder the system before it is relaxed under a constant pressure regime.

7.2 Accommodation of Actinides

7.2.1 Pyrochlore

Assuming a model that can accurately simulate the monoclinic phases is developed, solution processes should be extended to cover these materials. Potentials can be developed to model americium and some of the other minor actinides, which are also long lived, in order to predict their solution properties in these materials. Following the suggestion of Fortner *et al.* [30] a U^{5+} potential should be developed and solution incorporating this should be examined.

The calcium compensated systems should be extended to compare the solution properties in the related zirconolite and betafite systems. And both experimental and simulation work should be carried out with the aim of examining the phase equilibria of these related systems. With this in mind, a similar study to that of Chapter 4 could be performed.

7.2.2 δ-Phase

If this very amorphisation resistant material is to be used as a waste form, it must be able to accommodate high concentrations of actinides and fission product ions. It should easily be possible to produce a set of simulations modeling the solution of these species in a similar manner to that done for the pyroclores in Chapter 5.

7.3 Doped MgO

7.3.1 Anisotropy

In order to identify whether the conclusions regarding the reduction in anisotropic behaviour of collision cascades in impure MgO are valid, a more detailed study should be performed examining the same set of directions with the same defect concentration but varying the defect distribution in the simulation cell. This is essential as a single cell is really only one defect configuration and the change in anisotropy may be specific to that configuration. In order to be sure of these conclusions an average over many configurations is required. Different dopants, such as Li^+ ions, should be considered to see if the same trapping effect is observed for oxygen interstitial ions at the oxygen vacancies (introduced to charge compensate for Li^+ substitutional cations). It would also be possible to simultaneously dope both Al^{3+} and Li^+ into the lattice. In this case the Li^+ and Al^{3+} substitutional cations are self compensating and thus no potentially trapping vacant sites are introduced into the lattice.

7.3.2 Long Timescale Processes

Accelerated dynamics techniques should be used to analyse some of the defect clusters found at the end of the conventional dynamics simulations taking into account the impurity ions in the lattice in order to see how impurities effect the long timescale affects of radiation damage in real materials. The conventional dynamics simulations should also be extended to consider larger systems so that more energetic PKA energies can be investigated. As the PKA impulse increases, the more impurity ions the cascade will encounter, making any small timescale effects that the impurity ions have on the cascade more apparent.

7.3.3 Analysis of the Cascades

Determining the cascade size by measuring the distance between the furthest two defects in the cascade is very simplistic. A better way to model this would be a cascade volume calculation. This would require the construction of a mesh encasing the outer cascade generated defects. While this sounds simple, the difficulty with this method originates from distinguishing between intrinsic defects and cascade generated defects.

MgO was chosen as an example of a simple material with the hope that the results would be clearly identifiable. The results turned out to be unexpectedly complex and far from simple to interpret. Nevertheless, further work should also consider prospective wasteform materials to find out if the the effects seen in MgO are typical for all systems. An intermediate step in this direction would be to repeat this work with $MgAl_2O_4$ (spinel).

References

[1] V. P. Red'ko and L. M. Lopato. *Izvestiya Akademii Nauk SSSR, Neorganicheskie Materialy*, 27:1905–1910, 1991.

[2] United Nations Framework Convention on Climate Change (UNFCCC). Report of the Conference of the Parties on its third session, held at Kyoto, from 1 to 11 December 1997. Technical Report FCCC/CP/1997/7, United Nations, 1998.

[3] A. Cleave, R. W. Grimes, and K. Sickafus. *Phil. Mag.*, 85(9):967–980, 2005.

[4] A. R. Cleave, R. W. Grimes, R. Smith, B. P. Uberuaga, and K. E. Sickafus. Simulations of cascades in pure and alumina doped magnesia: Implications for the Kinchin - Pease model. Awaiting publication in Nucl. Instrum. Meth. B, 2005.

[5] F.A. Kroger. *The chemistry of imperfect crystals*, volume 2. North-Holland Publishing Company, Ltd., 2nd edition, 1974.

[6] C. J. Dore, J. D. Watterson, J. W. L. Goodwin, T. P. Murrells, N. R. Passant, M. M. Hobson, S. L. Baggott, G. Thistlethwaite, P. J. Cole-

man, K. R. King, M. Adams, and P. R. Cumine. UK emissions of air pollutants 1970 to 2002. Technical report, UK National Atmospheric Emissions Inventory (NAEI), October 2004.

[7] G. W. Bush and M. Gorbachev. The Treaty Between The United States Of America And The Union Of Soviet Socialist Republics On The Reduction And Limitation Of Strategic Offensive Arms. Treaty, July 1991.

[8] G. W. Bush and V. V. Putin. Treaty Between The United States Of America And The Russian Federation On Further Reduction And Limitation Of Strategic Offensive Arms (Start II). Treaty, January 1993.

[9] G. W. Bush and V. V. Putin. Treaty between the united states of america and the russian federation on strategic offensive reductions. Treaty, May 2002.

[10] P. Boczar, A. Dastur, K. Dormuth, A. Lee, and D. Meneley. *Prog. Nucl. Energ.*, 32(3/4):297–304, 1998.

[11] H. W. Whittington. *Phil. Trans. R. Soc. Lond. A*, 360:1653–1668, 2002.

[12] Department of Trade and Industry. Our energy future - creating a low carbon economy. White Paper Cm 5761, DTI, February 2003.

[13] T. H. Hammons and H. K. Toh. *Electr. Pow. Compo. Sys.*, 29:277–295, 2001.

[14] Nuclear power in the UK. Technical report, The Institution of Electrical Engineers, The Institution of Electrical Engineers, Savoy Place, London, February 2003.

[15] P. D. Wilson, editor. *The Nuclear Fuel Cycle From Ore to Wastes.* Oxford University Press, Walton Street, Oxford, 1996.

[16] H. Kleykamp. *J. Nucl. Mater.*, 131:221–246, 1985.

[17] H. Kleykamp. *J. Nucl. Mater.*, 206:82–86, 1993.

[18] R. W. Grimes and C. R. A. Catlow. *Phil. Trans. R. Soc. Lond. A*, 335:609–634, 1991.

[19] S. Nicoll, H. J. Matzke, R. W. Grimes, and C. R. A. Catlow. *J. Nucl. Mater.*, 240:185–195, 1997.

[20] J. T. Rogers, editor. *Fission Product Transport Processes in Reactor Accidents.* Hemisphere Publishing Corporation, 1990.

[21] E. H. P. Cordfunke and R. J.M. Konings. *J. Nucl. Mater.*, 201:57–69, 1993.

[22] S. T. Arm, R. P. Bush, and J. C. Mcgurk. *Prog. Nucl. Energ.*, 32:389–395, 1998.

[23] Webster. Partitioning and transmutation of actinides and fission products consideration of medium and low level waste streams. In *Proceedings of the Third International Information Exchange Meeting on Actinide and Fission Product Partitioning and Transmutation.* OECD Nuclear Energy Agency, 1994.

[24] National report on compliance with the obligations of the joint convention on the safety of spent fuel management and on the safety of radioactive waste management. National report, Health and Safety Executive, 2003.

[25] Managing the nuclear legacy - a strategy for action. Technical Report cm5552, Department tor Trade and Industry, 2002.

[26] W. J. Weber, R. C. Ewing, C. A. Angell, G. W. Arnold, A. N. Cormack, J. M. Delaye, D. L. Griscom, L. W. Hobbs, A. Navrotsky, D. L. Price, A. M. Stonham, and M. C. Weinberg. *J. Mat. Res*, 12:1946–1978, 1997.

[27] I. W. Donald, B. L. Metcaffe, and N.J. Taylor. *J. Mat. Sci.*, 32:5851–5887, 1997.

[28] S. King. Management of plutonium: Disposal considerations. Technical Note 360756, Nirex, 2002.

[29] L. A. Chick, G. F. Piepel, G. B. Mellinger, R. P. May, W. J. Gray, and L. Q. Buckwalter. The effects of composition on the properties in an 11 component nuclear-waste glass system. Technical Report PNL-3188, Pacific Northwest Laboratory, Battelle, 1981.

[30] J. A. Fortner, A. J. Kropf, R. J. Finch, A. J. Bakel, M. C. Hash, and D. B. Chamberlain. *J. Nucl. Mater.*, 304(1):56–62, 2002.

[31] R. C. Ewing, W. J. Weber, and J. Lian. *J. Applied Phys.*, 95(11):5949–5971, 2004.

[32] K. Trachenko, M. T. Dove, and E. K. H. Salje. *Phys. Rev. B*, 65(18), 2002. Article No. 180102.

[33] E. R. Vance, N. N.Watson, M. L. Carter, R. A. Day, and B. D. Begg. *J. Am. Ceram. Soc.*, 84(1):141–144, 2001.

[34] K. B. Helean, A. Navrotsky, G. R. Lumpkin, M.colella, J. Lian, R. C. Ewing, B Ebbinghaus, and J. G. Catalano. *J. Nucl. Mater.*, 320:231–244, 2003.

[35] S. X. Wang, B. D. Begg, L. M. Wang, R. C. Ewing, W. J. Weber, and K. V. G. Kutty. *J. Mater. Res.*, 12(12):4470–4473, 1999.

[36] S. S. Shoup, C. E. Bamberger, and R. G. Haire. *J. Am. Ceram. Soc.*, 79(6):1489–1493, 1996.

[37] H. Xu, Y. Wang, P. Zhao, W. L. Bourcier, R. Van Konynenburg, and H. Shaw. *Environ. Sci. Technol.*, 38:1480–1486, 2004. and references therein.

[38] F. J. Dickson, K. D. Hawkins, and T. J. White. *J. Solid State Chem.*, 82:146–150, 1989.

[39] A. E. Ringwood, S. E. Kesson, N. G. Ware, W. Hibberson, and A. Major. *Nature*, 278(5701):219–223, 1979.

[40] A. E. Ringwood, S. E. Kesson, N. G. Ware, W. O. Hibberson, and A. Major. *Geochem. J.*, 13(4):141–165, 1979.

[41] E. R. Vance, G. R. Lumpkin, M. L. Carter, D. J. Cassidy, C. J. Ball, R. A. Day, and B. D. Begg. *J. Am. Ceram. Soc.*, 85(7):1853–1859, 2002.

[42] S. E. Kesson, W. J. Sinclair, and A. E. Ringwood. *Nucl. Chem. Waste Man.*, 4(3):259–265, 1983.

[43] K. L. Smith, G. R. Lumpkin, M. G. Blackford, R. A. Day, and K. P. Hart. *J. Nucl. Mater.*, 190:287–294, 1992.

[44] B. D. Begg, E. R. Vance, and G. R. Lumpkin. *Mat. Res. Symp. Proc.*, 506:79–86, 1998.

[45] B. D. Begg, E. R. Vance, R. A. Day, M. Hambley, and S. D. Conradson. *Mat. Res. Symp. Proc.*, 465:325–340, 1997.

[46] E. R. Vance, A. Jostsons, R. A. Day, B. D. Begg, , and P. J. Angel. *Mat. Res. Symp. Proc.*, 412:41–47, 1996.

[47] E. R. Vance, P. J. Angel, B. D. Begg, and R. A. Day. *Mat. Res. Symp. Proc.*, 333:293–298, 1994.

[48] E. R. Vance, B. D. Begg, R. A. Day, and C. J. Ball. *Mat. Res. Symp. Proc.*, 353:767–774, 1995.

[49] A. Jostsons, E. R. Vance, D. J. Mercer, and V. M. Oversby. *Mat. Res. Symp. Proc.*, 353:775–781, 1995.

[50] B. D. Begg, R. A. Day, and A. Brownscombe. *Mat. Res. Symp. Proc.*, 663:259–266, 2001.

[51] R. L. Putnam, A. Navrotsky, B. F. Woodfield, J. Boerio-Goates, and J. L. Shapiro. *J. Chem. Thermodyn.*, 31(2):229–243, 1999.

[52] B. F. Woodfield, J. Boerio-Goates, J. L. Shapiro, R. L. Putnam, and A. Navrotsky. *J. Chem. Thermodyn.*, 31(2):245–253, 1999.

[53] R. Stevens, B. K. Hom, J. Boerio-Goates, B. F. Woodfield, R. L. Putnam, J. Gutierriez, and A. Navrotsky. *J. Chem. Thermodyn.*, 33(11):1441–1455, 2001.

[54] R. L. Putnam, A. Navrotsky, B. F. Woodfield, J. L. Shapiro, R. Stevens, and J. Boerio-Goates. *Mat. Res. Soc. Symp. Proc.*, 556:11–18, 1999.

[55] C. Meis, J. D. Gale, L. Boyer, J. Carpena, and D. Gosset. *J. Phys. Chem. A*, 104:5380–5387, 2000.

[56] Hj. Matzke, E. Toscano, C. T. Walker, and A. G. Solomah. *Adv. Ceram. Mater.*, 3(3):285–288, 1988.

[57] B. E. Burakov, E. E. Anderson, M. V. Zamoryanskaya, and M. A. Petrova. *Mat. Res. Soc. Symp. Proc*, 608:419, 2000.

[58] S. V. Yudintsev, S. V. Stefanovskii, O. I. Kir'yanova, J. Lian, and R. Ewing. *Atom. Energy*, 90(6), 2001.

[59] S. Luo, L. Li, B. Tang, and D. Wang. *Waste Manage.*, 18:55–59, 1998.

[60] D. R. Clarke. *Annu. Rev. Mater. Sci.*, 13:191–218, 1983.

[61] W. J. Weber, R. C. Ewing., C. R. A. Catlow, T. D. de la Rubia, L. W. Hobbs, C. Kinoshita, H. Matzke, A. T. Motta, M. Nastasi, E. K. H.

Salje, E. R. Vance, and S. J. Zinkle. Radiation effects in crystalline ceramics for the immobilization of high-level nuclear waste and plutonium. *J. Mater. Res.*, 13(6):1434–1484, 1998.

[62] E. Fanchon, J. L. Hodeau, J. Vicat, and J. A. Watts. *J. Solid State Chem.*, 92:88–100, 1991.

[63] H. J. Rossell. *J. Solid State Chem.*, 99:52–57, 1992.

[64] A. R. Chakhmouradian and R. H. Mitchell. *J. Solid State Chem.*, 138:272–277, 1998.

[65] F. W. Clinard, Jr., L. W. Hobbs, C. C. Land, D. E. Peterson, D. L. Rohr, and R. B. Roof. *J. Nucl. Mater.*, 105(2-3):248–256, 1982.

[66] F. W. Clinard, Jr., D. E. Peterson, D. L. Rohr, and L. W. Hobbs. *J. Nucl. Mater.*, 126(3):245–254, 1984.

[67] W. J. Weber, J. W. Wald, and Hj. Matzke. *J. Nucl. Mater.*, 138(2-3):196–209, 1986.

[68] P. Martin, G. Carlot, A. Chevarie, C. Den-Auwer, and G.Panczer. *J. Nucl. Mater.*, 275:268–276, 1999.

[69] W. J. Weber, R. C. Ewing, and A. Meldrum. *J. Nucl. Mater.*, 250(2-3):147–155, 1997.

[70] A. Meldrum, L. A. Boatner, W. J. Weber, and R. C. Ewing. *Geochim. Cosmochim. Ac.*, 62(14):2509–2520, 1998.

[71] R. C. Ewing. *P. Natl. A. Sci. USA.*, 96(7):3432–3439, 1999.

[72] K. Trachenko, M. T. Dove, and E. K. H. Salje. *Phys. Rev. B*, 65(18), 2002.

[73] K. Trachenko, M. T. Dove, and E. K. H. Salje. *J. Phys.-Cond. Matter.*, 15(2):L1–L7, 2003.

[74] C. S. Palenik, L. Nasdala, and R. C. Ewing. *Am. Mineral.*, 88(5-6):770–781, 2003.

[75] M. Zhang, E. K. H. Salje, and R. C. Ewing. *J. Phys.-Cond. Matter.*, 15(20):3445–3470, 2003.

[76] T. Geisler, K. Trachenko, S. Rios, M. T. Dove, and E. K. H. Salje. *J. Phys.-Cond. Matter.*, 15(37):L597–L605, 2003.

[77] R. C. Ewing, W. J. Weber, and F. W. Clinard. *Prog. Nucl. Energ.*, 150(1):209–212, 2000.

[78] G. R. Lumpkin. *J. Nucl. Mater.*, 289(1-2):136–166, 2001.

[79] J. F. DeNatale and D. G. Howitt. *Am. Ceram. Soc. Bull.*, 66:1393–1396, 1987.

[80] W. J. Weber. *J. Minerals, Metals Mater. Soc.*, 43:35–39, 1991.

[81] L. McFarland. Technical Report LALP 97-134, Los Alamos National Laboratory, Los Alamos, NM. U.S.A., November 1997 1997.

[82] L. W. Hobbs and M. R. Pascucci. *J. Physique*, 41:237–241, 1980.

[83] D. E. Beller, G. J. Van Tuyle, D. Bennett, G. Lawrence, K. Thomas, K. Pasamehmetoglu, N. Li, D. Hill, J. Laidler, and P. Fink. *Nucl.*

Instrum. Methods Phys. Res., Sect. A, Accel. Spectrom., 463(3):468–486, 2001.

[84] H. Nifenecker, S. David, J. M. Loiseaux, and O. Meplan. *Nucl. Instrum. Methods Phys. Res., Sect. A, Accel. Spectrom.*, 463(3):428–467, 2001.

[85] M. Beauvy, T. Duverneix, C. Berlanga, R. Mazoyer, and C. Duriez. *J. Alloy. Compd.*, 271:557–562, 1998.

[86] Asashi Kitamoto and Mulyanto. *Prog. Nucl. Energ.*, 32(3/4):429–437, 1997.

[87] Mulyanto and A. Kitamoto. *Annals of Nuclear Energy*, 22(11):697–709, 1995.

[88] R. C. Ewing and A. Macfarlane. *Science*, 296:659–660, April 2002.

[89] N. Morner. *Eng. Geol.*, 61(2-3):75–82, 2001.

[90] A. M. Beauchesne and J. Boese. Technical report, National Governors Association Center for Best Practices, National Governors Association, 444 North Capitol Street,Washington, D.C., 2000.

[91] Accelerating cleanup - paths to closure. Technical Report DOE/EM-0362, U.S. Department of Energy (DOE), U.S. Department of Energy (DOE) Office of Environmental Management, Washington, DC., June 1998.

[92] M. Holt. Civilian nuclear waste disposal. Technical Report IB92059, The National Council for Science and the Environment, April 2001.

[93] J. E. Mielke. Proposed high-level nuclear waste repository: Yucca mountain site characterization progress. Report for Congress RL30190, The Committee for the National Institute for the Environment, May 1999.

[94] Scientific and technical basis for geological disposal of radioactive wastes. Technical Report STI/DOC/010/413, International Atomic Energy Agency, Vienna, 2003.

[95] A. Hedin. Technical Report 9713, Swedish Nuclear Fuel and Waste Management Co, 1997.

[96] L. L. Hench, D. E. Clark, and A. B. Harker. *J. Mater. Sci.*, 21:1457–1478, 1986.

[97] P. Toulhoat. Confinement and migration of radionuclides in a nuclear waste deep repository. In Press C. R. Physique 0 (2002) 112.

[98] S. Stewart. *Eng. Geol.*, 67(1-2):139–168, 2002.

[99] M. Born. *Atomtheorie des Festen Zustandes.* Teubner, Leipzig, 1923.

[100] P. P. Ewald. *Ann. der Physik*, 65:253, 1921.

[101] C. Kittel. *Introduction to Solid State Physics.* John Wiley & Sons, New York, 1st printing edition, 1953.

[102] M. Leslie. Dl/sci/tm31t. Technical report, SERC Daresbury Laboratory, 1982.

[103] J. D. Gale. *J. Chem. Soc. Faraday T.*, 93(4):629–637, 1997.

[104] W. Pauli. *Z. Physik*, 31:765, 1925.

[105] F. London. *Z. Physik*, 63:245, 1930.

[106] F. London. *Z. Physik Chem.*, 11:222, 1930.

[107] R. Eisenschitz and F. London. *Z. Physik*, 60:491, 1930.

[108] M. Born and A. Landé. *Verhandlungen der Deutschen Physik Gesellschaft*, 21/24:210, 1918.

[109] M. Born and J.E. Mayer. *Z. Physik*, 75:1, 1932.

[110] J. E. Lennard-Jones. *Proc. R. Soc. Lon. A*, page 463, 1924.

[111] R. A. Buckingham. *Proc. Royal Soc. London. Series A, Math. Phys. Sci.*, 168:264–283, 1938.

[112] L. Minervini, R. W. Grimes, Y. Tabira, R. L. Withers, and K. E. Sickafus. *Phil. Mag. A*, 82:123–135, 2002.

[113] B. G. Dick and A. W. Overhauser. *Phys. Rev.*, 112:90–112, 1958.

[114] C. R. A. Catlow and W. C. Mackrodt. Theory of simulation methods for lattice and defect energy calculations in crystals. In C. R. A. Catlow and W. C. Mackrodt, editors, *Computer Simulation of Solids*, Berlin, 1982. Springer-Verlag.

[115] U. Schroder. *Solid State Commun.*, 4(7):347–349, 1966.

[116] M. J. L. Sangster. *J. Phys. Chem. Solids*, 35:195–200, 1974.

[117] N. F. Mott and M. J. Littleton. *Trans. Faraday Soc.*, 34:485, 1932.

[118] J. F. Ziegler, J. P. Biersack, and U. Littmark. *The Stopping and Range of Ions in Solids*, volume 1. Pergamon, Oxford, 1985.

[119] R. Smith, D. Bacorisen, B. P. Uberuaga, K. E. Sickafus, J. A. Ball, and R. W. Grimes. *J. Phys.-Cond. Matter.*, 17(6):875=891, 2005.

[120] W. T. Rankin and J. A. Board Jr. A portable distributed implementation of the parallel multipole tree algorithm. In *Fourth IEEE International Symposium on High Performance Distributed Computing (HPDC-4 '95)*, page 17, Los Alamitos, CA, 1995. IEEE Comput. Soc. Press.

[121] L. Greengard. *The Rapid Evaluation of Potential Fields in Particle Systems.* MIT Press, Cambridge, MA, 1988.

[122] R. D. Adamson. *Novel Methods for Large Molecules in Quantum Chemistry.* Phd thesis, University of Cambridge, Trinity College, Cambridge, January 1999.

[123] L. Verlet. *Phys. Rev.*, 159(1):98–103, 1967.

[124] M. J. Norgett. A general formulation of the problem of calculating the energies of lattice defects in ionic crystals. Technical Report R.7650 HL74/335, Atomic Energy Research Establishment, Harwell, 1974.

[125] R. Smith. *Atom and Ion Collisions in Solids and at Surfaces.* Cambridge University Press, Cambridge, 1997.

[126] Hj. Matzke. *Nucl. Instrum. Meth. B*, 65:30–39, 1992.

[127] K. E. Sickafus, Hj. Matzke, Th. Hartmann, K. Yasuda, J. A. Valdez, P. Chodak III, M. Nastasi, and R. A. Verrall. *J. Nucl. Mater.*, 274(1-2):66–77, 1999.

[128] N. Yu, K. E. Sickafus, P. Kodali, and M. Nastasi. *J. Nucl. Mater.*, 244(3):266–272, 1997.

[129] K. Yasuda, M. Nastasi, K. E. Sickafus, C. J. Maggiore, and N. Yu. *Nucl. Instrum. Meth. B*, 136-138:499–504, 1998.

[130] K. E. Sickafus, J. A. Valdez, J. R. Williams, R. W. Grimes, and H. T. Hawkins. *Nucl. Instrum. Meth. B*, 191(1-4):549–558, 2002.

[131] K. E. Sickafus, L. Minervini, R. W. Grimes, J. A. Valdez, and T. Hartmann. *Radiat. Eff. Defect. S.*, 155(1-4):133–137, 2001.

[132] K. E. Sickafus, L. Minervini, R. W. Grimes, J. A. Valdez, M. Ishimaru, F. Li, K. J. McClellan, and T. Hartmann. *Science*, 289(5480):748–751, 2000.

[133] C. Degueldre and C. Hellwig. *J. Nucl. Mater.*, 320(1-2):96–105, 2003.

[134] K.E. Sickafus, R.J. Hanrahan, K.J. McClellan, J.N. Mitchell, C.J. Wetteland, D.P. Butt, P. Chodak, K.B. Ramsey, T.H. Blair, K. Chidester, Hj. Matzke, K. Yasuda, R.A. Verrall, and N. Yu. *Am. Ceram. Soc. Bull.*, 78(1):69–74, 1999.

[135] M. A. Subramanian, G. Aravamudan, and G. V. Subba Rao. *Prog. Solid St. Chem*, 15:55–143, 1983.

[136] J. Wang, Y. Xie, Z. Zhang, R. Liu, and Z. Li. *Mater. Res. Bull.*, 40(8):1294–1302, 2005.

[137] Y. Shimizu and K. Maeda. *Sensor. Actuat. B-Chem.*, 52(1-2):84–89, 1998.

[138] Tetsuo Shimura, Masakage Komori, and Hiroyasu Iwahara. *Solid State Ionics*, 86-88(Part 1):685–689, 1996.

[139] A. Weyl and D. Janke. *J. Am. Ceram. Soc.*, 79(8):2145–2155, 1996.

[140] O. Porat, M. A. Spears, C. Heremans, I. Kosacki, and H. L. Tuller. *Solid State Ionics*, 86-8:285–288, 1996. Part 1.

[141] J. T. S. Irvine S. Tao. *The Chemical Record*, 4(2):83–95, 2004.

[142] O. Porat, C. Heremans, and H. L. Tuller. *Solid State Ionics*, 94(1-4):75–83, 1997.

[143] O. Porat, C. Heremans, and H. L. Tuller. *J. Am. Ceram. Soc.*, 80(9):2278–2284, 1997.

[144] J. J. Sprague and H. L. Tuller. *J. Eur. Ceram. Soc.*, 19(6-7):803–806, 1999.

[145] T. Takeda, R. Kanno, Y. Kawamoto, Y. Takeda, and O. Yamamoto. *J. Electrochem. Soc.*, 147(5):1730–1733, 2000.

[146] T. Takeda, R. Kanno, K. Tsubosaka, and Y. Takeda. *Electrochemistry*, 70(12):969–971, 2002.

[147] J. M. Bae and B. C. H. Steele. *J. Electroceram.*, 3(1):37–46, 1999.

[148] J. H. Ke, A. S. Kumar, J. W. Sue, S. Venkatesan, and J. M. Zen. *J. Mol. Catal. A-Chem.*, 233(1-2):111–120, 2005.

[149] J. M. Zen, A. S. Kumar, and H. P. Chen. *Electroanal.*, 15(20):1584–1588, 2003.

[150] J. M. Sohn, M. R. Kim, and S. I. Woo. *Catal. Today*, 83(1-4):289–297, 2003.

[151] H. Wang, H. L. Du, Z. Peng, M. L. Zhang, and X. Yao. *Ceram. Int.*, 30(7):1225–1229, 2004.

[152] H. L. Du, H. Wang, and X. Yao. *Ceram. Int.*, 30(7):1383–1387, 2004.

[153] G. K. Choi, D. W. Kim, S. Y. Cho, and K. S. Hong. *Ceram. Int.*, 30(7):1187–1190, 2004. Sp. Iss. SI.

[154] A. Dimoulas, G. Vellianitis, G. Mavrou, G. Apostolopoulos, A. Travlos, C. Wiemer, M. Fanciulli, and Z. M. Rittersma. *Appl. Phys. Lett.*, 85(15):3205–3207, 2004.

[155] C. Ang and Z. Yu. *Phys. Rev. B*, 70(13), 2004.

[156] N. Nadaud, N. Lequeux, M. Nanot, J. Jové, and T. Roisnel. *J. Solid State Chem.*, 135:140–148, 1998.

[157] A. Bogicevic and C. Wolverton. *Phys. Rev. B*, 67:024106, 2003.

[158] A. Bogicevic, C. Wolverton, G. M. Crosbie, and E. B. Stechel. *Phys. Rev. B*, 64:014106, 2001.

[159] M. Chen, B. Hallstedt, and L. J. Gaukler. *Solid State Ionics*, 170:255–274, 2004.

[160] L. M. Lopato, V. P. Red'ko, G. I. Gerasimyuk, and A. V. Shevchenko. *Izvestiya Akademii Nauk SSSR, Neorganicheskie Materialy*, 27:1718–1722, 1991.

[161] M. R. Thornber, D. J. M. Bevan, and J. Graham. *Acta Cryst. B*, 24:1183–1190, 1968.

[162] B.J. Kennedy, B.A. Hunter, and C.J. Howard. *J. Solid State Chem.*, 130:58–65, 1997.

[163] N. F. M. Henry and K. Lonsdale, editors. *International Tables for X-ray Crystallgraphy*, volume 1. The Kynoch Press, Birmingham, 1952.

[164] C.K. Jorgensen and E. Rittershaus. *Kongelige Danske Videnskabernes Selskab, Matematisk-Fysike Meddelelser*, 35:1–37, 1967.

[165] M. Glerup, O. F. Nielsen, and F. W. Poulsen. *J. Solid State Chem.*, 160:25–32, 2001.

[166] H.W. Schmalle, T. Williams, A. Reller, A. Linden, and J.G. Bednorz. *Acta Cryst. B*, 49:235–244, 1993.

[167] P. Duran and C. Pascual. *J. Mater. Sci.*, 19:1178–1184, 1984.

[168] A. V. Zagorodnyuk, L. V. Sadkovskaya, G. V. Shamrai, I.P. Kovalevskaya, R. L. Magunov, and G. A. Teterin. *Russ. J. Inorg. Chem.*, 31:1377, 1986.

[169] G. V. Shamrai, R. L. Magunov, I. V. Stasenko, and A. P. Zhirnova. *Inorg. Chem.*, 25:233, 1989.

[170] A.V. Zagorodnyuk G.A. Teterin, V.F. Zinchenko and I.M. *Sov. Progr. Chem.*, 54:31, 1988.

[171] N. Mizutani, Y. Tajima, and M. Kato. *J. Am. Ceram. Soc.*, 59:168, 1976.

[172] G. V. Shamrai, R. L. Magunov, and I. P. Kovalevskaya. *Inorg. Mater.*, 22:1695, 1986.

[173] A. V. Kolesnikov, G. E. Sukhanova, A. P. Zaitseva, and L. G. Scherbakova. *Inorg. Mater.*, 23:222, 1987.

[174] R. D. Shannon. *Acta Cryst.*, 32:751–767, 1976.

[175] A. V. Shevchenko, L. M. Lopato, and I. E. Kiryakova. *Inorg. Mater.*, 20:1731, 1984.

[176] A. V. Shevchenko and L. M. Lopato. *Inorg. Mater.*, 18:1583, 1982.

[177] L. M. Lopato A. V. Shevchenko and L. V. Nazarenko. *Inorg. Mater.*, 20:1615, 1984.

[178] L. M. Lopato A. V. Shevchenko and Z. A. Zaitseva. *Inorg. Mater.*, 20:1316, 1984.

[179] S. S. Kiparisov, R. A. Belyaev, A. I. Belyakov, V. V. Kondarenko, V. P. Vyskubov, V. G. Kozlov, S. A. Kuznetsov, and L. P. Melikhova. *Inorg. Mater.*, 12:1393, 1976.

[180] M. P. y Jorba. *Ann. Chim. (Paris)*, 7:479, 1962.

[181] A. Rouanet. *Rev. Int. Hautes Temp. Refract.*, 8:161, 1971.

[182] F. H. Brown Jr. and P. Duwez. *J. Am. Ceram. Soc.*, 38:95, 1955.

[183] R. S. Roth. *J. Res. Natl. Bur. Std.*, 56:24, 1956.

[184] H. Yokokawa, N. Sakai, T. Horita, K. Yamaji, T. Otake, H. Yugami, T. Kawada, and J. Mizusaki. *J. Phase Equilib.*, 22:331, 2001.

[185] V. S. Stubican, R. C. Hink, and S. P. Ray. *J. Am. Ceram. Soc.*, 61:17, 1978.

[186] P. S. Duwez and F. H. Brown Jr. *J. Electrochem. Soc.*, 98:360, 1951.

[187] K. K. Srivastava, R. N. Patil, C. B. Choudhary, K. V. G. K. Gokhale, and E. C. Subbarao. *Trans. J. Br. Ceram. Soc.*, 73:85, 1974.

[188] H.G. Scott. *J. Mater. Sci.*, 10:1527, 1975.

[189] H.G. Scott. *J. Aust. Ceram. Soc.*, 17:16, 1982.

[190] V. S. Stubican and J. R. Hellmann. *Adv. Ceram.*, 3:25, 1981.

[191] FIZ Karlsruhe Information Services. Inorganic crystal structure database. http://icsdweb.fiz-karlsruhe.de/, 2005.

[192] A. W. Sleight. *Inorg. Chem*, 8(8):1807–1808, 1969.

[193] O. Knop, F. Brisse, L. Castelliz, and R. Sutarno. *Can. J. Chem.*, 43:2812–2826, 1965.

[194] F. Brisse and O. Knop. *Can. J. Chem.*, 46:859–873, 1968.

[195] O. Knop, F. Brisse, and L. Castelliz. *Can. J. Chem.*, 47:971–990, 1969.

[196] H.-J. Deiseroth and H. Mueller-Buschbaum. *Z. Anorg. Allg. Chem.*, 375:152–156, 1970.

[197] M. Faucher and P. Caro. *J. Solid State Chem.*, 12:1–11, 1975.

[198] M.P. van Dijk, J.H.H. Ter Maat, G. Roelofs, H. Bosch, G.M.H. van de Velde, P.J. Gellings, and A.J. Burggraaf. *Mater. Res. Bull.*, 19:1149–1156, 1984.

[199] G.M.H. van de Velde, B.C. Lippens, S.J. Korf, and J. Boeijsma. *Powder Diffr.*, 5:229–231, 1990.

[200] T. Yamamoto, R. Kanno, Y. Takeda, O. Yamamoto, Y. Kawamoto, and M. Takano. *J. Solid State Chem.*, 109:372–383, 1994.

[201] H. Kobayashi, R. Kanno, Y. Kawamoto, T. Kamiyama, F. Izumi, and A.W. Sleight. *J. Solid State Chem.*, 114:15–23, 1995.

[202] B.J. Kennedy. *Mater. Sci. Forum*, 228:753–758, 1996.

[203] B.J. Kennedy and T. Vogt. *J. Solid State Chem.*, 126:261–270, 1996.

[204] E. Chtoun, L. Hanebali, P. Garnier, and J.-M. Kiat. *Eur. J. Solid State Inorg. Chem.*, 34:553–561, 1997.

[205] B.J. Kennedy, B.A. Hunter, and C.J. Howard. *J. Solid State Chem.*, 130:58–65, 1997.

[206] M. Field, B.J. Kennedy, and B.A. Hunter. *J. Solid State Chem.*, 151:25–30, 2000.

[207] E. Chtoun, L. Hanebali, and P. Garnier. *Ann. Chim.*, 26:27–32, 2001.

[208] Y. Tabira, R.L. Withers, T. Yamada, and N. Ishizawa. *Z. Kristallogr.*, 216:92–98, 2001.

[209] C. Bansal, H. Kawanaka, H. Bando, and Y. Nishihara. *Phys. Rev., Serie 3. B - Condensed Matter*, 66:052406–1–052406–4, 2002.

[210] N. Taira, M. Wakeshima, Y. Hinatsu, A. Tobo, and K. Ohoyama. *J. Solid State Chem.*, 176:165–169, 2003.

[211] Y. Moritomo, Sh. Xu, A. Machida, T. Katsufuji, E. Nishibori, M. Takata, M. Sakata, and S-W. Cheong. *Phys. Rev. B*, 63:144425, 2001.

[212] L.M. Red'ko, V.P.;Lopato. *Dopov. Akad. Nauk. A*, 1990:78–81, 1990.

[213] H.J. Rossell. *J. Solid State Chem.*, 19:103–111, 1976.

[214] M.R. Thornber and D.J.M. Bevan. *J. Solid State Chem.*, 1:536–544, 1970.

[215] G. Brauer and H. Gradinger. *Zeitschrift fuer Anorganische und Allgemeine Chemie*, 276:209–226, 1954.

[216] A. Rabenau. *Zeitschrift fuer Anorganische und Allgemeine Chemie*, 288:221–234, 1956.

[217] C.K. Jorgensen and E. Rittershaus. *Kongelige Danske Videnskabernes Selskab, Matematisk-Fysike Meddelelser*, 35:1–37, 1967.

[218] T. Moriga, A. Yoshiasa, F. Kanamaru, K. Koto, M. Yoshimura, and S. Somiya. *Solid State Ionics*, 31:319–328, 1989.

[219] B. J. Wuensch, K. W. Eberman, C. Heremans, E. M. Ku, P. Onnerud, E. M. E. Yeo, S. M. Haile, J. K. Stalick, and J. D. Jorgensen. *Solid State Ionics*, 129(1-4):111–133, 2000.

[220] C. R. Stanek, L. Minervini, and R.W. Grimes. *J. Am. Ceram. Soc.*, 85(11):2792–2798, 2002.

[221] M. Pirzada, R. W. Grimes, L. Minervini, J. F. Maguire, and K. E. Sickafus. *Solid State Ionics*, 140:201–208, 2001.

[222] M. P. van Dijk, A. J. Burggraaf, A. N. Cormack, and C. R. A. Catlow. *Solid State Ionics*, 17(2):159–167, 1985.

[223] L. Minervini, R. W. Grimes, and K. E. Sickafus. *J. Am. Ceram. Soc.*, 83:1873–78, 2000.

[224] W. R. Panero, L. P. Stixrude, and R. C. Ewing. *Phys. Rev. B.*, 70(5):054110, 2004.

[225] C. R. Stanek and R. W. Grimes. *J. Am. Ceram. Soc.*, 85(8):2139–2141, 2002.

[226] M. J. D. Rushton, R. W. Grimes, C. R. Stanek, and S. Owens. *J. Mater. Res.*, 19(6):1603–1604, 2004.

[227] P. J. Wilde and C. R. A. Catlow. *Solid State Ionics*, 112(3-4):173–183, 1998.

[228] P. J. Wilde and C. R. A. Catlow. *Solid State Ionics*, 112(3-4):185–195, 1998.

[229] G. Kresse and J. Hafner. *Phys. Rev. B*, 47:558, 1993.

[230] C. R. Stanek and R. W. Grimes. *J. Am. Ceram. Soc.*, 85:2139–2141, 2002.

[231] K. E. Sickafus and J. Valdez. Private Communication, 2005.

[232] K. E. Sickafus, L. Minervini, R. W. Grimes, J. E. Valdez, and T. Hartmann. *Rad. Eff. Defects Solids*, 155:133–137, 2001.

[233] J. Lian, X. T. Zu, K. V. G. Kutty, J. Chen, L. M. Wang, and R. C. Ewing. *Phys. Rev. B*, 66(5), 2002.

[234] R. E. Williford and W. J. Weber. Computer simulation of Pu^{3+} and Pu^{4+} substitutions in gadolinium zirconate. *J. Nucl. Mater.*, 299(2):140–147, 2001.

[235] J. Lian, L. M. Wang, G. R. Lumpkin, and R. C. Ewing. *Nucl. Instrum. Methods Phys. Res. Sect. B: Beam Interact. Mater.*, 191:565–570, 2002.

[236] W. L. Gong, W. Lutze, and R. C. Ewing. *J. Nucl. Mater.*, 277:239–249, 2000.

[237] A. R. Boccaccini, S. Atiq, and R. W. Grimes. *Adv. Eng. Mater.*, 5(7):501–508, 2003.

[238] H. Xu and Y. Wang. *J. Nucl. Mater.*, 275:216–220, 1999.

[239] K. B. Helean, A. Navrotsky, E. R. Vance, M. L. Carter, B. Ebbinghaus, O. Krikorian, J. Lian, L. M. Wang, and J. G. Catalano. *J. Nucl. Mater.*, 303:226–239, 2002.

[240] S. Yamazaki, T. Yamashita, T. Matsui, and T. Nagasaki. *J. Nucl. Mater.*, 294:183–187, 2001.

[241] I. Hayakawa and H. Kamizono. *J. Nucl. Mater.*, 202:163–168, 1993.

[242] N. K. Kulkarni, S. Sampath, and V. Venugopal. *J. Nucl. Mater.*, 281:248–250, 2000.

[243] H. Yokoi, Y. Arita, T. Matsui, H. Ohno, and K. Kobayashi. *J. Nucl. Mater.*, 238:163–168, 1996.

[244] Laurence A. J. Garvie, Huifang Xu, Yifeng Wang, and Robert L. Putnam. *J. Phys. Chem. Solids*, 66:902–905, 2005.

[245] E. R. Vance, M. L. Carter, M. W. A. Stewart, R. A. Day, B. D. Begg, and C. J. Ball. *Mat. Res. Soc. Symp. Proc.*, 713:319–326, 2002.

[246] S. X. Wang, L. M. Wang, R. C. Ewing, and K. V. Govindan Kutty. *Nucl. Instrum. Meth. B*, 169:135–140, 2000.

[247] J. Lian, L. Wang, J. Chen, K. Sun, R. C. Ewing, J. Matt Farmer, and L. A. Boatner. *Acta Mater.*, 51:1493–1502, 2003.

[248] B. C. Chakoumakos. *J. Solid State Chem.*, 53(1):120–129, 1984.

[249] D. D. Hogarth, C. T. Williams, and P. Jones. *Mineral. Mag.*, 64(4):683–697, 2000.

[250] R. E. Sykora, P. E. Raison, and R. G. Haire. *J. Solid State Chem.*, 178(2):578–583, 2005. Sp. Iss. SI.

[251] M. J. Apted, D. Langmuir, D. W. Moeller, J. A., A. E. Waltar, D. von Winterfeldt, R. C. Ewing, and A. Macfarlane. *Science*, pages 2333–2335, 2002.

[252] D. M. Strachan, R. D. Scheele, E. C. Buck, J. P. Icenhower, A. E. Kozelisky, R. L. Sell, R. J. Elovich, and W. C. Buchmiller. *J. Nucl. Mater.*, 345(2-3):109–135, 2005.

[253] D. M. Strachan, R. D. Scheele, W. C. Buchmiller, J. D. Vienna, R. L. Sell, and R. J. Elovich. Preparation and characterization of 238 Pu-ceramics for radiation damage experiments. Technical Report PNNL-13251, Pacific Northwest Laboratory, Richland, Washington 99352, May 2000.

[254] D. M. Strachan, R. D. Scheele, J. P. Icenhower, A. E. Kozelisky, R. L. Sell, V. L. Legore, H. T. Schaef, M. J. OHara, C. F. Brown, and W. C. Buchmiller. The status of radiation damage experiments. Technical Report PNNL-13721, Pacific Northwest Laboratory, Richland, Washington 99352, November 2001.

[255] G. R. Lumpkin, K. R. Whittle, S. Rios, K. L. Smith, and N. J. Zaluzec. *J. Phys.-Cond. Matter.*, 16(47):8557–8570, 2004.

[256] J. Lian, R. C. Ewing, L. M. Wang, and K. B. Helean. *J. Mater. Res.*, 19(5):1575–1580, 2004.

[257] J. Lian, L. M. Wang, R. G. Haire, K. B. Helean, and R. C. Ewing. *Nucl. Instrum. Meth. B*, 218:236–243, 2004.

[258] Y. Zhang, W. J. Weber, V. Shutthanandan, R. Devanathan, S. Thevuthasan, G. Balakrishnan, and D. M. Paul. *J. Appl. Phys.*, 95(5):2866–2872, 2004.

[259] J. Lian, J. Chen, L. M. Wang, R. C. Ewing, J. M. Farmer, L. A. Boatner, and K. B. Helean. *Phys. Rev. B*, 68(13), 2003.

[260] B. D. Begg, N. J. Hess, W. J. Weber, R. Devanathan, J. P. Icenhower, S. Thevuthasan, and B. P. McGrail. *J. Nucl. Mater.*, 288(2-3):208–216, 2001.

[261] G. R. Lumpkin, K. L. Smith, and M. G. Blackford. *J. Nucl. Mater.*, 289(1-2):177–187, 2001.

[262] A. Meldrum, C. W. White, V. Keppens, L. A. Boatner, and R. C. Ewing. *Phys. Rev. B*, 6310(10), 2001.

[263] S. X. Wang, L. M. Wang, R. C. Ewing, G. S. Was, and G. R. Lumpkin. *Nucl. Instrum. Meth. B*, 148(1-4):704–709, 1999.

[264] J. A. Purton and N. L. Allan. *J. Mater. Chem.*, 12(10):2923–2926, 2002.

[265] A. Chartier, C. Meis, J. P. Crocombette, L. R. Corrales, and W. J. Weber. *Phys. Rev. B*, 67(17), 2003.

[266] A. Chartier, C. Meis, J. P. Crocombette, W. J. Weber, and L. R. Corrales. *Phys. Rev. Lett.*, 94(2), 2005.

[267] G. Busker, A. Chroneos, and R. W. Grimes. *J. Am. Ceram. Soc.*, 82:1553–1559, 1999.

[268] V. Butler, C. R. A. Catlow, and B. E. F. Fender. *Radit. Eff.*, 73:273, 1983.

[269] R.E. Williford, W.J. Weber, R. Devanathan, and J.D. Gale. *J. Electroceram.*, 3:409–424, 1999.

[270] N. L. Allan, G. D. Barrera, T. H. K. Barron, and M. B. Taylor. *Int. J. Thermophysics*, 22(2):535–546, 2001.

[271] M. Samaras, P. M. Derlet, H. Van Swygenhoven, and M. Victoria. *Phil. Mag.*, 83(31-34):3599–3607, 2003.

[272] M. J. Giacobbe, N. Q. Lam, L. E. Rehn, P. M. Baldo, L. Funk, and J. F. Stubbins. *J. Nucl. Mater.*, 281(2-3):213–224, 2000.

[273] F. J. Perez-Perez and R. Smith. *Nucl. Instrum. Meth. B*, 164:487–494, 2000.

[274] S. J. Zinkle and C. Kinoshita. *J. Nucl. Mater.*, 251:200–217, 1997.

[275] R. H. Jones, D. Steiner, H. L. Heinisch, G. A. Newsome, and H. M. Kerch. *J. Nucl. Mater.*, 245(2-3):87–107, 1997.

[276] T. D. delaRubia, J. M. Perlado, and M. Tobin. *J. Nucl. Mater.*, 237:1096–1101, 1996. Part B.

[277] S. Vyas, R. W. Grimes, D. J. Binks, and F. Rey. *J. Phys. Chem. Solids*, 58(10):1619–1624, 1997.

[278] C. Kinoshita, K. Hayashi, and S. Kitajima. *Nucl. Instrum. Meth. B*, 229(2-3):209–218, 1984.

[279] G. H. Kinchen and R. S Pease. *Rep. Prog. Phys.*, 18:1, 1955.

[280] M. J. Norgett and M. T. Robinson. *Nucl.Eng.Des.*, 33:50, 1975.

[281] D. J. Bacon, F. Gao, and Yu. N. Osetsky. *Nucl. Instrum. Meth. B*, 153(1-4):87–98, June 1999.

[282] J. Gittus. *Irradiation Effects in Crystalline Solids.* Applied Science Publishers Ltd, London, 1978.

[283] S. J. Zinkle and B. N. Singh. *J. Nucl. Mater.*, 199:173–191, 1993.

[284] H. Huang and N. Ghoniem. *J. Nucl. Mater.*, 199:221–230, 1993.

[285] B. P. Uberuaga, R. Smith, A. R. Cleave, G. Henkelman, R. W. Grimes, A. F. Voter, and K. E. Sickafus. *Phys. Rev. B*, 71(10):104102, 2005.

[286] R. E. Williford, R. Devanathan, and W. J. Weber. *Nucl. Instrum. Meth. B*, 141(1-4):94–98, 1998.

[287] B. Park, W. J. Weber, and L. R. Corrales. *Nucl. Instrum. Meth. B*, 166-167:357–363, 2000.

[288] C. Y. Tang, X. Yao, J. Hu, Q. L. Rao, Y. R. Li, and B. W. Tao. *Supercond. Sci. Tech.*, 18(6):L31–L34, 2005.

[289] Watlow Electric. Smart technology to heat up the foodservice industry. Report, Watlow Electric Manufacturing Company, 2000.

[290] R. W. Grimes. *J. Am. Ceram. Soc*, 77(2):378–384, 1994.

[291] C. R. A. Catlow, I. D. Faux, and M. J. Norgett. *J. Phys. C: Solid State Phys.*, 9:419–429, 1976.

[292] A. Aguado and P. A. Madden. *Phys. Rev. Lett.*, 94(6), 2005.

[293] G. Busker, M. A. van Huis, R. W. Grimes, and A. van Veen. *Nucl. Instrum. Meth. B*, 171(4):528–536, 2000.

[294] V.G. Tsirel'son, A.S. Avilov, Yu.A. Abramov, E.L. Belokoneva, R. Kitaneh, and D. Feil. *Acta Cryst. B*, 54:8–17, 1998.

[295] E. Alves, R. C. da Silva, J.V. Pinto, T. Monteiro, B. Savoini, D. Cáceres, R. González, and Y. Chen. *Nucl. Instrum. Meth. B*, 206:148–152, 2003.

[296] R. González, I. Vergara, D. Cáceres, and Y. Chen. *Phys. Rev. B*, 65:224108, 2002.

[297] W. A. Sibley and Y. Chen. *Phys. Rev.*, 160(3):412–716, 1967.

[298] B. Henderson, D. H. Bowen, A. Briggs, and R. D. King. *J. Phys. C: Solid State*, 4(12):1496–1504, 1971.

[299] B. P. Uberuaga, R. Smith, A. R. Cleave, F. Montalenti, G. Henkelman, R. W. Grimes, A. F. Voter, and K. E. Sickafus. *Phys. Rev. Lett.*, 92(11):115505, 2004.

[300] J. F. Ziegler, J. P. Bierrsack, and U. Littmark. *The Stopping and Range of Ions*, volume Volume 1. Pergamon, Oxford, 1985.

[301] M.I. McCarthy and N.M. Harrison. *Phys. Rev. B*, 49:8574–8582, 1994.

[302] D. Taylor. *Brit. Ceram. Trans. Soc.*, 83:5–9, 1984.

[303] K. Hirata, K. Moriya, and Y. Waseda. *J. Mater. Sci.*, 83:5–9, 1977.

Appendices

Appendix A

Calculation of the Configurational Entropy Term

Configurational entropy:

$$S = k \ln \Omega \tag{A.1}$$

where S is the configuration entropy, k is Boltzmann's constant and Ω is the configurational term taking account the number of ways it is possible to arrange the ions on the site(s). This is calculated as in

$$\Omega = \frac{N!}{n!(N-n)!} \tag{A.2}$$

Using the structural information regarding the δ-phase (see table A.1). There is 1 Sc ion and 2 Hf ions on the 3a cation site and 11 Sc ions and 7 Hf ions on the 18f cation site.

Table A.1: Structural information for $Sc_4Hf_3O_{12}$ from [1]

Atom	Site	a	b	c	Occupancy
Hf	3a	0	0	0	$\frac{2}{3}$
Sc	3a	0	0	0	$\frac{1}{3}$
Hf	18f	0.2894	0.4084	0.0179	0.4
Sc	18f	0.2894	0.4084	0.0179	0.6
O	18f	0.306	0.459	-0.224	1.0
O	18f	0.309	0.441	0.269	1.0

Therefore for the 3a site

$$\Omega = \frac{3!}{1!2!} = 3 \tag{A.3}$$

and for the 18f site

$$\Omega = \frac{18!}{7!11!} = 31824 \tag{A.4}$$

In total

$$S = k\ln(31824 \times 3) = 9.88 \times 10^{-4}\text{eV/K} \tag{A.5}$$

This is for the full unit cell so the value of S for one formula unit is 3.29×10^{-4}eV/K.

Appendix B

Normalisation of Solution Mechanisms

Here is an example of using mass action analysis for the simple solution of Pu_2O_3 onto both the A site of a pyrochlore.

$$2Pu_2O_3 + 4A_A^{\times} + 2B_B^{\times} + O_O^{\times} \longrightarrow 4Pu_A^{\times} + 2A_B^{'} + V_O^{\bullet\bullet} + A_2B_2O_7 \tag{B.1}$$

$$\left[Pu_A^{\times}\right]^4 \left[A_B^{'}\right]^2 \left[V_O^{\bullet\bullet}\right] = \exp\left(\frac{\Delta H_{sol}}{kT}\right) \tag{B.2}$$

From charge neutrality:

$$\left[Pu_A^{\times}\right] = 2\left[A_B^{'}\right] = 4\left[V_O^{\bullet\bullet}\right] \tag{B.3}$$

Substituting equation B.3 into equation B.2

$$\left[Pu_A^{\times}\right]^4 \frac{1}{4}\left[Pu_A^{\times}\right]^2 \frac{1}{4}\left[Pu_A^{\times}\right] = \exp\left(\frac{\Delta H_{sol}}{kT}\right) \tag{B.4}$$

$$\frac{1}{16}\left[Pu_A^{\times}\right]^7 = \exp\left(\frac{\Delta H_{sol}}{kT}\right) \tag{B.5}$$

$$\left[Pu_A^{\times}\right] = 16^{-7}\exp\left(\frac{\Delta H_{sol}}{7kT}\right) \tag{B.6}$$

Therefore the normalisation factor is 7.

Appendix C

Other Publications

C.1 Structure and Mobility of Defects Formed from Collision Cascades in MgO

My contribution to this work consisted of running molecular statics calculations using CASCADE [102] as described in chapter 3. More specifically the barriers for interstitial ion migration for both O and Mg ions were identified by stepping the interstitial ion along the trajectory between two interstitial sites and identifying the saddle point. The other contribution to this paper included generating the binding energy data for the interstitial clusters shown in figure 3. This involved calculating many different configurations of Mg and O interstitial ions for each defect cluster size in an attempt to identify the lowest energy state. The energy gain over the isolated case was calculated and then plotted to show how the defects will tend to aggregate.

C.2 Dynamical simulations of radiation damage and defect mobility in MgO

This paper is a more detailed follow up to the previous paper. The main contributions to this were the sections on molecular statics in the methodology and the first few paragraphs in the results sections. I also produced figures 1-6, 9, 10 and 12 from the raw data to ensure consistent use of colour and shapes for the different species throughout the paper.

Structure and Mobility of Defects Formed from Collision Cascades in MgO

B. P. Uberuaga,[1] R. Smith,[1,*] A. R. Cleave,[2] F. Montalenti,[3] G. Henkelman,[1] R.W. Grimes,[2]
A. F. Voter,[1] and K. E. Sickafus[1]
[1]*Los Alamos National Laboratory, Los Alamos, New Mexico 87545, USA*
[2]*Department of Materials, Imperial College, Prince Consort Road, London SW7 2BP, United Kingdom*
[3]*INFM, L-NESS, and Dipartimento di Scienza dei Materiali, Università degli Studi di Milano-Bicocca, Via Cozzi 53, I-20125 Milan, Italy*

(Received 12 November 2003; published 19 March 2004)

We study radiation-damage events in MgO on experimental time scales by augmenting molecular dynamics cascade simulations with temperature accelerated dynamics, molecular statics, and density functional theory. At 400 eV, vacancies and mono- and di-interstitials form, but often annihilate within milliseconds. At 2 and 5 keV, larger clusters can form and persist. While vacancies are immobile, interstitials aggregate into clusters (I_n) with surprising properties; e.g., an I_4 is immobile, but an impinging I_2 can create a metastable I_6 that diffuses on the nanosecond time scale but is stable for years.

DOI: 10.1103/PhysRevLett.92.115505 PACS numbers: 61.72.Ji, 61.72.Cc, 61.80.Az, 61.82.Ms

In this Letter, we combine four computational techniques to perform multi-time-scale simulations of radiation-damage effects in solids. For the first time, we predict, without any prior assumptions about the dynamics, the fate of defects generated under ballistic radiation-damage conditions out to time scales approaching those which can be probed experimentally (i.e., order of seconds). A typical molecular dynamics (MD) simulation of radiation damage follows the evolution of an isolated collision cascade over picosecond (ps) time scales, which is sufficient to observe the collisional phase of the cascade and to identify characteristic features of the residual defects left by the cascade process (see, e.g., Ref. [1]). However, the actual behavior of a material is determined not only by the number and nature of the residual defects associated with a cascade event, but also by the long-time evolution of those defects. Over time scales much greater than ps, residual defects can both annihilate and aggregate. Annihilation events effectively promote radiation tolerance; aggregation events, on the other hand, lead to decreased probability for annihilation and consequently exacerbate radiation-damage susceptibility. In order to effectively predict radiation-damage evolution in a material, one must necessarily gain access to longer time-scale processes such as defect mobility, annihilation, and aggregation. The work presented here represents our inaugural attempt to expand radiation-damage predictive capabilities via computation. By merging conventional MD cascade simulations with accelerated dynamics methods, we can monitor the evolution of cascade debris to times of the order of milliseconds (ms) to seconds (s).

As a model material for this study, we chose the oxide magnesia (MgO). Oxides are the conventional nuclear fuel form used in light water reactors (UO_2 and mixed oxides [2]) and are attractive as insulators for fusion reactor diagnostics [3]. Also, there is growing interest in their use as host materials for the immobilization and long-term storage of toxic radionuclides such as the transuranics found in spent nuclear fuel [4,5]. MgO is a classic engineering ceramic with well-understood properties, and its radiation-damage behavior has been the subject of numerous experimental and computational investigations. Finally, well-established empirical potentials exist for MgO.

The computational procedure used here consisted of four components. As detailed below, we first generated collision cascades in MgO at selected energies using MD for a few ps. We adopted representative defect configurations from the cascades and used these as starting configurations for long-time simulations via temperature accelerated dynamics (TAD) [6,7]. We also used static energy minimization to assess the relative stability of defects observed in MD or TAD simulations against alternative crystallographic arrangements of the same defect. Finally, key findings were verified using the higher-quality description afforded by density functional theory (DFT).

Using this approach, an interesting picture emerges for the room-temperature evolution of radiation damage after a low-energy cascade in MgO. In the first 10 ps, a primary knockon atom (PKA) (the atom imparted with the collision energy from, for instance, an energetic neutron) event typically creates a small number of interstitials and vacancies. While the vacancies are essentially immobile, isolated interstitials diffuse on the nanosecond (ns) time scale. Point defects are charged, so the interstitials are quickly drawn to either a vacancy and annihilated or to another interstitial to form a neutral di-interstitial cluster, which is mobile on the ms time scale. While clusters generally become less mobile with size, we have observed a surprising nonmonotonicity. A hexa-interstitial cluster can form which diffuses much faster than the smaller clusters. This behavior impacts both the expected level of damage produced per cascade, as well as the interaction between cascades.

0031-9007/04/92(11)/115505(4)$22.50

The potential used here, based on that given by Lewis and Catlow [8], is pairwise additive, consisting of an electrostatic part and a standard short-range Buckingham term. Shells were not included in the MD and TAD simulations but were included in some energy minimizations for comparison. The potential is a full charge model, which recent *ab initio* calculations confirm is maintained by the ions in this lattice [9]. The potential is not sufficiently repulsive for the small distances encountered during cascades and so was modified by a screened Coulomb potential [10]. We applied a smooth cutoff to the Buckingham term at distances greater than 8 Å for the O-O interactions and 5.5 Å for the Mg-O interactions. Both Ewald sums and the fast multipole method implemented by Rankin [11] were used to calculate the Coulombic interactions. This model does not account for charge transfer. Specifically, we do not account for defects such as F^+ and F centers (anion vacancies with one and two trapped electrons, respectively) in our calculations. An anion vacancy in our model is formally an F^{++} center with no trapped electrons. The same is true for cation vacancies.

Collision cascades with PKAs at energies of 0.4, 2, and 5 keV were investigated. Crystal sizes varied from 4000 to 160 000 atoms, the size chosen to ensure that the cascades did not interact strongly with the cell boundaries. Trajectories were run for up to 8 ps or until the thermal spike of the cascade had dissipated throughout the cell. Initial trajectory directions were randomly distributed over a solid angle representative of the crystal symmetry. In total, 20 trajectories were run at 0.4 keV, and 12 each at 2 and 5 keV, evenly distributed between an O and a Mg PKA. Each trajectory was begun at a temperature of $T = 0$ K. Previous MD work has indicated [12] that the displacement energy threshold in MgO is very high: about 65 eV for an O and 90 eV for a Mg PKA. We obtain similar but slightly higher values.

Figure 1 shows a typical cascade with a PKA energy of 0.4 keV. Shortly after the initial knockon, a large number of atoms are displaced from their original lattice site, peaking at $t = 80$ fs [Fig. 1(a)]. After 260 fs, most of the damage has annealed, leaving only two vacancies and two separated interstitials [Fig. 1(b)]. However, by $t =$ 6.5 ps, by which time the cascade has settled down, the two interstitials have attracted one another and formed a MgO di-interstitial [Fig. 1(c)]. In other cases, the interstitial recombined with a nearby vacancy. Whether the interstitial prefers to move toward another interstitial or toward a vacancy depends on the complex electric field created by these scattered point defects.

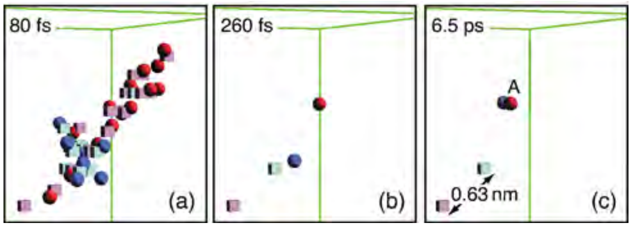

FIG. 1 (color). The defects in a cascade generated from a 0.4 keV O PKA. The scheme—used in all figures—is dark blue spheres for Mg interstitials, dark red spheres for O interstitials, light blue cubes for Mg vacancies, and light red cubes for O vacancies. (a) At $t = 80$ fs, the number of displaced atoms peaks. (b) By $t = 260$ fs, most of the defects have recombined and only a few isolated defects remain. (c) By $t =$ 6.5 ps, the interstitials have formed a di-interstitial (labeled A).

For 0.4 keV, only a small number of defects formed. The number of Frenkel pairs, or atoms that were still displaced after the 8 ps simulation time, was 0.5 per trajectory. These were evenly divided between interstitial-vacancy pairs separated by over 1 nm (pairs separated by less than 1 nm quickly recombined) and MgO di-interstitials. Interstitials were located at the body center of the 8-atom MgO cell, or the 8c site. The number of atoms displaced from their original lattice site was much larger, averaging nine per trajectory. Most recombined with vacancies very quickly, as shown in Figs. 1(a) and 1(b). The results of each of the cascade energies simulated are summarized in Table I.

As expected, the number of defects that survive the collisional phase of a cascade ($t = 8$ ps) increases dramatically with PKA energy. At 2 keV, seven Frenkel pairs formed per trajectory while 18 formed at an energy of 5 keV. The number of displaced atoms also rose, to 48 atoms per trajectory at 2 keV and 124 at 5 keV. The increase in the number of defects with PKA energy was accompanied by an increase in the size of interstitial clusters. At 0.4 keV, only isolated interstitials and di-interstitials were formed. Tri-interstitials began to appear at 2 keV and, at 5 keV, a number of larger clusters, including four tri-interstitials, a tetra-interstitial, and one 7-atom cluster, formed. A similar trend is seen for vacancy clusters. For all energies, the isolated interstitials were roughly evenly divided between O and Mg. Examples of defects at the end of the higher energy cascades are shown in Fig. 2.

Typical defects found in the cascade simulations were analyzed via static energy minimization using the procedure described in Ref. [13]. The binding energies ($E_{\text{isolated defects}} - E_{\text{cluster}}$), calculated without shells, for

TABLE I. The total number of Frenkel pairs (N_{FP}), principal defect types, and times the lattice reformed perfectly (N_{PL}) for PKA energies of 0.4, 2, and 5 keV remaining after the collisional phase ($t = 8$ ps) of a cascade. In addition, one tri-interstitial formed at 2 keV and four tri-interstitials, one tetra-interstitial, and one 7-interstitial cluster formed at 5 keV.

PKA energy (keV)	No. of trajs.	N_{FP}	No. of defects mono-int O/Mg	 mono-vac O/Mg	 di-int	 di-vac	N_{PL}
0.4	20	10	3/1	5/3	3	1	13
2	12	84	21/24	33/30	15	6	0
5	12	216	57/62	78/80	39	15	0

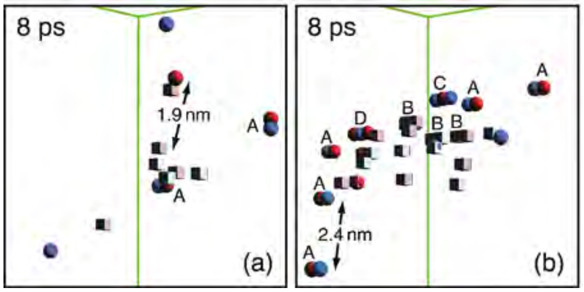

FIG. 2 (color). (a) Typical defects remaining after the collisional phase ($t = 8$ ps) of a cascade for a PKA energy of 2 keV. Shown are several isolated vacancies and interstitials plus two di-interstitials (labeled A). (b) Residual defects 8 ps after a 5 keV PKA event. In addition to isolated vacancies, interstitials and di-interstitials (A), di-vacancies (B), and tri-interstitials of both types—Mg-O-Mg (C) and O-Mg-O (D)— form.

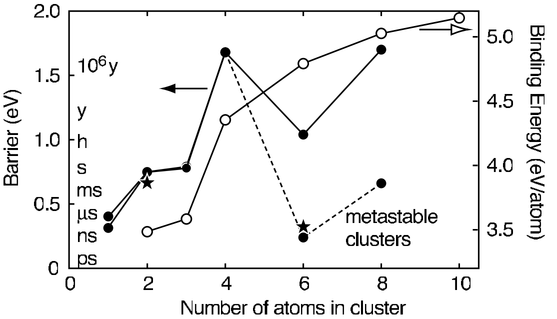

FIG. 3. Binding energy and diffusion barriers for interstitial clusters versus cluster size. The time scale for diffusion at 300 K is also shown. The binding energy increases with the cluster size, while the energy barriers do not follow any obvious trend. The dashed line indicates barriers for metastable clusters. The ★s indicate barriers calculated with DFT.

the most stable interstitial configurations are shown in Fig. 3. The interstitial clusters exhibit strong binding energies which increase from 3.49 eV per atom for the di-interstitial to 5.15 eV per atom for the deca-interstitial cluster. The same trend occurs when shells are included, although the binding energies are about 0.7 eV smaller per atom. As suggested by the cascade simulations, isolated interstitials were found to be most stable at the 8c site. This result is in agreement with other calculations for the charged interstitial [14], although calculations on neutral interstitials find the split interstitial is more stable [15]. Static simulations were also used to identify the saddle points associated with the diffusion of the single interstitials and thus we predict the energy barriers for diffusion: 0.40 eV for O and 0.32 eV for Mg.

The cascade simulations can only follow the evolution of the resulting defects for ps. We applied TAD [6,7] to representative defects to achieve experimental time scales. TAD involves running MD at a high temperature T_{high} in a way that constrains the dynamics to the current basin. The times of attempted events seen at T_{high} are extrapolated to the temperature of interest T_{low} and the event occurring earliest at T_{low} is accepted. The process is repeated in the new state. Here, T_{low} was set to 300 K.

In MgO, the barriers for defect diffusion range from 0.25 to over 2 eV. To enhance the speed of the TAD simulations, we used a recently developed extension to TAD, the dimer-TAD method [16], which exploits the dimer method [17] to find the minimum barrier to leave a state. This barrier is used to reduce the amount of MD that must be performed at T_{high} and to tune T_{high} for each state, resulting in values between 300 and 2000 K.

In the TAD simulations, we employed systems containing 512 and 1728 atoms. A periodic cell was used to study neutral defects and a cell with free surfaces was used for the tri-interstitials. The diffusion barriers found from the TAD simulations for the key interstitial clusters are summarized in Fig. 3. At 300 K, vacancies are immobile (barrier > 2 eV) while interstitials diffuse on ns time scales. For small clusters, the diffusion barrier increases with size: mono-interstitials diffuse quickly, di- and tri-interstitials diffuse more slowly with barriers of 0.75 eV (di-interstitial) and 0.79 eV (Mg-O-Mg) or 0.80 eV (O-Mg-O) (s time scale), and tetra-interstitials, with a barrier of 1.68 eV, are immobile (see Fig. 4). Tetra-interstitials are also very stable: the barrier to split them is 2.5 eV, a process that basically never occurs at 300 K.

This trend suggests that clusters of four or more interstitials act as immobile interstitial sinks. Surprisingly, however, the hexa-interstitial is mobile, with a diffusion barrier of 1.04 eV in its ground state (100 s time scale). Moreover, it can exist in a metastable state, a state actually formed in an encounter between a di- and a tetra-interstitial during the TAD simulation shown in Fig. 4. This state diffuses on the ns time scale with a barrier of 0.24 eV and is limited to one-dimensional diffusion along a $\langle 110 \rangle$ direction. The barrier to decay to the ground state is 1.31 eV, so a cluster formed in this metastable state will last for years.

While we have not explored it completely, we find the behavior of the octa-interstitial is similar to that of the hexa-interstitial. A metastable structure diffuses one dimensionally with a barrier of 0.66 eV, trapped by a barrier of 1.52 eV for decay to the immobile ground state. Larger clusters may have interesting properties as well.

TAD simulations also show that, as in other systems [7], activated processes often involve concerted motion of many atoms. For example, the metastable hexa-interstitial moves by a 12-atom mechanism. In addition, as interstitial and vacancy defects interact in the strong Coulomb field, long-range concerted events can lead to their annihilation over distances of many angstroms.

For convenience, all simulations were performed on systems held at the $T = 0$ K lattice constant. Expanding to the $T = 300$ K lattice constant changes the barriers slightly; e.g., the barrier for the tetra-interstitial changes from 1.68 to 1.61 eV and that for the metastable hexa-interstitial changes from 0.24 to 0.21 eV.

We have tested some of the empirical potential results with DFT, using the VASP code [18] with the PW91

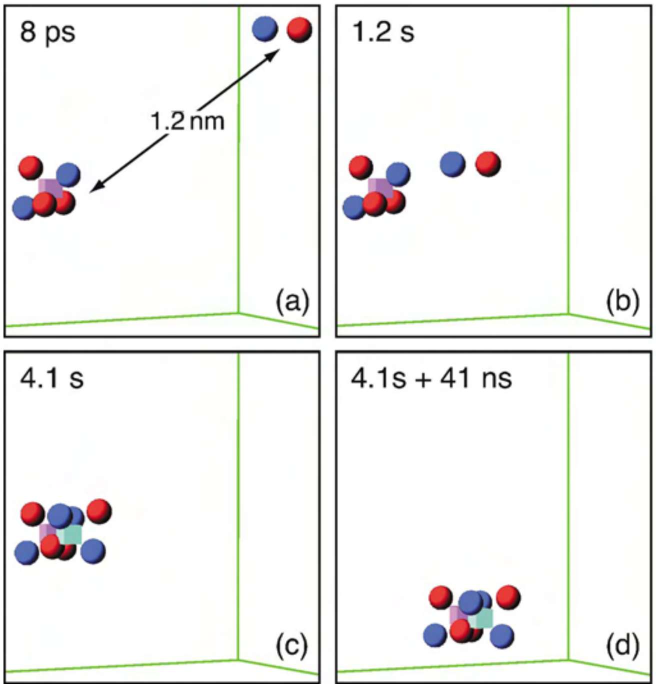

FIG. 4 (color). TAD simulation of the formation of a hexa-interstitial at 300 K. (a) A di- and a tetra-interstitial began about 1.2 nm apart. (b) By $t = 1.2$ s, the di-interstitial approached the immobile tetra-interstitial. (c) By $t = 4.1$ s, the combined cluster annealed to form the metastable hexa-interstitial, (d) which diffuses on the ns time scale with a barrier of 0.24 eV.

functional and the projector augmented wave method [19] on supercells containing 216 lattice atoms. A plane wave basis with energies up to 400 eV was used. It was determined that a single Γ-point sampling of k space was sufficient to converge energies for this cell size. We compared DFT and the empirical potential for both the formation and the migration energy of the di- and metastable hexa-interstitials. The DFT formation energies are 12.8 and 31.1 eV, respectively, which compare well with the empirical potential values of 11.9 and 28.5 eV, considering the high energies involved in the collision cascades. The diffusion barriers for both defects agree very well: 0.66 and 0.33 eV using DFT compared to the empirical potential values of 0.75 and 0.24 eV (see Fig. 3).

Combining the results from these four computational methods has led to the picture described above for the evolution of radiation damage in MgO. Point defects and small clusters form during low-energy cascades. While vacancies are immobile at room temperature, interstitials diffuse quickly, either recombining with vacancies or clustering with other interstitials. Interstitial clusters become more stable with size, but certain sizes and forms can be very mobile. They can thus aggregate with clusters from other cascades, increasing the overall damage accumulation rate. In the case of the hexa- and octa-interstitials, the long-range one-dimensional diffusion along $\langle 110 \rangle$ in the metastable state could result in an experimentally detectable signature.

In summary, combining MD cascade simulations, static energy minimization, temperature accelerated dynamics, and DFT, we find that it is possible to study the radiation-damage properties of MgO on time scales relevant to experiment. Complex events are important, and higher level models should account for them in order to simulate the correct damage evolution.

We acknowledge helpful discussions with G. Pacchioni, J. H. Harding, and D. J. Harris. This work was supported by the United States Department of Energy, Office of Science, Office of Basic Energy Sciences, Division of Materials Sciences and Engineering.

---

*Permanent address: Department of Mathematical Sciences, Loughborough University, LE11 3TU, Loughborough, United Kingdom.

[1] D. J. Bacon and T. D. de la Rubia, J. Nucl. Mater. **216**, 275 (1994).
[2] D. R. Olander, "Fundamental Aspects of Nuclear Reactor Fuel Elements," Technical Information Center, Office of Public Affairs, Energy Research and Development Administration, Springfield, Virginia, 1976.
[3] C. Kinoshita and S. J. Zinkle, J. Nucl. Mater. **233–237**, 100 (1996).
[4] S. X. Wang *et al.*, J. Mater. Res. **14**, 4470 (1999).
[5] K. E. Sickafus *et al.*, Science **289**, 748 (2000).
[6] M. R. Sørensen and A. F. Voter, J. Chem. Phys. **112**, 9599 (2000).
[7] A. F. Voter, F. Montalenti, and T. C. Germann, Annu. Rev. Mater. Res. **32**, 321 (2002).
[8] G. V. Lewis and C. R. A. Catlow, J. Phys. C **18**, 1149 (1985).
[9] K. Doll, M. Dolg, and H. Stoll, Phys. Rev. B **54**, 13 529 (1996).
[10] J. F. Ziegler, J. P. Biersack, and U. Littmark, *The Stopping and Range of Ions in Solids* (Pergamon, New York, 1985), Vol. 1.
[11] W. T. Rankin and J. A. Board, Jr., in *Proceedings of the 1995 IEEE Symposium on High Performance Distributed Computing* (IEEE Comput. Soc. Press, Los Alamitos, CA, 1995), p. 17.
[12] B. Park, W. J. Weber, and L. R. Corrales, Nucl. Instrum. Methods Phys. Res., Sect. B **166–167**, 357 (2000).
[13] G. Busker *et al.*, Nucl. Instrum. Methods Phys. Res., Sect. B **171**, 528 (2000).
[14] T. Sonoda, C. Kinoshita, and Y. Isobe, Ann. Phys. (Paris) **20**, C3-33 (1995).
[15] E. A. Kotomin *et al.*, Defect Diffus. Forum **143–147**, 1231 (1997).
[16] F. Montalenti, B. P. Uberuaga, G. Henkelman, and A. F. Voter (to be published).
[17] G. Henkelman and H. Jónsson, J. Chem. Phys. **111**, 7010 (1999).
[18] G. Kresse and J. Hafner, Phys. Rev. B **47**, 558 (1993); **49**, 14 251 (1994); G. Kresse and J. Furthmüller, Comput. Mater. Sci. **6**, 15 (1996); Phys. Rev. B **54**, 11 169 (1996).
[19] G. Kresse and J. Joubert, Phys. Rev. B **59**, 1758 (1999); P. E. Blöchl, Phys. Rev. B **50**, 17 953 (1994).

PHYSICAL REVIEW B **71**, 104102 (2005)

Dynamical simulations of radiation damage and defect mobility in MgO

B. P. Uberuaga,[1] R. Smith,[1,*] A. R. Cleave,[2] G. Henkelman,[1] R. W. Grimes,[2] A. F. Voter,[1] and K. E. Sickafus[1]
[1]*Los Alamos National Laboratory, Los Alamos, New Mexico 87545, USA*
[2]*Department of Materials, Imperial College, Prince Consort Road, London SW7 2BP, United Kingdom*
(Received 24 June 2004; revised manuscript received 4 October 2004; published 3 March 2005)

Collision cascades are investigated in MgO at energies ranging from 400 eV to 5 keV. Initial energy is imparted to the principle knock-on atom in the lattice and the cascade development is tracked using classical molecular dynamics. Temperature accelerated dynamics is performed on representative defects to follow the behavior to experimental time scales. Molecular statics is used to calculate basic properties of these defects, while density functional theory calculations are used to verify the potential. In the cascades performed at the lowest energy, the lattice either reforms perfectly or, if residual defects remain, these consist of isolated interstitials and vacancies and charge-neutral Mg-O divacancies and di-interstitials. As the energy is increased to 5 keV, isolated interstitials and di-interstitials remain the most common defects but more vacancy clustering can occur and interstitial defects consisting of up to seven atoms have been observed. Molecular statics calculations find that the binding energy per atom of the interstitial clusters increases from 3.5 to over 5 eV as the size increases from 2 to 16 atoms. Long-time-scale dynamics reveal that vacancies essentially never move at room temperature but that some interstitial clusters can diffuse quickly. Although tetrainterstitial interstitial clusters are essentially immobile, there is a long-lived metastable state of the hexainterstitial that diffuses one dimensionally on the nanosecond time scale at room temperature.

DOI: 10.1103/PhysRevB.71.104102 PACS number(s): 61.72.Ji, 61.72.Cc, 61.80.Az, 61.82.Ms

INTRODUCTION

Radiation effects in materials have received much attention, both experimentally and theoretically, for a number of years. Ideally, one would like to combine the results of both to form a more detailed understanding of radiation damage. Because of the disparity in the time scales involved in each approach, however, this is often difficult to do. A typical molecular dynamics (MD) simulation of radiation damage follows the evolution of an isolated collision cascade over picosecond (ps) time scales, which is sufficient to observe the collisional phase of the cascade and to identify characteristic features of the residual defects left by the cascade process (see, e.g., Ref. 1). However, the behavior of a real material is determined not only by the number and nature of the residual defects associated with a cascade event, but also by the long-time evolution of those defects. In particular, over time scales much greater than ps, residual defects can both annihilate and aggregate. Annihilation events lead to radiation tolerance, as they remove the damage formed in the cascade; aggregation events, on the other hand, decrease the probability for annihilation and consequently exacerbate radiation damage susceptibility. To accurately predict radiation damage response in a material, it is necessary to simulate longer time scale processes such as defect mobility, annihilation, and aggregation. We recently presented theoretical results on radiation damage in MgO, where we began to bridge this time scale gap.[2] In this paper, we expand on that initial report, discussing in more detail our results as well as their implications.

While we are interested in the question of radiation damage in oxides in general, here we focus on the specific oxide magnesia (MgO). There are a number of reasons why we chose MgO for this initial study. First, MgO is a simple oxide and should be more amenable to study than more complicated oxides. Second, MgO is a classic engineering ceramic with well-understood properties, and its radiation damage behavior has been the subject of numerous experimental and computational investigations. Finally, well established, good quality empirical potentials exist for MgO. Of course, oxides in general are very important technologically. For example, they are the conventional nuclear fuel form used in light water reactors (UO_2 and mixed oxides[3]) and are attractive as insulators for fusion reactor diagnostics.[4] Also, there is growing interest in using oxides as host materials for the immobilization and long-term storage of toxic radionuclides such as the transuranics found in spent nuclear fuel.[5,6]

The computational procedure used here consisted of four components. As detailed below, we first generated collision cascades in MgO at selected energies using MD for a few ps. We adopted representative defect configurations from the cascades and used these as starting configurations for long-time simulations via temperature accelerated dynamics (TAD).[7,8] We also used static energy minimization to assess the relative stability of defects observed in MD or TAD simulations against alternative crystallographic arrangements of the same defect. Finally, key findings were verified using the higher-quality description afforded by density functional theory (DFT).

In this paper, we follow up on the presentation given in Ref. 2. In Sec. I, we describe the methodologies used in this study. We provide details on the molecular dynamics (MD) simulations, the molecular statics calculations, and, along with a brief description of the algorithm, the temperature accelerated dynamics (TAD) simulations. In Sec. II, we present the results of these simulations. We begin with the results of the cascade simulations performed via MD. We then apply molecular statics and TAD to representative defects found in the cascade simulations to better understand both their static and dynamic properties. We discuss the im-

TABLE I. The Buckingham parameters for the Mg-O interaction.

	r_a (Å)	r_b (Å)	ρ (Å)	A (eV)	C (eV/Å^6)
Mg-Mg	0.5	1.01	0	0	0
Mg-O	0.3	0.8	0.2945	1428.5	0
O-O	0.5	1.01	0.149	22764.0	27.88

plications this study has on the understanding of radiation damage in MgO, as well as some of the limitations of this work, in Sec. III. Finally, we summarize and conclude.

I. METHODOLOGY

A. Cascade simulations

The potential used in the following work is based on that given by Lewis and Catlow.[9] It is pairwise additive and consists of two parts: an electrostatic part and a standard Buckingham term.[10] For the cascade simulations, where, because of the energetic collisions, the distances between atoms can become very small, this potential was modified by adding a screened Coulomb potential for small particle separation,[11] smoothly joined to the outer potential so that continuous first and second derivatives were preserved. A smooth cutoff of the Buckingham potential term at an interatomic distance greater than r_0 was also implemented. Thus calculation of the overly attractive forces for small separation and the nonelectrostatic part for large separation can be avoided.

Three different ion-ion interactions are required for this system. The Mg^{2+}—Mg^{2+} interaction is purely Coulombic. For O^{2-}—O^{2-}, in addition to the Coulombic interaction, we use a Buckingham potential which includes a van der Waal's interaction[9] together with an electrostatic term. For Mg^{2+}—O^{2-} the van der Waal's term is assumed to be zero. The cutoff r_0 was set to 8 Å for the O—O interactions and 5.5 Å for Mg—O interactions. The original potential as given in Ref. 9 also includes a polarizable shell. In the MD and TAD simulations reported here we do not include shells, using instead a rigid-ion approximation. However, we have included shells in some of the molecular statics calculations of isolated defects for comparison and have found that they do not qualitatively change the results presented here.

As mentioned above, to avoid having a strong electrostatic attraction for close particle separation, the interactions were modeled using the Universal ZBL potential[11] smoothly splined to the Buckingham potential and the electrostatic term with continuous first and second derivatives. The potential for the Mg—O interactions is summarized in Eq. (1):

$$V = \begin{cases} \text{ZBL}, & r_{ij} < r_b, \\ \exp(f_1 + f_2 r_{ij} + f_3 r_{ij}^2 + f_4 r_{ij}^3 + f_5 r_{ij}^4 + f_6 r_{ij}^5), & r_b \leqslant r_{ij} < r_a, \\ A \exp\left(-\dfrac{r_{ij}}{\rho}\right) - \dfrac{C}{r_{ij}^6} + E_P, & r_a \leqslant r_{ij} < r_0, \\ E_P, & r_{ij} \geqslant r_0, \end{cases} \tag{1}$$

where $E_P = \pm Z_j e / 4\pi\epsilon_0 r_{ij}$ is the electrostatic term and r_{ij} is the interatomic spacing between atoms i and j. The constants in the electrostatic part have their usual meaning. The parameters for the Buckingham potential are given in Table I and those for the spline to the ZBL potential in Table II.

This model does not account for charge transfer. Specifically, we do not account for defects such as F^+ and F centers (anion vacancies with one and two trapped electrons, respectively) in our calculations. An anion vacancy in our model is formally an F^{++} center with no trapped electrons. The same is true for cation vacancies. We will discuss the implications of this on our results below.

We use the fast multipole method implemented by Rankin[12] to calculate the long-range Coulombic interactions in the MD simulations while, in the TAD simulations, we employed standard Ewald sum techniques. Although the fast multipole method has a similar scaling to the Ewald sum techniques for the system sizes studied here, it is more flexible since it does not rely on periodic boundary conditions, although periodic boundary conditions can be implemented if desired. In the implementation of the algorithm we choose not to impose periodic boundary conditions but instead to use a charge-neutral cube with charge-neutral {100} faces and embed the active part of the crystal in two fixed outer

TABLE II. The parameters for the spline to the ZBL interaction.

	f_1	f_2	f_3	f_4	f_5	f_6
Mg-Mg	14.451	−47.798	122.421	−176.000	125.130	−34.148
Mg-O	13.739	−60.640	233.169	−491.210	499.133	−196.197
O-O	−0.913	64.435	−209.550	295.875	−194.796	48.998

layers. The reason for choosing this embedded approach as opposed to periodic boundary conditions was just a matter of computational convenience. The fast multipole method is more efficient for an embedded geometry than for a periodic geometry. In principle, this geometry could result in sound waves reflecting from the boundaries, though similar issues would exist for periodic boundary conditions. In fact, for MgO, because the barriers for diffusion are typically high relative to the energy in any reflected wave, we expect little to no impact from the fixed boundaries. A few tests in which we thermalized the boundary layers resulted in very similar results. However, we have also taken care in choosing the sizes of our simulation cells, as will be addressed below. All cascade simulations were carried out at an initial temperature of 0 K.

Previous MD work has indicated[13] that the displacement energy threshold in MgO is very high: about 65 eV for an O primary knock-on atom (PKA) and about 90 eV for the Mg PKA. We obtain similar values with this potential.

Primary knock-on atoms at energies of 400 eV, 2 keV, and 5 keV were investigated. The small value of 400 eV was chosen to investigate the types of defects that form when the energy is near the displacement threshold, where the defects are expected to be small in number. Values larger than 5 keV require more computational resources and have not been studied at this time. Trajectories were evenly distributed between PKAs of both O and Mg and run for up to 8 ps, or until the defects had thermalized. Initial trajectory directions were randomly distributed over a solid angle representative of the crystal symmetry. In total 20 trajectories were run at 400 eV, and 12 each for the 2 keV and 5 keV PKA. The actual simulations consisted of imparting a kinetic energy of either 400 eV, 2 keV, or 5 keV to the primary knock-on atom. The dynamics of the system with this extra kinetic energy were evolved in time using standard molecular dynamics techniques including the velocity Verlet algorithm for time integration, linked neighbor lists to achieve order N scaling, and a variable time step dependent on the maximum kinetic energy in the system; see Ref. 14 for details.

A word should be said about the size of the systems studied. These varied from 4000 to 160 000 atoms depending on the size and extent of the cascade. We verified that the atoms displaced by the cascade were sufficiently far away (at least four nearest-neighbor distances) from the outer boundary of the embedded geometry, thus ensuring that effects due to interaction with the boundary were minimal. In the 400 eV cascades, the maximum kinetic energy imparted to atoms near the boundary was only 0.05 eV, too small to activate migration in this system. The cells do tend to heat up because of the added energy. For example, in the case of the 400 eV PKAs, the temperature of the system increased to about 370 K. This could accelerate the recombination process, compared to $T=0$ K, but in a way that should be consistent with a system at finite temperature. We are interested in longer-time dynamics at $T=300$ K, so the systems that went above $T=300$ K could bias the results slightly, but the acceleration of events for a few ps at this higher T is probably negligible. For the higher energy cascades, there was less heating of the system, leading to final temperatures below $T=300$ K.

B. Temperature accelerated dynamics

To follow the long time behavior of the defects seen in the cascade simulations, temperature accelerated dynamics was applied to representative defect structures. TAD[7,15] is one of a number of accelerated molecular dynamics techniques[8] that allow for the simulation of much longer time scales than conventional MD. The TAD algorithm involves running MD at a high temperature T_{high}, typically much higher than the temperature of interest T_{low}, in a way that constrains the dynamics to the current state of the system (referred to as basin constrained MD, BCMD). The times of events seen at this high temperature are extrapolated to times at T_{low}. The BCMD procedure is continued until the stopping criteria is met. This stopping criteria depends on two parameters—δ, the uncertainty of missing an event and ν_{min}, an assumed minimum prefactor in the system. These two parameters thus control the accuracy of a TAD simulation. Once the stopping time has been reached, the event that occurs earliest at T_{low} is then accepted and the entire process repeated in the new state. The extrapolation of event times from T_{high} to T_{low} is exact if harmonic transition state theory holds for the system being studied at both temperatures. It requires knowledge of the energy barrier for the event, which we find using the nudged elastic band method.[16,17]

A critical requirement of the TAD algorithm is detecting transitions from the current state. In these simulations, a transition was declared if, upon minimization, any atom had moved more than 0.25 Å from the minimum of the current state.

The system sizes that can be studied with TAD are smaller than those accessible with conventional MD. In the work described here, TAD was applied to representative defects observed to form in the larger MD simulations, but in a reduced system size containing 512 ions in a periodic cell. A few simulations on periodic cells containing 1728 atoms were performed to ensure that effects due to periodic boundary conditions were not significant, which was indeed the case for the simulations reported here.

In MgO, the barriers for different defects to diffuse vary greatly, ranging from 0.3 to over 2 eV. To enhance the speed of the TAD simulations, we have employed a recently developed extension to TAD that incorporates the dimer method.[18] This so-called dimer-TAD algorithm[19] uses the dimer method to find the minimum barrier to leave the state. This minimum barrier is then used to redefine the time at which the BCMD can be stopped, often reducing it dramatically. This new stopping criteria no longer depends on δ and ν_{min}. Instead, it depends on the minimum barrier in the system. This new TAD algorithm also allows us to tune T_{high} for the current state based on the minimum barrier, resulting in typical values between 300 and 2000 K. In the simulations reported here, we used $T_{\mathrm{low}}=300$ K. We performed ten dimer searches per state, focused on the "active" region of the system, or that part of the system in which interstitials or vacancies resided. We can never be 100% certain that the dimer searches have found the lowest barrier for escape from the state. In the simulations reported here, the BCMD found a lower barrier than the dimer searches about once per 17 escapes. When this occurred, the difference between the dimer-found minimum barrier and the lower discovered barrier was usually small, on the order of 0.05 eV or less. Such errors would affect the time scales over which the simulations occurred and the particular events a simulation followed, but the final structures and their migration barriers reported here are likely unaffected.

For consistency with the molecular statics calculations described below, which were performed at the minimum-energy lattice constant of the potential, all TAD simulations were also performed at the fixed volume corresponding to this minimum-energy lattice constant. Although the finite-temperature TAD simulations were thus under pressure, the temperature dependence of each activated process at $T=300$ K (as well as at the higher temperature used in TAD) is given by the same barrier height computed in the molecular statics.

Finally, investigating charged defects is more computationally challenging than neutral defects. This is because a net charge resides within the simulation cell, so standard Ewald techniques and periodic boundary conditions are no longer applicable and the Coulomb sum is instead done directly on cells with free boundaries. Such cells require a layer of frozen material at the boundary with a thickness equal to the cutoff of the potential which, in turn, results in cells that are much bigger. For the charged tri-interstitial defects investigated in the TAD simulations reported below, we used a cell containing 1728 atoms, within which 512 atoms were allowed to move. (The skin size was chosen to be one unit cell in each direction. For example, the 512-atom interior consists of the 8 atom unit cell replicated 4 times in each dimension. The total cell is thus the unit cell replicated 6 times in each direction, so that the moving interior has a skin of one unit cell on each face.) We performed tests with even larger cells on key barriers and found that this size gave values to within 0.05 eV of the converged values.

C. Molecular statics

In the molecular statics calculations, the perfect lattice structure and energy is determined by starting with the experimental values and adjusting both ion positions and lattice vectors, using the Newton-Raphson minimization procedure, until each ion experiences close to zero force (the short-range parameters were chosen to reproduce the lattice structure very closely). The internal energy of a defect, or a cluster of defects, can then be calculated via the Mott-Littleton approximation.[20] This begins with the relaxed perfect lattice, which is partitioned into spherical concentric regions. A defect is then placed in the center of region I. All ion positions in region I are allowed to relax in response to the defect, and interactions are summed over all pairs of ions within this region. Here the radius of region I is limited to 12.1 Å since the calculated defect energies remain constant at increased radius values, i.e., the defect energy has converged with respect to region size. The outer region II extends to infinity and responds to the defect as a dielectric continuum according to the Mott-Littleton approximation. To ensure a smooth transition between regions I and II, an interfacial region IIa, of radius 32.9 Å, is introduced. Ion positions within region IIa are allowed to vary, subject to forces determined via the Mott-Littleton approximation; however, the interaction energies between region I and II ions are calculated explicitly. Here calculations are carried out using the code CASCADE.[21]

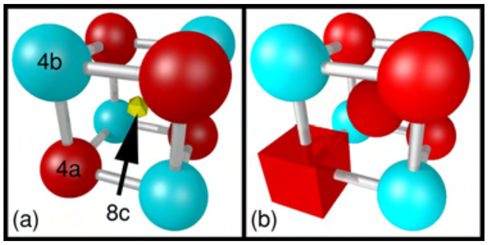

FIG. 1. (Color online) (a) The basic structure of the MgO crystal. O atoms (dark/red color) occupy the 4*a* Wyckoff sites and Mg atoms (light/blue color) occupy the 4*b* Wyckoff sites of the two interpenetrating tetrahedra. The interstice site lies in the middle of this repeating unit, in the 8*c* site (represented by the octahedron). (b) Structure of the most elementary Frenkel pair, in which one of the atoms is removed from a lattice site (represented by the cube) and placed in the 8*c* site. This structure is not stable in MgO. The Frenkel pair must be separated by four nearest-neighbor sites before it is stable.

These perfect lattice calculations are referred to as "static" since vibrational entropy contributions are not included in the model. The energies calculated therefore relate, via the quasiharmonic approximation, to the temperature of the lattice to which the potential parameters were fitted, in this case, room temperature. For further details see Ref. 22. Because we are interested in room temperature in this study, we kept our systems at the minimum-energy lattice constant predicted by this potential.

II. RESULTS

A. MD simulations for large systems and picosecond time scales

MgO belongs to the space group $Fm\overline{3}m$. The structure of the basic repeating unit, shown in Fig. 1(a), consists of two interpenetrating tetrahedra in which O atoms are placed on the corners of one tetrahedron, in the 4*a* Wyckoff sites, and Mg atoms are in the corners of the other tetrahedron on 4*b* sites. The interstices of this structure lie in the center of this octant of the unit cell, or on the 8*c* sites. Figure 1(b) shows the structure of the simplest Frenkel pair for this system in which one of the atoms is removed and placed in the 8*c* site. In MgO, this particular configuration of the Frenkel pair is not stable—it collapses to the perfect crystal.

Figure 2 shows a typical cascade simulation in MgO for a PKA energy of 400 eV. At $t=0$, the initial knock-on event occurs. Very quickly, the damage saturates ($t=80$ fs) and settles ($t=260$ fs), after which only a few isolated defects remain. In this particular case, these defects consist of two vacancies and two interstitials, one of each type [Fig. 2(b)]. Due to the strong electrostatic attraction between the oppositely charged interstitials, they move toward one another and by $t=6.5$ ps they have combined to form an MgO di-interstitial [Fig. 2(c)].

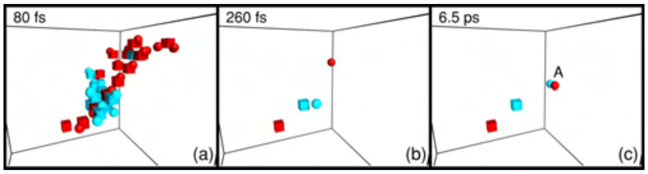

FIG. 2. (Color online) The defects in a cascade generated from a 0.4 keV O PKA. The color scheme, used in this and all subsequent figures, is dark (red) for O defects and light (blue) for Mg defects. Spheres indicate interstitials, or atoms more than 0.8 Å from a lattice site, and cubes indicate vacancies, or lattice sites with no atom within 0.8 Å. (a) At $t=80$ fs, the number of displaced atoms peaks. (b) By $t=260$ fs, most of the defects have recombined and only a few isolated defects remain. (c) By $t=6.5$ ps, the interstitials have formed a di-interstitial (labeled A). Taken from Ref. 2.

Figures 3 and 4 illustrate other scenarios occurring for 400 eV. In Fig. 3, as in Fig. 2, after the initial cascade has settled, a Mg interstitial is situated one lattice spacing from a Mg vacancy. In contrast to the simulation of Fig. 2, in which the Mg interstitial combines with an O interstitial to form a stable di-interstitial, in the case of Fig. 3, the O interstitial hops toward the Mg interstitial to form a di-interstitial which is still very close to the original Mg and O vacancies and soon annihilates with them. Whether the interstitial annihilates with a vacancy, as shown in Fig. 3, or aggregates with another interstitial depends on the complex electric field created by all of the defects in the vicinity.

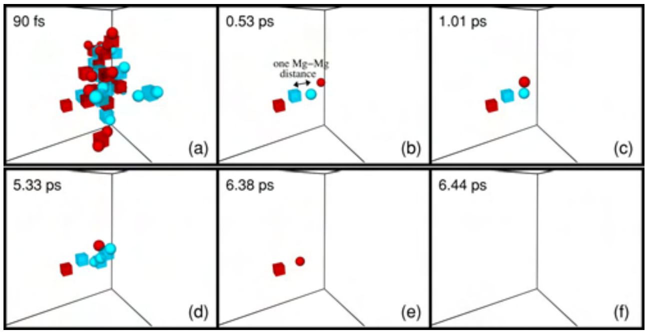

FIG. 3. (Color online) Recombination events in a cascade generated by a 400 eV PKA in MgO. Spheres indicate interstitials, or atoms more than 0.8 Å from a lattice site, and cubes indicate vacancies, or lattice sites with no atom within 0.8 Å. (a) The peak number of displacements at 90 fs. (b) 0.53 ps where most of the defects have recombined. At this stage the Mg interstitial is only 1 lattice unit from the Mg vacancy. Normally, this would be an unstable position for the Mg interstitial, but the nearby O interstitial and O vacancy act to partially cancel the attractive pull of the Mg vacancy, stabilizing the Mg interstitial in this position. (c) After 1.01 ps an MgO di-interstitial forms. (d) The Mg atom in the di-interstitial recombines with the nearby vacancy after 5.33 ps (the large number of objects present in this figure illustrate the number of atoms involved in the process). (e) The remaining O atom hops closer to the remaining O vacancy after 6.38 ps. (f) The final event leading to complete recombination occurs after 6.44 ps.

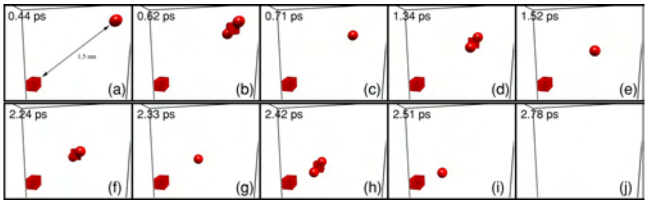

FIG. 4. (Color online) The recombination of an O^{2-} interstitial, generated from a 400 eV O PKA, with an O vacancy. (a) 0.44 ps after the start of the cascade, by which time the cascade has settled, leaving an isolated interstitial and vacancy separated by 1.5 nm. (b) Motion via the ⟨111⟩ interstitialcy event after 0.62 ps. (c) Interstitial moves to a new 8*c* site, 1.26 nm from the vacancy after 0.71 ps. (d) Motion via the same ⟨111⟩ mechanism to new site after 1.34 ps. (e) 0.9 nm from the vacancy after 1.52 ps, (f) 2.24 ps, and (g) 0.68 nm from the vacancy after 2.33 ps; (h) 2.42 ps, (i) 2.51 ps, (j) The event leading to final recombination occurs after 2.78 ps. The last recombination event occurs quickly, appearing as a two-stage hop and not directly via the ⟨111⟩ mechanism. However, further analysis reveals that events such as these are really one event, characterized by one saddle point (see the discussion in Sec. II C).

In another simulation, illustrated in Fig. 4, an O interstitial is formed ~15 Å from the vacancy. In many cases, interstitials that were this far away from a vacancy were stable over picosecond time scales. However, in this particular case, perhaps because of the residual thermal energy from the PKA event ($T=370$ K, as discussed above), the interstitial jumps to the vacancy site and recombines. The main mechanism is to move between 8*c* sites [see Fig. 1(a)] in the ⟨111⟩ direction via a collinear interstitialcy mechanism, in which the interstitial in one 8*c* site replaces a lattice atom which simultaneously moves to another 8*c* site. This is in agreement with the prediction of Ref. 23.

In general, for the 400 eV PKA, only a small number of defects form due to a tendency for nearby defects to recombine over the time scale of a few picoseconds. Indeed, previous work on MgO has shown that Frenkel pairs are stable only if the separation is greater than the fourth-nearest-neighbor distance.[23] As seen in the snapshots from the three cascades shown in Figs. 2–4, the only defects observed were isolated vacancies, isolated interstitials or di-interstitial pairs where an Mg and an O atom were situated at adjacent 8*c* sites so that the di-interstitial axis was always parallel to the cell edges, or in ⟨100⟩ directions. In only one case at 400 eV was a divacancy formed.

The results of all of the cascade simulations are summarized in Table III. The lattice completely or very nearly completely reannealed within 8 ps of the impact event in 13 of the 20 trajectories investigated at 400 eV. In four simulations a single Frenkel pair formed that was sufficiently well separated—by at least 1 nm—so that it had not moved at all over the 8 ps time scale. MgO di-interstitials formed three times. These di-interstitials were stable over the 8 ps time scale when separated by more than 2 lattice units (1 lattice unit=4.1986 Å with the Lewis and Catlow potential) from a nearby vacancy. Summarizing all of these simulations, we saw about one Frenkel pair formed for every two simulations. However, the number of atoms displaced from their original lattice sites and moved to others is about twenty times larger, averaging about 9 per trajectory.

When the PKA energy is increased, the same types of defects seen at 400 eV still predominate, typically separated

TABLE III. The total number of Frenkel pairs and principal defect types (monointerstitials and di-interstitials and monovacancies and di-vacancies) for PKA energies of 0.4, 2, and 5 keV remaining after the collisional phase ($t = 8$ ps) of a cascade. In addition, one tri-interstitial formed at 2 keV and 4 tri-interstitials, one tetrainterstitial, and one 7-interstitial cluster formed at 5 keV. Taken from Ref. 2.

PKA energy (keV)	No. of trajs.	number of defects					
		Frenkel pairs	monoint. O/Mg	monovac. O/Mg	di-int	di-vac	perfect lattice
0.4	20	10	3/1	5/3	3	1	13
2	12	84	21/24	33/30	15	6	0
5	12	216	57/62	78/80	39	15	0

by much larger distances, though some clustering of defects also begins to occur. Figure 5 shows examples of this for two typical cascades at 2 keV. As in the case of 400 eV cascades, the di-interstitial pairs form not by direct collision but rather over picosecond time scales due to the strong Coulomb interaction between nearby interstitials. The vacancy clusters, however, form during the collisional phase of the cascade and are immobile. Indeed, in all of the simulations we have performed at all energies, we have never seen a vacancy move during the 8 ps collisional phase. At 2 keV, an average of 7 Frenkel pairs remain after 8 ps with an average of 48 atoms displaced from their initial lattice sites. In 12 trajectories, 15 MgO di-interstitials formed in addition to 20 isolated O and 20 isolated Mg interstitials. Out of the 12 trajectories, a single O-Mg-O tri-interstitial also formed, which, like the di-interstitial, consisted of linear interstitials located at adjacent 8*c* sites parallel to a unit cell axis. There were also a few examples of vacancy clusters. Specifically, five divacancies and one trivacancy cluster were observed.

One interesting observation at all energies was that trajectories initiated in either {110} or {100} planes, irrespective of direction, produced defects which were confined to the original plane of propagation or one lattice unit on either side. The defect clusters of size three and larger observed in the cascades occurred generally for PKA atoms initiated in these low index planes.

Typical defect distributions at the end of a 5 keV cascade are shown in Fig. 6. At this energy, an average of 18 Frenkel pairs survived after 8 ps of simulation time, with an average of 124 displaced atoms produced in the collisional phase of the cascade per trajectory. Compared to lower energy cascades, while isolated defects still predominate, there is evidence of more defect clustering. Out of the 12 trajectories simulated, 62 Mg interstitials and 57 O interstitials survived. In addition to these isolated interstitials, there were 39 MgO di-interstitials—an average of more than 3 per cascade—and 4 tri-interstitials, two each of O-Mg-O and Mg-O-Mg. Both of these tri-interstitial structures had the same linear structure. In one case an interstitial cluster of 4 atoms formed and in another case we saw a cluster containing 7 interstitial

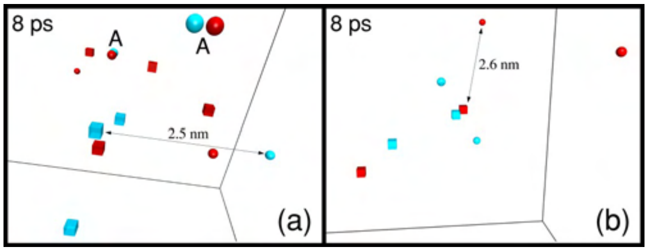

FIG. 5. (Color online) Examples of the spread-out residual damage after the collisional phase of the cascade at 2 keV. (a) The image shows three separated Mg vacancies and four O vacancies. There are two MgO di-interstitials (labeled A), one Mg interstitial, and two O interstitials. (b) In this case, only well-separated monointerstitials and vacancies occur.

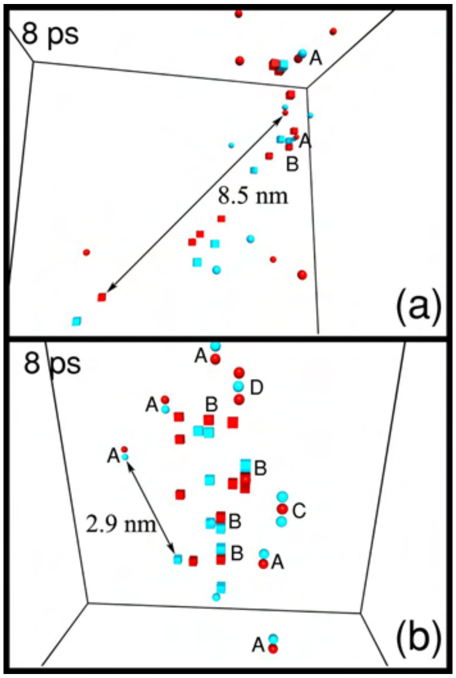

FIG. 6. (Color online) Typical defects remaining after 8 ps for a PKA energy of 5 keV. Defects are labeled as (A) di-interstitials, (B) divacancies, (C) Mg-O-Mg tri-interstitials, and (D) O-Mg-O tri-interstitials. (a) The image shows two MgO di-interstitials and one divacancy in addition to isolated interstitials and vacancies. (b) In this case the cascade is more compact and there are four divacancies in addition to five di-interstitials, two tri-interstitials, three O interstitials, and one Mg interstitial. The distance between the two tri-interstitials is 1.9 nm. The length of each side of the cubic simulation cell, shown for perspective purposes, is 11.9 nm.

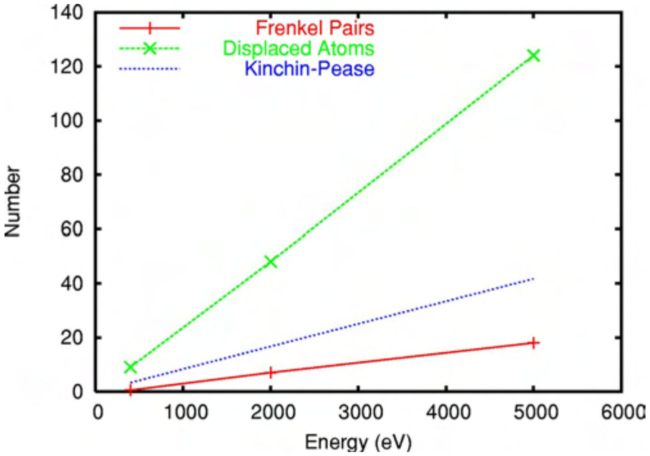

FIG. 7. (Color online) The number of defects and displaced atoms as a function of PKA energy. The displacement energy threshold for the Kinchin-Pease formula was taken as $E_D = 60$ eV. The lines are guides for the eye.

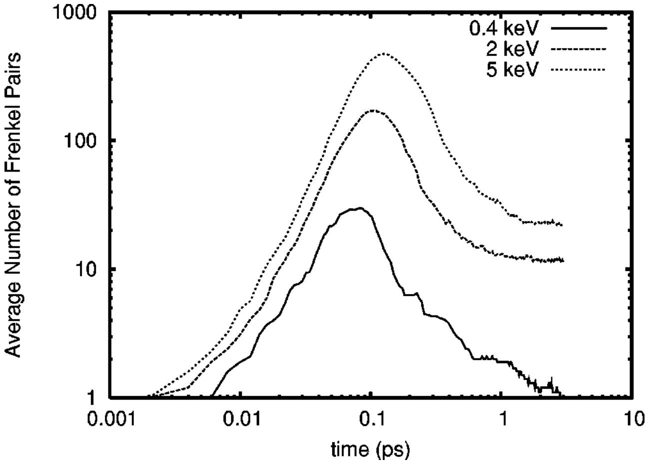

FIG. 8. The average number of Frenkel pairs versus time in cascades with PKA energies of 400 eV, 2 keV, and 5 keV. The average time of peak damage increases with PKA energy, as does both the peak number of Frenkel pairs and the number of residual Frenkel pairs.

atoms. Clustering of vacancies was also more prevalent: 15 divacancies, 6 trivacancies, and one case of an 8 atom vacancy cluster were observed. For the 2 and 5 keV cascades, the isolated interstitials do not so readily recombine with nearby vacancies in the collisional phase of the cascade compared to the 400 eV cascade. This is probably due to the longer distances between vacancies and interstitials and the complex Coulomb field due to the larger number of defects formed.

Over the energy range 400 eV to 5 keV, there is an almost linear dependence with energy for both the total displaced atoms and the number of residual Frenkel pairs, as shown in Fig. 7. Assuming a displacement energy threshold E_d of 60 eV, the number of Frenkel pairs remaining after the cascade for all three energies is about 45% of the Kinchin-Pease value, similar to the result for metals.[24]

Finally, in addition to an increase in both the number of residual Frenkel pairs and the maximum number of Frenkel pairs produced during the cascade with PKA energy, the time at which the damage peaks also increases. This is illustrated in Fig. 8. The average time of peak damage increases from 82 fs at 400 eV to 126 fs at 5 keV.

B. Defect energies via molecular statics

The binding energy of isolated small interstitial clusters and vacancies was examined using static energy minimization via a Mott-Littleton approach similar to that used in Ref. 25 and compared to those occurring at the end of the cascades. Here, we have defined the binding energy as $E_{\text{isolated defects}} - E_{\text{cluster}}$. The results for the most stable configurations are shown in Table IV. Some of these results have been previously reported in Ref. 2. In addition to those results, we have calculated the binding energy for clusters containing 12, 14, and 16 interstitials. The binding energy increases from 3.49 eV per atom for the Mg-O di-interstitial to about 5.2 eV per atom for clusters containing 10 or more interstitials. Although the isolated interstitials at the 8*c* site were found to be the most stable configuration, ⟨110⟩ split interstitials of both types—Mg and O—were also found to be stable, but higher in energy by over 0.5 eV. The energy barrier for this metastable structure to decay to the 8*c* structure is very small—less than 0.01 eV—and consequently these were never observed in the collision cascades. In contrast the energy barrier for migration of O^{2-} between 8*c* sites was found to be 0.40 eV and for Mg^{2+} it was 0.32 eV.

While we find the 8*c* site to be most stable for a charged interstitial, others have found that this is not the most favorable site for the *neutral* interstitial. Different electronic structure calculations find either the O ⟨111⟩ split interstitial[26] or the O ⟨110⟩ split interstitial[27] as the most stable neutral interstitial. While the source of the discrepancy between these two studies is not clear, it may at least be partially due to differences in cell size.[23] In our study, because of the limitations of our model, the interstitial is fully charged and prefers the 8*c* site.

TABLE IV. The energy of the most strongly bound isolated small clusters in MgO found to date, up to size 8. The structures of the clusters containing 6 and 8 interstitials are shown in Fig. 9.

No. in cluster	defect type	geometry	energy (eV)	binding energy (eV/atom)
1	Mg_i	cell center	−10.63	
1	O_i	cell center	−11.90	
1	Mg_v		+24.73	
1	O_v		+25.47	
2	$(MgO)_i$	⟨100⟩	−29.50	3.49
2	$(MgO)_v$	⟨100⟩	+46.85	
3	$(MgOMg)_i$	⟨100⟩	−43.96	3.60
3	$(OMgO)_i$	⟨100⟩	−45.17	3.58
4	$(2Mg2O)_i$		−62.46	4.35
6	$(3Mg3O)_i$		−95.61	4.79
8	$(4Mg4O)_i$		−129.71	5.03

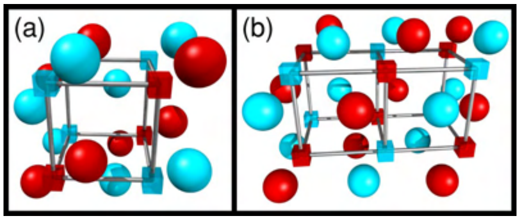

FIG. 9. (Color online) Ground-state structure of the (a) hexainterstitial and the (b) octainterstitial. The hexainterstitial is centered around one MgO fundamental structural unit (the bars and vacant lattice sites, represented by cubes) while the octainterstitial extends over two structural units. Each of the bars connecting the vacant sites lies along a ⟨100⟩ direction. In the hexainterstitial structure, six atoms have been inserted into the basic MgO structural unit, displacing the crystallographic atoms away from their lattice sites. The octainterstitial exhibits a similar structure in which eight atoms have been inserted into two MgO structural units.

As discussed below, the TAD simulations have revealed the ground state structure for the hexainterstitial and octainterstitial clusters. Shown in Fig. 9, the structure of the ground-state octainterstitial is an extended version of that of the hexainterstitial. This suggests that extended interstitial defects can be created by adding the basic building block seen in the hexainterstitial cluster, that is, a compact MgO di-interstitial pair. This common structural motif was extended to build interstitial clusters containing more than eight interstitials. All of these proved stable when relaxed, except for the dodecainterstitial cluster. In this case, the relaxation involves a twisting of the end of the cluster so that this end lies along a new ⟨100⟩ direction, forming an "L-shaped" structure in which each branch is composed of the motif seen in the hexainterstitial. This structure has a slightly higher binding energy than those of the neighboring interstitial cluster sizes. We have yet to determine what impact this structure has on the mobility of the dodecainterstitial cluster or if other cluster sizes also exhibit this lower energy structure.

We emphasize that we do not know for certain if the structures investigated for the larger cluster sizes are indeed the ground state structure, and the fact that the dodecainterstitial cluster exhibits a different structure suggests that it is very possible that even more compact structures will be more stable. However, as the number of possible cluster geometries grows exponentially with cluster size, it is very difficult to explore the structure space fully. The trends discussed here are not necessarily definitive. Even if these extended ⟨100⟩ structures are not the ground state, they are still very stable structures. Experimentally, under certain conditions, interstitial dislocation loops in MgO are seen to grow preferentially in the ⟨100⟩ direction and the defect clusters we see here may be precursors to the dislocation loops seen in experiment. However, more work needs to be done before any definite comparisons can be made.

C. Long time behavior via temperature accelerated dynamics

The cascade simulations described above can only follow the dynamics of the resulting defects for time scales on the order of ps. To truly understand the behavior of these defects, longer times must be simulated. We applied TAD to representative defect structures seen in the cascades to achieve experimental time scales.

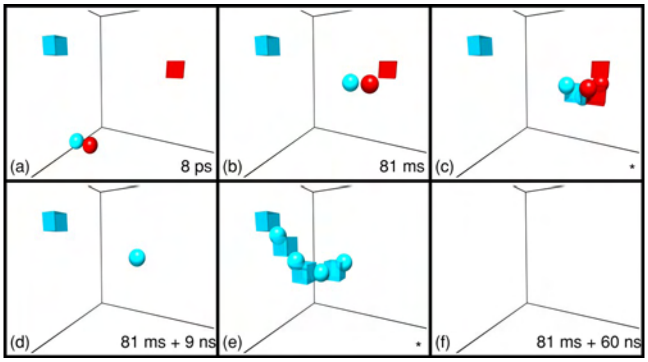

FIG. 10. (Color online) Results of a typical TAD simulation. (a) The initial configuration contains a di-interstitial and two vacancies, similar to the final state of Fig. 2(c). (b) By $t=81$ ms, the di-interstitial has diffused toward the O vacancy and, (c) via a concerted event involving several atoms, (d) the O atom of the di-interstitial annihilates the O vacancy 9 ns later. The remaining Mg interstitial then recombines with the Mg vacancy via a long-range, concerted mechanism involving many atoms (e) which results in the reformation of the perfect crystal (f) 51 ns after the first annihilation event. The asterisks indicate structures interpolated between the initial and final states of the events. See the text for discussion on the details of the event.

Figure 10 shows results from a long-time scale TAD simulation of the annealing, at 300 K, of the typical damage seen at 400 eV. The initial configuration is very similar to that seen in Fig. 2(c), consisting of two isolated vacancies and a di-interstitial. At 300 K, vacancies are immobile even on the time scale of centuries. In contrast, an isolated MgO di-interstitial, moving in ⟨111⟩ directions via a collinear interstitialcy mechanism, diffuses on the time scale of tenths of seconds with a barrier of 0.75 eV. In the presence of the vacancies, because of the strong electrostatic interactions, this barrier is reduced so that by $t=0.08$ s, the di-interstitial reaches the O vacancy and partly annihilates with the vacancy. The remaining Mg interstitial quickly (within 51 ns) finds the Mg vacancy, completing the annealing process and resulting in a perfect crystal.

The annihilation event shown in Fig. 10(e) is an interpolation between the states before and after annihilation occurs. The interpolation shows the concerted nature of the event in which four atoms are involved. The actual minimum energy path, found with NEB, shows a more complex behavior. Initially, the interstitial atom executes a hop very similar to the collinear interstitialcy mechanism describing isolated interstitial diffusion, with the saddle point geometry appearing very similar to that mechanism. Once the system passes over the saddle point, the three remaining atoms are moved by two successive interstitialcy hops, but the process is all downhill once the saddle has been cleared. There are no barriers for the subsequent hops. Thus, although the minimum energy path shows a sequence of three, seemingly independent hops, this is actually a single concerted event with

TABLE V. The energy barriers and event time scales for some of the typical defects observed in the collision cascades.

No. in cluster	species	barrier (eV)	event time at 300 K (s)	note
1	Mg_i	0.32	10^{-8}	
1	V_{Mg}	2.12	10^{21}	
1	O_i	0.40	10^{-7}	
1	V_{O}	2.00	10^{21}	
2	$(\mathrm{MgO})_i$	0.75	0.1	
		0.66	0.01	DFT
2	V_{MgO}	2.49	10^{27},	V_{O} hop,
		0.99	10^{3}	V_{Mg} catch up
2	V_{MgO}	2.53,	10^{27},	V_{Mg} hop,
		1.03	10^{3}	V_{O} catch up
3	$(\mathrm{MgOMg})_i$	0.59	10^{-4}	diffusion
		1.23		rotation
3	$(\mathrm{OMgO})_i$	0.61	10^{-4}	diffusion
		1.27		rotation
4	$(\mathrm{2Mg2O})_i$	1.68	10^{15}	
6	$(\mathrm{3Mg3O})_i$	0.24,	10^{-9}	metastable state
		0.33	10^{-8}	metastable state, DFT
		1.04	100	ground state
8	$(\mathrm{4Mg4O})_i$	0.66	0.01	metastable state
		1.70	10^{15}	ground state

one saddle point. Analysis of trajectories initiated from the saddle plane shows that this entire sequence takes place in roughly 0.5 ps.

From this and other TAD simulations, we find that, for small interstitial clusters, the migration energy tends to increase with cluster size. Isolated interstitials diffuse quickly, on the nanosecond time scale, with barriers of 0.32 eV for the Mg interstitial and 0.40 eV for the O interstitial. Di-interstitials are somewhat less mobile, diffusing on the time scale of a fraction of a second at 300 K with a barrier of 0.75 eV. As discussed below, the trend is broken for tri-interstitials, which, with a barrier of about 0.6 eV, diffuse faster than di-interstitials. However, tetrainterstitials are immobile, diffusing on a time scale of 10^8 yr. These tetrainterstitials can form when two di-interstitials meet during the diffusion process. The results of all of the TAD simulations are summarized in Table V and Fig. 11.

Tri-interstitials diffuse in a manner similar to the di-interstitial, though with a significantly lower barrier. We originally reported in Ref. 2 migration barriers of 0.79 eV and 0.80 eV for the Mg-O-Mg and O-Mg-O tri-interstitials, respectively. Those calculations used the free boundary geometry discussed above, but with the interior region consisting of $N=216$ moving atoms. More recently, we have improved upon those calculations and have found that the barriers are actually somewhat lower. For $N=512$ moving atoms, we find barriers of 0.59 and 0.61 eV for Mg-O-Mg and O-Mg-O, respectively. We have further tested the dependence of the diffusion barrier of Mg-O-Mg versus N. For $N=1003$, the barrier is 0.54 eV and remains essentially unchanged at $N=1731$. Thus, the value of 0.59 eV at $N=512$ is within 0.05 eV of the converged value. As with the di-interstitial structure, these tri-interstitial structures diffuse via moves in ⟨111⟩ directions, displacing three atoms from the lattice to form a new tri-interstitial via this collinear interstitialcy mechanism. For both the di- and tri-interstitials, diffusion via these ⟨111⟩ moves is isotropic; i.e., all eight ⟨111⟩ diffusion directions are accessible from a given trimer orientation.

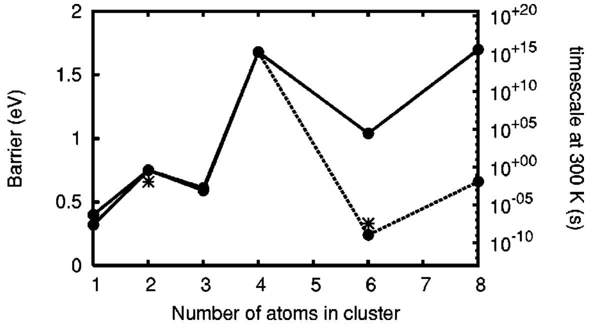

FIG. 11. Migration barriers for interstitial clusters versus cluster size. The time scale for diffusion at 300 K is also shown. The binding energy increases with the cluster size, while the energy barriers do not follow any obvious trend. The dashed line indicates barriers for metastable clusters. Asterisks indicate barriers calculated with DFT.

Both di- and tri-interstitials can also rotate to a new ⟨100⟩ direction. For the di-interstitial, this rotation mechanism has a barrier of 1.20 eV. In this process, the Mg ion of the di-interstitial remains in its original 8*c* site while the O ion displaces a lattice atom, very similar to a single interstitial hop. If the O ion remains fixed instead, the barrier for this rotation is very similar at 1.24 eV. For the tri-interstitials, the corresponding mechanism has a barrier of 1.23 eV for the Mg-O-Mg tri-interstitial and 1.27 eV for the O-Mg-O tri-interstitial. In this mechanism, one of the end atoms of the tri-interstitial remains stationary while the other two atoms displace lattice atoms in a way that results in a tri-interstitial aligned along a different ⟨100⟩ axis. These rotational mechanisms do not change the isotropic diffusive character of the clusters. However, they would allow the clusters to change orientation as they approach other defects, possibly affecting cluster aggregation.

The immobility of the tetrainterstitial suggests that when clusters of four atoms form, they might act as interstitial sinks. Surprisingly, however, this is not necessarily the case. For example, the hexainterstitial, formed when a di-interstitial encounters a tetrainterstitial, is mobile, diffusing with a barrier of 1.04 eV in its ground state (100 s time scale). The structure of this ground state is shown in Fig. 9(a). More interestingly, the hexainterstitial can also exist in a metastable state, 0.89 eV above the ground state, in which it diffuses much faster. Diffusion of this metastable

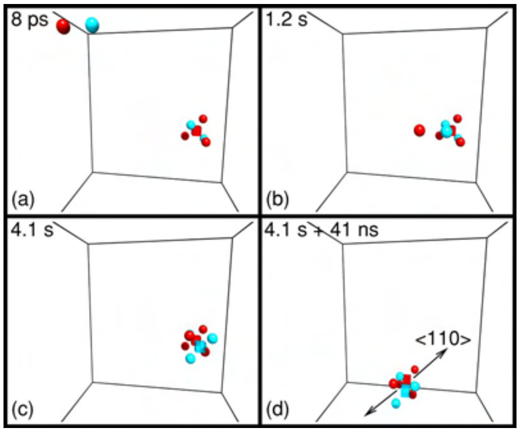

FIG. 12. (Color online) TAD simulation of the formation of a mobile hexainterstitial at 300 K. (a) A di-interstitial and tetrainterstitial begin about 1.2 nm apart. The tetrainterstitial contains four interstitial atoms, but an additional atom is displaced from its lattice site so that in this representation it appears to be composed of two Mg interstitials, three O interstitials, and one O vacancy. (b) $t = 1.2$ s; the di-interstitial has approached the immobile tetrainterstitial. (c) By $t = 4.1$ s, the combined cluster has annealed to form a persistent metastable state of the hexainterstitial. (d) This metastable form diffuses on the ns time scale with a barrier of 0.24 eV. The one-dimensional ⟨110⟩ diffusion direction is indicated. Taken from Ref. 2.

hexainterstitial occurs in two stages, with an overall barrier of 0.24 eV, but is limited to diffusion along a single ⟨110⟩ direction. At 300 K, this diffusion occurs on the nanosecond time scale. This metastable structure was found by running a TAD simulation that began with a di-interstitial and a tetrainterstitial, as illustrated in Fig. 12. When the two defects met, after some rearrangement, they formed the metastable hexainterstitial. The smallest barrier we have found to go from the metastable structure to the most stable hexainterstitial is about 1.3 eV, a process that takes years to occur at room temperature. This means that on the order of 10^{16} diffusion events will occur in the metastable state before it decays to the ground state. We do not know how often this metastable hexainterstitial will form versus the true ground state, but the fact that it did form in the single TAD simulation we performed on this di-interstitial plus tetrainterstitial encounter suggests that it will not be infrequent.

As discussed in Ref. 2, we find the behavior of the octainterstitial is similar to that of the hexainterstitial. A metastable structure diffuses in one dimension with a barrier of 0.66 eV (0.01 s time scale), trapped by a barrier of 1.52 eV against decay to the ground state, which diffuses with the larger barrier of 1.7 eV. It is tempting to speculate that yet larger clusters may also have interesting kinetic properties. The structure of the ground state of the octainterstitial, as described above and shown in Fig. 9(b), can be viewed as an extension of the hexainterstitial structure. One can imagine placing two hexainterstitials in adjacent cells and then removing any atoms which overlap. Such a construction gives the octainterstitial structure.

Finally, TAD simulations have also revealed that, as interstitial defects approach vacancies, annihilation occurs via long-range concerted events. In the case of a di-interstitial close to a vacancy, many atoms are involved in the transition which eventually annihilates part or all of the di-interstitial [see Figs. 10(e) and 10(f)]. Concerted events are also important in the diffusion of interstitial clusters, with the diffusion mechanism for the metastable hexainterstitial involving 12 atoms. That is, the metastable hexainterstitial diffuses via an interstitialcy mechanism in which all six atoms composing the cluster displace and replace six atoms in the lattice; these six displaced atoms then become the hexainterstitial on the other side of the saddle point.

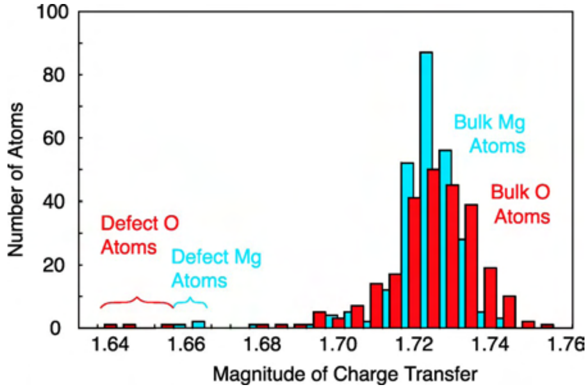

FIG. 13. (Color online) Bader decomposition of the DFT charge transfer in and around the metastable hexainterstitial cluster, relative to an isolated atom. In the bulk, each Mg atom has a net charge of 1.72 while each O atom has a net charge of −1.72, illustrated by the peak in the charge transfer (the location of the O values have been shifted slightly to higher charge transfer for clarity). The atoms in the metastable hexainterstitial cluster, labeled in the figure, transfer slightly less charge than the bulk.

D. Density functional theory

Previously,[2] we tested some of our empirical-potential results against DFT calculations, where we found that the formation energies of the di-interstitial and metastable hexainterstitial predicted by the empirical potential agreed with the DFT calculations to within about 8%—or 0.5 eV per atom in the cluster—while the diffusion barriers for these two species agreed to within 0.1 eV. The results for the barriers are included in Fig. 11.

This is very good agreement, giving us confidence that our results are not an artifact of the potential. To understand the origin of this good agreement, we have calculated the Bader charges[30,31] for the atoms in and around the metastable hexainterstitial configuration. In these calculations, as for those in Ref. 2, we employed the VASP code[28] with the PW91 functional and the projector augmented wave method[29] on supercells containing 216 lattice atoms and a plane wave basis with energies up to 400 eV. It was determined that a single Γ-point sampling of k space was sufficient to converge energies for this cell size. For example, increasing the k-point mesh to $2 \times 2 \times 2$ changed barrier heights by less than 0.001 eV.

The result of the Bader charge decomposition is shown in Fig. 13 in which the net charge transferred to or from each atom in the cell is given. In the bulk, Mg atoms transfer 1.72 electrons to O atoms. This value is about 0.3 electrons less than the formal charge of 2 electrons, supporting the validity of the ionic model for this system. The atoms composing the metastable hexainterstitial transfer slightly less charge, with the least amount of charge transferred being about 1.64 electrons. Thus, the amount of charge transferred in the atoms composing the defect is very similar to the charge transfer occurring in the bulk, possibly explaining why the ionic model does so well in describing these bulk defects.

The value for the charge transferred of 1.72 is less than the full charge of 2 assumed in our model. This suggests that we might be able to improve the model by using partial charges instead of the full formal charge. This may indeed improve the ability of the potential to model certain aspects of the system, but one must take care before proceeding in this direction. Partial charge models are less transferable; a parameter set for the O-O interaction developed for MgO will be different from one developed for Al-doped MgO, for example, making comparisons of defect energies more difficult. In addition, while some properties are typically improved when a partial charge model is used, others, such as dielectric constants, can be made worse.[32] Finally, the Bader charge decomposition is one of several such methods for partitioning charge. While we might expect other schemes to give qualitatively similar results, especially for the change in charge transferred among the ions in the defects, the absolute magnitude of transferred charge might differ. Thus, there is no unique value for the transferred charge to use in a partial charge model. For these reasons, while using partial charges may improve our ability to model MgO, we feel that a full charge model is more appropriate for studying a variety of complex materials.

III. DISCUSSION AND CONCLUSIONS

Combining the results from molecular dynamics, molecular statics, temperature accelerated dynamics, and density functional theory reveals an interesting picture for the room-temperature evolution of radiation damage after a low-energy cascade in MgO. Point defects and small clusters form during the first 10 ps after the impact. While vacancies are immobile at room temperature, interstitial ions diffuse quickly. They can either recombine with vacancies, effectively healing the crystal, or aggregate with other interstitials, forming successively larger interstitial clusters. These clusters become more stable with size. They also generally become less mobile with size, but there are some dramatic and important exceptions. For example, the tetrainterstitial is immobile at room temperature, but combining with a di-interstitial can give a hexainterstitial in a long-lived metastable state that diffuses faster than any other species we have observed in MgO. These mobile clusters can thus diffuse over long ranges, interacting and aggregating with clusters from other cascades which will increase the overall damage accumulation rate. In the case of the hexainterstitials and octainterstitials, the long range one-dimensional diffusion along $\langle 110\rangle$ in their metastable states could result in an experimentally detectable signature.

As mentioned above, the potential used in this study does not account for any charge transfer between species. It is important to consider what impact this property of our model has on the results described in this work. The largest effect is in the Coulomb interactions. If charge transfer were allowed, then the charge on individual defects would be reduced and the interaction would be reduced as well. The most immediate consequence of this would be that long-range attraction between oppositely charged defects would be reduced and the time scale for, for example, annihilation would be increased. Interstitials would have to move closer to vacancies in order for there to be a high probability of recombination. There would also likely be differences in the ground state structure, as shown by density functional theory calculations,[33] and migration barriers, though the magnitude of these differences are impossible to know without direct calculation.

The impact of charge transfer on the net-neutral species we describe would likely be much less. The fact that the density functional theory calculations we have done on the di-interstitials and metastable hexainterstitials agree well with the empirical potential calculations suggests that our fully charged model describes these defects well. The DFT calculations also show that the charge transfer among atoms in the metastable hexainterstitial is similar to that in the bulk and that charge transfer does not play a big role in these neutral clusters. Thus, while the behavior we see for charged defects may not be as indicative of their behavior in real MgO, our predicted properties of neutral clusters are likely to be much more reliable.

At this point, it is difficult to directly compare our simulation results with known properties of MgO. Experimental estimates of the vacancy (likely O) migration barrier of 1.9 eV (Ref. 34) agree well with the value of about 2.1 eV predicted by this and other theoretical studies (e.g., see Ref. 36). More recent experiments find a range of activation energies for the annealing of F centers, from 1.9 to 3.4 eV.[35] The interpretation in those experiments is that the value of 3.4 eV corresponds to the diffusion of F centers and that lower values represent more complex mechanisms. The discrepancy between that result and ours may be due to the fact that they are examining the behavior of F^+ and F centers, while our simulations can only consider F^{++} defects at this time. However, whether F centers diffuse with a barrier of 2 eV or 3.4 eV would not change the results presented here; they would be immobile at room temperature in either case. The key result is the fast diffusivity of large interstitial clusters, which is confirmed by our DFT calculations.

Most experimental work on MgO, however, can only reveal properties of larger scale defects, such as interstitial dislocation loops and vacancy voids. We have not addressed the length scales necessary to describe these larger defects. Speculation that the $\langle 100\rangle$ character of the larger clusters in our simulations is connected to the $\langle 100\rangle$ growth direction of some interstitial dislocation loops is, for the moment, exactly that: speculation. In our ongoing effort, we hope to make more direct comparisons between theory and experiment.

We point out that while this study has revealed intriguing properties of defect clusters in MgO, it is not a comprehensive study of all small defects in MgO. We have not examined, for example, the properties of the pentainterstitial, nor some of the other possible small-cluster coalescence processes. Rather, we have focused on the characteristic of defects seen in low-energy cascades. Future work will expand on this.

In summary, combining MD cascade simulations, static energy minimization, temperature accelerated dynamics, and DFT, we find that it is possible to study the radiation damage properties of MgO on time scales relevant to experiment. Complex events are important, and higher level models should account for them in order to simulate the correct damage evolution.

ACKNOWLEDGMENTS

We acknowledge helpful discussions with F. Montalenti, G. Pacchioni, J. H. Harding, and D. J. Harris. This work was supported by the United States Department of Energy, Office of Science, Office of Basic Energy Sciences, Division of Materials Sciences and Engineering.

---

*Permanent address: Department of Mathematical Sciences, Loughborough University, LE11 3TU, UK.

[1] D. J. Bacon and T. D. de la Rubia, J. Nucl. Mater. **216**, 275 (1994).

[2] B. P. Uberuaga, R. Smith, A. R. Cleave, F. Montalenti, G. Henkelman, R. W. Grimes, A. F. Voter, and K. E. Sickafus, Phys. Rev. Lett. **92**, 115505 (2004).

[3] D. R. Olander, *Fundamental Aspects of Nuclear Reactor Fuel Elements*, Technical Information Center, Office of Public Affairs, Energy Research and Development Administration (DOE, Springfield, VA, 1976).

[4] C. Kinoshita and S. J. Zinkle, J. Nucl. Mater. **233–237**, 100 (1996).

[5] W. J. Weber, R. C. Ewing, C. R. A. Catlow, T. D. de la Rubia, L. W. Hobbs, C. Kinoshita, H. Matzke, A. T. Motta, M. Nastasi, E. K. H. Salje, E. R. Vance, and S. J. Zinkle, J. Mater. Res. **13**, 1434 (1998).

[6] K. E. Sickafus, L. Minervini, R. W. Grimes, J. A. Valdez, M. Ishimaru, F. Li, K. J. McClellan, and T. Hartmann, Science **289**, 748 (2000).

[7] M. R. Sørensen and A. F. Voter, J. Chem. Phys. **112**, 9599 (2000).

[8] A. F. Voter, F. Montalenti, and T. C. Germann, Annu. Rev. Mater. Sci. **32**, 321 (2002).

[9] G. V. Lewis and C. R. A. Catlow, J. Phys. C **18**, 1149 (1985).

[10] R. A. Buckingham, Proc. R. Soc. London, Ser. A **168**, 264 (1938).

[11] J. F. Ziegler, J. P. Biersack, and U. Littmark, *The Stopping and Range of Ions in Solids* (Pergamon Press, New York, 1985), Vol. 1.

[12] W. T. Rankin and J. A. Board, Jr., *Proceedings, 1995 IEEE Symposium on High Performance Distributed Computing p 81* (1995).

[13] B. Park, W. J. Weber, and L. R. Corrales, Nucl. Instrum. Methods Phys. Res. B **166–167**, 357 (2000).

[14] R. Smith, *Atom and Ion Collisions in Solids and at Surfaces* (Cambridge University Press, Cambridge, 1997).

[15] F. Montalenti, M. R. Sørensen, and A. F. Voter, Phys. Rev. Lett. **87**, 126101 (2001).

[16] G. Henkelman, B. P. Uberuaga, and H. Jónsson, J. Chem. Phys. **113**, 9901 (2000).

[17] G. Henkelman and H. Jónsson, J. Chem. Phys. **113**, 9978 (2000).

[18] G. Henkelman and H. Jónsson, J. Chem. Phys. **111**, 7010 (1999).

[19] F. Montalenti and A. F. Voter, J. Chem. Phys. **116**, 4819 (2002).

[20] N. F. Mott and M. J. Littleton, Trans. Faraday Soc. **34**, 485 (1932).

[21] M. Leslie, SERC Daresbury Laboratory Tech. Report No. DL/SCI/TM31T., 1982 (unpublished).

[22] *Computer Simulation of Solids*, edited by C. R. A. Catlow and W. C. Mackrodt (Springer-Verlag, Berlin, 1982).

[23] E. A. Kotomin and A. I. Popov, Nucl. Instrum. Methods Phys. Res. B **141**, 1 (1998).

[24] D. J. Bacon, F. Gao, and Y. N. Osetsky, Nucl. Instrum. Methods Phys. Res. B **153**, 87 (1999).

[25] G. Busker, M. A. van Huis, R. W. Grimes, and A. van Veen, Nucl. Instrum. Methods Phys. Res. B **171**, 528 (2000).

[26] T. Brudevoll, E. A. Kotomin, and N. E. Christensen, Phys. Rev. B **53**, 7731 (1996).

[27] R. A. Evarestov, P. W. M. Jacobs, and A. V. Leko, Phys. Rev. B **54**, 8969 (1996).

[28] G. Kresse and J. Hafner, Phys. Rev. B **47**, 558 (1993); **49**, 14 251 (1994); G. Kresse and J. Furthmüller, Comput. Mater. Sci. **6**, 16 (1996); Phys. Rev. B **55**, 11 169 (1996).

[29] G. Kresse and J. Joubert, Phys. Rev. B **59**, 1758 (1999); P. E. Blöchl, *ibid.* **50**, 17 953 (1994).

[30] R. F. W. Bader, *Atoms in Molecules—A Quantum Theory* (Oxford University Press, Oxford, 1990).

[31] G. Henkelman, A. Arnaldsson, and H. Jónsson (unpublished).

[32] R. W. Grimes (unpublished).

[33] E. A. Kotomin, P. W. M. Jacobs, N. E. Christensen, T. Brudevoll, M. M. Kuklja, and A. I. Popov, Defect Diffus. Forum **143–147**, 1231 (1997).

[34] C. Kinoshita and K. Hayashi, Adv. Ceram. **10**, 490 (1985).

[35] A. I. Popov, M. A. Monge, R. González, Y. Chen, and E. A. Kotomin, Solid State Commun. **118**, 163 (2001).

[36] P. W. M. Jacobs, E. A. Kotomin, N. E. Christensen, and T. Brudevoll, Mater. Sci. Forum **239–241**, 391 (1997).